D4.5 REPORT ON UNIFIED AND DATA DRIVEN AIR-INTERFACE FOR 6G-NTN

Revision: v.1.0

Work package	4
Task	Task 4.1
Due date	31/12/2025
Submission date	12/01/2026
Deliverable lead	University of Bologna
Version	1.0
Authors	Carla Amatetti, Bruno De Filppo, Alessandro Vanelli-Coralli (UNIBO), Musbah Shaat, Marius Caus, Husnain Shahid (CTTC), Estefania Recayte (DLR), Chao Zhang C, Eduardo Medeiros, Per-Erik Eriksson (ERIS), Juan Bucheli (QCM), Nathan Borios (TASF), Dorin Panaitopol, Serdar Sahin, Sorya Tong (TH-SIX)
Reviewers	Miguel Angel Vazquez (CTTC), Sebastian Euler (ERIS), Mårten Sundberg (ERIS), Joel Grotz (SES), Mehmet Gurelli (QCM)
Abstract	D4.5 is the last version of the deliverable on the unified and data-driven air interface for 6G non-terrestrial networks (NTN), whose primary purpose is to provide guidance related to the design of the flexible waveform for 6G NTN systems based on the outcomes of the evaluation of a set of waveforms identified by the project as potential candidates for the NTN component of 6G. Deliverable D4.1 identified a set of potential waveforms for 6G NTN (i.e., CP-OFDM, DFT-s-OFDM, WOLA-OFDM, UFMC, F-OFDM, BF-OFDM, and OTFS) and provided their preliminary performance evaluation. Building upon this foundation, deliverable D4.5 extends the analysis by assessing the candidate waveforms under additional key performance indicators (KPIs) and by developing and testing advanced solutions to enable robust system operation under typical NTN impairments, such as high propagation delays and Doppler shifts. The work is organized into three main activities: i) Waveform analysis and comparative evaluation; ii) Definition of wireless propagation models for NTN within the new frequency bands addressed in the project (i.e., C, Q, and V bands) by means of ray tracing simulations of specific scenarios; iii) Design and assessment of advanced solutions for the 6G NTN air interface.

Grant Agreement No.: 101096479
Call: HORIZON-JU-SNS-2022
Topic: HORIZON-JU-SNS-2022-STREAM-B-01-03
Type of action: HORIZON-JU-RIA

Keywords	Waveform, BLER, PSD, channel models, design drivers

Document Revision History

Version	Date	Description of change	List of contributor(s)
V0.1	11/11/2024	Creation of the document	Carla Amatetti, Alessandro Vanelli-Coralli (UNIBO)
V0.2	02/11/2025	Document ready for the internal review	UNIBO, CTTC, DLR, ERIS, QCM, TAS-F, TH-SIX
V1.0	12/01/2026	Approved for submission	Alessandro Vanelli-Coralli (UniBo)

DISCLAIMER

Co-funded by the European Union

6GSNS

Project funded by
Schweizerische Eidgenossenschaft
Confédération suisse
Confederazione Svizzera
Confederaziun svizra
Swiss Confederation
Federal Department of Economic Affairs, Education and Research EAER
State Secretariat for Education, Research and Innovation SERI

6G-NTN (*6G Non-Terrestrial Network*) project has received funding from the Smart Networks and Services Joint Undertaking (SNS JU) under the European Union's Horizon Europe research and innovation programme under Grant Agreement No 101096479. Views and opinions expressed are however those of the author(s) only and do not necessarily reflect those of the European Union. Neither the European Union nor the granting authority can be held responsible for them. This work has received funding from the Swiss State Secretariat for Education, Research and Innovation (SERI).

COPYRIGHT NOTICE

Project co-funded by the European Commission in the Horizon Europe Programme		
Nature of the deliverable:	**R**	
Dissemination Level		
PU	*Public, fully open, e.g., web (Deliverables flagged as public will be automatically published in CORDIS project's page)*	✓
SEN	*Sensitive, limited under the conditions of the Grant Agreement*	
Classified R-UE/ EU-R	*EU RESTRICTED under the Commission Decision No2015/ 444*	
Classified C-UE/ EU-C	*EU CONFIDENTIAL under the Commission Decision No2015/ 444*	
Classified S-UE/ EU-S	*EU SECRET under the Commission Decision No2015/ 444*	

* R: Document, report (excluding the periodic and final reports)
DEM: Demonstrator, pilot, prototype, plan designs
DEC: Websites, patents filing, press & media actions, videos, etc.
DATA: Data sets, microdata, etc.
DMP: Data management plan
ETHICS: Deliverables related to ethics issues.
SECURITY: Deliverables related to security issues
OTHER: Software, technical diagram, algorithms, models, etc.

Co-funded by the European Union

EXECUTIVE SUMMARY

D4.5 is the last version of the deliverable on the unified and data-driven air interface for 6G non-terrestrial networks (NTN), whose primary purpose is to provide guidance related to the design of the flexible waveform for 6G NTN systems based on the outcomes of the evaluation of a set of waveforms identified by the project as potential candidates for the NTN component of 6G.

Deliverable D4.1 identified a set of potential waveforms for 6G NTN (i.e., CP-OFDM, DFT-s-OFDM, WOLA-OFDM, UFMC, F-OFDM, BF-OFDM, and OTFS) and provided their preliminary performance evaluation. Building upon this foundation, deliverable D4.5 extends the analysis by assessing the candidate waveforms under additional key performance indicators (KPIs) and by developing and testing advanced solutions to enable robust system operation under typical NTN impairments, such as high propagation delays and Doppler shifts.

The work is organized into three main activities, described in the following.

i. Waveform analysis and comparative evaluation

- Evaluation of robustness to time and frequency synchronization errors. By testing different values of time and frequency offset, results, in terms of bit error rate (BER) and block error rate (BLER), show that WOLA-OFDM offers a good alternative to CP-OFDM, owing to its enhanced robustness to frequency offset at a small impact on robustness to time synchronization errors.
- Measurement of in-band distortions and out-of-band emissions following the high-power amplifier (HPA) stage and analysis of an additional waveform variant integrating resource block (RB)-level filtering and peak-to-average power ratio (PAPR) reduction, using BF-OFDM and discrete Fourier transform (DFT) spreading, respectively. Numerical results, in the form of total degradation (TD) and adjacent channel leakage ratio (ACLR), indicate that filtering techniques shall be considered secondary to low PAPR techniques for simultaneous in-band and out-of-band emissions reductions at 30 dB of ACLR requirements.
- Assessment of the number and configuration of demodulation reference signals (DMRS) for CP-OFDM and OTFS
  - CP-OFDM: results show that increasing the number of DMRS symbols improves BER under large frequency offsets but not under timing offset. However, adding more than two DMRS symbols per slot does not yield further improvement.
  - OTFS: results show that the impulsive pilot studied in this deliverable provides accurate high time and frequency offset estimation. The higher the number of protecting symbols that surround the pilot, the higher the equivalent power of the pilot, more accurate the estimation of the channel parameters is. However, it comes at the expense of higher PAPR.
- Scoring of the candidate waveforms: the results produced in both D4.1 and D4.5 have been merged to compare the waveforms. The analyses show that there is no waveform better than CP-OFDM in all KPIs. On the contrary, each waveform exhibits distinct trade-offs relative to the evaluated technical metrics.
- Assessment of DFT-s-OFDM PAPR in multi-user multi-beam scenario. In the single-user single-beam scenario, DFT precoding remains the most cost-effective

technique, among the ones considered in this deliverable, for improving TD and ACLR. Thus, the PAPR reduction performance of DFT-s-OFDM and PTS-enhanced DFT-s-OFDM was analyzed over frequency and space division multiplexing. The results show that the PAPR advantage of DFT-s-OFDM over CP-OFDM rapidly collapses with increasing multiuser load in all multiplexing schemes and their orders (either frequency multiplexing, space multiplexing, or their combination).

ii. Definition of wireless propagation models for NTN within the new frequency bands addressed in the project (i.e., C, Q, and V bands) by means of ray tracing simulations of specific scenarios has been conducted.

- Ray tracing simulations are used to obtain the rice factor and the delay spread under three different propagation scenarios, i.e., suburban, urban, dense urban, considering elevation angles in the range of [10°, 90°] with random azimuth angle.

iii. Design and assessment of advanced solutions for the 6G NTN air interface.

- Artificial intelligence (AI) based 6G NTN air interface: two solutions have been explored to tackle the important issues of i) the knowledge of the channel state information at the satellite and the increase of the throughput and ii) the collisions during the random access. Results show that in both cases AI helps to reach the ultimate goal, i.e., on one hand, to predict the channel frequency response that effectively halves the overhead associated with pilot symbols; on the other hand, to learn an optimal policy that minimizes access delay while maintaining a low collision probability. However, hardware implementations of both solutions should be developed to assess the real-world inference latency and verify the real-time feasibility of the considered models under strict power constraints.
- Review and modification of the hybrid automatic repeat request (HARQ) mechanism: maximum-distance separable (MDS)-HARQ approach has been proposed as an effective compromise between reliability and efficiency. The proposed scheme reduces feedback overhead and improves throughput compared to fully disabled feedback, while maintaining competitive reliability performance.
- Assessment and adaptation of the downlink and uplink synchronization procedures during the initial access to work without the global navigation satellite system (GNSS) or with erroneous position information.
  - The downlink synchronization procedure has been modified by including 2 synchronization signal blocks (SSB) for the fine detection, leading to an improvement of 10-25% of the signal detection probability between -15 and -11 dB signal-to-noise ratio (SNR) region
  - For the uplink synchronization procedure, two different solutions have been proposed considering two distinct waveforms:
    - CP-OFDM: SSB and position reference signal (PRS) have been compared as candidate solutions to allow the computation of the user equipment (UE) position after the downlink synchronization. The PRS proves to be a good candidate, due to its flexibility. However, it is not a broadcast signal.
    - OTFS: design of a preamble based on identical Zadoff-Chu (ZC) sequences modulated into a delay–Doppler domain OTFS waveform, which ensures more reliable random-access success under challenging synchronization conditions.

The frequency bands considered, along with the simulated hardware (e.g., definition of the HPA) and channel impairments (such as time and frequency offsets), have been selected to ensure consistency with the reference scenarios and system conditions defined in the 6G-NTN project.

Based on the analyses performed in this project, UNIBO, TASF, TH-SIX, CTTC, and DLR prepared and submitted the technical contribution to 3GPP RAN1 Meeting #122bis, co-signed also by the European Space Agency.

Finally, it is worthwhile noticing that the analysis and conclusions of the 6G-NTN project on the waveforms for 6G NTN align with the decision taken by 3GPP to select as a baseline CP-OFDM and DFT-s-OFDM and to further investigate improvements for the NTN component.

Co-funded by the European Union

TABLE OF CONTENTS

LIST OF FIGURES

LIST OF TABLES

ABBREVIATIONS

3D	Three-Dimensional
6G	Sixth Generation
ACE	Active Constellation Extension
ADC	Analog to Digital Converters
AI	Artificial Intelligence
AWGN	Additive White Gaussian Noise
BER	Bit Error Rate
BFN	Beam Forming Network
BLER	Block Error Rate
BT	Bandwidth Time
CDF	Cumulative Distributed Function
CP	Cyclic Prefix
CPFSK	Continuous-Phase Frequency Shift Keying
CPM	Continuous-Phase Modulation
CQI	Channel Quality Indicator
CSI-RS	Channel State Information Reference Signal
DAC	Digital to Analog Conversion
DD	Delay-Doppler
DFT-s-OFDM	Discrete Fourier Transform spread OFDM
DL	Downlink
DMRS	Demodulation Reference Signal
DRA	Direct Radiating Antenna
DVB-S2	Digital Video Broadcasting Second Generation
DVB-S2X	Digital Video Broadcasting Second Generation - eXtension
F-OFDM	Filtered OFDM
FBMC	Filter Bank Multi-carrier
FDD	Frequency Division Duplex

FDE	Frequency Domain Equalization
FER	Frame Error Rate
FFT	Fast Fourier Transform
FMT	Filtered multitone
FWD	Forward Link
G-OFDM	Generalized OFDM
GI	Guard Interval
GMSK	Gaussian Minimum Shift Keying
GNSS	Global Navigation Satellite System
GSO	Geostationary Orbit
HPA	High Power Amplifier
HW	Hardware
IBO	Input Backoff
ICI	Inter-Carrier Interference
ISFFT	Inverse Symplectic Finite Fourier Transform
ISI	Inter-Symbol Interference
KPIs	Key Performance Indicators
LDPC	Low Density Parity Check
LEO	Low Earth Orbit
LLR	Log Likelihood Ratio
LMMSE	Linear Minimum Mean Square Error
LoS	Line-of-Sight
MCS	Modulation and Coding Scheme
MIMO	Multiple Input Multiple Output
MP	Message Passing
MRC	Maximum-Ratio Combining
MSE	Mean Square Error
MSK	Minimum Shift Keying
MSR	Multiple Signal Representation

NGSO	Non-Geostationary Orbit
NLoS	Non-Line of Sight
NR	New Radio
NTN	Non-Terrestrial Network
OBO	Output Backoff
OFDM	Orthogonal Frequency Division Multiplexing
OOB	Out-of-band emissions
OTFS	Orthogonal Time-Frequency Space
PA	Power Amplifier
PAPR	Peak to Average Power Ratio
PBCH	Physical Broadcast Channel
PDSCH	Physical Downlink Shared Channel
PN	Phase Noise
PSD	Power Spectral Density
PSS	Primary synchronization signal
PTRS	Phase Tracking Reference Signal
PTS	Partial Transmit Sequences
PUSCH	Physical Uplink Shared Channel
RAT	Radio Access Technology
RCS	Return Channel Satellite
RIC	Radio Intelligent Controller
RRM	Radio Resource Management
RS	Reference Signal
RTN	Return Link
RX	Receiver
SC-FDE	Single Carrier FDE
SC-QAM	Single Carrier-Quadrature Amplitude Modulation
SFN	Single Frequency Network
SoA	State of the Art

SSS	Secondary Synchronization Signal
SW	Software
TDD	Time Division Duplex
TDE	Time Domain Equalization
TF	Time-Frequency
TN	Terrestrial Network
TRP	Transmission/Reception Points
TX	Transmitter
UAV	Unmanned Aerial Vehicle
UE	User Equipment
UFMC	Universal Filtered Multi-carrier
UL	Uplink
UW DFT-s-OFDM	Unique Word DFT-s-OFDM
WOLA	Weighted Overlap and Add
ZC	Zadoff-Chu
ZT DFT-s-OFDM	Zero-tail DFT-s-OFDM

1 INTRODUCTION

The broader ambition of the 6G-NTN project is the design of a non-terrestrial network (NTN) component fully integrated into future 6G infrastructure, which allows to meet the vertical industry's needs and consumer market expectations thanks to its greater coverage, increased resilience, and improved sustainability. To achieve this objective, the 6G-NTN project has researched and developed a revolutionary three-dimensional (3D) network infrastructure concept for 6G with the ambition to provide, through unification with the terrestrial network (TN) component, a ubiquitous coverage with high data rate communication at quasi ultra-low latency (in the case of low Earth orbit (LEO) satellites) while providing a disruptive concept of high accuracy and reliable location service. This infrastructure leverages: i) more effective terminals in terms of cost, size, and power consumption, compatible with both TN and NTN access; ii) flexible software defined payloads; iii) a flexible waveform; iv) artificial intelligence (AI)-enhanced radio intelligent controller (RIC) to provide effective radio resource management (RRM) solutions; and v) solutions relying on cloud native architecture and open interfaces mainly focused on securing the communication scheme.

Deliverable D4.5 is the final deliverable on the unified and data-driven air interface for 6G-NTN. The general purpose of this document is to provide insights and guidelines related to the design of the flexible waveform of 6G NTN.

1.1 OBJECTIVE OF THE DOCUMENT

Deliverable D4.1 identified a set of potential waveforms for 6G NTN and provided their preliminary performance evaluation. Building upon this foundation, deliverable D4.5 extends the analysis by assessing the candidate waveforms under additional key performance indicators (KPIs) and by developing and testing advanced solutions to enable robust system operation under typical NTN impairments, such as high propagation delays and Doppler shifts.

The work is organized into three main activities, described in the following.

i. Waveform analysis and comparative evaluation:
   - Evaluation of robustness to time and frequency synchronization errors.
   - Measurement of in-band distortions and out-of-band emissions following the high power amplifier (HPA) stage and analysis of an additional waveform variant integrating resource block (RB)-level filtering and peak-to-average power ratio (PAPR) reduction, using BF-OFDM and discrete Fourier transform (DFT) spreading, respectively.
   - Assessment of the number and configuration of demodulation reference signals (DMRS) for CP-OFDM and OTFS.
   - Scoring of the candidate waveforms.
   - Assessment of the performance of DFT-s-OFDM in multi-user multi beam scenario.

ii. Definition of wireless propagation models for NTN within the new frequency bands addressed in the project (i.e., C, Q, and V bands) by means of ray tracing simulations of specific scenarios.

iii. Design and assessment of advanced solutions for the 6G NTN air interface.

- Design of a deep learning (DL)-based channel predictor and a deep reinforcement learning (DRL)-based adaptive back-off indicator (BI) optimization framework to enhance the random access (RA) procedure.
- Review and modification of the hybrid automatic repeat request (HARQ) mechanism.
- Assessment and adaptation of the downlink and uplink synchronization procedures during the initial access to work without the global navigation satellite system (GNSS).

1.2 STRUCTURE OF THE DOCUMENT

The document is organized in the following way:

- Section 2 describes the KPIs and design drivers of the waveform.
- Section 3 reports the simulation results of the selected waveforms, the scoring of the waveforms, and the analysis of the PAPR in multi-user-multi-beam scenario.
- Section 4 is dedicated to the description of the NTN channel models in C band and Q/V band and reports the outputs of the ray tracing simulations.
- Section 5 provides a state of the art of AI/ machine learning (ML) applied to the PHY layer and to NTN and the designed DL-based channel predictor and DRL-based adaptive BI optimization framework.
- Section 6 focuses on the HARQ protocol and the enhancements agreed upon in 3GPP to enable more efficient HARQ operation in NTN networks. The HARQ protocol combined with maximum-distance separable (MDS) codes is assessed in an NTN scenario with a partial feedback configuration.
- Section 7 is dedicated to the downlink and uplink synchronization procedures in Global Navigation Satellite System (GNSS) free operation.
- Section 8 concludes the deliverable, highlighting the major results and guidance regarding future works for waveform in NTN.

Co-funded by the European Union

2 AIR INTERFACE/WAVEFORMS FEATURES AND KPIS

To evaluate the candidate waveforms for the NTN component of 6G, which are intended to meet the requirements identified in this project, specifically in D2.3 'Report on system requirements', a comprehensive list of desirable features is presented in this chapter. Then, a set of KPIs has been selected to rigorously assess the candidate waveforms. The KPIs were carefully chosen to provide a robust framework for assessing the performance of each waveform candidate in meeting the specific demands and objectives of the NTN scenario.

In Section 2.1, the set of features is introduced and their relationship to the project's objectives are detailed. In Section 2.2 the set of KPIs is described.

2.1 WAVEFORM DESIGN FEATURES

In this section, we provide an outline of the desired features based on their importance level attributed by the project consortium. The rationale for considering specific features when choosing the waveform is provided, along with an explanation of how waveform design affects these features. Following this discussion, Table 1 presents a summary of the prioritized features and their implications in NTN waveform design.

- F1: Compatibility with terrestrial network

Compatibility with the terrestrial network refers to the capability for the waveform to be utilized in both TN and NTN in the context of 6G to seamlessly coexist and interact. This compatibility holds significance as it ensures several key functionalities and advantages within the 6G ecosystem. Firstly, it facilitates seamless handover between terrestrial and non-terrestrial networks, ensuring seamless connectivity for users moving between different coverage areas or network types. Secondly, it promotes device compatibility, i.e., enabling devices (i.e., User Equipment - UE) to operate seamlessly across both terrestrial and non-terrestrial networks without necessitating significant modifications or additional hardware (i.e., using the same chipset), thereby enhancing user experience and device versatility. Finally, utilizing a compatible waveform across TN and NTN components simplifies hardware design and implementation, reducing overall complexity and cost associated with network deployment and maintenance.

- F2: Possibility for spectrum sharing

The possibility for spectrum sharing, facilitated by a flexible waveform design, denotes the capability to allocate and utilize available frequency bands efficiently across both TN and NTN. This feature enables a sharing of spectrum resources under various scenarios and use cases, enhancing spectrum utilization efficiency and accommodating diverse network requirements. Spectrum sharing between TN and NTN needs a compatible design of waveform for seamless coordination and allocation of spectral resources between TN and NTN networks, allowing for optimized utilization with minimal interference or degradation of service quality.

- F3: Robustness to co-channel interference

Robustness to co-channel interference refers to the network's ability to maintain reliable and effective communication when facing interference from signals transmitted on the same frequency channels. This ensures that the NTN system can provide a large coverage in a cost-effective manner, while also enabling the possibility to properly coexist with terrestrial network deployments.

- F4: Possibility for seamless connectivity

This feature ensures continuous and reliable connectivity for UE across diverse deployment scenarios and geographical regions, regardless of the type or location of the NTN platform being accessed. A well-designed waveform for NTN facilitates seamless connectivity by enabling efficient handovers and seamless transition between TN and NTN, thus ensuring good end-user experience throughout the coverage area.

- F5: Ability to provide an additional link margin

The ability to provide an additional link margin (especially in C band, where regular smartphones are expected to operate) refers to the air interface's capability to improve the signal strength and reliability, particularly to accommodate users in light indoor and in-vehicle environments in NTN. These scenarios typically involve increased penetration loss, requiring an enhanced link margin to ensure reliable communication.

- F6: Support of accurate network-based positioning

Support of accurate network-based positioning refers to one waveform's capacity to facilitate robust localization capabilities, allowing network operators to accurately track the geographic locations of UE devices for various applications, such as emergency services, location-based services, and network optimization. This could entail, for example, the provision of dedicated pilot symbols or reference signals within the waveform to enable precise timing and phase measurements for accurate estimation of UE positions within the network infrastructure. Furthermore, waveform parameters, such as symbol duration, subcarrier spacing, and transmission power levels, can be carefully optimized to balance between localization accuracy and spectral efficiency.

- F7: Support to UE without GNSS receiver

The support for UE without GNSS refers to the air interface's capability to enable UE connectivity to NTN for UEs without GNSS support or in scenarios where GNSS signals are unavailable or unreliable, such as indoor environments or areas with limited GNSS visibility. This feature ensures that UE can establish and maintain communication with NTN platforms without relying on GNSS-based location services. In 5G NTN, the UE uses its position and satellite ephemeris information to compensate for Doppler shift, introducing a dependency on GNSS availability.

- F8: Backward compatibility with 5G

Backward compatibility with 5G refers to the ability of the air interface to integrate with and support existing 5G New Radio (NR) standards. This feature ensures that 6G NTN can leverage the infrastructure, devices, and protocols established by 5G deployments, promoting smooth migration paths from 5G to 6G. By maintaining backward compatibility, the air interface promotes immediate compatibility with 5G smartphones and devices, enabling efficient utilization of existing network resources and enhancing the user experience across both 5G and 6G networks.

- F9: Support of Frequency Division Duplexing (FDD) and Time Division Duplexing (TDD)

By supporting both FDD and TDD, the air interface enables flexibility in spectrum utilization. The choice between FDD and TDD modes depends on specific deployment scenarios and use cases, with each mode offering distinct advantages in terms of spectral efficiency, coverage, and latency management.

- F10: Computational complexity

Computational complexity in the context of air interface design refers to the level of computational resources required for the signal processing, e.g., modulation, demodulation, error correction, and other algorithms needed for efficient communication within the network.

This aspect is crucial as it directly impacts the efficiency, performance, and scalability of the network infrastructure. For NTN, the computational complexity may influence the payload design and overall capacity, since satellites may be power limited. Minimizing computational complexity ensures that the network operates effectively, meeting communication demands while optimizing resource utilization and minimizing energy consumption.

Table 1: *Summary of the waveform features*

Name	Definition
Compatibility with terrestrial network	If TN and NTN 6G components have a compatible waveform, that would improve 1) seamless handover between the networks, 2) device compatibility, 3) potential to integrate and use 5G/6G infrastructure, 4) coexistence 5) hardware complexity
Possibility for spectrum sharing	It is desirable to have a waveform design that allows efficient spectrum sharing between TN and NTN.
Robustness to co-channel interference	The network should be able to maintain reliable and effective communication in the presence of interference from signals transmitted on the same frequency channels.
Possibility for seamless connectivity	The air interface should support seamless connectivity to NTN platforms including flying nodes, NGSO satellites, and GEO satellites.
Ability to provide an additional link margin (especially in C band)	To serve smartphone users in light indoor and in-vehicle conditions, the air interface should be able to provide additional link margin to combat extra penetration loss.
Support of accurate network-based positioning	Dedicate pilot signals or reference symbols to facilitate accurate timing and phase measurements for accurate positioning.
Support to UE without GNSS	UE should still be able to connect to NTN when GNSS is not available or unreliable, such as indoor environment.
Backward compatibility with 5G	3GPP 5G NR specifications support NTN since Release 17. An air interface having backward compatibility with 5G will benefit from 5G flexibility and immediate compatibility with 5G smartphones.
Support of FDD and TDD	Supporting both FDD and TDD enables more deployment possibilities when spectrum is scarce (or only available for one type of duplexing). The choice of using FDD or TDD is dependent on scenarios and use cases.
Computational complexity	The air interface design should ensure that the network operates effectively while minimizing the demand on processing resources.

2.2 WAVEFORMS KPIS

In the previous section, we present the desired features within the NTN framework, which can be addressed by having a flexible waveform design. To assess the performance of waveform candidates, we have carefully chosen several KPIs, and ordered them based on their importance levels (from high to low). By using these KPIs, researchers and stakeholders can systematically evaluate different waveform candidates and make decisions regarding their

suitability. Additionally, these KPIs offer valuable insights into the trade-offs involved in waveform design, helping to refine the process for optimal performance and functionality.

Below we provide the definitions of various KPIs selected in the project. Table 2 summarizes the information presented in the text and the metric used to evaluate the KPI.

- K1: Spectral efficiency

Efficient utilization of the spectrum is essential to meet demanding data rate requirements. In this project, we consider operating frequency bands including C band and Q/V band. These frequency bands are limited and possibly shared among multiple services. Evaluating waveform spectral efficiency helps maximize the utilization of available spectrum resources, enabling more efficient communication, and accommodating more users within the allocated frequency bands.

- K2: Robustness to Doppler

NTN is used under a high Doppler environment (as opposed to TN). It is particularly important to test the 6G-NTN waveform against high Doppler to choose the most adapted 6G-NTN waveform with high resilience to Doppler. In NTN, UE must calculate the relative speed and Round-Trip Time (RTT) of the service link, for timing and Doppler resolution. There is also a proposition to connect UEs to NTN without relying on GNSS support. Instead, UEs can be localized using standalone Radio Access Technology (RAT) methods, thereby establishing a connection with NTN. Enhancing the waveform design to exhibit improved robustness to Doppler in the NTN scenario can significantly increase the feasibility of UEs connecting to NTN without GNSS support.

- K3: Flexibility/scalability

Waveform flexibility refers to the ability of a communication system to adapt and adjust its waveform parameters to meet varying requirements, conditions, or constraints. A flexible design of waveforms in NTN system allows the network to operate in multiple frequency bands, different bandwidth, various scenarios, etc. The flexible design can also enhance network scalability, i.e., increase the coverage, harmonize different use cases and improve the resource management of the NTN system.

- K4: Robustness to Timing error

Timing error variation for NTN has to be considered especially for Low Earth Orbit (LEO) satellite scenarios. It is particularly important to test the 6G-NTN waveform against timing errors. Furthermore, in TDD setups, a waveform design resilient to timing errors leads to notable enhancements in synchronization performance. This improvement, in turn, enhances overall performance in TDD networks. By addressing timing error challenges through appropriate waveform design, NTN can achieve heightened efficiency, accuracy, and reliability, particularly in LEO scenarios and TDD networks.

- K5: PAPR/PA backoff

Power amplifiers can introduce non-linear distortion when operating near their saturation point. High peak to average power ratio (PAPR) signals may exceed the amplifier's linear range, leading to distortion and intermodulation products. Evaluating PAPR allows for determining the required power amplifier (PA) backoff, which ensures the amplifier operates within its linear range, minimizing distortions and maintaining signal quality. The performance of the PA is evaluated by comparing its output backoff to input backoff (OBO-IBO) characteristics. This is particularly important in non-terrestrial networks where signal degradation due to non-linear distortion can have a significant impact on system performance. Specifically, this improvement in the link budget will be particularly advantageous in scenarios such as light indoor

environments or when users are in vehicles, where additional penetration loss occurs due to the material blockage.

- K6: Robustness against phase noise

Phase noise refers to the random fluctuations in the phase of a signal, which can occur due to various factors such as imperfections in oscillators or frequency synthesizers. Phase noise affects all types of transmitters and receivers, but especially where high-quality oscillators may not be feasible for economical or other reasons.

Phase noise levels increase with carrier frequency. In this project, we have a candidate frequency band i.e., Q/V band, operating at mm-wave bands, where signals are more sensitive to phase noise.

By designing waveforms that are robust to phase noise, NTNs can maintain reliable communication links and efficient deployment of communication systems in space.

- K7: Out-of-band emissions (OoBE)

Non-terrestrial networks often coexist with other communication services and systems, such as terrestrial wireless networks, other satellite systems, or radio astronomy observatories. Evaluating out-of-band emissions helps ensure that the non-terrestrial network's emissions do not cause harmful interference to these coexisting services. This coexistence is crucial for maintaining harmonious operation, preventing service degradation, and fostering efficient utilization of the radio spectrum. This will also impact the adjacent-channel interference since the co-existence of 6G-NTN and 6G-TN is also within the scope of the study of the project.

- K8: Robustness to frequency-selective channels

The use of very narrow beams in NTNs can substantially reduce the frequency selectivity of the channel. By tightly focusing the transmission beams, the received signal experiences less multipath propagation and reduces the effects of frequency-selective fading. In scenarios where Line-of-Sight (LoS) propagation is dominant, the channel may reduce to a single tap, indicating minimal frequency selectivity.

On the contrary, extreme bandwidths can increase the frequency selectivity of the channel. A wider bandwidth results in a larger range of frequency components, potentially leading to greater variations in attenuation and phase distortion across the frequency spectrum.

The impact and importance of frequency selectivity for waveform design in NTN are strongly dependent on the specific use case.

- K9: Robustness to time-selective channels

Generally, a propagation channel is time selective when the transmitted signal is reflected and scattered (multi-path propagation) and not stationary. In NTN scenarios, in most cases the propagation path can be seen as a LoS for outdoor users, making the channel less time selective. However, due to the interest in ubiquitous coverage it is desirable to serve users in Non LoS (NLoS) conditions, with high time-dispersion as well. Good candidate waveforms are expected to provide high robustness to time-selective channels.

Table 2: *Summary of the waveform KPIs*

Name	**Metrics for evaluation**	**Definition**
Spectral efficiency	Bit/s/Hz	To maximize data throughput while ensuring efficient spectrum use.
Robustness to Doppler	BER, BLER	The fast movement of LEO satellites and high carrier frequency create large Doppler shifts in NTN system.
Flexibility/scalability	-	The ability to operate in multiple frequency bands, different bandwidths, various scenarios in NTN system.
Robustness to timing error	BER, BLER	Precise time synchronization is required to ensure system performance in NTN.
PAPR/HPA IBO-OBO	BER, BLER, TD for a given IBO level	Power amplifiers can introduce non-linear distortion when operating near their saturation point. High PAPR signals may exceed the amplifier's linear range, leading to distortion and degraded performance.
Robustness to phase noise	BER, BLER	Phase noise levels increase with carrier frequency. Choosing waveforms that are robust to phase noise is crucial for reliable operation and increased coverage.
Out of Band Emission	ACLR, SEM	Evaluating out-of-band emissions helps ensure that the NTN's emissions do not cause harmful interference to coexisting services (e.g., coexist with TN).
Robustness to frequency selective channel	BER, BLER	Frequency selective fading becomes more prominent in NTN scenarios due to high mobility and/or dynamic channel conditions. Techniques such as adaptive modulation, coding and MIMO compatibility are crucial in waveform design to combat the issue.
Robustness to time selective channel	BER, BLER	The movement of satellites and the high operating frequency, such as in the Q/V band, introduces time selectivity to the channel.

3 WAVEFORMS COMPARISON

In D4.1, we retained for assessment and simulation in the 6G-NTN identified scenarios the following waveforms:

- Cyclic Prefix (CP)-Orthogonal Frequency Division Multiplexing (OFDM)
- Weighted Overlap and Add (WOLA)-OFDM
- Discrete Fourier Transform (DFT)-spread (s)-OFDM
- Filtered-OFDM (F-OFDM)
- Block Filtered – OFDM (BF-OFDM)
- Universal Filtered Multi-Carrier (UFMC)
- Orthogonal Time Frequency Space (OTFS)

In particular, we compared them in terms of Bit Error Rate (BER), Block Error Rate (BLER), Peak to Average Power Ratio (PAPR), and Power Spectral Density (PSD) considering both hardware impairments due to the phase noise and high-power amplifiers (HPA), as well as channel impairments, such as Tapped Delay Channel (TDL) models in both LoS and NLoS, for instance NTN-TDL-D (with 50 and 100 ns as delay spread) and NTN-TDL-A (with 50 ns of delay spread), respectively.

Thus, this section aims at continuing the comparison among the identified waveforms considering other impairments. In particular, the robustness to time and frequency synchronization errors is studied. Likewise, in order to expand the performance study in terms of out-of-band emissions and in-band distortion, the adjacent channel leakage ratio (ACLR) and total degradation (TD) for the considered waveforms are taken into account. Next, drawing on its relation to ACLR and TD, we look into the impact of the main multiple access schemes of relevance frequency division multiplexing (FDM) and space division multiple access (SDMA) on the PAPR for the challenging case of downlink in NTN in section 3.4.

3.1 IMPACT OF HARDWARE AND CHANNEL IMPAIRMENTS ON THE WAVEFORM

3.1.1 Satellite using active antennas

The satellite industry has significantly turned towards active antenna usage especially for massive LEO constellations. Modern satellites can generate simultaneously tens or hundreds of beams at the same time. For active antenna systems represented in Figure 1 with hundreds or thousands of antenna elements, each radiant element is responsible for the amplification of the sum of the uncorrelated signals to be sent in all beams. In these conditions, the input signal PAPR before amplification will be high regardless of the waveform characteristics. This is simply explained by the result of the sum of numerous uncorrelated signals sharing the same frequency band. As a consequence, the PAPR challenges/requirements that need to be overcome for future satellite payload designs using active antenna are not necessarily waveform specific, since they are more related to the number of carriers/beams used at the same time by the satellite payload. For this reason, OFDM-based waveforms are good candidates for the future and existent satellite communications [1]-[4] giving the simplicity of the transmission/ reception (TX/RX) and flexibility of the resource allocation. However, “transparent” PAPR reduction methods (e.g., clipping and filtering, weighted overlap and add, etc.) may still be used.

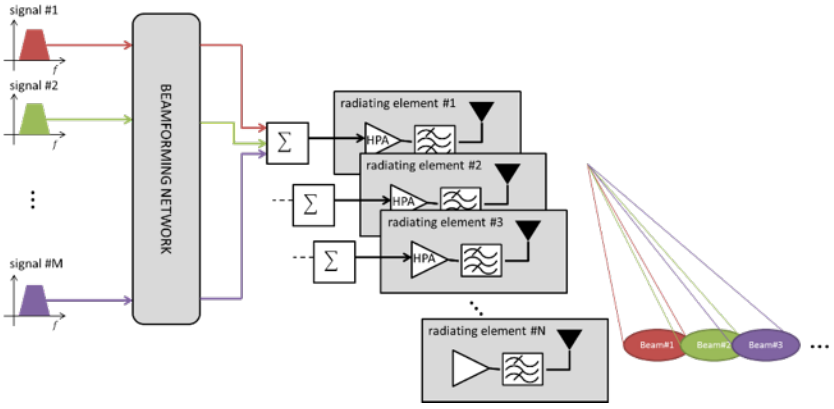

Figure 1: *Active antenna architecture with beamforming capabilities*

A similar example can be also given for a more classic architecture with very high throughput legacy satellite payloads requiring up to 2.9 GHz transmission bandwidth (see for instance the downlink (DL) of Ka-bands n512, n511, n510), where a single HPA might be used for transmission of several carriers to one or to multiple different beams. As a matter of fact, this is a classical/traditional implementation for high-capacity geostationary Earth orbit (GEO) satellites.

Very high throughput satellite (VHTS) payloads are composed of several tens of traveling-wave tube amplifier (TWTA). A TWTA amplifies several gigahertz of bandwidth (typically 2.9 GHz in Ka-band but it can be less). Typically, the satellite operator will plan several time division multiplexing (TDM) carriers on this frequency band that will be redirected on several satellite beams (e.g., 4 beams). Each carrier will occupy its own sub-band. An illustration of such configuration is given in Figure 2.

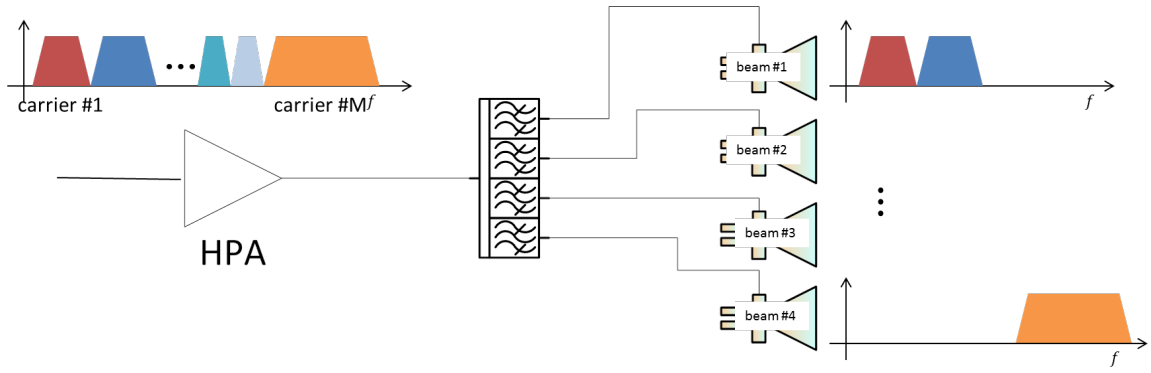

Figure 2: *Example of VHTS amplification architecture*

If we make the reasonable assumption that 200 Mbps digital video broadcasting second generation satellite extension (DVB-S2X) carriers are used, then it means that at least 5 to 10 carriers will be simultaneously amplified by the same HPA. As a consequence, the input signal PAPR will increase significantly with respect to the case where a single DVB-S2X carrier is considered, as it can be seen in Figure 3, where PAPR outage probability is compared between a DVB-S2X signal using one APSK carrier (see left-hand side sub-figure, where a 6dB power back-off is required for a 10^{-4} PAPR outage probability) and a DVB-S2X signal using ten APSK carriers (see right-hand side sub-figure, where a 9dB power back-off is required for a 10^{-4} PAPR outage probability).

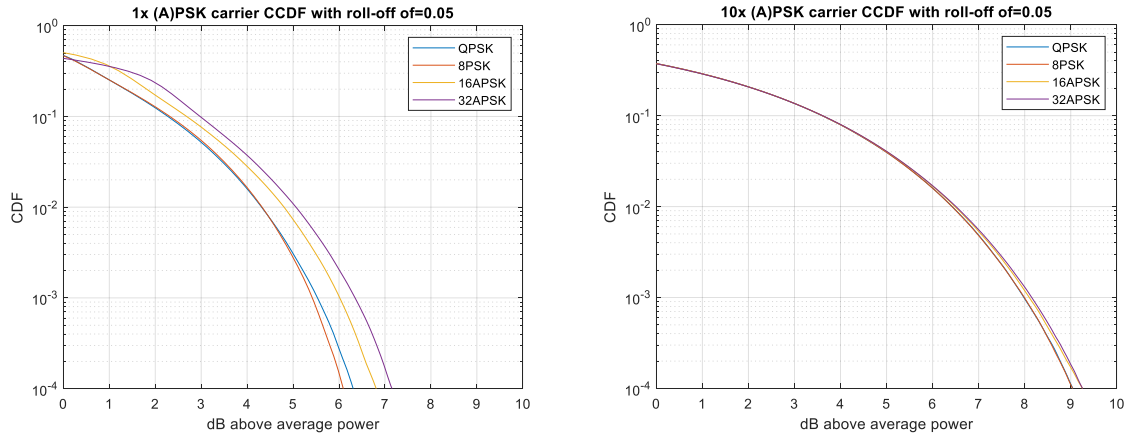

Figure 3: *CCDF of 1 (A)PSK and 10 (A)PSK carriers*

In VHTS payload, it is common to have several carriers amplified simultaneously by the same amplifier. Therefore, at the end, even for high-throughput satellites, the PAPR of a signal composed from several DVB-S2X carriers will be comparable with the PAPR of an OFDM-based (4G/5G) signal. For this reason, even for GEO VHTS payloads, OFDM-based waveform is now a very reasonable implementation option.

3.1.2 Time and frequency synchronization errors

In non-geostationary (NGSO) systems, Doppler effects are more pronounced than in terrestrial networks due to the higher relative velocity between satellites and users. Propagation delays on the service link are also longer than those observed in terrestrial systems. Both delay and Doppler shift can be compensated. 3GPP NTN uses UE-based pre-compensation in the uplink, based on GNSS and a broadcast System Information containing satellite ephemeris. Other approaches use proprietary methods in the downlink to calculate compensation values for the beam center. In all cases, residual errors persist. On the one hand, in the uplink, they are caused by GNSS inaccuracies; on the other hand, in the downlink, they depend on the reduced compensation accuracy for users located away from the beam center or errors in the post-compensation process at the UE side. Although these synchronization errors are smaller than the initial Doppler shifts and propagation delays, they can still significantly impair system performance.

Impact of misalignment due to frequency synchronization errors in the case of single user access may be readily studied via numerical simulation by combining the complex-baseband signal representation with the complex exponential $e^{(j2\pi\varepsilon T_s n)}$ as presented in ***Figure 4***, where ε is the frequency synchronization error in Hertz, T_s represents the sampling interval in seconds, and n is the sample time discrete index.

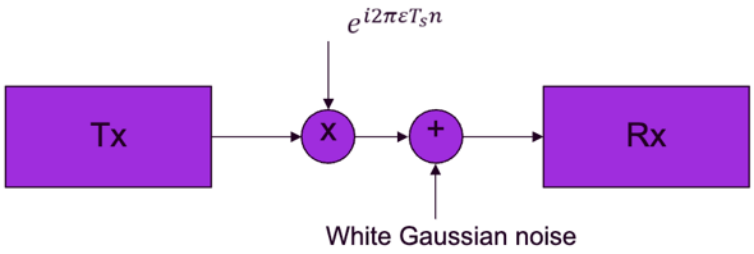

Figure 4: *Simulation blocks for frequency synchronization errors*

As shown in ***Figure 5***, misalignment in frequency causes the loss of orthogonality between subcarriers as they are not anymore *sampled* at their maxima and nulls, inducing both signal-to-noise ratio (SNR) losses and inter-carrier interference (ICI). Likewise, frequency misalignment causes attenuation and phase rotation to the constellation at the receiver side, in addition to inter-symbol interference (ISI) in the case of DFT-spread precoding [5]. Consequently, the assessment of the relative detriment of the considered waveforms under these impairments is of high importance for NTN.

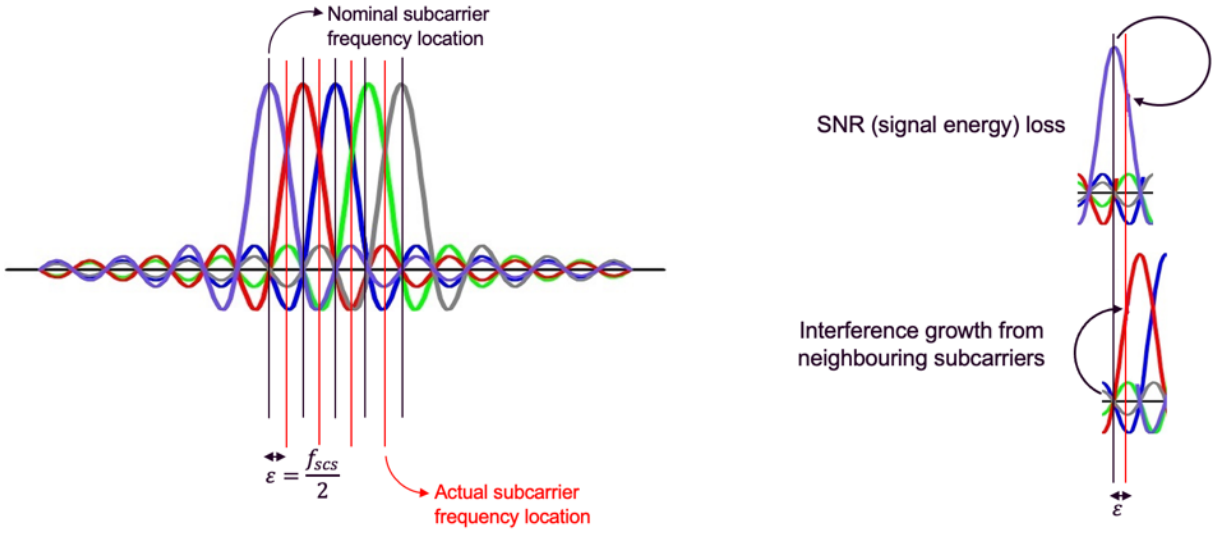

Figure 5: *SNR loss and ICI introduced by frequency synchronization errors*

Time synchronization errors produce two effects on the signal as perceived by the receiver:

- A circular shift on the complex-baseband for drifts within the window of protection of the CP, as well as,
- SNR degradation and inter-symbol interference for misalignments beyond the window of protection of the CP.

The above-mentioned window of protection of the CP depends on several factors, such as the FFT window placement at the receiver side, the effective CP length, among others. As may be easily verified, the placement of the FFT window determines the location of the protection window, albeit retaining its length or size.

In what follows, without loss of generality, the FFT window will be placed at the end of the symbol duration as shown in Figure 6.

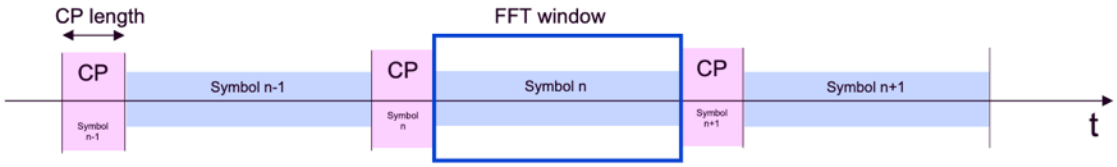

Figure 6: *Negligible time offset*

As pictured in ***Figure 7***, it is possible to observe that the robustness to the time misalignments is provided by the cyclic prefix, and that the region of tolerated misalignments corresponds to time drifts within the range [0, CP].

Indeed, within the window of protection, the receiver effectively evidences no ISI, but a circular shift that can be estimated and compensated. As can be further verified, the window of tolerance may easily be centered around zero, i.e., for a tolerance to drifts within [-CP/2, CP/2], by centering the FFT window in the symbol duration (including CP).

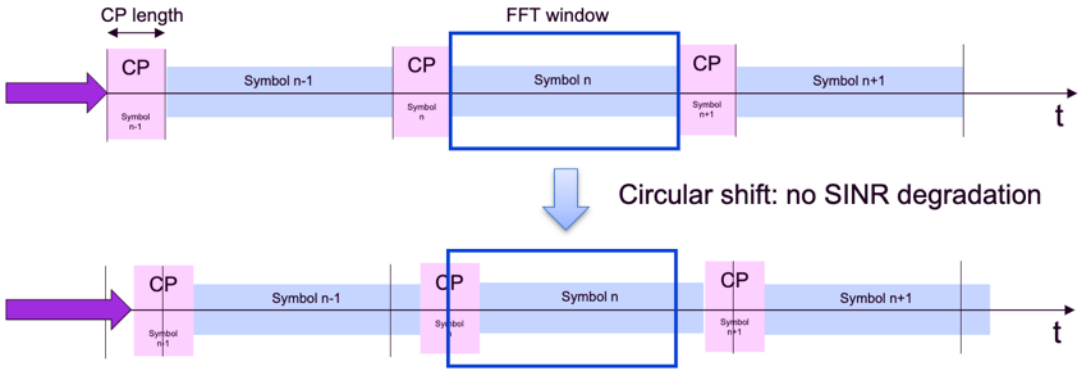

Figure 7: *Time offsets within the window of protection of the CP*

Alternatively, as observed in ***Figure 8***, ISI and energy loss appear as the time drift gets outside the window of protection of the CP:

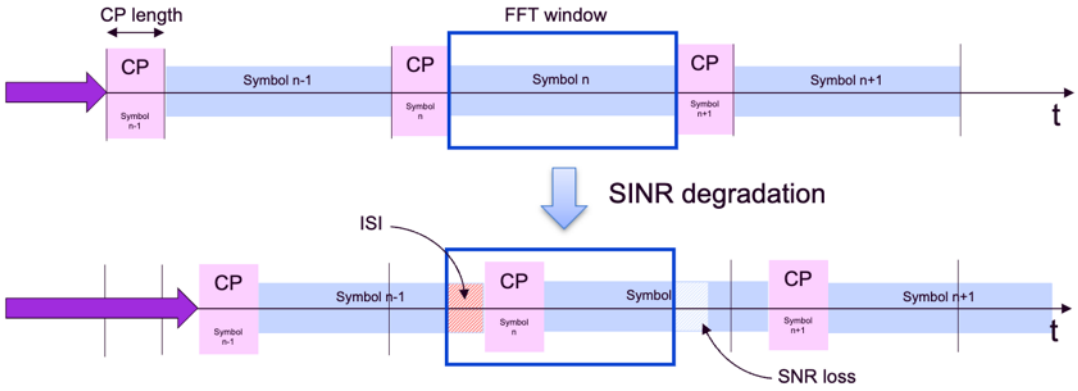

Figure 8: *Time offsets beyond the window of protencion of the CP*

In what follows, the receiver will be assumed to compensate for the circular shift (e.g., by applying an opposite linear phase ramp in the frequency domain), thereby assuming perfect time drift information at the receiver side. The latter, as such a step is common across waveforms and extrinsic to the waveform itself. Therefore, we will analyze and compare the ability of the considered waveforms to withstand the unavoidable ISI and ICI related to residual time synchronization errors [5].

3.2 NUMERICAL RESULTS

3.2.1 Robustness to time and frequency synchronization errors

For this analysis, we identified the two scenarios reported in ***Table 3***. The robustness of waveforms will therefore be evaluated in terms of their BER and BLER performance against time and frequency synchronization errors.

Table 3: *Simulation parameters for time & frequency synchronization errors*

Parameters				Q1	C3
TX	SCS			120kHz	30 kHz
	# PRBs			32	133
	Modulation			QPSK	
	Code rate			679/1024	
	Rv			0	
	# OFDM symbols			12	
	# DMRS symbols			1	
Channel	AWGN		SNR values	[0,5,10] dB	
	Fading channel	NTN TDL D	Delay spread		50ns
			K factor		First tap K=11.707dB
	Impairments		Normalized Doppler on the SCS	Values in the range $[10^{-4}, 10^{-1}]$	
			Normalized delay on symbol duration	Values in the range [0, 8192] round(256*logspace(0, log10(8192/256), 20))	
RX	Synchr.		Algorithm	Not considered	
	Channel Estimation		Algorithm	MMSE	
	Equalization		Algorithm	MMSE	

3.2.1.1 Scenario Q1

Figure 9 shows the uncoded BER and ***Figure 10*** shows the BLER of the considered OFDM-based waveform variants (left plot) and OTFS (right plot) in the presence of frequency synchronization errors. The introduced frequency offset is expressed in units of frequency

normalized on the sub-carrier spacing (SCS). From these two figures, it is possible to observe that most OFDM-based waveforms, as well as OTFS, withstand similarly to the considered frequency offsets under this scenario.

We note, however, that the UFMC variant shows an inferior performance due to ISI related to filter dispersion beyond its guard interval (see [6]), on top of suffering from its waveform-specific noise enhancement [8]. Remarkably, and unlike in previous studies [6], DFT-s-OFDM does not exhibit a superior performance despite its reduced PAPR as power amplifier degradations are not considered for this study. Finally, OTFS follows closely the performance of most considered waveforms variants in both BER and BLER metrics. This is primarily because the interference caused by CFO follows a sinc-like dependence.

Notably, the sensitivity to frequency offset grows with SNR as its contribution to the performance detriment becomes more predominant relative to noise. Therefore, three distinct regions of operation can be formulated depending on whether BER/BLER degradation is dominated by noise (region I), by frequency offset (region III), and one of which corresponds to the intermediate region where the transition takes place (region II).

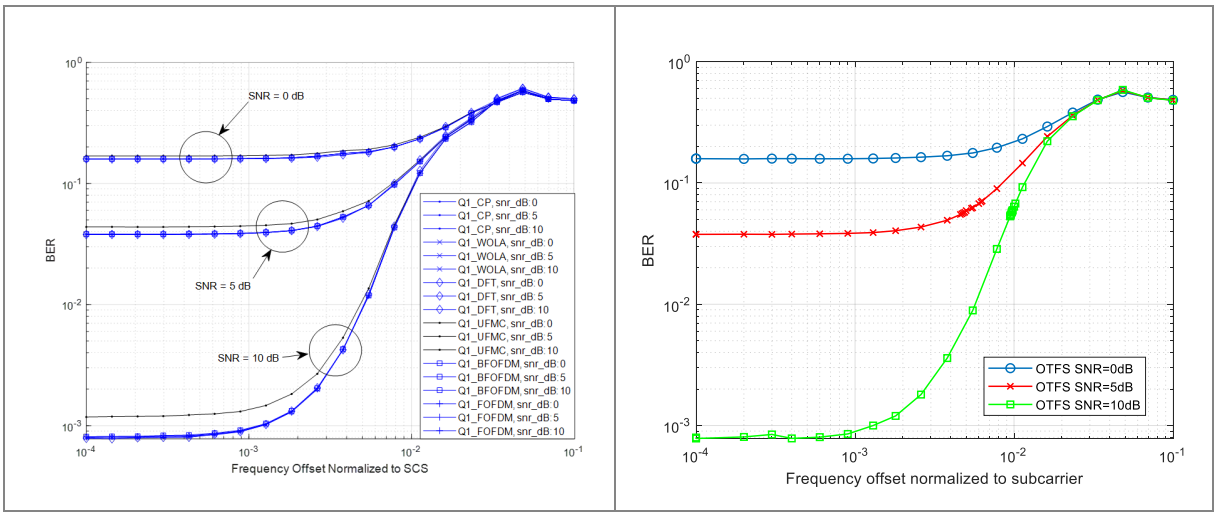

Figure 9: *BER for the considered OFDM-based waveform variants (left) and OFTS (right) in the presence of frequency synchronization errors over the Q1 scenario. Frequency drift $\in [10^{-4}, 10^{-1}]$ normalized to subcarrier spacing and SNR $\in$ [0, 10] DB*

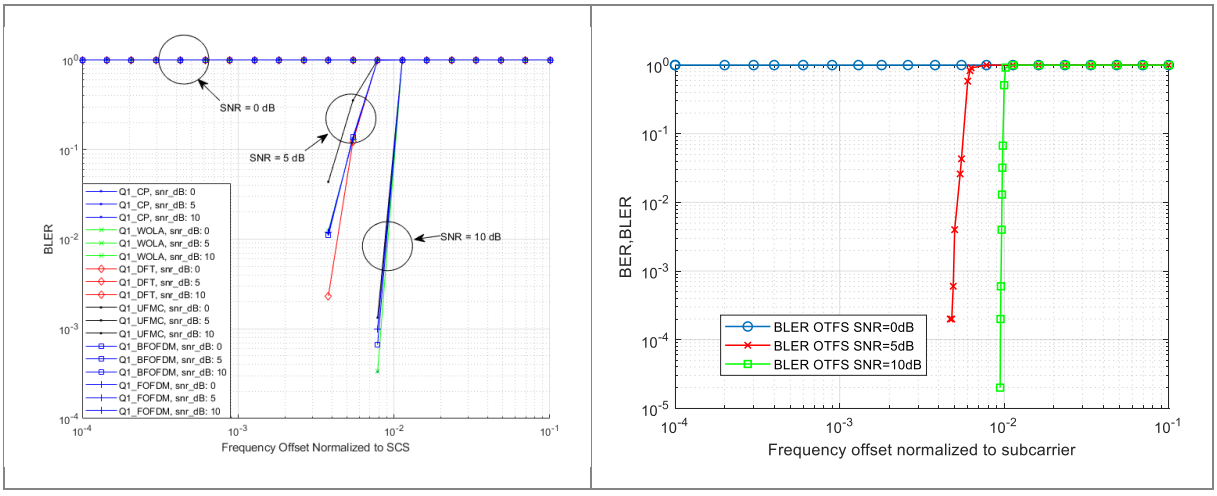

Figure 10: *BLER for the considered OFDM-based waveform variants (left) and OFTS (right) in the presence of frequency synchronization errors over the Q1 scenario. Frequency drift $\in [10^{-4}, 10^{-1}]$ normalized to subcarrier spacing and SNR $\in$ [0, 10] DB*

Taking as reference the uncoded BER performance of CP-OFDM, Figure 11 delineates what the abovementioned regions of operation may look like, as well as surface and contour plots for a range of values for the SNR and frequency offset, namely 0 dB to 12 dB and 10^{-4} to 10^{-1}, respectively.

The so-called region I comprises the noise-limited region, where performance is less dominated by the impact of frequency offset. As we can see, the contour plot shows lines roughly parallel to the frequency offset axis resulting from its independence to synchronization errors within this region. On the contrary, region III involves performance dominated by energy loss and interference linked to the loss of orthogonality for a significant frequency offset [5]. Likewise, we may observe that the contour plot shows lines parallel to the SNR axis resulting from its independence to noise within this region. Finally, within region II, noise and frequency offset related degradations dominate similarly as the transition between region I and III occurs.

It is worth highlighting that, as a rough approximation, region I can be observed to extend up to 10^{-3} of frequency offset normalized to SCS, which may be adopted as a conservative limit of tolerance to frequency misalignment. The latter can be further said about most waveforms as observed in ***Figure 9*** where in fact these show a relatively constant BER performance up to such a synchronization error limit.

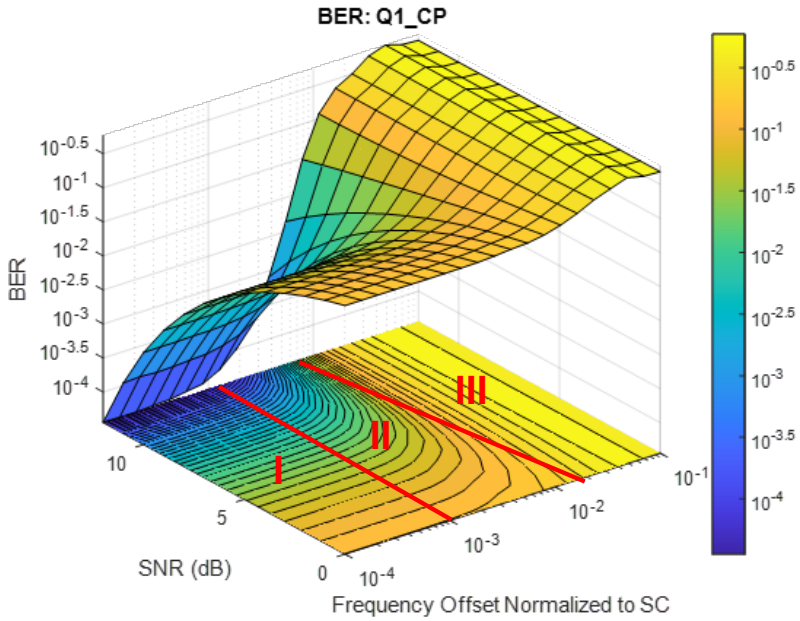

Figure 11: *Contour and surface plot of BER OF CP-OFDM in the presence of frequency synchronization errors and AWGN over the Q1 scenario*

Moreover, Figure 12 shows the BER performance of all waveform variants relative to that of CP-OFDM in terms of the so-called BER loss, whose percentage is computed as follows:

$$BER_{loss} = \left[\frac{BER}{BER_{CP-OFDM}} - 1\right] \times 100$$

Based on the visualization of Figure 12, the following is concluded:

a. Filtered waveform variants (UFMC, BF-OFDM and F-OFDM) show a similar dependence with SNR in region I and II due to the impact of the filter dispersion on ISI [5] [6]. The degradation is especially noticeable in the case of UFMC due to its additional noise enhancement limitation [8]. On the other hand, the low yet positive

BER loss at higher frequency offset values (especially by region III) confirms that ICI is not significantly reduced by the RB-level (i.e., UFMC and BF-OFDM) nor full-band (i.e., F-OFDM) filtering waveform variants. Indeed, the BER loss remains low within region III for these variants possibly because the intercarrier interference (ICI) is dominated by contributions from immediately neighboring subcarriers, which are not sufficiently absorbed by the improved frequency localization of the considered waveforms.

b. WOLA's improved performance (i.e., negative degradation), albeit minor, is linked to the improved phase continuity of the windowing, overlapping and addition operations [7].

c. DFT-s-OFDM exhibits a higher degradation above 10^{-2} of frequency offset within region III due to the additionally induced ISI, in contrast to the sole ICI observed in the case of CP-OFDM [5]. Despite the latter, BER loss remains low (under 5%) throughout the evaluated SNR and frequency offset ranges.

d. Across region I, OTFS maintains robust performance with minimal degradation. The BER loss remains low across the SNR range, which indicates high resilience to minor frequency synchronization errors. In region II, the BER exhibits negative degradation but trends upward toward zero as the combined effects of noise and frequency offset grow, reinforcing OTFS's superiority over CP-OFDM in this transitional regime. When entering region III, the BER loss for OTFS shifts to low positive values at the highest offsets; however, the degradation remains bounded.

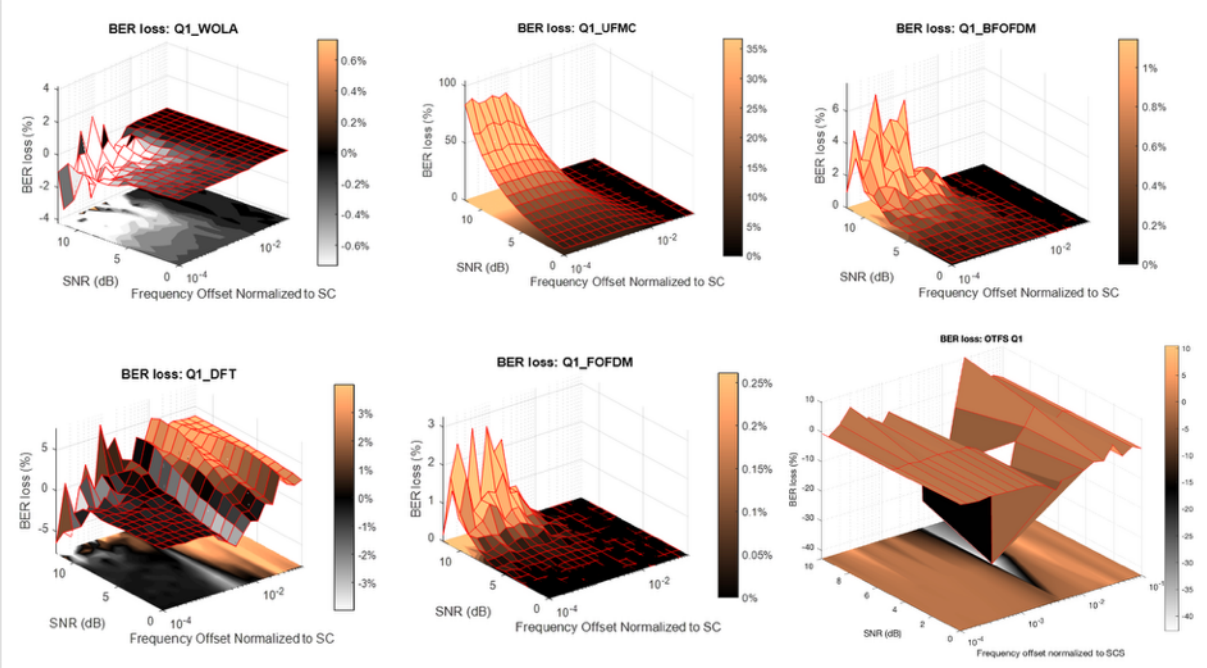

Figure 12: *BER loss for the considered waveform variants relative to CP-OFDM in the presence of frequency synchronization errors over the Q1 scenario*

3.2.1.2 Scenario C3

The previous analysis is reproduced over scenario C3 in this section, where a TDL-based fading channel is considered. As before, ***Figure 13:*** *BER for the considered OFDM-based waveform variants (left) and OTFS (right) in the presence of frequency synchronization errors over the c3 scenario. Frequency drift ∈ [10-4, 10-1] normalized to subcarrier spacing and SNR ∈ [0, 10] DB* and ***Figure 14:*** *BLER for the considered OFDM-based waveform variants (left)*

and OTFS (right) in the presence of frequency synchronization errors over the c3 scenario. Frequency drift ∈ [10-4, 10-1] normalized to subcarrier spacing and SNR ∈ [0, 10] DB show the performance of the OFDM-based waveform variants and OTFS in terms of their uncoded BER and BLER.

The considered waveforms display a performance akin to that observed in scenario Q1. Despite the latter, and unlike scenario Q1, DFT-s-OFDM provides a relative benefit with respect to OFDM-based variants in the uncoded BER due to its improved frequency diversity, resulting from the spreading of symbols in the frequency domain. Nevertheless, as observed in the BLER of ***Figure 14:*** *BLER for the considered OFDM-based waveform variants (left) and OTFS (right) in the presence of frequency synchronization errors over the c3 scenario. Frequency drift ∈ [10-4, 10-1] normalized to subcarrier spacing and SNR ∈ [0, 10] DB*, the superiority of DFT-s-OFDM over the alternative waveforms disappears once channel coding is considered. OTFS shows improved performance in the high SNR regime, where the estimation of the channel coefficient is more reliable.

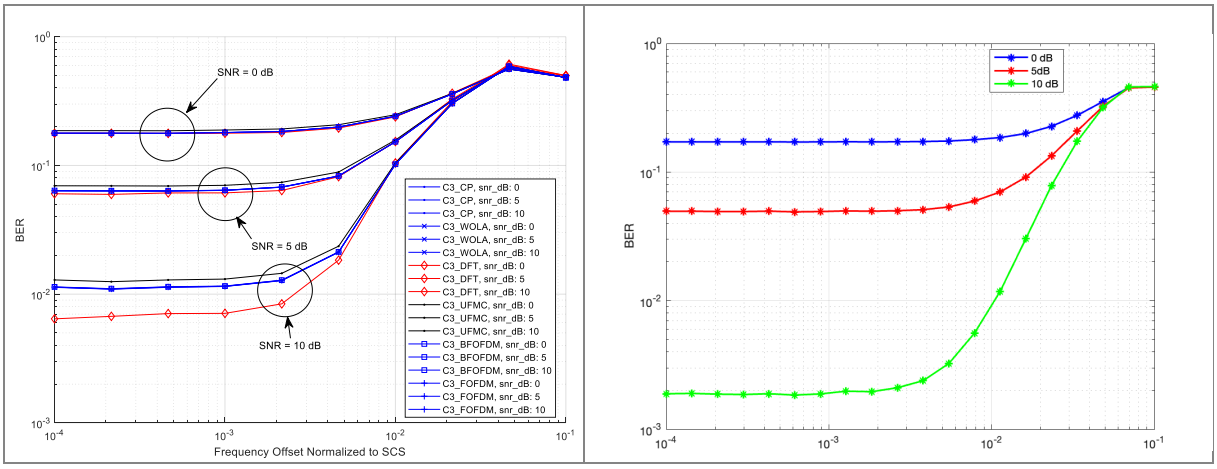

Figure 13: *BER for the considered OFDM-based waveform variants (left) and OTFS (right) in the presence of frequency synchronization errors over the c3 scenario. Frequency drift ∈ [10-4, 10-1] normalized to subcarrier spacing and SNR ∈ [0, 10] DB*

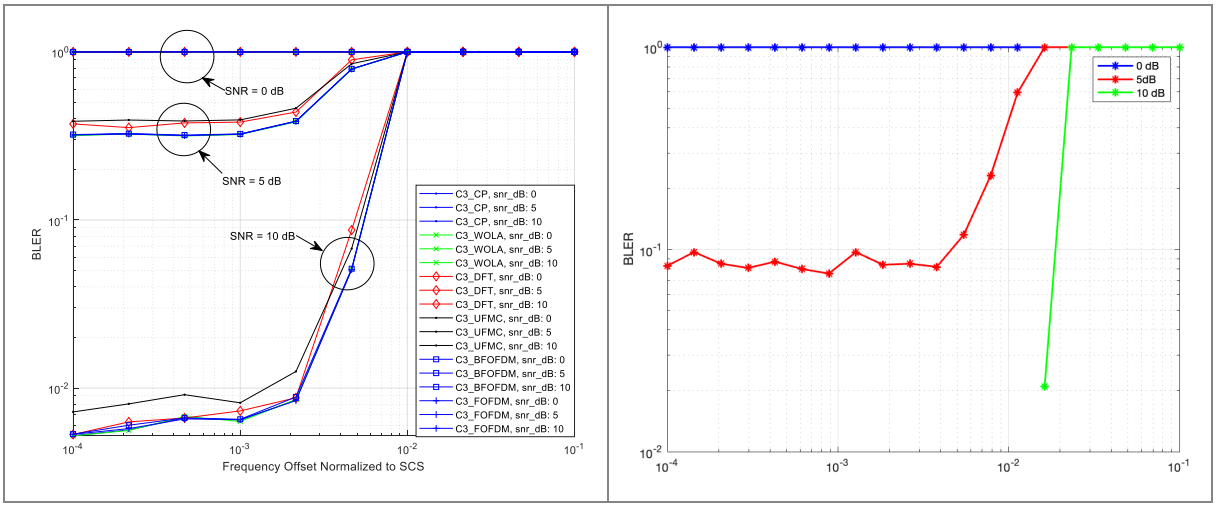

Figure 14: *BLER for the considered OFDM-based waveform variants (left) and OTFS (right) in the presence of frequency synchronization errors over the c3 scenario. Frequency drift ∈ [10-4, 10-1] normalized to subcarrier spacing and SNR ∈ [0, 10] DB*

Directing our attention to the uncoded BER over CP-OFDM, FIGURE 15 shows its regions of operation as a function of the SNR and frequency offset. As highlighted above, the same three regions as in scenario Q1 may be roughly identified, namely: region I, the noise limited region, where performance is not noticeably impacted by frequency offset; region III, the interference limited region, where performance is largely insensitive to noise; and region II, where noise and interference related degradations are of competing magnitudes.

As previously highlighted, the contour lines in FIGURE 15 are roughly parallel within region I up to a roughly equivalent value of $10^{-3}$of frequency offset. Thus, CP-OFDM can be seen as offering a strong tolerance to frequency offsets up to that order in this scenario as well.

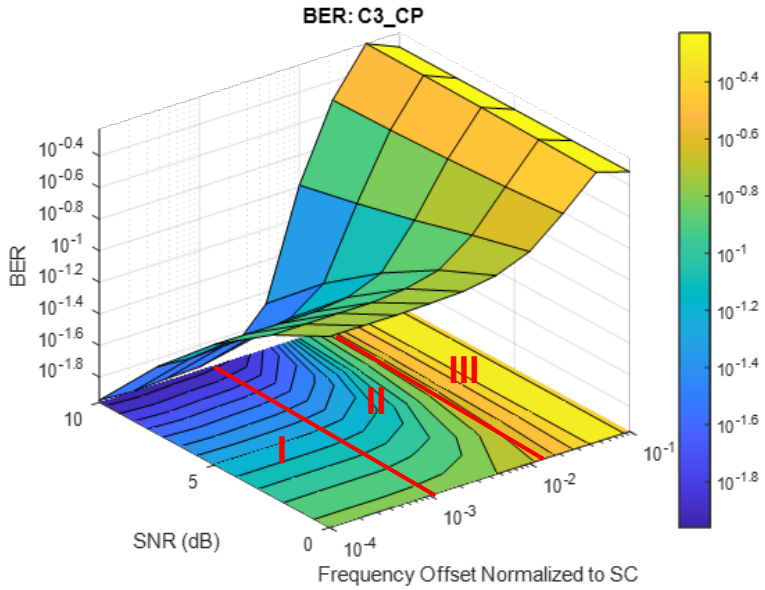

Figure 15: *Contour and surface plot of BER for CP-OFDM in the presence of frequency synchronization errors and AWGN over the C3 scenario*

Finally, FIGURE 16 provides the percentage BER loss for the remaining waveform variants with respect to CP-OFDM, to recall:

$$BER_{loss} = \left[\frac{BER}{BER_{CP-OFDM}} - 1\right] \times 100.$$

It is possible to observe that filtered variants degrade with increasing SNR within region I due to their intrinsic ISI [6], with UFMC particularly impacted by noise enhancement [8], as observed in scenario Q1. Likewise, WOLA exhibits a minor increase in robustness to ICI related to residual frequency synchronization errors due to its enhanced frequency containment and improved symbol transitions with respect to CP-OFDM [7].

Finally, as observed and highlighted in FIGURE 16, DFT-s-OFDM shows an enhanced robustness (i.e., a negative BER loss) due to its improved frequency diversity and reliance over the frequency selective TDL-A channel model for scenario C3. Likewise, OTFS shows a negative BER loss owing to its improved robustness to multipath channels, where the delay of each path is an integer multiple of the delay resolution. As for the Q1 scenario, region II is the part where OTFS provides better performance compared to CP-OFDM.

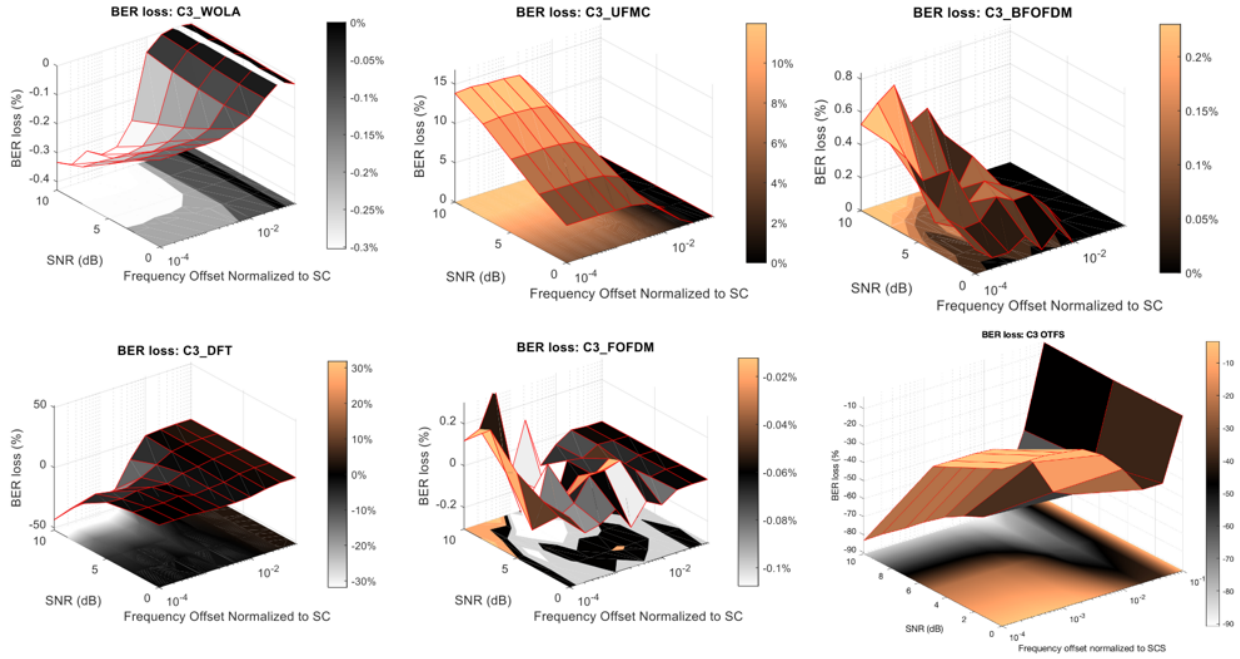

Figure 16: *BER loss for the considered waveform variants relative to CP-ofdm in the presence of frequency synchronization errors over the C3 Scenario*

3.2.2 Robustness to time synchronization errors

This section is devoted to the analysis of the impact of misalignment due to time synchronization errors in the case of single-user access.

3.2.2.1 Scenario Q1

To begin, ***Figure 17*** shows the contour plot of the uncoded BER for CP-OFDM, which helps (as in the previous study on robustness to frequency synchronization errors) to identify the regions of operation of the waveform. We can distinguish the same three operating regimes as in the previous section, namely: the noise-limited region (region I), where performance is not noticeably degraded by time drifts; an interference-limited region (region III), where the degradation is dominated by ISI and ICI and, therefore, performance is not sensitive to SNR; lastly, the intermediate region (region II), where noise and interference related degradations are of competing magnitude. The interested reader is referred to [5] for a characterization of the ISI and ICI degradations linked to such time drifts in the case of CP-OFDM.

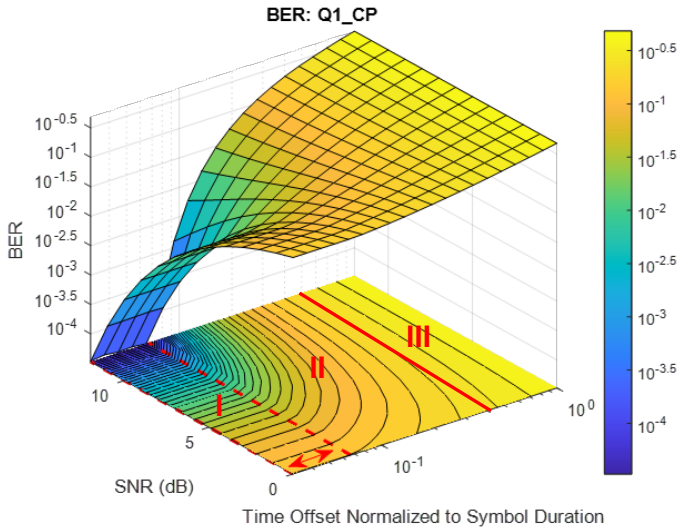

Figure 17: *Contour and surface plot of BER of CP-OFDM in the presence of residual time synchronization errors and AWGN over the Q1 Scenario*

Correspondingly, Figure 18 shows the uncoded BER: the left side picture shows the performance of the waveforms considering both positive and negative time offsets at 10 dB of SNR; while in the plot on the right side only positive time offset are simulated under 0, 5, and 10 dB of SNR. As evidenced, it is possible to observe that most of them perform well under the Q1 scenario for offsets within the window of protection. However, WOLA, UFMC, and BF-OFDM undergo a tapering around the boundaries of the effective CP protection window related to the involved filtering/windowing processes. Indeed, by looking at ***Figure 18***, one may notice how smoothing of the sharp beginning and end of the protection window results from filters effectively dispersing energy into neighboring symbols.

On the contrary, F-OFDM does not suffer a noticeable impact relative to CP-OFDM by virtue of its short filter. Importantly, the reliance of a guard interval instead of a CP [6] in the case of UFMC, as well as its filtering and noise enhancement [8], cause it to exhibit a shift of the protection window, as well as tapering and degradation in its nominal BER performance, respectively.

Lastly, as observed in ***Figure 19***, unlike in the case of OFDM variants, OTFS maintains a relatively flat BER curve across varying time offsets. This robustness arises because the time offset range is lower than the CP duration. It is important to remark that the CP can be longer for OTFS than for OFDM variants. However, the overhead is not increased as a single CP block is appended at the beginning of the slot rather than on a symbol-by-symbol basis as in OFDM. This suggests that SNR is not degraded if the time offset is within the CP block. In such a case, the performance is more tied to the SNR regime of operation than the time misalignment. OTFS ability to maintain steady BER across time offsets implies potential advantages in high-mobility environments if sufficient SNR is present.

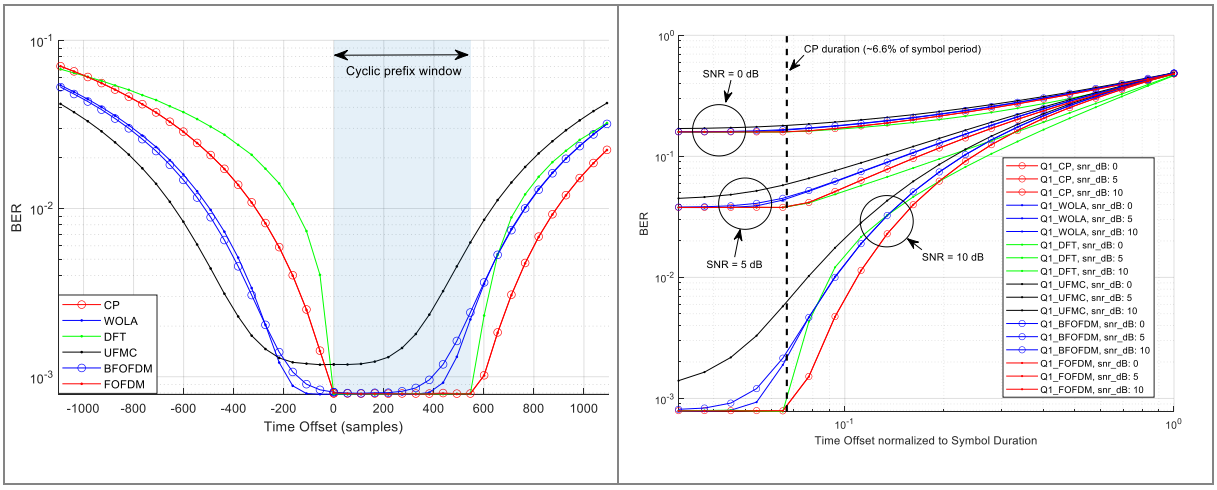

Figure 18: *BER in the presence of residual time synchronization errors over the Q1 scenario. Time drift ∈ [-1024, 1024] samples and 10 dB of SNR, left. Time drift ∈ [3 x 10^{-2}, 1] normalized to symbol duration and SNR ∈ [0, 5, 10] DB, RIGHT*

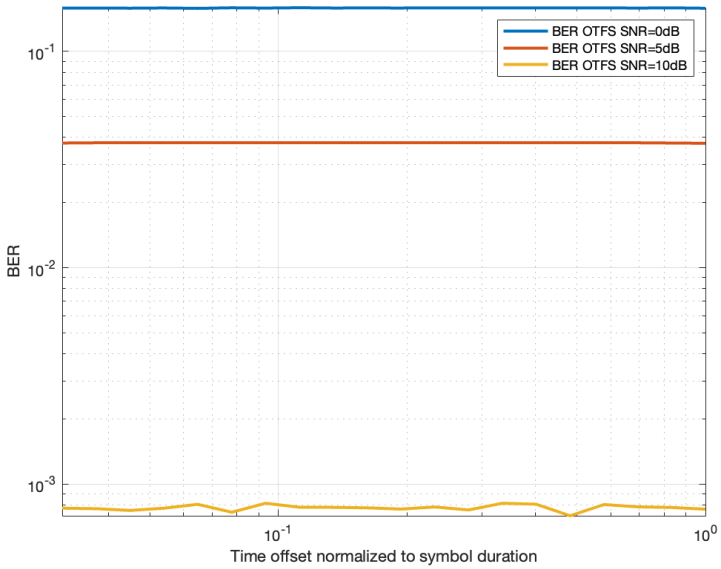

Figure 19: *OTFS BER in the presence of residual time synchronization errors over the Q1 scenario*

3.2.2.2 Scenario C3

The analysis is now performed for scenario C3. As observed in ***Figure 20*** and ***Figure 21***, most OFDM-based waveforms perform well for offsets within the CP protection window, in agreement with observations for the Q1 scenario. Accordingly, WOLA, UFMC, BF-OFDM exhibit the tapering in the boundaries of the effective CP protection window related to filtering process and additional channel dispersion. In the case of UFMC, noise enhancement explains the degradation of its performance at lower time offsets [8].

Unlike the Q1 scenario, but as also evidenced in the study on the robustness to frequency synchronization errors, the DFT-s-OFDM waveform variant provides a benefit here, especially at high SNR, attributed to the increased frequency diversity in the C3 frequency fading scenario. Finally, as expected, F-OFDM sees almost no detriment relative to CP-OFDM, by virtue of its short filter length.

As in Q1 scenario, OTFS maintains a relatively flat BER curve across varying time offsets, however at 10 dB of SNR a variation of the BER mainly due to the TDL. Overall, this robustness arises because the time offset range is lower than the CP duration.

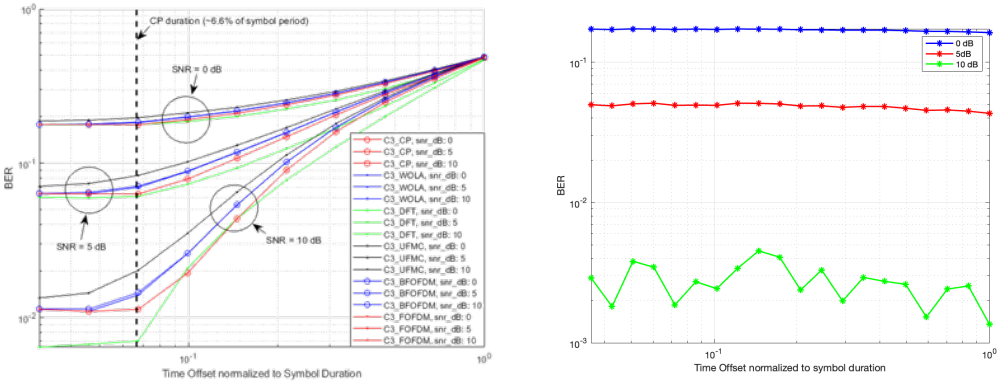

Figure 20: *BER in the presence of residual time synchronization errors over the C3 scenario. Time offset ∈ [3 X 10^{-2}, 1] normalized to symbol duration and SNR ∈ [0, 10] DB*

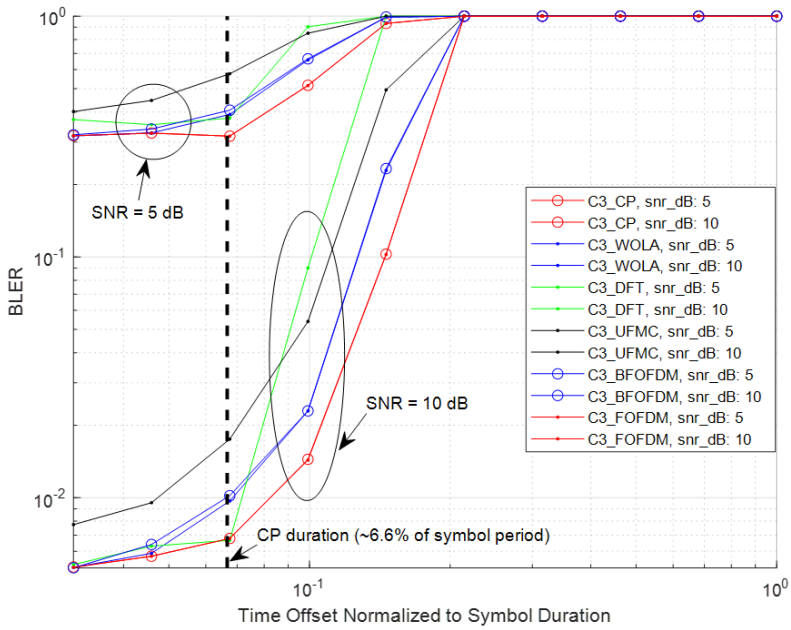

Figure 21: *BLER in the presence of residual time synchronization errors over the C3 scenario. Time drift ∈ [3 X 10^{-2}, 1] Normalized to symbol duration and SNR ∈ [5, 10] DB*

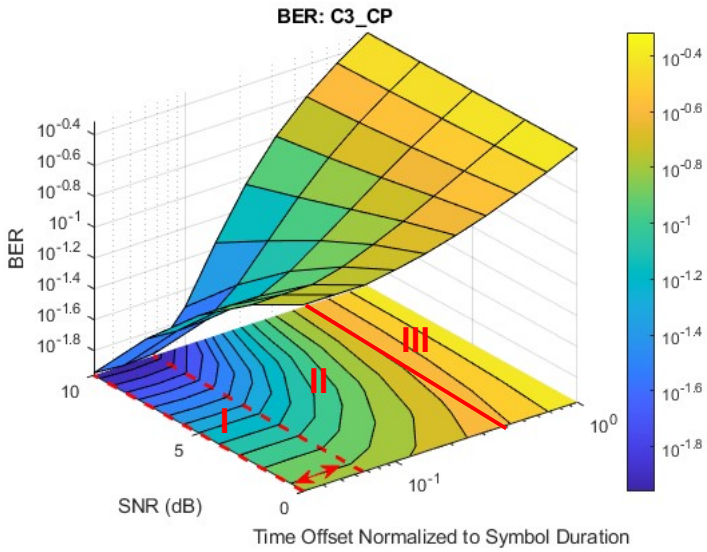

Figure 22: *Contour and surface plot of BER for CP-OFDM in the presence of residual time synchronization errors and AWGN over the C3 scenario*

Finally, the contour plot in ***Figure 22*** helps locate the different regions of operation for CP-OFDM over the C3 scenario. As in the previous cases, three regions may be identified: the noise limited region (region I), where performance is not sensitive to time offset thanks to the CP protection window; the interference limited region (region III), where the degradation performance is less sensitive to noise as it is dominated by ISI and ICI [5]; and region II, where the transition of the impact between noise and interference occurs.

3.2.3 Assessment of DMRS configuration for time and frequency synchronization errors

3.2.3.1 Analysis for CP-OFDM waveform

In terrestrial networks, it is common to employ additional DMRS signals for channel estimation and decoding when channel quality is challenging. For NR, 3GPP has specified several DMRS allocation patterns. This subsection explores the performance of BER results when additional DMRS signals are allocated in NTN scenarios.

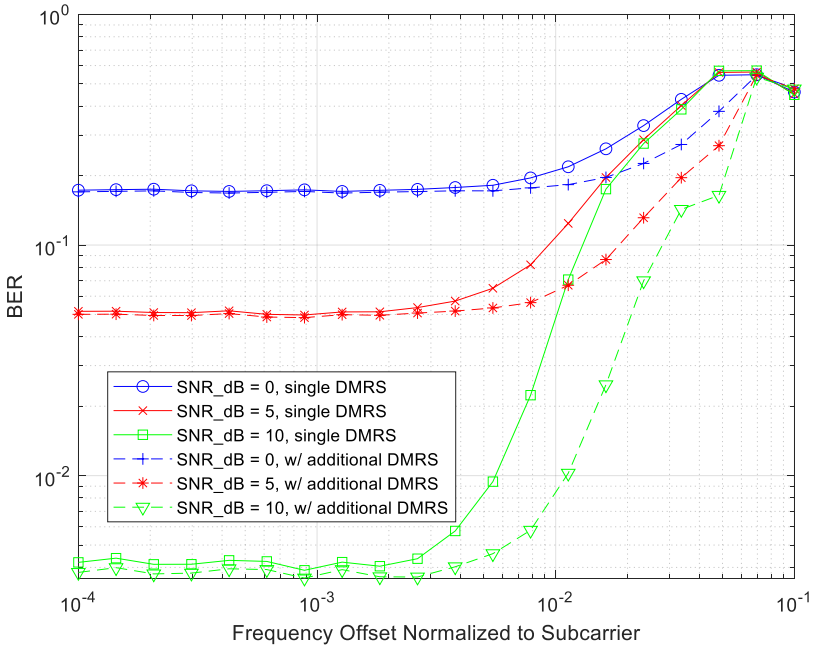

Figure 23: *CP-OFDM BER vs frequency offset with more than one DMRS. Scenario Q1*

Figure 23 illustrates the impact of additional DMRS across different SNR levels (0 dB, 5 dB, and 10 dB) compared to single DMRS configurations in Q1 scenario. For SNR of 0 dB, the performance with additional DMRS shows a marginal improvement over single DMRS, indicating limited benefit at low SNR. At SNR of 5 dB and 10 dB, the curves with additional DMRS exhibit a steeper decline in error rates as frequency offset increases, demonstrating a clear advantage in maintaining decoding performance under larger frequency deviations.

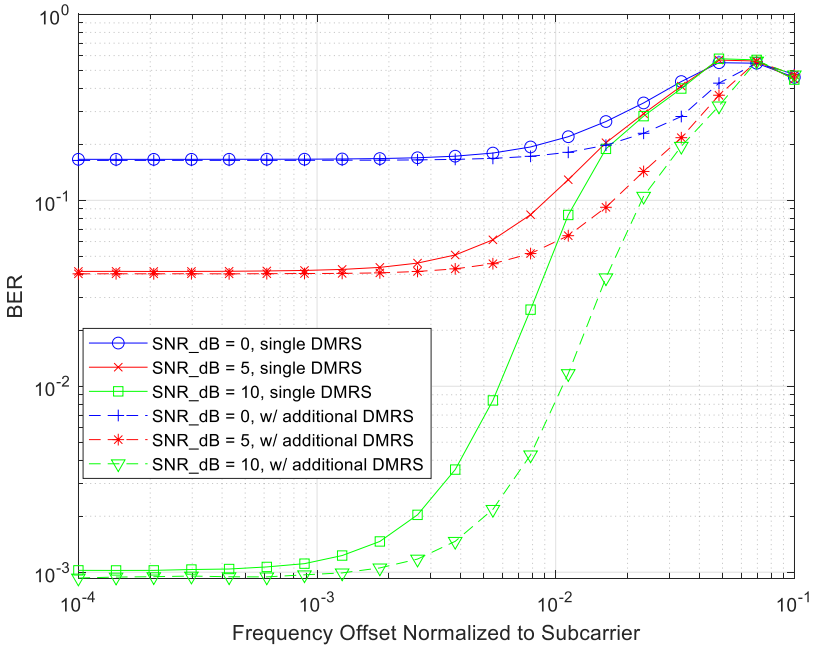

Figure 24: *CP-OFDM BER vs frequency offset with more than one DMRS. Scenario C3*

Figure 24 further supports this trend with results in C3 scenario. The plots for SNR of 0 dB, 5 dB, and 10 dB with additional DMRS consistently outperform their single DMRS counterparts. Notably, at SNR of 10 dB with additional DMRS, the error rate drops significantly even at higher frequency offsets, highlighting the effectiveness of additional DMRS in enhancing synchronization and decoding accuracy in challenging NTN environments.

To further study the impact of different DMRS patterns on the system performance, we extend the analysis to a broader and more challenging set of scenarios. The objective is to comprehensively assess the robustness of four DMRS configurations under diverse channel dynamics, focusing on DL performance at SNR = 5 dB and 10 dB. The DMRS configurations follow 3GPP NR specification [9]. The extension considers realistic Doppler spread in C band, high-mobility UEs, and Doppler variation in Q/V band within one slot.

3.2.3.1.1 C3 scenario with Doppler spread component

In this scenario, we consider the Doppler spread effect on the channel model under two UE speeds of 3km/h and 50km/h.

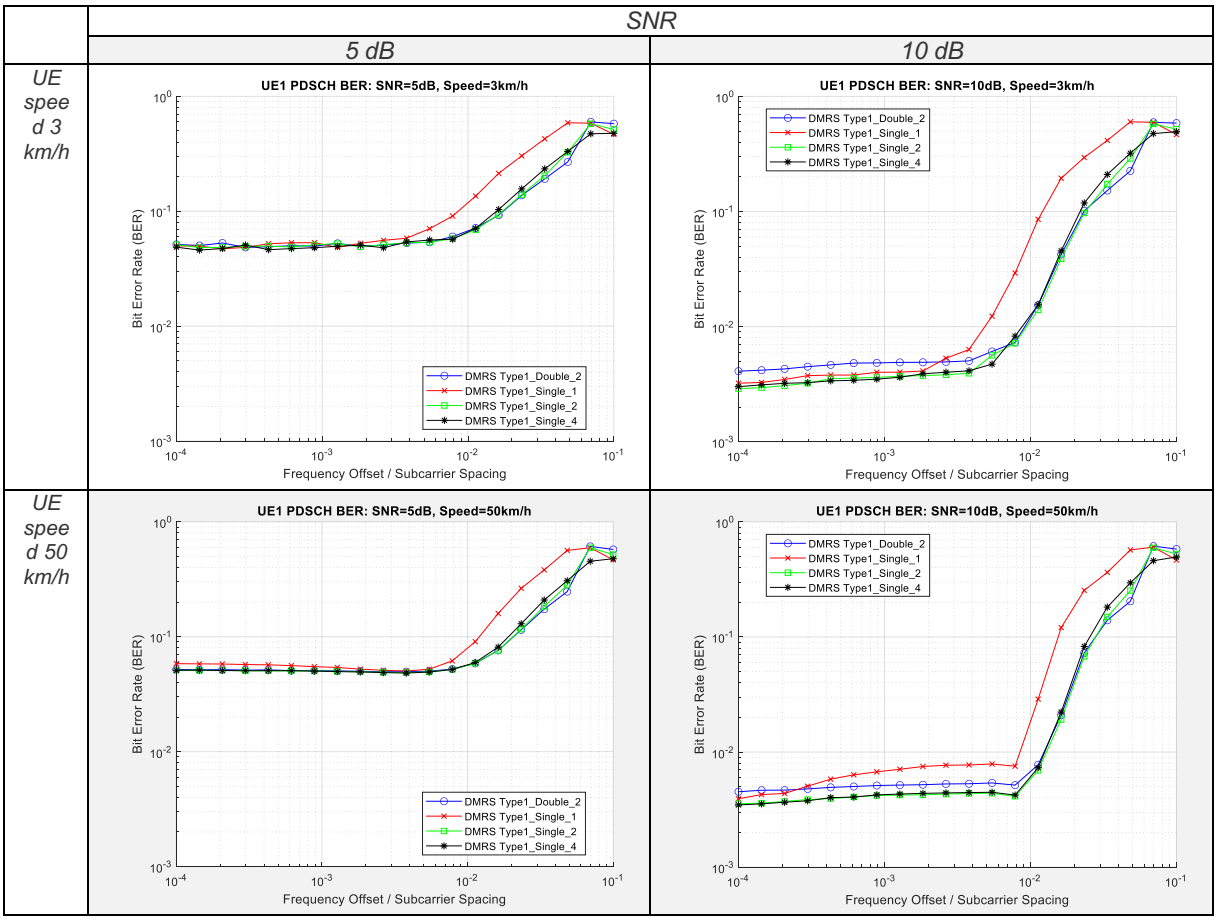

Figure 25: *CP-OFDM BER VS frequency offset with different dmrs configurations at 5 and 10 DB SNR and UE speed of 3 and 50 KM/H. Scenario C3 with doppler spread*

In the following simulation results, we analyze four different type A DMRS patterns, i.e., *Type_1_Single_1* denotes one DMRS allocation following DMRSConfigurationType = 1, DMRS length = 1, and DMRSAdditionalPosition = 0 setup. Double_2 represents DMRS length = 2, and DMRSAdditionalPosition = 1, resulting in a total of four DMRS symbols in one slot. For the C3 scenario considering Doppler spread in the channel model, results, presented in ***Figure 25***, show that adding more DMRS symbols per slot improves BER, especially with

larger frequency offset. The red curve with the fewest symbols (one DMRS symbol per slot) performs worst. However, going beyond two DMRS symbols does not bring further gain, i.e., four DMRS symbols give nearly the same BER as two DMRS symbols. From spectral efficiency point of view, two DMRS symbols per slot are sufficient in this case.

3.2.3.1.2 Q1 scenario with Doppler variation within one slot

In this scenario, we consider the Doppler variation within one slot and two UE speeds of 500 km/h and 1200 km/h. For Doppler variations, we follow the methodology mentioned in 3GPP 38.811 [11] section 5.3. Table 7.3.2.4.1-1 summarizes the potential maximum Doppler shift in one slot in NTN based on the observed maximum Doppler variation rate during the field tests. In the simulation, the Doppler shift offset is implemented as a frequency mismatch between the satellite and UE, and Doppler variation within one slot reflecting Doppler shift changes over the slot duration. In the Q1 scenario, considering Doppler variation within one slot, the BER performance exhibits the same behavior observed in C3, as shown in Figure 26. That is, two DMRS symbols per slot achieve near-optimal channel estimation accuracy, with four symbols yielding negligible additional gain even under Doppler shifts corresponding to 1200 km/h. It is also worth mentioning that we observe worse BER performance for DMRS length = 2 in high SNR scenarios at low frequency offsets, The reason could be that the dominant factors for BER performance is not channel estimation error when channel condition is good. In such cases, allocating consecutive pilots produce highly correlated observations, which underperforms single DMRS configuration in NTN scenario.

	SNR	
	5 dB	10 dB
UE speed 500 km/h	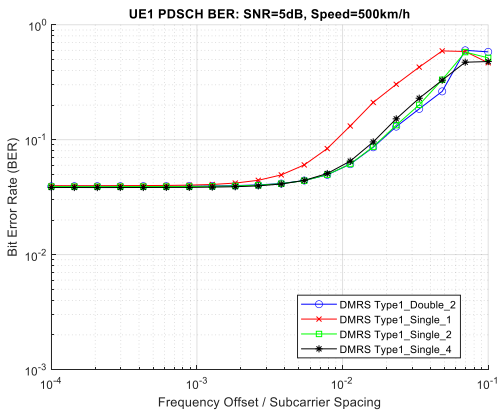	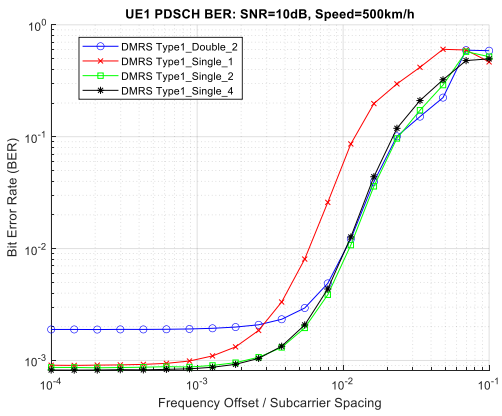

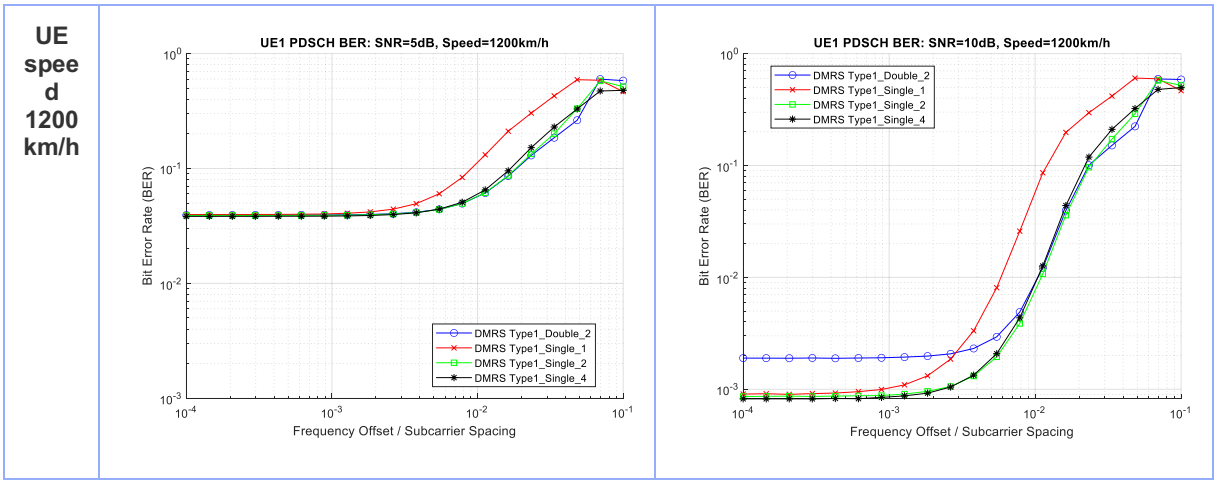

Figure 26: *CP-OFDM BER VS frequency offset with different DMRS configurations at 5 and 10 DB SNR and UE speed of 500 and 1200 KM/H. Scenario Q1 with Doppler variation within one slot*

3.2.3.2 OTFS based analysis

The OTFS signal includes M delay bins and N Doppler bins with a delay resolution $\Delta\tau = 1/(M\Delta f)$ and a Doppler resolution of $\Delta\nu = 1/(NT)$, where Δf is the sub-carrier spacing, i.e., the inverse of the symbol time T.

The data and one pilot symbol are multiplexed together to form the matrix $Z_X[m,n]$ with $m \epsilon [0, M-1]$ and $n \epsilon [0, N-1]$. The pilot symbol is drawn from a QPSK constellation and occupies the position $[m_{p,}n_p]$ in the DD grid surrounded by zero guard symbols. The guard symbols occupy at least $2L+1$ bins along the delay dimensions (with L being the length of the channel impulse response) and N bins along the Doppler dimension.

The symbols (data and pilots) in the DD domain are converted to the time domain by applying the inverse discrete Fourier transform (IDFT) along the Doppler dimension, resulting in the following time-domain sequence:

$$X[m,k] = \sum_{n=0}^{N-1} Z_X[m,n] e^{j2\pi kn/N}$$

where $m \epsilon [0, M-1]$ is the delay index and $k \epsilon [0, N-1]$ is the time index, respectively. The signal is then converted from parallel to serial, i.e, x[q] = X[m,k] with q = m + Mk. In order to avoid interference among OTFS frames and to achieve a circular structure of the transmitted signal, a cyclic prefix (CP) is appended at the beginning of the discrete-time sequence. Thus, we use one CP per OTFS frame.

After that, the signal passes through the channel. Here both large common effects and small scale effects are imposed on the signal. For common effects we mean the satellite Doppler shift (η) due to the satellite motion, and the time offset (TO) (ϑ), i.e., propagation delay due to the distance between the transmitter and the receiver. On the contrary, the small scale effects represent the multipaths, i.e., the multiple delayed replicas of the signal, each one affected by its own amplitude, delay, and Doppler shift. The propagation delay and the Doppler shift of the satellite are common to all the paths. The multipath is represented by a TDL channel model. Thus, the received signal can be expressed as:

$$\mathrm{y[q]} = e^{j2\pi\eta q/MN} \sum_{l=0}^{P-1} \rho_l \, x[q-\vartheta-m_l] e^{j2\pi\varepsilon_l(q-m_l)/MN} + w[q]$$

Where $w[q] \sim \mathcal{N}(0, \sigma_0^2)$ is the complex additive white Gaussian noise (AWGN) with variance σ_0^2, P represents the number of paths, , ρ_l m_l, and ε_l are the amplitude, the delay, and the Doppler shift of each path, respectively.

The received signal is converted from serial to parallel, with blocks of M samples in each parallel stream that represent the samples on the columns of the grid. Consequently, we rearrange the received signal as $y[m,k] = y[q]$, with $q = m + kM$.

In order to estimate the TO, for a given row m on the delay-time grid, we accumulate the energy considering a sliding window of length N:

$$\mathrm{R[m,k]} = \sum_{\mathrm{q=0}}^{\mathrm{N-1}} |\mathrm{y[m,k+q]}|^2$$

The value of m and k for which the correlation is maximized, indicated as $\tilde{m}$ and $\tilde{k}$, are used to estimate the TO:

$$\hat{\vartheta} = \tilde{m} + M \cdot \tilde{k} - m_p - L_{CP}$$

After the TO estimation and compensation, the frequency offset is estimated by means of the pilot symbol originally placed at the position $[m_p, n_p]$ in the DD grid. Indeed, after the IDFT the pilot has been spread out along the row. This sequence has a constant amplitude $\sqrt{(\rho_\mathrm{p})/\mathrm{N}}$ and a constant phase difference of $\mathrm{e}^{\mathrm{j}2\pi n_\mathrm{p} k/\mathrm{N}}$ for $\mathrm{k} \in [0, \mathrm{N}-1]$ and can be split into two halves, each with the same amplitude.

Since we have already transformed our signal from serial to parallel and the TO has been compensated, we consider the row $\tilde{m}$, i.e., the row where the strongest signal is after the TO compensation, and the modified Morelli's algorithm is employed to compute the following correlation:

$$R_{fcfo}[s] = \sum_{k=s}^{N-1} \bar{y}[\tilde{m_p}, k]\overline{y^*}[\tilde{m_p}, k-s] \qquad 0 \le s \le N/2$$

where $\bar{y}$ represents the received signal after the compensation of the TO. The phase increment

$$\varphi[s] = [\angle(\mathrm{R_{fcfo}[s]}) - \angle(\mathrm{R_{fcfo}[s-1]})]_{2\pi}$$

is used to estimate the frequency offset η_{fcfo}, with $\eta_{fcfo} \le N/2$. Thus, $\widehat{\eta_{fcfo}}$ (in Hz) is computed as follow:

$$\widehat{\eta_{fcfo}} = \frac{N}{2\pi}\bar{\varphi}$$

Where, $\bar{\varphi}$ is the average value of $\varphi[s]$.

To test the algorithm and the pilot configuration, we considered two different scenarios: i) scenario C1 (i.e., 5 MHz bandwidth with SCS equal to 30 kHz and the same modulation and coding scheme reported in ***Table 3*** in DL) and ii) scenario Q1 in AWGN varying the Doppler shift within the OTFS frame duration.

In both cases, the equivalent of 2 or 4 DMRS in configuration type 1 (to make a fair comparison with CP-OFDM) was simulated as guard symbols. Increasing the number of guard symbols increases the equivalent power of the pilot.

The TO is in the range of [-MN/2, MN/2] and two SNR values are simulated: 5 and 10 dB.

For the first scenario, the NTN-TDL-D channel model (as reported in ***Table 3***) with Doppler spread is adopted, simulating a maximum UE speed of 50 km/h. The Jakes spectrum is adopted to simulate the Doppler spread.

The results are shown in ***Figure 27*** and ***Figure 28***. The first one represents the accuracy of the channel parameters estimation in terms of root mean square error (RMSE) of the carrier frequency offset (CFO) of the strongest path and the mean absolute error (MAE) for the TO (of the strongest path). It is possible to observe that by increasing the number of guard symbols, the accuracy of the CFO increases as well. Indeed, having an increased power of the pilot reduces the errors on the phase estimation. On the contrary, an increased number of guard symbols does not produce benefits in terms of TO estimation, which already achieves an accurate estimate (lower than 1 sample) with a number of guard symbols equivalent to two DMRS.

Figure 28 shows the performance in terms of spectral efficiency (SE) assuming a perfect TO estimation and residual errors in the CFO estimation. As expected, increasing the SNR the SE increases as well in both the cases (i.e., with an equivalent number of guard symbols equal to 2 DMRS or 4 DMRS). However, considering a number of guard symbols equal to 4 DMRS the SE decreases and the PAPR increases as shown in the picture on the right side.

In addition, it is worth emphasizing that with an equivalent number of two DMRS, the number of delay bins of the guard symbols in the DD domain is longer than the channel impulse response (CIR). When the CIR is not very long, it is possible to reduce the number of guard symbols by allocating a number of resources in the Doppler domain equal to the length of the Doppler spread (if known).

In scenario Q1, we consider the Doppler shift variation within one slot and one UE speeds 1200 km/h, following the same methodology used for the analysis of the DMRS in CP-OFDM.

Since we only consider the AWGN, the resource allocated to the guard symbols corresponds to two DMRS. It is worth emphasizing that the estimation of the TO is always zero for the considered SNR range [0-10] dB, while the CFO estimation accuracy increases with the SNR as shown in ***Figure 29***.

This demonstrates the robustness to the algorithms and pilot arrangement to the Doppler variation within the slot.

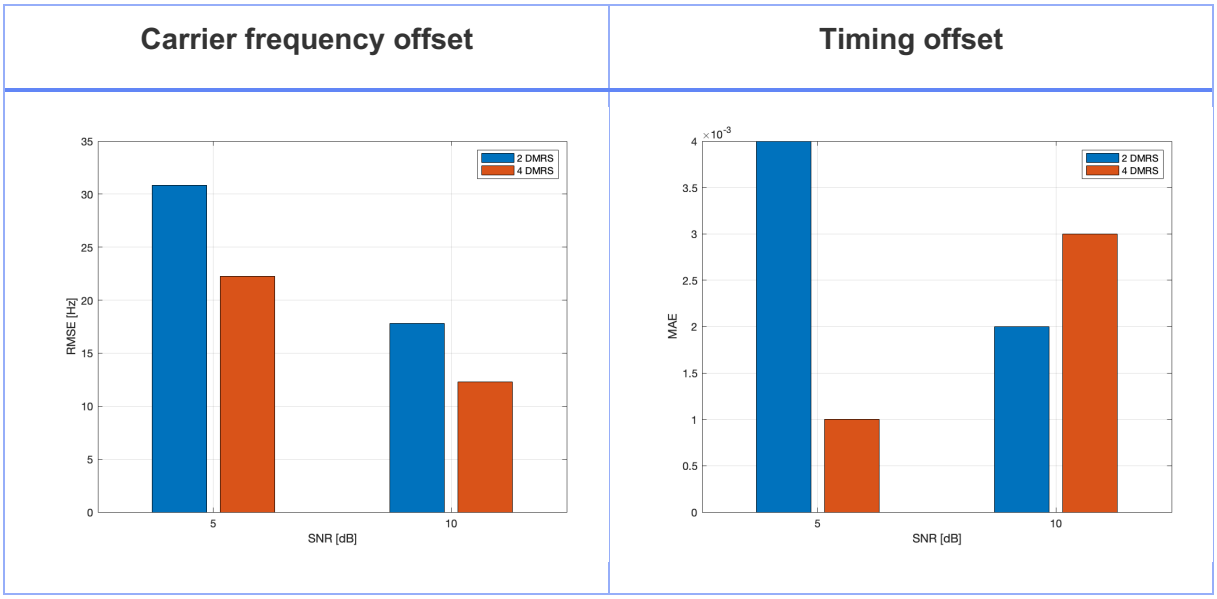

Figure 27: *Parameters estimation accuracy in scenario C1*

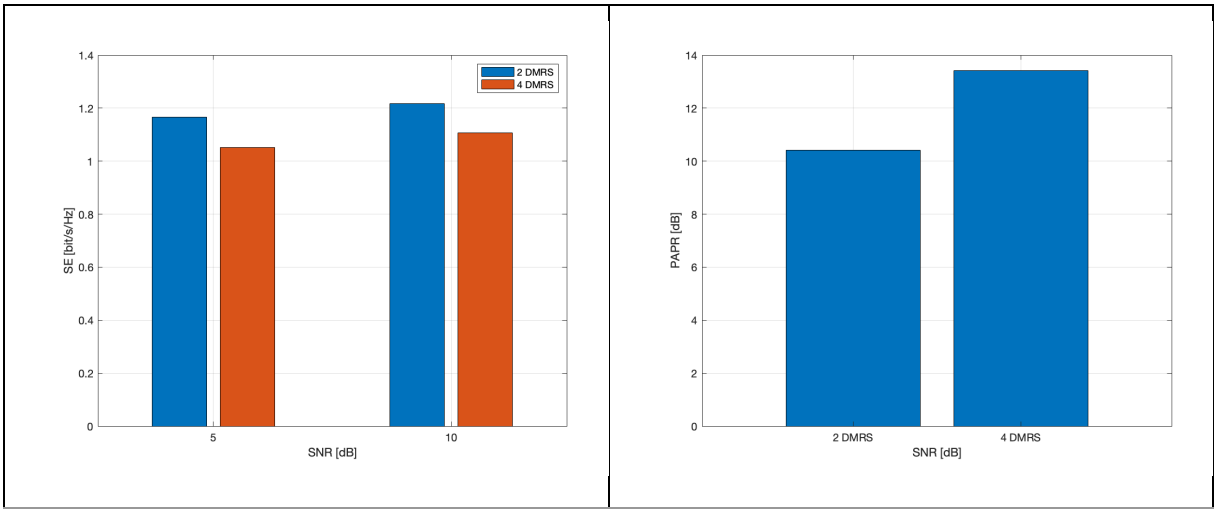

Figure 28: *Spectral efficiency and 99th percentile PAPR*

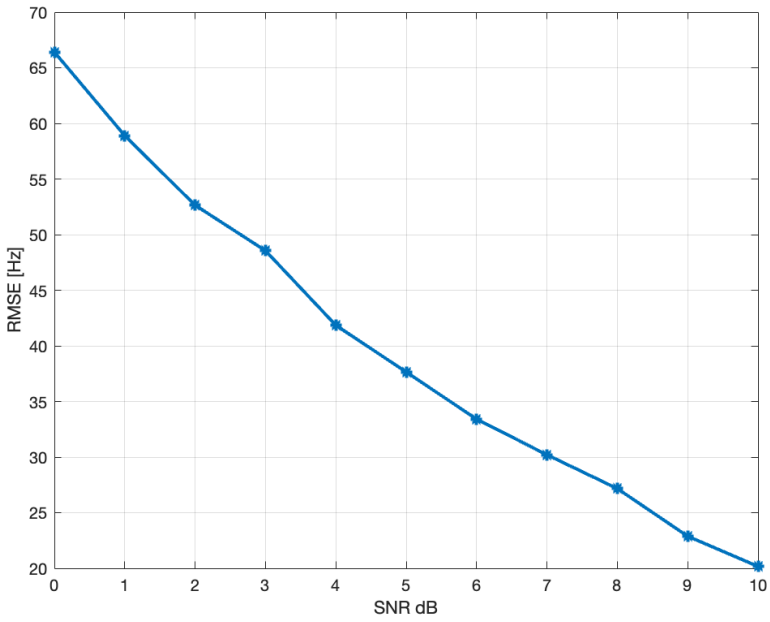

Figure 29: *CFO estimation in Q1 scenario*

3.2.4 Evaluation of in-band distortion and out-of-band emissions via Total Degradation and ACLR

3.2.4.1 The Adjacent Channel Leakage Ratio

As presented in [6], the PSD enables us to compare the containment of energy in the frequency domain across the considered waveforms. As indicated by the end of such a document, the ACLR is further deemed an important KPI for the assessment of out-of-band emissions. Particularly as, unlike the PSD:

- It allows to concisely quantify the impact of frequency containment via a single scalar metric.
- It inherently neglects the impact of emissions in frequency guard-bands designated to protect neighboring channels.
- Along with the receiver's Adjacent Channel Selectivity (ACS), it is commonly combined in system-level analyses to study the joint tendency to generate (at Tx, via ACLR) and be impacted (at Rx, via ACS) by adjacent channel interference.

Defined by 3GPP in TS 38.101 [3], the ACLR is the ratio of the filtered mean power centered on the assigned channel frequency to the filtered mean power centered on an adjacent channel frequency at nominal channel spacing. The 3GPP specifications also designate the type of measurement filter used, and the value of adjacent channel power above which the ACLR must meet a certain requirement. Particularly, a value of 30 dB of ACLR is indicated as a requirement for compliance under those circumstances.

As presented in ***Figure 30*** via a power spectral density plot, the ACLR is measured at the transmitter side for the intended allocation over the main channel (in blue) and based on emissions at neighboring channels (in red). Moreover, as abovementioned, the setup is defined to avoid accounting for the impact of emissions over the guard-interval region where the channel transition occurs.

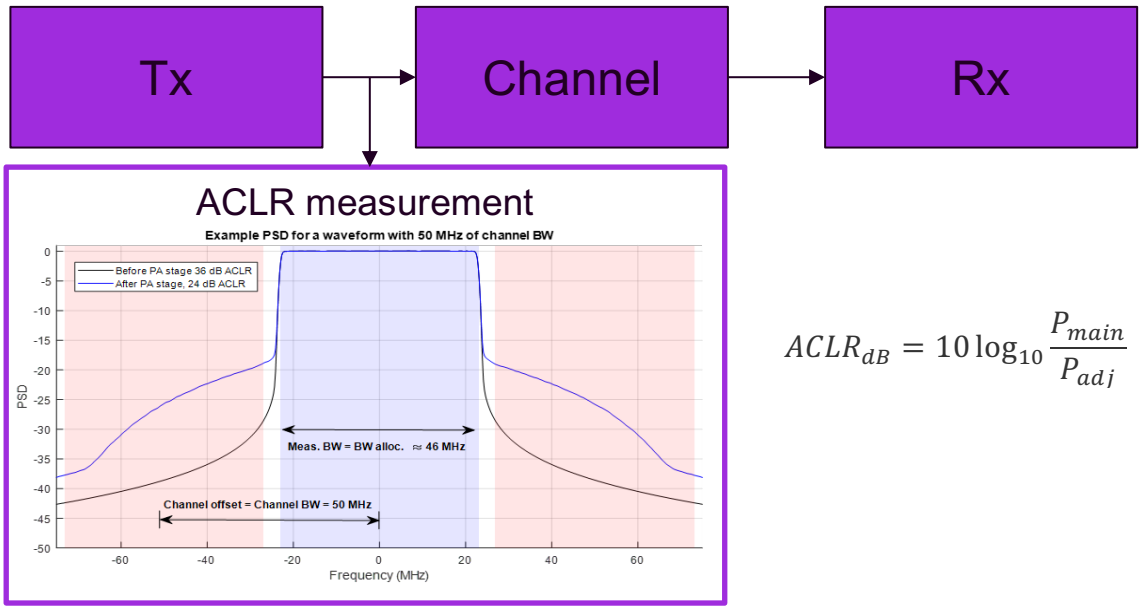

$$ACLR_{dB} = 10\log_{10}\frac{P_{main}}{P_{adj}}$$

Figure 30: *ACLR measurement setup and its relation to the power spectral density*

3.2.4.2 The total degradation

In-band distortion, along with out-of-band emissions, is one of the two main sources of performance degradation induced by power amplifier non-linearities. Accordingly, [6] presented studies in which power amplifiers were enabled and disabled, as well as their backoff varied to show their relation to the BER/BLER drop for every waveform under the identified scenarios of interest.

The current section introduces a new KPI that allows us to concisely evaluate the extent of the loss induced by in-band distortion for a specific operational BLER requirement. In particular, the total degradation [10] measures two kinds of losses in the system related to the operation of high-power amplifiers. First, it quantifies the increase in SNR requirements for the BLER target due to the PA-related distortion of the signal relative to a perfectly linear PA. The total degradation also accounts for the power loss incurred at the PA output (i.e., the backoff) required to sustain said BLER target.

Importantly, the losses quantified by the total degradation exhibit a tradeoff behavior: namely, the larger the backoff, the lesser the growth to the SNR requirement, and vice-versa. Therefore, the total degradation may be minimized to find the optimal backoff in the above sense.

The total degradation is therefore defined [10]:

$$TD_{dB} = \frac{E_s}{N_0}\bigg|_{non-linear,dB} - \frac{E_s}{N_0}\bigg|_{linear,dB} + OBO_{dB},$$

Where TD_{dB} is the total degradation, $E_s/N_0|_{non-linear,dB}$ is the SNR required to obtain the BLER target when the non-linear PA is considered at a backoff such that the mean output power is OBO_{dB} below the saturation level at its output. Lastly, $E_s/N_0|_{linear,dB}$ is the SNR required to obtain the same BLER target when a perfectly linear PA is considered instead.

The reader shall note that the total degradation is a function of the backoff both explicitly via the OBO_{dB} term and implicitly via $E_s/N_0|_{non-linear,dB}$. As mentioned, a larger backoff implies a

smaller distortion and, therefore, a smaller difference between the SNR terms in the equation above.

As a side note, for its numerical computation, a three-stage process ought to be implemented via the adopted link-level Monte-Carlo simulation tool. First, the BLER vs. SNR profile must be computed one input backoff value at a time. Afterwards, based on these results, the SNR required to achieve the BLER target at every backoff value shall be approximated via any numerical method of choice. Lastly, an additional simulation is required to obtain the SNR requirement when a linear PA is used instead.

3.2.4.3 Evaluation results

The current section analyzes now the obtained ACLR and total degradation for the waveform variants under consideration both over the Q1 and C1 scenarios described in ***Table 4***.

Table 4: *Simulation scenarios for TD and ACLR studies*

Parameters			**Q1 Scenario**		**C1 Scenario**	
			Uplink	Downlink	Uplink	Downlink
TX	SCS		120kHz		30kHz	
	# PRBs		32		11	
	Modulation		QPSK		QPSK	
	Code rate		379/1024	679/1024	379/1024	679/1024
	Rv		0		0	
	# OFDM symbols		14	12	14	12
	# DMRS symbols		1		1	
	Transport Block Size		3695	5601	1385	2100
	HPA	PA model [6]	UE PA model in Q/V band	Satellite PA model in Q/V band	UE PA model in C band	Satellite PA model in C band
		IBO (used also for OBO computation)	From 0 dB to 7 dB in steps of 1 dB			
Channel	AWGN	SNR values (linear interp. for SNR requirement computation)	From -2 dB to 10 dB in steps of 0.5 dB			

RX	Channel Estimation	Algorithm	MMSE
	Equalization	Algorithm	MMSE

Particularly, by considering the uplink and downlink scenarios, the studied simulation conditions enable us to evaluate and compare the relative benefit of the considered waveforms under different PA specifications, subcarrier spacings, coding rates and slot configurations.

3.2.4.3.1 Adjacent Channel Leakage Ratio analysis

To begin with, the ACLR under the Q1 and C1 scenarios is presented in ***Figure 31***. As evidenced, the relative performance of the waveforms is consistent across the studied scenarios regardless of the configuration, notably exposing DFT-s-OFDM's ACLR superiority. On the contrary, the absolute ACLR ranges exhibit a dependence on the scenario, mainly driven by its PA model and coding rate specifications.

Scenario Q1	
DL	*UL*
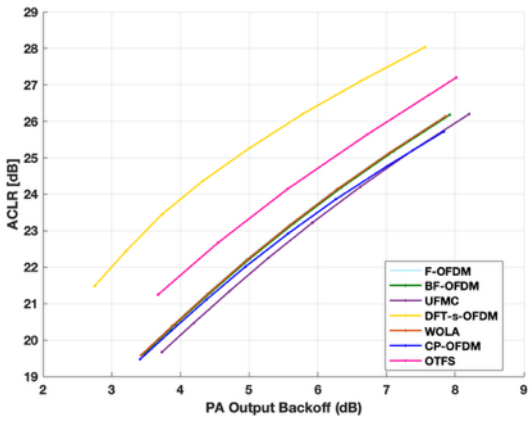	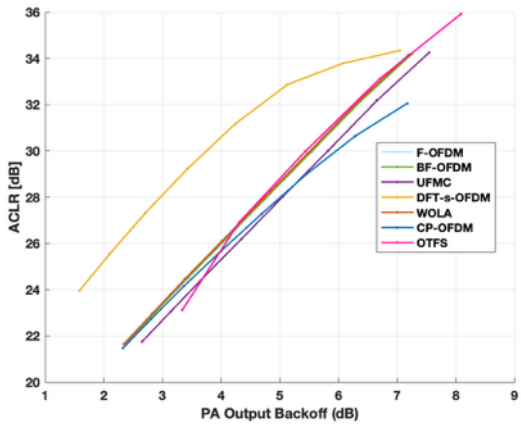
Scenario C1	
DL	*UL*

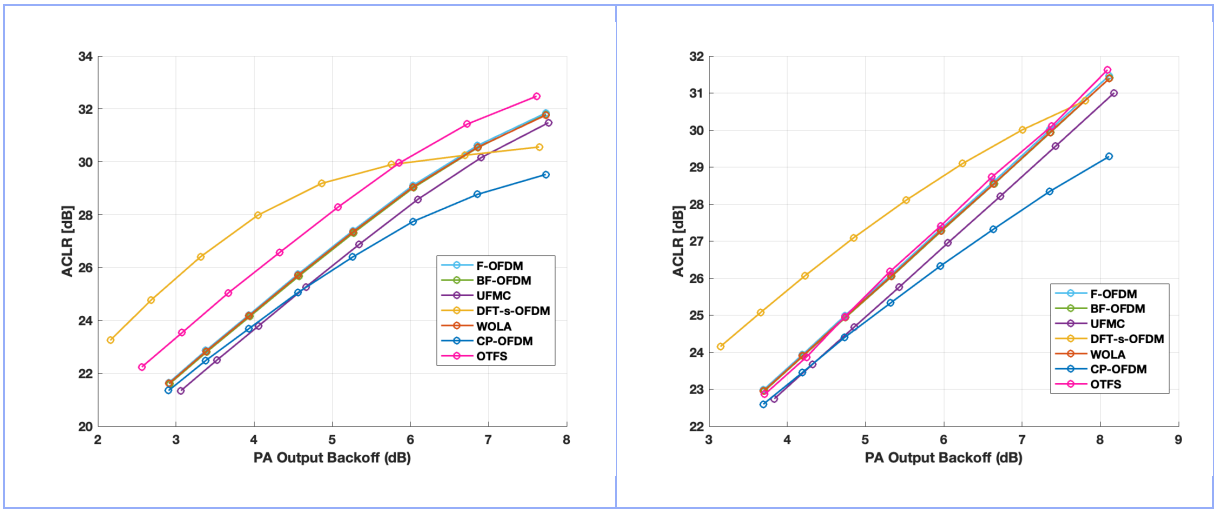

Figure 31: *ACLR comparison for the considered waveforms. Q1 and C1 scenario*

As mentioned, the ACLR performance is predominantly superior (i.e., the ACLR is higher) for the DFT-spread waveform variant. Owing to the inherent dependence of PA non-linear distortion on both PAPR and OBO, the evidenced superiority is suggestive of out-of-band emissions dominated by the impact of PA non-linearities in every case.

Indeed, as established via the PSD study in [6], the out-of-band emissions benefit of filtered waveform variants is drastically diminished by PA distortion. The present study allows us to confirm that the filtered waveform variants and OTFS seldom reduce the necessary OBO to meet ACLR requirements by more than 0.5 dB relative to CP-OFDM.

Remarkably, the DFT spreading technique provides a reduction of at least 1.5 dB (and at most 2 dB) in the required output backoff, which translates into an equivalent increase in the output power at equivalent PA specifications and ACLR requirements.

In contrast, the OTFS waveform exhibits a distinct ACLR behavior in Q1. OTFS proves highly efficient in uplink transmission scenarios. Specifically, OTFS uplink curve achieves ACLR levels exceeding 30 dB with an output BO of approximately 5.5 dB, outperforming CP-OFDM which reaches around 27 dB at the same BO level, though it still behind the DFT-spread technique. WOLA shows overlapping behavior with OTFS. This suggests OTFS's potential to minimize spectral leakage with reduced energy cost. However, OTFS downlink requires a higher backoff margin to meet ACLR thresholds, indicating slightly less favorable behavior for downlink use cases compared to DFT-spread approaches. For the C1 scenario, it is possible to observe the opposite behavior (common to all the waveforms).

The reader might also note that the ACLR of DFT-s-OFDM and CP-OFDM show signs of saturation for scenario Q1 in UL and C1 in DL. Indeed, intrinsic (as opposed to PA-related) out-of-band emissions gradually dominate the ACLR passed a certain OBO value, which can be mitigated by WOLA filtering.

As highlighted, the obtained results suggest that PA non-linear distortion dominates out-of-band emissions overall, as opposed to the intrinsic frequency containment of the waveform.

3.2.4.3.2 Total Degradation analysis

The current section analyses the relative impact of the power amplifier on every waveform and exposes their ability to withstand in-band distortion as measured by the TD. Particularly, ***Figure 32*** shows the total degradation over the Q1 and C1 scenarios.

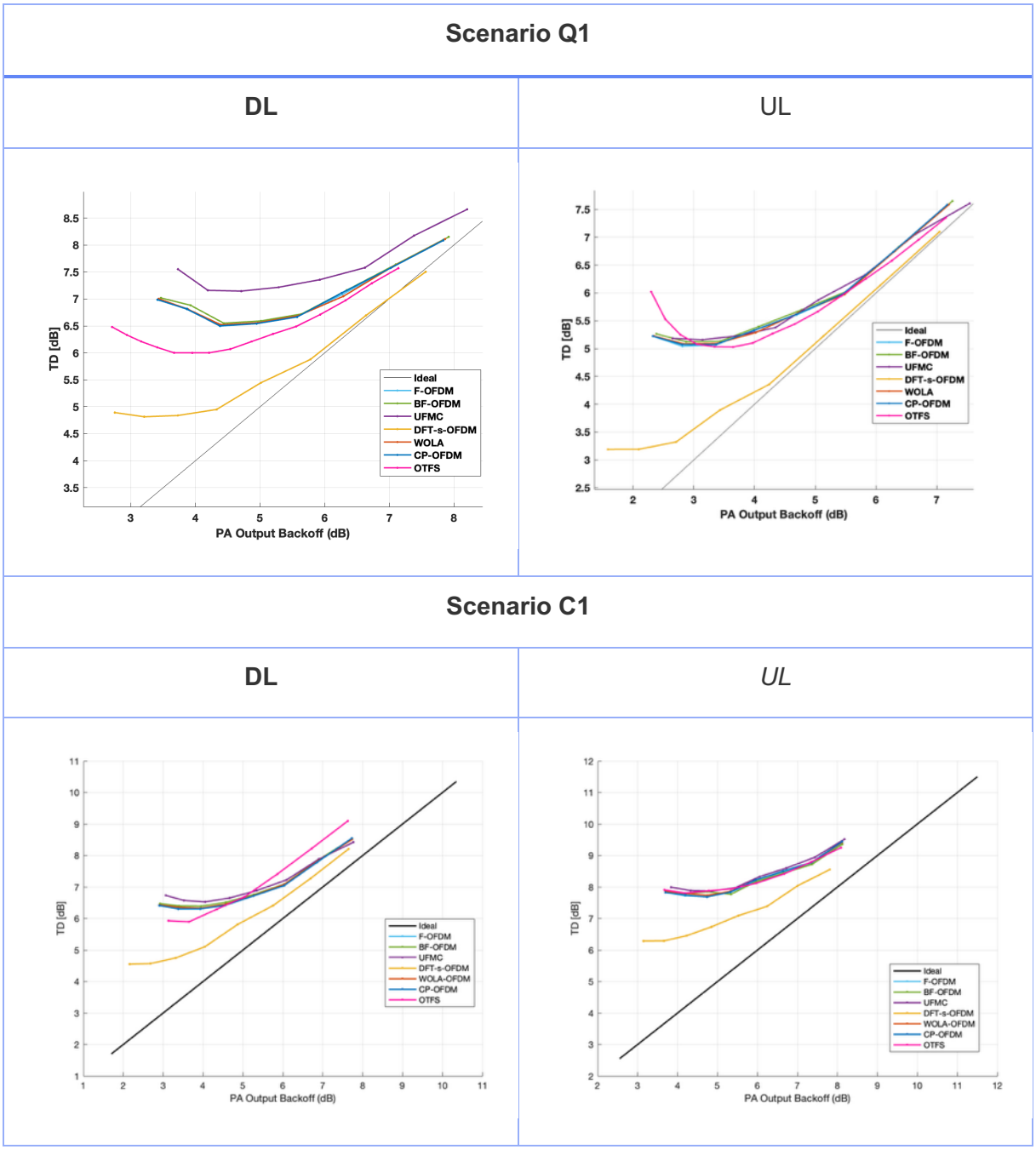

Figure 32: *Total degradation comparison for the considered waveforms. BLER Target 10%*

We remark the resemblance of the TD and the ACLR results: the relative performance of waveforms (i.e., their robustness, if to be ranked) is consistent across scenarios and link directions. Thus, we observe the superiority (i.e., the lower TD) of DFT-s-OFDM in its resilience to PA distortion, as expected, owing to its lower PAPR. Indeed, at any backoff, a lower PAPR reduces the extent to which waveforms enter the region of compression.

Extending the analysis to OTFS, we observe that its total degradation behavior diverges notably from the DFT-spread waveform pattern. As depicted, in the Q1 scenario, OTFS downlink exhibits slightly elevated TD across all output backoff values compared to OTFS uplink, indicating increased vulnerability to in-band distortion in downlink. The uplink case maintains a relatively lower TD profile and aligns more closely with the ideal curve, which reinforces the exceptional ACLR results previously noted. In the C1 scenario, OTFS performs

better in downlink than in uplink as the other waveform variants; however in downlink, after 5.5 dB of output BO, it reaches higher TD values than the other waveforms.

It may also be noted that, despite the relation of TD and ACLR to PA distortion, a better ACLR profile does not necessarily correlate to an improved total degradation. In particular, the Q1 scenario displays improved out-of-band emissions (higher ACLR as per ***Figure 31***) in uplink compared to the downlink case, whereas the latter exhibits an increased robustness to in-band distortion (lower TD as ***Figure 32***) compared to the former. On the contrary, the C1 scenario shows differences in tolerance to in-band distortion for similar out-of-band emission levels.

In summary, ***Table 5*** shows an overall reduction of 1.2-2.3 dB in the minimum total degradation for DFT-s-OFDM relative to alternative waveform variants in this study across both scenarios and link directions. Moreover, we note that both the lowest degradation and the lowest OBO values at minimum degradation are obtained for DFT-s-OFDM across all scenarios.

Table 5: *Minimum total degradation and its respective OBO over the analysed scenarios*

Scenario		Minimum TD (lowest in **bold**) [dB]				OBO at minimum TD (lowest in **bold**) [dB]			
		DFT-s-OFDM	OTFS	UFMC	Other[1]	DFT-s-OFDM	OTFS	UFMC	Other[1]
Q1	DL	**4.8**	6	7.1	6.5	**3.2**	3.67	4.7	4.4
	UL	**3.2**	5			**2**	3.65	3	
C1	DL	**4.6**	5.9	6.3		**2.5**	3.6	4	
	UL	**6.3**	7.8			**3.6**	4.2	4.7	

Despite the evidenced effectiveness of filtering in reducing emissions prior to the PA stage [6], the superiority of DFT-s-OFDM both in terms of its out-of-band emissions (via ACLR) and in-band distortion (via TD) demonstrates the dominant impact of a high PAPR when it meets PA non-linearities.

Therefore, as a means of relaxing the extent of the PA distortion, the authors consider an additional Q1 DPD (standing for Digitally Pre-Distorted) scenario in what follows. In particular, the denominated DPD scenario derives from the Q1 UL equivalent, but assumes ideal PA predistortion characteristics, namely, a perfect linear amplification prior to saturation [12]. The total degradation and ACLR performances of the waveforms over the Q1 DPD scenario are presented in ***Figure 33***.

[1] CP-OFDM, WOLA-OFDM, BF-OFDM and F-OFDM.

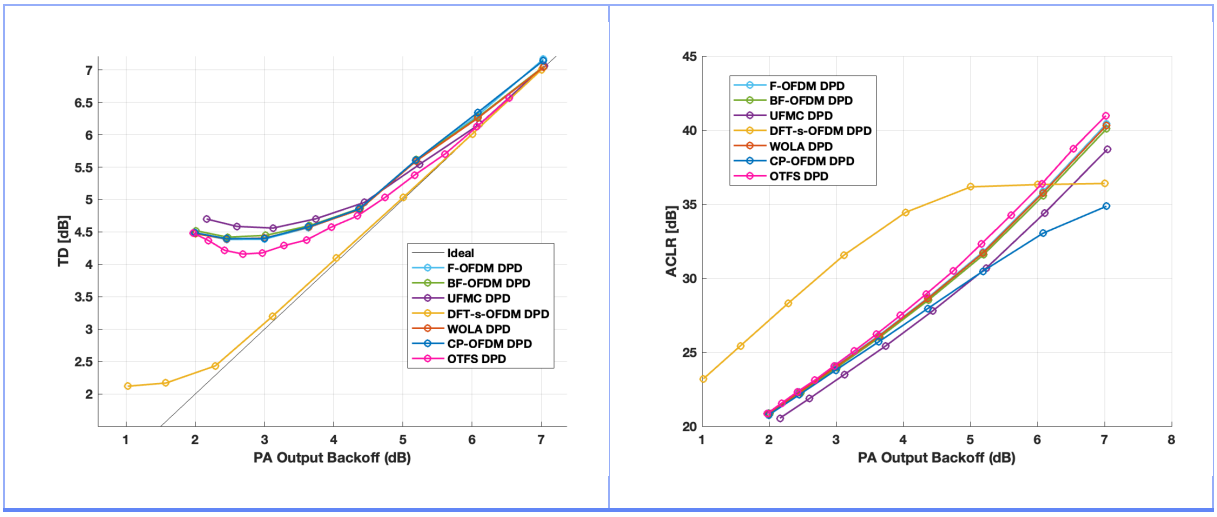

Figure 33: *Total Degradation (left) considering a BLER target of 10% and ACLR (right) for the considered waveforms variants based on the Q1 Uplink scenario under ideal DPD*

As observed, despite the linear amplification prior to saturation in the Q1 DPD scenario, the PAPR reduction in DFT-s-OFDM provides an improvement to ACLR roughly equivalent to the one observed in the Q1 UL scenario with respect to filtered waveform variants. Similarly, we observe that unfiltered waveform variants (i.e., CP-OFDM and DFT-s-OFDM) begin to saturate as their intrinsic emissions begin to dominate beyond a certain OBO.

Therefore, the obtained results indicate that PA saturation (clipping), as opposed to non-linearities before saturation, is responsible for most of the distortion both in terms of in-band distortion and out-of-band emissions. The authors proceed by merging both the filtering and PAPR reduction aspects into a single waveform as a means to further confirm the claim above.

Accordingly, ***Figure 34*** shows an extended analysis of both ACLR and TD over a waveform variant relying both on BF-OFDM and DFT precoding, denominated DFT-s-BF-OFDM over all scenarios and link directions. For reference, the TD and ACLR of DFT-s-OFDM are also included.

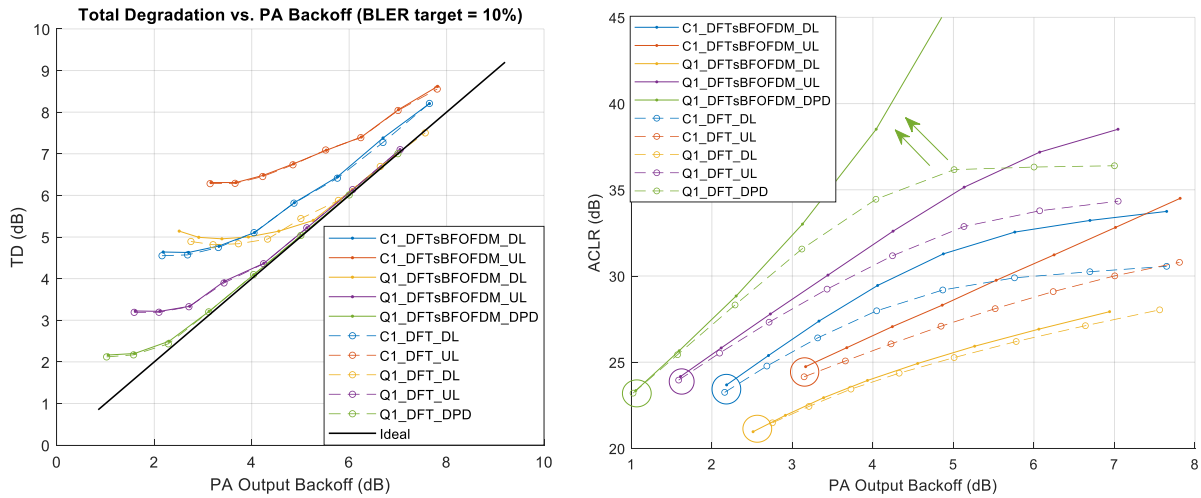

Figure 34: *TD (left) and ACLR (right) for waveform variant combining filtering (via BF-OFDM) and PAPR-reduction (via DFT precoding) in the four considered scenarios*

As observed, the total degradation remains unchanged by the addition of filtering stages to DFT-s-OFDM. On the contrary, the additional filtering leverages a reduction of the out-of-band emissions relative to DFT-s-OFDM alone, especially for some scenarios on the high OBO regime.

Notably, we can evidence that the gain from the additional filtering is negligible at the expense of its increased computational complexity over the Q1 DL scenario. Moreover, the additional gain from filtering at the Q1 UL scenario translates into an OBO reduction of less than 0.5 dB at 30 dB of ACLR. Interestingly, despite the vast improvement to ACLR at large OBO values, even the ideal Q1 DPD[3] scenario exhibits a minor OBO reduction at 30 dB of ACLR by the addition of the filtering operation. On the other hand, filtering gains over the C1 scenarios signify a reduction to the required OBO of 1 dB-1.5 dB at 30 dB of ACLR.

Moreover, the reader shall observe that any reduction to OBO due to ACLR gains shall be analyzed in connection with total degradation to consider the potential increase to in-band distortion. Thus, in order to consider the interplay between in-band distortion and out-of-band emissions, ***Table 6*** analyzes their relationship by comparing the ACLR obtained at optimal OBO in the sense of minimizing the total degradation for every waveform and scenario.

Table 6: *ACLR at minimum total degradation over the analyzed scenarios*

Scenario		ACLR at minimum total degradation (highest in **bold**)				
		CP-OFDM	OTFS (Δ to **CP**)	DFT-s-OFDM (Δ to **CP**)	Filtered variants[2] (Δ to **CP**)	DFT-s-BF-OFDM
C1	DL	23.9 dB	24.9 dB (+1 dB)	24.3 dB **(+ 0.4 dB)**	24.3 dB **(+ 0.4 dB)**	**24.7 dB**
	UL	24.3 dB	23.8 **(- 0.5 dB**)	25 dB **(+ 0.7 dB)**	24.4 dB (+0.1 dB)	**25.7 dB**
Q1	DL	21.2 dB	21.24 dB **(+0.4 dB**)	**22.5 dB (+ 1.3 dB)**	21.3 dB (+0.1 dB)	**22.5 dB**
	UL	23.2 dB	24.3 dB **(+1.1 dB)**	25 dB **(+ 1.8 dB)**	23.2 dB (+ 0 dB)	**25.5 dB**
	DPD[3]	23.8 dB	**26.4 dB (+2.6 dB)**	26 dB (+ 2.2 dB)	24 dB (+ 0.2 dB)	26 dB

[2] WOLA-OFDM, UFMC, BF-OFDM and F-OFDM.

[3] Q1 scenario considering an ideal digital predistortion (DPD) algorithm via the adoption of the clipping PA model, otherwise identical to Q1 UL.

As highlighted via the ΔACLR values relative to CP-OFDM, the ACLR at minimum total degradation is overall improved to the largest extent by the PAPR reduction in DFT-s-OFDM, as opposed to filtering via the pulse-shaped waveform variants[2]. Additionally, as exemplified via DFT-s-BF-OFDM, combining both filtering and PAPR reduction provides an extra improvement to ACLR, albeit modest (≤ 0.5 dB) in most of the scenarios considered. It should be noted that when DPD is applied, OTFS provides the highest ACLR at minimum total degradation.

As the previous study exposes the out-of-band emissions at the waveform's optimal (yet different) OBO level in the sense of minimizing the impact of in-band distortion, one may wonder about the fairness of comparing them exclusively on ACLR grounds. Therefore, let us now instead focus on the intersection of TD and ACLR allowing us to compare waveforms based on their TD for common ACLR requirements.

In particular, Table 7 shows the total degradation obtained for every waveform when a requirement of 30 dB ACLR is imposed on the out-of-band emissions. Notably, CP-OFDM fails to reach the target ACLR in the C1 scenarios within the backoff ranges considered in this study by less than 1 dB. Likewise, no waveform reaches the ACLR requirement in the Q1 DL scenario.

Table 7: *Total Degradation at 30 dB of ACLR over the analysed scenarios*

Scenario		Total degradation at 30 dB ACLR (lowest in **bold**)				
		CP-OFDM	OTFS (Δ to **CP**)	**DFT-s-OFDM** (Δ to **CP**)	Filtered variants[2] (Δ to **CP**)	DFT-s-BF-OFDM (Δ to **DFT**)
C1	DL	TD ≥ 8.6 dB[4]	7.5 dB (Δ ≤ -1.1 dB)	6.6 dB **(Δ ≤ - 2 dB)**	7.5 dB (Δ ≤ - 1.1 dB)	**5.3 dB** (- 1.3 dB)
	UL	TD ≥ 9.4 dB[5]	8.7 dB (Δ ≤ -0.7 dB)	8 dB **(Δ ≤ - 1.4 dB)**	8.7 dB (Δ ≤ - 0.7 dB)	**7.2 dB** (- 0.8 dB)
Q1	DL	Not achievable for OBO ≤ 8 dB.				
	UL	6.4 dB	5.95 dB **(- 0.45 dB)**	4.1 dB **(- 2.3 dB)**	6 dB (- 0.4 dB)	**3.9 dB** (- 0.2 dB)

[4] Reported value corresponds to the TD for an ACLR of 29.5 dB.

[5] Reported value corresponds to the TD for an ACLR of 29.3 dB

	DPD[3]	5.4 dB	4.94 dB **(- 0.46 dB**)	2.9 dB **(- 2.5 dB)**	5.2 dB (- 0.2 dB)	**2.6 dB** (- 0.3 dB)

As observed, Table 7 confirms that the total degradation improvement at 30 dB of ACLR requirement is, as in the preceding analysis, greater by the inclusion of the DFT precoding stage than by the adoption of filtering. Overall, the reduction to the total degradation corresponds to 1 – 2 dB for the former compared to the latter. By contrast, highlighted via the Δ ACLR to DFT-s-OFDM, the addition of filtering to the DFT spread waveform variant offers a reduction in the total degradation mostly under 1 dB.

3.2.4.4 Conclusion

In-band distortion and out-of-band emissions, characterized via TD and ACLR, respectively, were both introduced at the beginning of the current section. TD and ACLR were computed via numerical simulation over a diverse set of Q/V-band and C-band scenarios for multiple OFDM-based waveform variants and OTFS, among which we may distinguish three types: namely, OTFS, windowed/filtered variants (i.e., WOLA-OFDM, UFMC, BF-OFDM and F-OFDM), and one variant leveraging PAPR reduction but no special filtering (i.e., DFT-s-OFDM), on top of CP-OFDM as performance baseline. Moreover, by the end of the study, we have made two additions. First, we considered an additional waveform variant combining filtering and PAPR reduction via DFT-spreading and BF-OFDM. Similarly, a supplementary Q/V-band based scenario was adopted in which the PA model was modified to relax the impact of PA non-linear distortion, precisely, by accounting for the influence of a digital predistortion stage.

We identify three root causes to in-band distortion and out-of-band emissions, namely: the inherent frequency localization properties of the waveform (countered by the adoption of filtering techniques), the non-linear PA gain prior to saturation (addressable via PA digital predistortion) and the PA-related compression/clipping (unavoidable). It is worth highlighting that a reduced PAPR (considered via DFT precoding) mitigates the extent of both listed PA-related disturbances, but it does not impact out-of-band emissions intrinsic to the waveform itself.

Analyses based both on raw PA performance and on PA with a digital predistortion stage show that DFT precoding provides a greater improvement to CP-OFDM in terms of both ACLR and TD compared to filtering alone, in all considered scenarios, by virtue of its lower PAPR. Notably, the further addition of filtering to the DFT-spread waveform variant provides an extra improvement, albeit to a smaller extent (and inconsistent across scenarios) unlike the relative gain from the PAPR reduction technique alone. Consequently, based on our diverse simulation scenarios, our results suggest that the unavoidable PA compression\clipping dominates the detriment to out-of-band emissions and in-band distortion up to 30 dB of ACLR.

Particularly, the waveform variant based on DFT-spread PAPR reduction in combination with BF-OFDM was further analyzed with the intent to further reduce the backoff while keeping ACLR and TD under control. Nevertheless, while the TD for 30 dB ACLR requirements is reduced by more than 2 dB by addition of a DFT precoding stage relative to CP-OFDM overall, the equivalent reduction obtained via combined filtering and DFT precoding relative to DFT precoding alone remains predominantly under 1 dB in the considered scenarios. These results suggest that, even under the presence of PA predistortion techniques, PAPR reduction via DFT precoding is a cost-effective technique for TD and ACLR improvement, only followed by filtering.

Finally, as highlighted throughout, the above conclusions hold primarily for out-of-band emission requirements of up to 30 dB ACLR. Nevertheless, as emphasized, filtering becomes the leading performance enhancing technique at further increased (> 30 dB) ACLR requirements where, operating at higher OBO values, the impact of PAPR is diminished and the contribution of intrinsic waveform emissions begin to dominate.

3.2.5 Waveforms complexity

OFDM-based waveforms are central to modern wireless systems, especially in 5G and beyond. The motivation for introducing variants of OFDM (such as DFT-s-OFDM, WOLA, F-OFDM/UFMC, and BF-OFDM) is to address specific requirements: spectral efficiency, power consumption, robustness to channel impairments, and flexibility for diverse use cases. OTFS has been considered to address communications in high mobility scenarios.

However, each variant introduces additional processing steps, which translate into higher computational complexity, typically measured in terms of the number of real multiplications per symbol. Following, are the considered waveforms increasing order of complexity.

CP-OFDM complexity is the lowest among the considered waveforms. The TX and receiver RX complexity is dominated by the FFT/IFFT operations and cyclic prefix addition/removal. It is mainly used for its simplicity and efficiency for high-throughput scenarios. CP-OFDM is the baseline for comparison and is widely used due to its straightforward implementation and compatibility with multiple input multiple output (MIMO).

DFT-s-OFDM introduces a DFT precoding stage to the standard OFDM process, resulting in a slightly higher computational complexity compared to CP-OFDM. The primary motivation for this waveform is its ability to significantly reduce the PAPR, which is especially beneficial for uplink transmissions in battery-powered devices such as smartphones.

WOLA builds upon CP-OFDM by incorporating windowing operations that smooth transitions between OFDM symbols. This additional processing step modestly increases complexity but brings notable improvements in spectral containment, reducing out-of-band emissions and interference with adjacent channels. The motivation for WOLA lies in its ability to enhance spectral efficiency without a substantial rise in computational demands, making it suitable for environments where spectrum usage is dense and regulatory requirements for emissions are stringent.

BF-OFDM, involves multiple IFFT stages and filtering per carrier, often with overlapping blocks. This substantial increase in processing is motivated by the need for extreme flexibility and precise spectral shaping, making BF-OFDM particularly well-suited for multi-service scenarios in future wireless technologies.

UFMC and F-OFDM further increase complexity by applying filtering operations at the resource block and resource block allocation levels, respectively. This approach enables improved spectral localization and flexibility, particularly valuable in fragmented spectrum scenarios where different services may operate in close proximity. The motivation for these waveforms is to achieve better isolation between users and services, allowing for more efficient use of available spectrum and supporting diverse deployment requirements.

OTFS modulation is a generalized signaling framework where precoding and post-processing units are added to the modulator and demodulator of a multicarrier waveform allowing for taking advantage of full time and frequency diversity gain of doubly dispersive channels. This process also converts the TV channel to a time-invariant one. This modulation scheme has two stages. First, a set of complex data symbols in the Doppler-delay domain are converted to the time-frequency domain through an inverse symplectic finite Fourier transform ($SFFT^{-1}$). In

the second stage, the resulting time-frequency samples are fed into a multicarrier modulator to form the time domain transmit signal [16]. The reverse operations are performed at the receiver to map the received signal back to the Doppler-delay domain. It should be noted that OFDM is used for transmission of the generated time-frequency signals. In the following we consider one CP per OTFS frame. When considering one CP per frame, more complex algorithms should be considered at the receiver for the detection of the symbols. Indeed, different detection methods have been proposed in the literature, such as: i) linear minimum mean square error (LMMSE) with a complexity $O((MN)^3)$, with M number of delay bins and N number of Doppler bins. The cubic complexity can be reduced by taking advantage of the banded and sparse structure of the channel matrix. ii) message passing algorithm (MPA) with a complexity $O(n_{iter}, M, N, P, Q)$, where n_{iter} is the number of the iterations of the MPA, P is the number of paths, and Q is the modulation order, iii) maximum ratio combining (MRC) with a complexity $O(M(N^3 + n_{iter}N^2\mathrm{K}))$ where K represents different delay branches.

3.2.5.1 Computational complexity

Computational complexity is expressed in terms of the number of operations (real multiplications) per symbol. Complexity expressions have been simplified by omitting constant factors since we aim at highlighting relative computational trends rather than providing exact operation counts (which highly depends on the implementation aspects).

To compute the computational complexity (shown in

Table 8) the following parameters are used:

- N_{FFT}: FFT/IFFT size in CP-OFDM
- M_{D}: number of points in the DFT (precoder) in DFT-s-ODFM
- N_{W}: number of windowed samples in WOLA
- U: number of resource blocks in UFMC
- N_{U}: number of subcarriers per resource block in UFMC
- K: overlap factor in BF-OFDM
- N_{B}: size of each OFDM precoder (IFFT) per carrier in BF-OFDM
- M_{B}: number of carriers (OFDM stages) feeding the filter bank in BF-OFDM
- M: number of delay bins in OTFS
- N: number of Doppler bins in OTFS

Table 8: *Complexity analysis per symbol*

	Complexity Tx	Complexity Rx	Reference	Complexity Rank	Main Motivation
CP-ODFM	$N_{\mathrm{FFT}}\log(N_{\mathrm{FFT}}) + N_{\mathrm{FFT}} + L_{\mathrm{CP}}$	$N_{\mathrm{FFT}}\log(N_{\mathrm{FFT}}) + N_{\mathrm{FFT}}$	**[13]**	1 (Lowest)	Simplicity, baseline
DFT-s-OFDM	CP-OFDM + $M_{\mathrm{D}}\log(M_{\mathrm{D}})$	CP-OFDM +$M_{\mathrm{D}}\log(M_{\mathrm{D}})$		2	Low PAPR, uplink efficiency
WOLA	CP-OFDM + N_{W}	CP-OFDM + N_{W}	**[14]**	3	Spectral containment
BF-OFDM	$M_{\mathrm{B}}[N_{\mathrm{B}}\log(N_{\mathrm{B}}) + N_{\mathrm{B}} + KN_{\mathrm{B}}]$ ≅ 4 CP-OFDM	CP-OFDM	**[15]**	4	Multi-service flexibility

F-OFDM / UFMC	$U[N_{\mathrm{U}}\log(N_{\mathrm{U}}) + N_{\mathrm{U}}] + N_{\mathrm{FFT}}\log(N_{\mathrm{FFT}})$	CP-OFDM	**[13]**	5	Spectral localization
OTFS	$M(\log(N) + 2Mlog(M) + 1) + \frac{L_{CP}}{N}$	$M(\log(N) + 2Mlog(M) + 1)$	**[16]**	6 (Highest)	High mobility scenarios

3.3 WAVEFORM COMPARISON

Until now, the waveforms have been evaluated across various scenarios and impairments, with results presented in deliverables D4.1 and D4.5. To effectively summarize these outcomes and facilitate reader comprehension, a radar chart has been included (***Figure 35***).

Specifically, the radar chart provides a qualitative comparison of the waveforms based on selected KPIs drawn from ***Table 2***:

- K2 Robustness to Doppler synchronization errors
- K4 Robustness to timing synchronization errors
- K5 In band distortion (PAPR/ HPA IBO-OBO) to measure the emissions originating from HPA spectral regrowth
- K6 Robustness to phase noise
- K7 Out-of-band emission to measure the intrinsic emission of the waveform
- K8 Robustness to frequency-selective channel

It should be noted that the evaluation considers a subset of KPIs compared to the full list in ***Table 2***, justified by the following reasons: i) K1 relates to spectral efficiency. Given that all waveforms were analyzed using the same modulation and coding scheme, performance variations are attributable solely to the multiplexing scheme. Consequently, a comparative analysis based on BLER sufficiently captures performance differences. ii) Flexibility/scalability, labeled as K3 has been excluded as it lacks a straightforward and quantifiable performance metric (like BER loss, which is used for several other KPIs) suitable for representation. iii) K9, i.e., robustness to time-selective channels, will undergo dedicated evaluation in subsequent analyses focused on pilot configuration design. Moreover, the evaluated KPIs allow to compare waveforms with regard to the dominant impairments inherent to NTN, namely, the propagation delay and the Doppler shift as well as the nonlinear distortions induced by HPAs.

3.3.1 Methodology

To generate the radar chart, the following methodological approach has been adopted.
Initially, suitable metrics were established for each KPI. Specifically, the BER loss was selected as the metric for KPIs K2, K4, K6, and K8. For K5, the metric is defined as the difference between the total degradation observed in a waveform and the total degradation of CP-OFDM at their optimal back-off point. K7 is evaluated by measuring the difference in IBO between a given waveform and CP-OFDM, with the reference point for IBO set to achieve an ACLR of 30 dB. In all cases, CP-OFDM serves as the reference waveform.
Given that the waveforms have been assessed across multiple simulation scenarios, the most pertinent scenario has been identified for each KPI. Specifically, scenario Q1 is utilized for the evaluation of KPIs K2, K4, K6 (considering 5dB of SNR) K5 and K7, whereas scenario C3 is applied for K8.

The scoring system is structured as follows: if a waveform performs better than CP-OFDM, it yields a score of +1, if it achieves same performance the score is 0, and if the performance is worsen, a score of -1is assigned to the waveform. Since CP-OFDM is used as a reference, its score is zero.
It is important to note that the conducted analysis exclusively evaluates waveform robustness and does not incorporate receiver design considerations. Furthermore, this analysis does not account for receiver complexity, compatibility with terrestrial and 5G waveform or waveform behavior in multi-user scenarios.

3.3.2 Considerations

Referring to ***Figure 35***, the comparative analysis of waveform performance with respect to the defined KPIs yields the following insights:

- DFT-s-OFDM demonstrates superior robustness to both HPA induced in-band distortion and intrinsic out-of-band emission compared to CP-OFDM (K5 and K7), primarily due to its inherently low PAPR. For the remaining KPIs, its performance is comparable to that of CP-OFDM.
- OTFS surpasses CP-OFDM in KPIs K4, K6, and K8 Its enhanced robustness to frequency-selective channels is attributed to the DD domain mapping. Additionally, the transformation to the delay-time domain naturally spreads and interleaves the symbols over time, enhancing robustness by disrupting the temporal correlation of phase noise. Moreover, OTFS offers flexibility in incorporating a CP preceding the OTFS frame, equivalent in length to the cumulative CPs of the individual OFDM symbols.
- UFMC mirrors CP-OFDM performance across all KPIs, except for K2 and K6, where it underperforms. These degradations are primarily caused by its noise enhancement and ICI induced by frequency offset and phase noise.
- BF-OFDM aligns with CP-OFDM in all KPIs except K4, where its performance differs as a consequence of the filtering mechanism and a reduced CP length.
- WOLA and F-OFDM exhibit performance equivalent to that of CP-OFDM across all evaluated KPIs.

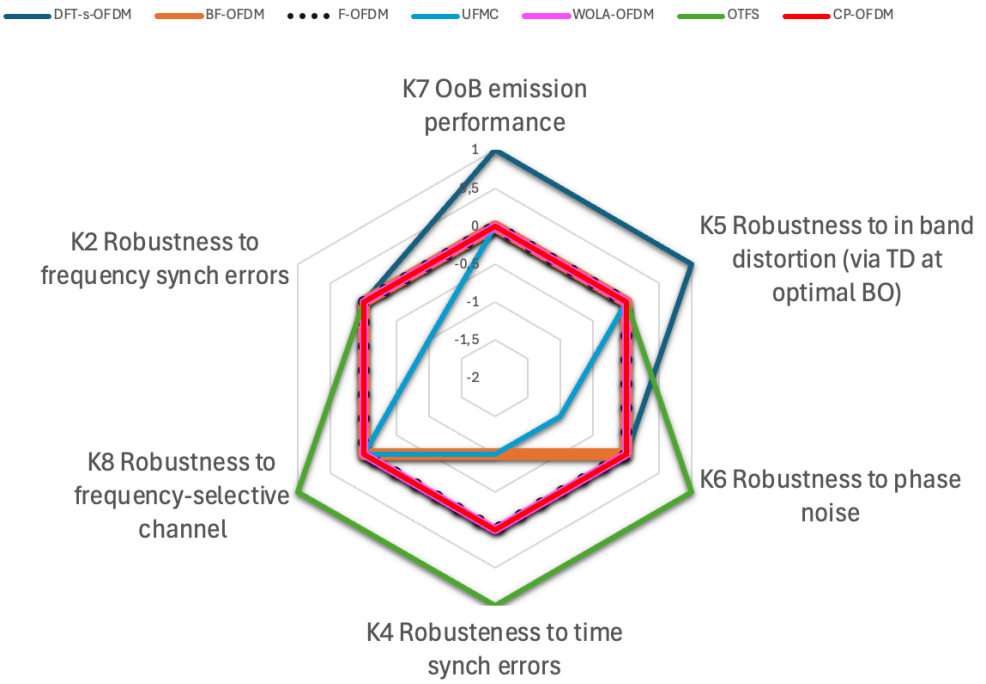

Figure 35: *Radar chart for waveform comparison considering only performance obtained with a single user*

It is worth mentioning that, considering the complexity of the message passing algorithm used in OTFS as well as the significantly different nature of the OTFS waveform compared to 4G/5G waveforms, higher complexity algorithms and more suitable DMRS designs could also be considered for the OFDM family of waveforms for improved performance under the KPIs considered for this evaluation.

3.4 MULTIPLE USER CONSIDERATIONS

Considering the fundamental role of the PAPR, this section aims at exploring the relationship between the PAPR and the adopted multiple access technique in the context of NTN. Particularly, we will show the PAPR reduction benefit of DFT spreading and partial transmit sequences (PTS)-enhanced DFT spreading when used in conjunction over frequency and space division multiplexing schemes.

As a side note, the reader will observe that the upcoming discussion centers exclusively around the downlink case. Indeed, as opposed to downlink, the uplink counterpart may rely on the PAPR reduction benefit of DFT-spread precoding in combination with any of the abovementioned multiplexing schemes at no detriment per additional user.

In what follows, we will show the PAPR reduction performance of the above techniques as users are multiplexed either in the spatial/beam domain or in the frequency domain; as well as the PAPR performance when both multiplexing schemes are combined.

3.4.1 Users multiplexed in the space/beam domain

As it has been readily established in the literature, multicarrier systems suffer from an increased PAPR due to the superposition of independently modulated subcarriers [17] (Anwar, et al., 2004). Likewise, the difficulty of achieving a low PAPR in the presence of beamforming has been identified as a bottleneck to energy efficient communications in the literature; where

multiple proposals have become available with tradeoffs on different aspects such as complexity and flexibility [18][19] [19].

Let us consider the simplified beam-forming architecture of ***Figure 36***, where we highlight the role of the superposition of beam streams at the input of the power amplifier stage, as well as its impact on the PAPR. Indeed, despite the precoder orthogonality and single carrier nature of the waveforms, the PAPR prior to the HPA stage is impacted when used in conjunction with space division multiple access (SDMA) [20].

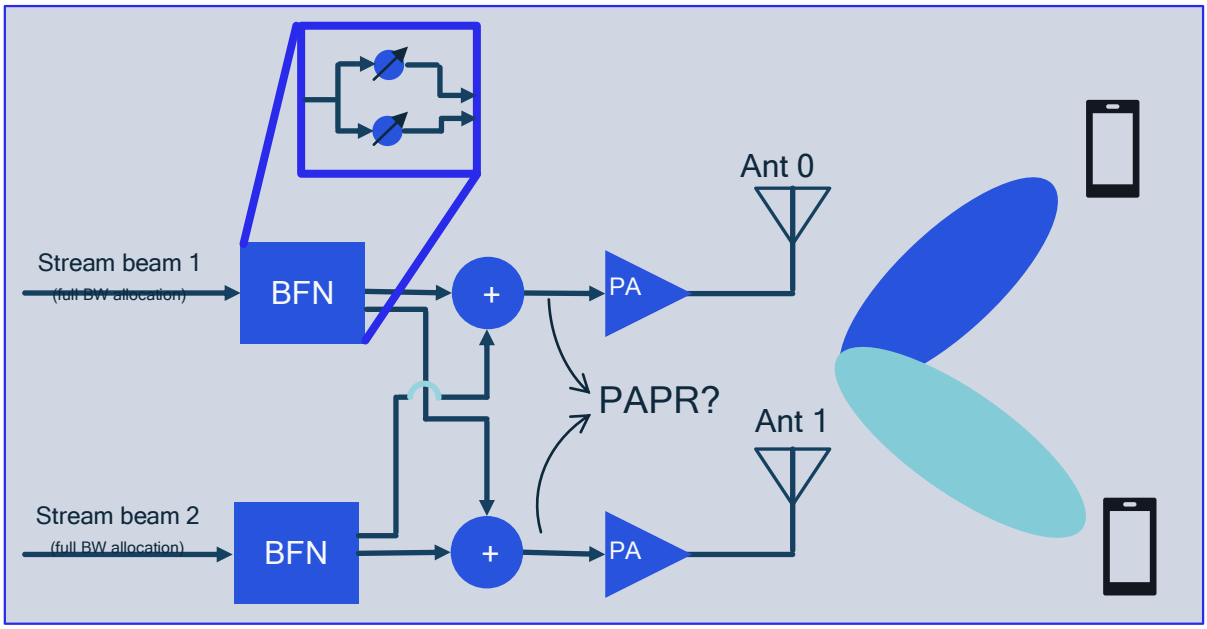

Figure 36: *Satellite Payload architecture representation for SDMA in Downlink*

The current section analyzes the extent of PAPR degradation of CP-OFDM and DFT-s-OFDM when SDMA (enabled via beamforming) is adopted as the multiplexing scheme for NTN in downlink. We further analyze the PAPR reduction performance for a scenario with an increased number of users via combined SDMA and FDMA, followed by an analysis of the gains stemming from PTS-enhanced DFT precoding based PAPR reduction.

3.4.1.1 PAPR reduction performance of DFT spreading with users multiplexed in the space or beam domain

Let us begin by considering a phase-array based satellite payload architecture with an increasing number of users to serve via SDMA such as the one in ***Figure 36***, each located on a different coverage beam. As the number of users grows, the satellite is required to multiplex users in the angular domain via their respective precoding matrices (in case of digital beamforming) or their physical ports (in case of analog beamforming).

In what follows we consider both CP-OFDM (baseline waveform) and DFT-s-OFDM (single carrier waveform for PAPR reduction) over the Q1 downlink scenario (parameters reported in ***Table 4***). Particularly, we analyze the PAPR distribution via its median, 90th and 99th percentile as the number of beams is swept from 1 to 32 when a single user transmission per beam is allocated the full bandwidth of 50 MHz.

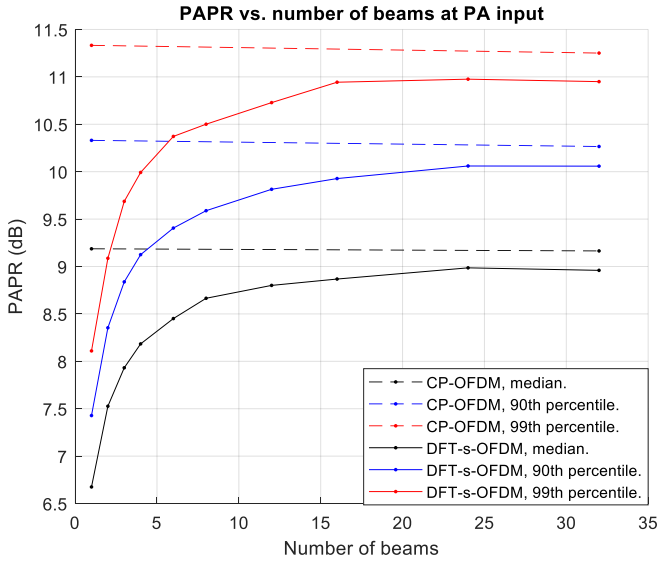

Figure 37: *PAPR vs. number of active beams for downlink SDMA*

As expected, ***Figure 37*** shows that the PAPR of CP-OFDM remains the highest across the distribution. It is also evidenced that its PAPR is insensitive to the number of active beams as CP-OFDM is a multicarrier waveform whose number of subcarriers does not vary with the number of beams (Dinur & Wulich, 2001)[21].

Likewise, it is possible to observe a PAPR reduction benefit of 3 dB for DFT-s-OFDM relative to CP-OFDM over a single beam as expected. Nonetheless, its relative PAPR benefit decreases rapidly below 1 dB for more than five active beams as their superposition begins to resemble more a multicarrier, a Gaussian-like random process [21] [21], than a single carrier waveform.

Table 9: *PAPR reduction benefit of DFT-s-OFDM relative to CP-OFDM with number of active beams*

Number of active beams	PAPR benefit of DFT-s-OFDM relative to CP-OFDM (dB)	
	90th Percentile	99th Percentile
1	2.8	3.1
2	1.9	2.2
3	1.4	1.6
4	1.2	1.3
6	0.9	0.9

As observed in Table 9, despite efficient radix-2 and mixed-radix FFT implementations, and in view of the rapid increase in the PAPR curves of Figure 37, the above results suggest that, in some cases, the obtained PAPR reduction may not justify the increase in system complexity of DFT spread precoding, especially at the UE receiver side in downlink where energy considerations are of utmost importance.

3.4.2 Users multiplexed in the frequency domain

In a practical deployment, the NTN system shall cover large areas with a considerable number of users. To enable efficient use of spectrum, while limiting the latency, users tend to be scheduled together, having access to a portion of a cell's bandwidth for a given transmit interval.

In ***Figure 38***, we illustrate the considered allocation scheme, with two users sharing the bandwidth during a slot.

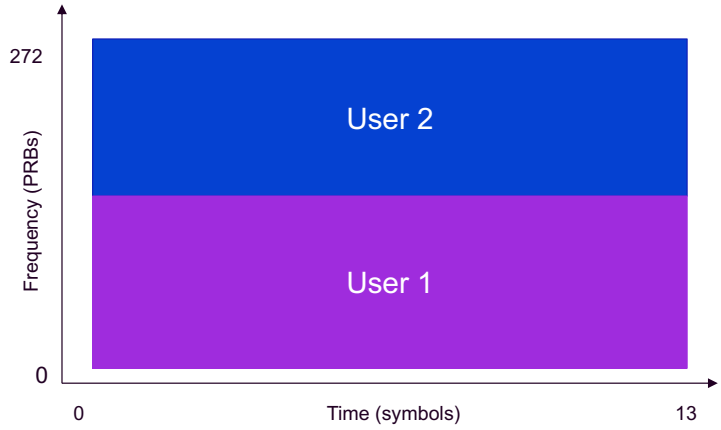

Figure 38: *FDM allocation in downlink. Two users divide the cell bandwidth and are served simultaneously*

Due to the potential high number of users, at low SNR, we expect that a high degree of frequency domain multiplexing will be used in NTN systems.

Meanwhile, the results in D4.1 suggest a PAPR advantage for DFT-s-OFDM. We intend to explore this once frequency domain multiplexing is considered.

3.4.2.1 PAPR reduction performance of DFT spreading with users multiplexed in the frequency domain

3.4.2.1.1 Methodology

We intend to compare the PAPR CCDF of the DL transmit signal of DFT-S-OFDM against CP-OFDM with the following parameters:

- A variable number of scheduled users per slot
  - 1, 2, 4, 8, 16, 32 frequency-domain multiplexed users.
- Using QPSK, 16QAM, 64QAM for all allocated users.
- The total number of PRBs (256) is divided equally between the scheduled UEs.
- UEs are allocated contiguously.
- FFT size of 4096 points, with a cyclic prefix of 128 samples.
- Number of transmitted symbols: 20000.

The PAPR is calculated in dB per transmit symbol, at the output of the modulator, before the DAC and PA.

3.4.2.1.2 Simulation results

The simulation results are presented here in sequence, with one figure per choice of modulation scheme. ***Figure 39*** depicts the results for QPSK, 16QAM and 64QAM respectively.

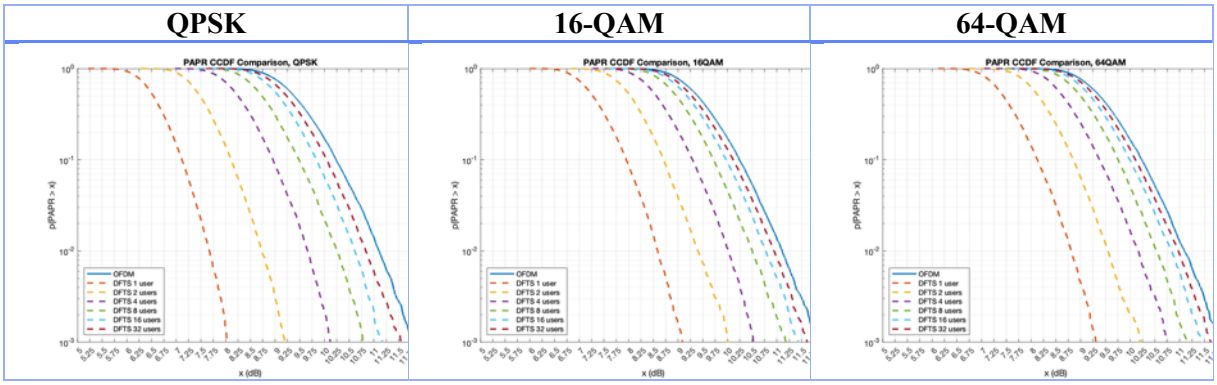

Figure 39: *CCDF of PAPR for DFT-S-OFDM Versus CP-OFDM with varying number of FDM scheduled users*

The PAPR for DFT-s-OFDM increases with the number of frequency-domain multiplexed users and with modulation order.

The cases investigated in [6] are the most optimistic for DFT-s-OFDM vs CP-OFDM.

It is likely that the performance advantage seem will not be the same in practical deployments, when multiple users are scheduled in parallel.

3.4.3 Users multiplexed in the combined space-frequency domain

The previous sections analyzed the impact of FDMA and SDMA on the PAPR when either multiple access scheme is considered. Let us now focus on the scenario where a satellite jointly relying on both FDMA and SDMA to multiplex users in the frequency and spatial domains to analyze their combined effect.

3.4.3.1 PAPR reduction performance of DFT spreading with users multiplexed in the frequency and space domains

We consider both CP-OFDM and DFT-s-OFDM over the Q1 downlink scenario. In this case, we will concentrate on the 90th percentile of the PAPR distribution as the number of beams or SDMA order is swept from 1 to 8 and the number of users served per beam or FDMA order is also swept from 1 to 8. In all cases the allocated bandwidth of 50 MHz is split across users supported by the same beam via FDMA.

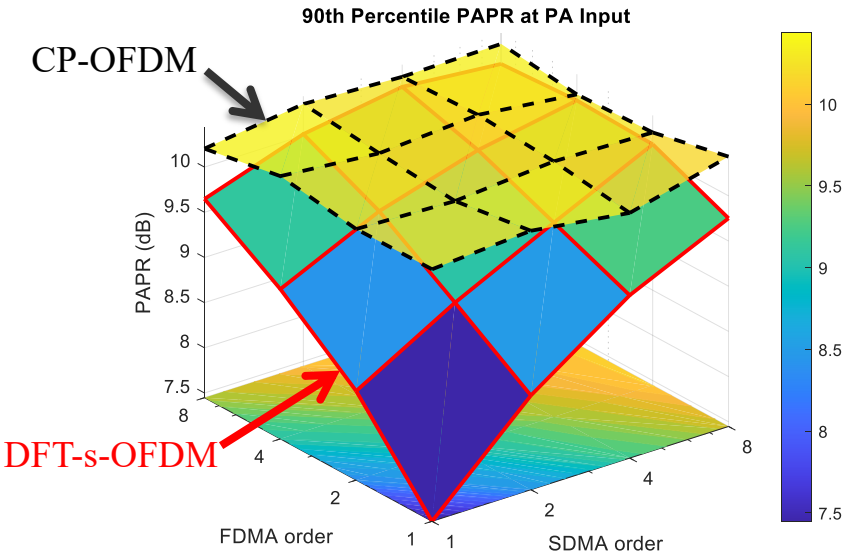

Figure 40: *90th Percentile PAPR at PA Input for joint SDMA and FDMA*

As observed in ***Figure 40***, the CP-OFDM variant is insensitive both to the multiple access technique and their order at the expense of providing the highest PAPR across the board. On the contrary, the DFT-s-OFDM alternative exhibits an improved PAPR performance as the FDMA and SDMA orders are reduced. Notably, the presented results uncover a symmetry on the multiplexing order and evidenced in Table 10 below.

Table 10: *PAPR benefit of DFT-s-OFDM relative to CP-OFDM for the considered FDMA and SDMA orders*

PAPR benefit of DFT-s-OFDM relative to CP-OFDM (dB)	1 beam	2 beams	4 beams	8 beams
Single user per beam	2.8	1.8	1	0.6
2 FDM'ed users per beam	1.8	1.1	0.7	0.3
4 FDM'ed users per beam	1.2	0.7	0.4	0.1
8 FDM'ed users per beam	0.6	0.3	0.1	0.2

As highlighted via the color grading in Table 10, the PAPR reduction benefit of DFT-s-OFDM relative to CP-OFDM is strongly driven by the total number of users served by the satellite and barely impacted by the specific multiplexing orders.

For example, the PAPR reduction benefit of DFT-s-OFDM relative to CP-OFDM is roughly the same for all viable SDMA and FDMA orders amounting to 8 users, namely: (8,1), (4,2), (2,4), and (1,8), with *(x,y)* denoting *x* frequency-multiplexed users per beam over *y* beams.

3.4.3.2 PAPR reduction performance of PTS-enhanced DFT spreading when users are multiplexed in the frequency and space domains

The current section aims at evaluating the benefit of PTS as a means of enhancing the PAPR reduction benefit of DFT-s-OFDM [22] [22] in the frequency when users are multiplexed both in frequency and space domains.

Let us consider the PTS architecture of Figure 41 within which DFT precoding reduces the per-user PAPR, whereas PTS reduces the evidenced PAPR detriment across users resulting from FDMA in downlink as evidenced in the previous subsection.

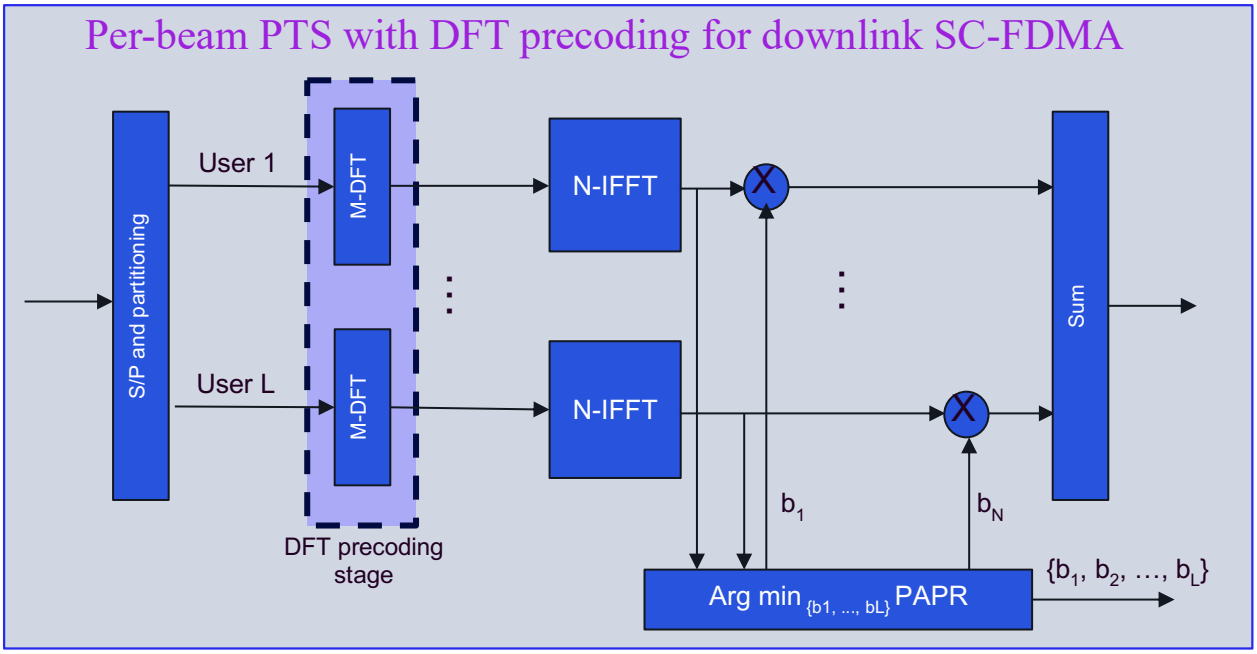

Figure 41: *Diagram of PTS with DFT precoding for enhanced PAPR reduction for FDMA in downlink*

As shown in the diagram above, PTS aims at computing the set of dephasing factors ($b_i = e^{j2\pi\theta_i}\ \forall\ i = 1, \dots, L$) that, applied to every beam transmission, minimizes the PAPR.

The amount of IDFT operations is increased by a factor of L with respect to conventional OFDM as the separate contribution of every user in the time domain must be known by the minimization algorithm. Moreover, note that the values $b_i\ \forall\ i$ must subsequently be transmitted over or estimated at the symbol rate by the receiver side for proper decoding.

The advantage of the presented PTS enhancement in the frequency domain of DFT spreading compared to conventional PTS includes a reduced side-information overhead, as well as a lower computational complexity related to a reduced number of PTS blocks. In particular, the number of PTS blocks is limited to the FDMA order as every user contribution (cascaded DFT + IFFT in Figure 41) is itself a waveform of low PAPR. Likewise, the combination of PTS in frequency with DFT spreading offers a reduced PAPR compared to DFT spreading based SC-FDMA; and whose performance was shown in the previous section.

Table 11: *Specifications for PTS-enhanced DFT-s-OFDM for FDMA*

Parameter	Value	Comment
FDMA order, L	1 to 8	Same as the number of PTS blocks
SDMA order	1 to 8	Number simultaneously active of beams
PTS domain	Frequency	PAPR **not** minimized across beams
Max. number of users	1 to 64	Across both FDMA and SDMA
Phase resolution	2 bits	Overhead per symbol per user. $\theta = \{0°, 90°, 180°, 270°\}$
User to PTS block mapping	One-to-one	Identical FDMA and PTS partitioning
Minimization technique	Exhaustive search	Optimal solution to PAPR minimization based on conventional PTS algorithm

The reader may note in Table 11 that the adopted PTS enhancement technique reduces the PAPR for frequency multiplexed users disjointly over each beam. Indeed, despite it being possible to adopt a PAPR minimization strategy across beams, the time complexity becomes prohibitive as the search space and number of terms in the minimization (one per power amplifier) rapidly grow with the number of beams.

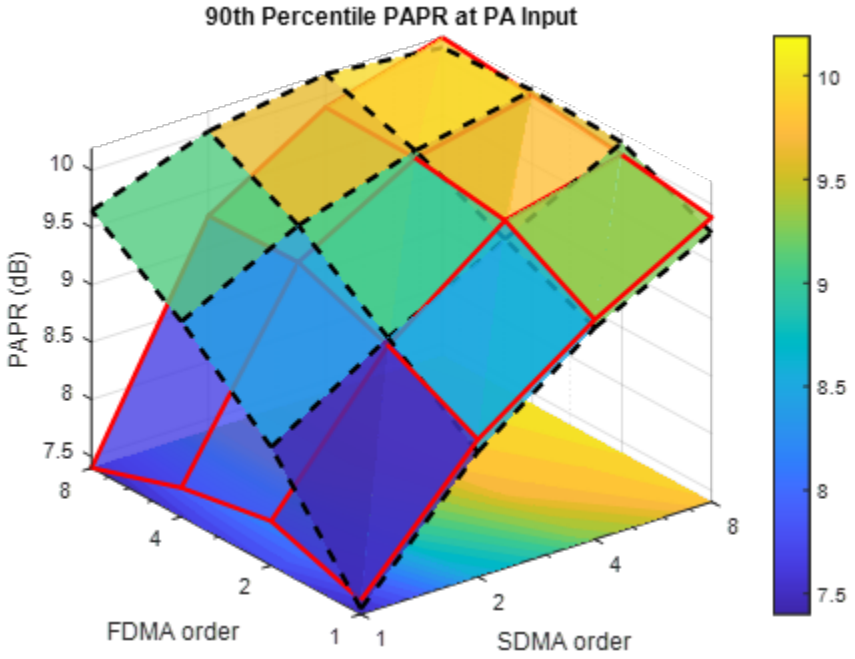

Figure 42: *90th percentile PAPR at PA input for joint SDMA and FDMA. The red grid indicates the PTS and the dashed black grid the DFT-s-OFDM*

As observed in Figure 42, the PTS-enhanced DFT spread scenario sees a stable PAPR performance across the considered FDMA orders over a single beam (SDMA of order one). The results also show that the benefit of the PTS enhancement with respect to DFT-s-OFDM is minor for low FDMA orders, as well as for SDMA orders larger than one.

3.4.4 Conclusions

The PAPR reduction performance of DFT-s-OFDM and PTS-enhanced DFT-s-OFDM was analyzed over FDMA and SDMA for NTN in downlink. In all cases, the results obtained show a significant sensitivity of the PAPR on the number of active users, regardless of the multiplexing scheme and order when relying on either frequency multiplexing, space multiplexing or their combination. Our evaluation results show the PAPR reduction benefit of DFT-s-OFDM decreases below 1 dB relative to CP-OFDM with as few as five users, compared to ~3 dB obtained over a single user.

Moreover, the considered PTS-enhanced DFT-s-OFDM scheme manages to maintain a roughly constant PAPR with the number of users in the frequency domain for a single beam but fails to sustain it over more than one beam. Particularly, above one beam, and owing to the inability to operate PTS across beams, the PAPR improvement of PTS enhanced DFT-s-OFDM stays well under 1 dB relative to conventional DFT-s-OFDM. Notably, the adoption of PTS enhanced DFT precoding across the frequency and space multiplexed users becomes impractical considering the rapid increase in the search space and computations with the number of simultaneous beams and power amplifiers.

In view of the large coverage area per beam, and the implied need to enable a high number of beams, the obtained results highlight the challenge of maintaining a low PAPR in modern beamformed satellite payload architectures. The studied PAPR reduction techniques devised for terrestrial networks therefore result impractical for payload architectures with tens of simultaneously active beams [23].

3.5 COMPATIBILITY WITH TERRESTRIAL WAVEFORMS

Future 6G deployments are expected to combine TN and NTN to achieve global connectivity in the current vision of both HEXA-X-II projects and 3GPP. 6G is expected to introduce new functional requirements including ubiquitous coverage, highlighting the importance of integration of TN and NTN.

For an integrated TN and NTN system with optimized resource allocation and efficient network performance, considerations should be given to the relative traffic volumes of both use cases. Thus, besides the technical metrics studied quantitatively in this deliverable, addressing compatibility with TN features is critical as the same waveforms should be supported by both the TN and NTN architectures without significant changes. Below, we summarize the studies in HEXA-X II project, which is the flagship project in 6G study, and discuss several benefits of having a compatible waveform design for TN and NTN.

- HEXA-X II study on terrestrial waveforms

The HEXA-X II project has conducted comprehensive investigations into waveform candidates for 6G with a strong focus on sub-THz communication. The studies, reported in [ref D4.5 HEXA-X II], have a strong emphasis on evolution of the 5G NR numerology for CP-OFDM and DFTS-OFDM, and explore new constellations, addressing challenges such as phase noise, energy-efficiency, etc. The studies conclude with a prioritization of OFDM-based waveforms, positioning them as candidates for the future 6G air interface.

- Benefits of a compatible TN-NTN waveform

Simplified UE design: In the envisioned 6G architecture, handheld devices and IoT devices will use a single type of receiver optimized for both TN and NTN. Having a compatible waveform between TN and NTN simplifies UE device design and enables cost-effective and scalable device deployments in 6G.

Seamless handover: In early 6G deployments, NTN will primarily serve to extend coverage beyond the reach of TN, rather than acting as a standalone solution. A compatible waveform design allows for seamless handovers, maintaining service continuity as the UE moves between network domains. Devices will connect to TN where available for optimal bandwidth and low latency, and switch to NTN in remote, maritime, or disaster-affected areas. A compatible waveform design enables UEs to use the same radio technology and signaling procedures when moving across TN and NTN.

Reducing network complexity: Common waveform standards across TN and NTN reduce system complexity and deployment costs. Waveform compatibility enables unified chipset development, transceiver design, and simplifies base station implementations. This generates economies of scale and accelerates 6G network rollout timelines.

4 CHANNEL MODEL AND IMPAIRMENTS

As a matter of fact, waveforms effectiveness for satellite communications also depends on the properties of the propagation channel, i.e. on the impairments experienced by the propagating signals as they travel over the earth-space link. Existing studies and recommendations mainly concern the S and the Ka-bands (see TR 38.811 and TR 38.821 for instance), and cannot be automatically extended to different bands as electromagnetic propagation is known to be frequency dependent. This section is therefore devoted to some discussion about wireless propagation in NTN networks in the frequency bands mostly addressed in the project (i.e. C, Q and V bands).

4.1 LARGE SCALE PROPAGATION IN NTN

According to [11], large scale channel characterization in wireless networks refers to the evaluation of the attenuation experienced by wireless signals over the travelled propagation path. In [11], the signal attenuation is computed as:

$$PL[dB] = PL_b + PL_a + PL_s + PL_e$$

where:

- PL_b: “basic” path loss [dB];
- PL_a: attenuation due atmospheric effect [dB]. It mainly accounts for absorption from gases and rain;
- PL_s: attenuation due to scintillation effects, either in the troposphere or in the ionosphere [dB];
- PL_e: building entry loss [dB]

4.1.1 Basic Path Loss

$$PL_b[dB] = FSPL + SF + CL$$

being:

- $FSPL$ - *free space loss*: from the Friis equation:

$$FSPL(d, f) = 32.45 + 20 \cdot \log_{10}(f_{GHz}) + 20 \cdot \log_{10}(d_m)$$

- SF - *shadow fading loss*: it usually accounts for extra-loss due to the possible obstruction of the wireless link coming from large obstacles like buildings or hills. Although satellite communications are expected to occur in line of sight (LOS) most of the time, non-line-of-sight conditions (NLOS) may be nevertheless experienced, especially at lower elevation angles and/or for hand-held reception at ground level. Shadowing fading loss is usually modelled as a log normal random variable $N(0, \sigma_{SH})$, i.e. the value of σ_{SH} must be provided to fully characterize the shadow loss.
- CL: *clutter loss*: it basically includes further extra-loss related to the presence of smaller items close to the ground equipment and not included in the shadowing loss factor.

Free space attenuation can be of course easily computed at any target frequency, and the FSPL equation clearly shows that heavier loss must be expected at greater frequency. On the other hand, similar, closed form formulas are instead not simply available for SF and CL, which

are just provided as tabular data in [11] for S and Ka bands only. Nevertheless, both SF and CL are likely to be heavier at greater frequency, at least according to what claimed and shown in [24] and in [11], respectively. Therefore, shadowing and clutter losses in Q and V band should be greater than what reported in [11] for Ka band. With reference to C band, it is so close to S band that the same values might be approximately considered for the two bands in lack of any further specific analysis.

4.1.2 Atmospheric Losses

These losses usually refer to the attenuation introduced by the presence of oxygen, water vapour (atmospheric absorption) and rain. Other effects can be considered (e.g. through cloud attenuation), but they usually represent minor contributions. The impact of the atmosphere on wireless communications is known to be negligible up to a threshold frequency, often set equal to 10 GHz [25][26]. Atmospheric effects are therefore expected to mostly impair satellite communications in the Q and V bands, with rather limited effect in the C band.

- *Atmospheric Absorption*: the earth-to-space additional loss accounting for energy absorption from atmospheric gases like oxygen and water vapour can be easily computed as [11] :

$$PL_G[dB] = \frac{PL_{zenith}(f)}{\sin(\theta)}$$

being θ the elevation angle and PL_{zenith} the attenuation experienced by a vertical link (i.e. θ=90°). The zenith loss is frequency sensitive and can be estimated by the following Figure 43 [27].

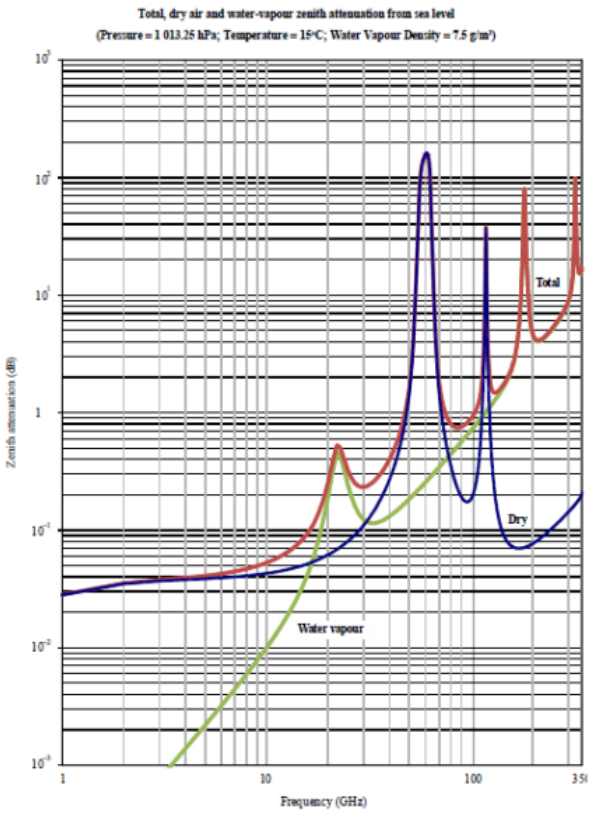

Figure 43: *Zenith attenuation through the whole atmosphere (ref. [27]])*

The atmospheric absorption losses are then represented in Figure 44 in different frequency bands and for different elevation. Clearly, absorption phenomena are negligible in C band regardless of the elevation[6], and are in general heavier at larger frequency. Interestingly, absorption is slightly greater in the Ka band compared to the Q band, and this is explained by the presence of an absorption peak around 22 GHz (Figure 44).

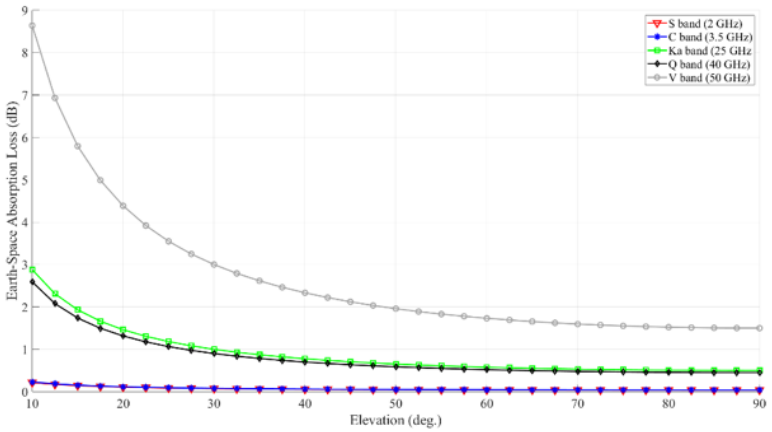

Figure 44: *Absorption loss in different frequency bands*

It is worth pointing out that the values reported in Figure 44 estimate the attenuation experienced by an electromagnetic wave propagating through the whole atmosphere, i.e. they refer to the communication between an earth station and a satellite (either GEO or LEO). In case the flying station is a drone or an high altitude platform station, Figure 44 is unreliable as the atmospheric loss are then likely to be negligible irrespective of both the elevation and the communication band.

- *Rain Loss*: it is usually computed as:

$$PL_R[dB] = \gamma_R \cdot L_E$$

being γ_R the rain specific loss [dB/km] and L_E an effective[7] path length. Details on the procedure suggested by ITU-R for the evaluation of γ_R and L_E can be found in [28]. Rain losses in Ka, Q and V bands are for instance compared in Figure 45, where PL_R is plotted against elevation for different polarization and for a target outage probability p=0.01.

[6] In general they are often claimed negligible at any frequency lower than 10 GHz

[7] To take into account that rain in general is not present all over the earth-space link.

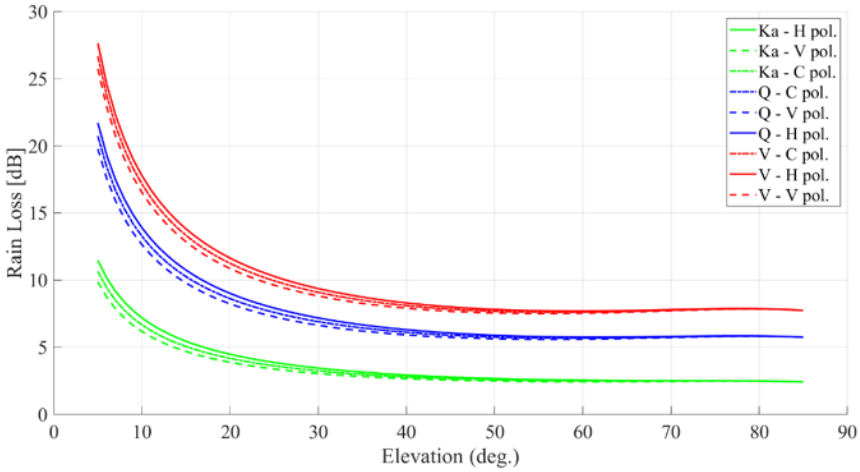

Figure 45: *Rain loss according to ITU-R model, comparison in different frequency bands*

It can be noted that the rain loss in Q/V band is roughly 10dB heavier than its value in the Ka-band, almost regardless of the elevation angle. Similarly to atmospheric absorption, rain losses are commonly neglected at frequency lower than 10 GHz, i.e. their impact on satellite communications in C band is expected to be very light.

4.1.3 Scintillation Losses

Scintillation includes unexpected, fast fluctuations of the received signal amplitude and phase that may occur in the ionosphere and/or in the troposphere. Although ionospheric scintillation has been observed up to 10 GHz, it is commonly neglected above 6 GHz. By contrast, tropospheric scintillation becomes increasingly important at larger frequency, and especially above 10 GHz [11]. Therefore, the impact of ionospheric scintillation must be investigated in the C band only, as it is not expected in the Q and V bands. Conversely, the assessment of tropospheric scintillation effects can be limited to Q and V bands, with no attention paid to C band.

- *Tropospheric scintillation*: it can be taken into account by means of an additional loss term to be included in the link budget equation:

$$PL_{TS}[dB] = a(p) \cdot \sigma(f_{GHz}, \theta_{el}, N_{wet})$$

being p the target outage probability, f_{GHz} the communication frequency, θ the elevation angle and N_{wet} a coefficient related to the (median) radio refractivity, i.e. to the tropospheric conditions. Details can be found in [28]. Some results returned by the model are presented in the following Figure 46.

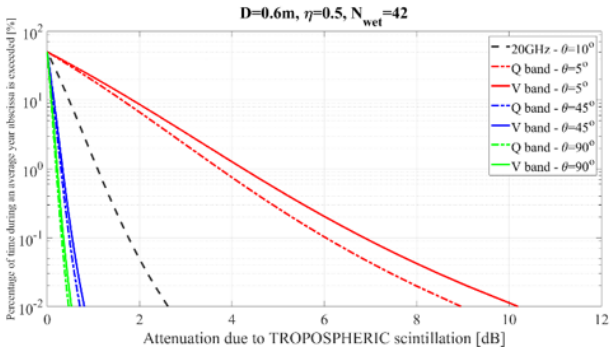

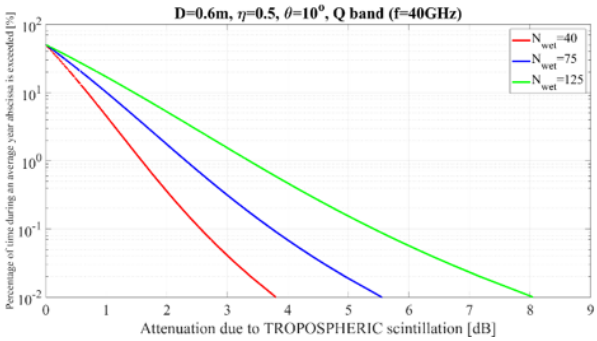

Figure 46: *Tropospheric scintillation loss. According to [FF6], D and η represent the ground antenna diameter and its efficiency*

Based on Figure 46, the following general trend can be highlighted:

- Tropospheric scintillation loss increases at larger frequency
- Tropospheric scintillation loss decreases as the elevation of the satellite link gets larger, to the extent that in Q and V bands it is likely to be important just at quite low elevation (around 5°)
- Tropospheric scintillation loss seems quite affected by radio refractivity through the N_{wet} coefficient.

In the worst case (θ=5°, N_{wet}=150), $PL_{TS,dB}$ at 50GHz can amount to 10dB.

➲ *Ionospheric scintillation*: a baseline model for the evaluation of the corresponding loss below 6 GHz and low latitude is based on the peak-to-peak fluctuation (P_{fluc}) level at 99% of the P3 curve in Figure 47 [11], which is roughly equal to 1.1. Then, signal loss due to ionospheric scintillation can be easily computed as $PL_{IS}[dB] = {P_{fluc}}/{\sqrt{2}}$. Since P_{fluc} is also known to scale in frequency as $(1/f)^{\upsilon}$, $\upsilon \in [1,2]$ [11], [29], the ionospheric scintillation loss at any frequency lower than 6 GHz and at low latitude can be finally computed as [11] [29]:

$$PL_{IS}[dB] = \frac{P_{fluc}(4GHz)}{\sqrt{2}} \cdot \left(\frac{4}{f_{GHz}}\right)^{1.5} \approx \frac{1.1}{\sqrt{2}} \cdot \left(\frac{4}{f_{GHz}}\right)^{1.5}$$

According to the equation, the scintillation loss corresponding to f = 3.5GHz (C band) is equal to just 0.95 dB.

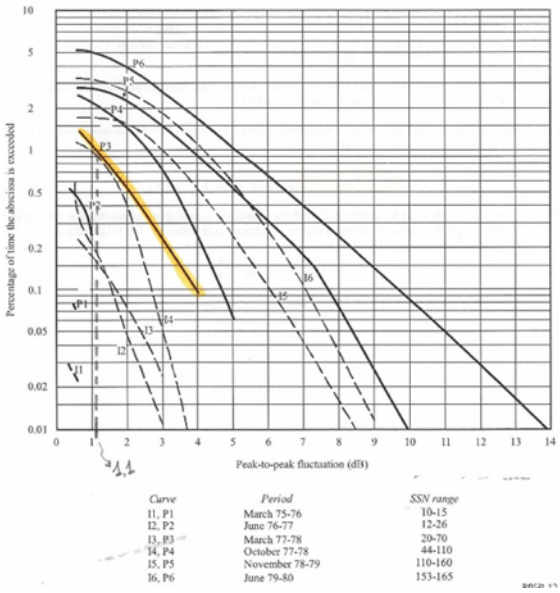

Figure 47: *CDFs of peak-to-peak fluctuations at 20o elevation (P curves) and 30o elevation (I curves)*

4.1.4 Building Entry Loss (BEL)

The simple model included in [30] may represent a starting reference for the computation of the BEL at the frequencies of interest:

$$PL_e(f) = 5 - 10 \cdot \log_{10}\left(p_g \cdot 10^{-L_{glass}/10} + p_c \cdot 10^{-L_{concrete}/10}\right)$$

where:

- p_g and p_c represent the percentage of glass and concrete on the façade of the illuminated wall (p_g+p_c=1);
- $L_{glass} = \begin{cases} 2 + 0.2 \cdot f & \text{standard glass} \\ 23 + 0.3 \cdot f & \text{infrared reflecting (IRR) glass} \end{cases}$
- $L_{concrete} = 5 + 4 \cdot f$

Building entry loss is plotted against frequency in Figure 48 for p_g=0.3 (higher loss case) and p_g=0.7 (lower loss case). The difference between C band and Q/V bands amounts to roughly 10 dB.

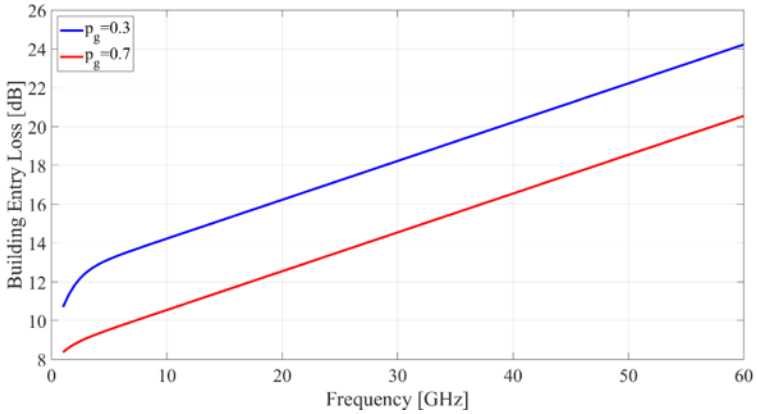

Figure 48: *Building entry loss model*

It is worth pointing out that standard glass is assumed in Figure 48, that means the diffusion of IRR glass (e.g. to contrast climate change) may result in a harsh problem for indoor wireless coverage in NTN.

4.2 MULTIPATH EFFECTS IN NTN

Although line of sight usually occurs in satellite communications with greater probability compared to terrestrial networks, multipath propagation can nevertheless affect the quality of service. The reason is – at least – twofold: *(i)* the atmosphere is not spatially uniform, i.e. the signal spreading from the transmitter can reach the receiver through different curved trajectories over the air, resulting in final multipath effects; *(ii)* the ground footprint of the satellite transmission is in general very large, that means the transmitted signal can experience multiple interactions also at earth level, further contributing to multipath propagation. Multipath effects are expected to become even more crucial in the next NTNs, which will complement terrestrial cellular networks to create a single, integrated communication infrastructure. In this framework, satellite (or UAVs and HAPs) might provide wireless connectivity also to (mobile) ground users at street level in (dense) urban environment, where NLoS, multipath propagation conditions in general occur with greater probability compared to ground equipment placed at building roof level or in open, rural areas. In the following, the attention is especially focused on multipath effects triggered by the urban propagation environment on the earth surface. The intensity of multipath effects can be evaluated by means of several parameters. Rice factor and delay spread are in particular addressed here in.

- *Rice Factor (K)*: from a mathematical point of view, the Rice factor represents the coefficient of the Rice distribution. When referred to multipath propagation channels, it can be also regarded as the ratio between the intensity of signal arriving at the receiver through the dominant path[8] and the overall intensity coming from all the other paths (often referred to as scattering contribution).
- *RMS Delay Spread (DS)*: it accounts for the channel dispersion properties in the delay domain. In presence of multipath, the same data reach the receiver through the different paths, but each paths has its own delay. Therefore, the energy embedded onto each transmitted symbol arrives at the receiver spread over a time period in general longer than the symbol time. The value of the rms delay spread is an estimate of such spreading.

Rice factor and rms delay spread have been estimated in three different propagation scenarios (dense urban - DU, urban – U, and suburban - SU) for different elevation of the earth-space link and by means of ray tracing simulations (RT). For each map, twenty ground locations have been spread all over the area (***Figure 49***). Each location actually corresponds to a grid of 15 × 15 uniformly spaced receivers. Eight different elevation angles have been considered for the satellite, that was placed at 500 km from the urban map, thus representing a LEO spacecraft. Six different azimuth angles have been randomly considered for the same elevation value, in order to somehow smooth any bias effect possibly coming from the azimuth domain. The main parameters describing the simulation environment are reported in ***Table 12***.

Table 12: *Main parameters of the simulated propagation scenarios*

	Dense Urban	**Urban**	**Suburban**
Map size	0.3 km × 0.3 km	0.4 km × 0.4 km	0.5 km × 0.5 km
No. of buildings	199	187	183

[8] It basically consists of the cluster of signal contributions carrying the greatest power to the receiver

Building density (no. / Km^2)	2210	1690	730
Mean buildings height	17.2 m	13.4 m	8 m
Elevation range	10º, 20º, 30º, 40º, 50º, 60º, 70º, 80º		
Grid size	4 m		

Regardless of the scenario, the receiving locations are assumed to be well included inside the footprint of the satellite antenna, which is circularly polarized in agreement with [11]. Three different antenna types are instead considered at the ground equipment, depending on the frequency and addressing different use cases [11]:

- *Isotropic antenna*: it accounts for Handheld (HH) or IoT devices, working in the lowest frequency band (3.5 GHz) at 1.5 m from the ground level.
- *Patch-like antenna*: it is conceived for vehicular application, still in the 3.5 GHz band, where the antenna is placed on car roofs, with a mild directivity and vertical boresight direction regardless of the satellite position;
- *60 cm equivalent aperture:* it represents a directive antenna for fixed reception at ground. Of course, this solution makes sense provided that LoS conditions occur with high likelihood. To this regard, the user equipment is placed at building roofs level, with antenna boresight always pointed towards the satellite position. This antenna is most suited to the higher frequency bands, i.e., Ka, Q and V bands. It is also worth pointing out that this 60 cm equivalent aperture is broadly aligned with the higher-gain NTN UE option discussed in section D4.8.

The main properties of the possible antenna at the end user are summed up in ***Table 13***.

Table 13: *Main parameters of the simulated environments*

Antenna Type	Polarization	Frequency Band	Directivity	HPBW	Position	Use Case
Isotropic	Linear (vertical)	C	0 dBi	--	1.5 m (Ground level)	HH / IoT
Patch-like			~ 6 dBi	120º	1.5 m (Car Roof)	Vehicular
60 cm Aperture	Circular	Ka	~ 44 dBi	2.9º	Average Building Height	Fixed
		Q	~ 48 dBi	1.8º		
		V	~ 50 dBi	1.5º		

The main features of the RT tool are described in [31][32]. Besides standard electromagnetic interactions, like reflection and diffraction, the model also includes diffuse scattering according to the “effective roughness” (ER) approach [32]. The ER model aims at effectively accounting for the multipath contributions generated by the urban clutter, i.e. by those medium-size items usually present along the streets (like cars, road signs, street lamps) or on the building walls (rain pipes, balconies, widows frames, etc.) but not included in any digital representation of the urban layout. To this aim, every surface included in the digital database describing the propagation environment is associated with a scattering parameter $S \in [0–1]$, with S^2 representing the percentage of power that is spread by the surface in spatial directions other than the specular one according to a simple scattering radiation pattern. Especially at greater elevation, where the wireless signal from the satellite easily drops down from roof to ground level, the multipath pattern is expected to be significantly affected by scattering from the objects lying on the ground and surrounding the ground stations. For this reason, simulations have

been run with the same scattering coefficient for every building wall, whereas a different, ad-hoc value has been considered for the ground.

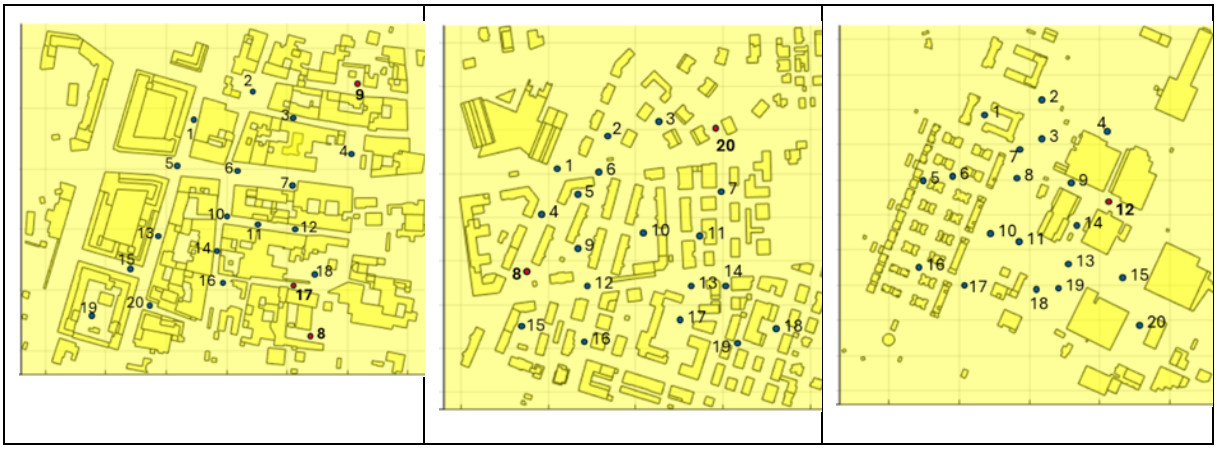

Figure 49: *Digital representation of the urban scenarios: dense urban (left), urban (centre) and suburban (right)*

RT simulations have been then run between each position of the satellite and each ground terminal inside each grid, according to the simulation parameters outlined in ***Table 14***.

If M different paths have been tracked between a (satellite, ground terminal) pair, and P_i, τ_i represent the intensity and the propagation delay of the i-th path, the rms delay spread at the k-th ground location has been then computed as:

$$DS_k = \sigma_{DS} = \sqrt{\sum_{i=1}^{M} \frac{P_i}{P} \cdot (\tau_i - \langle\tau\rangle)^2}$$

where $P = \sum_{i=1}^{M} P_i$ and $\langle\tau\rangle = \sum_{i=1}^{M} {}^{P_i}/_{P} \cdot \tau_i$.

Assuming that signal fluctuations over each grid are due to fast fading effect only, fast fading samples have been collected by normalizing each received signal amplitude by the spatial signal average over the grid [33]. Finally, a maximum likelihood estimating procedure has been set-up in order to compute the K value of the best Rice distribution that optimally fit the empirical distribution of the fast fading samples returned by the RT simulations.

Table 14: *Major simulation parameters*

		C band (3.5 GHz)	Q band (40 GHz)	V band (50 GHz)
Building & ground relative permittivity (ε_R)		5	5.5	5.5
Building & ground conductivity (σ) [S/m]		0.01	0.4	0.4
Building Scattering parameter (S)		0.4	0.6	0.6
Ground Scattering parameter (S)	**DU**	0.5	0.75	0.75
	U	0.4	0.6	0.6

	SU	0.25	0.375	0.375
No. reflection alone		3		
No. diffraction alone		1		
No. scattering alone		1		
No. reflection with diffraction		1		
No. reflection with scattering		1		
Antennas radiation pattern		see Table Table 13		

To begin with, LoS probability is easily computed from RT simulations, for the different urban type and deployment of the user equipment at roof or at street level (***Figure 50***). Regardless of the specific case, LoS occurrence increases with elevation, that is of course obvious. Of course, moving the ground station from street level to the roof top also greatly improve the LoS probability. Moreover, the greater the building density, the lower the LoS probability, that also makes physical sense. For instance, in dense urban environment and user equipment at street level, LoS probability approaches 100% when the satellite is close to zenith, whereas full LoS conditions already occur at 40° in the suburban case. It is worth noting the outcomes of RT simulations are in some disagreement with the LoS probability values suggested in [11], especially at low satellite elevation in the dense- and sub-urban case. Although no details are provided in [11], a LoS probability equal to about 25% in dense urban context when the satellite at 10° elevation looks actually too large. In this regard, on-field evaluations discussed in [24] (black dots in ***Figure 49***) seem in better agreement with RT results.

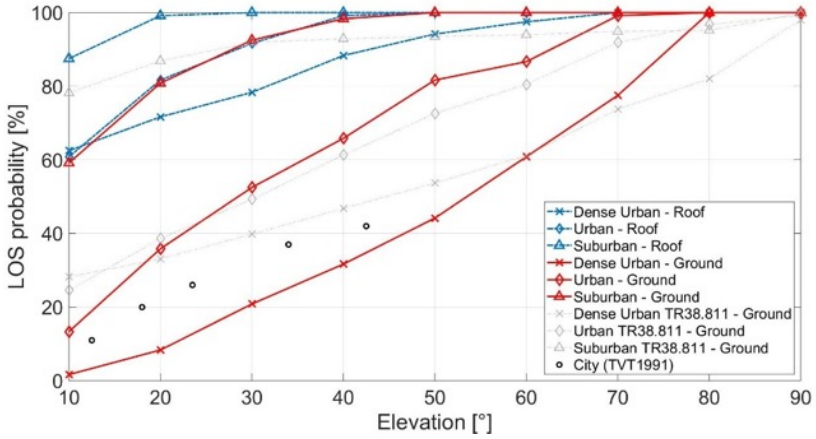

Figure 50: *Comparison of LoS probability vs. elevation for different urban layouts and different deployment of the ground station*

With reference to Rice factor and delay spread, results are shown in ***Figure 51*** and ***Figure 52***, where they are plotted against the satellite elevation for the three considered scenarios, in different frequency bands and different use cases. Besides C, Q and V band, S and Ka bands are also considered for the sake of comparison.

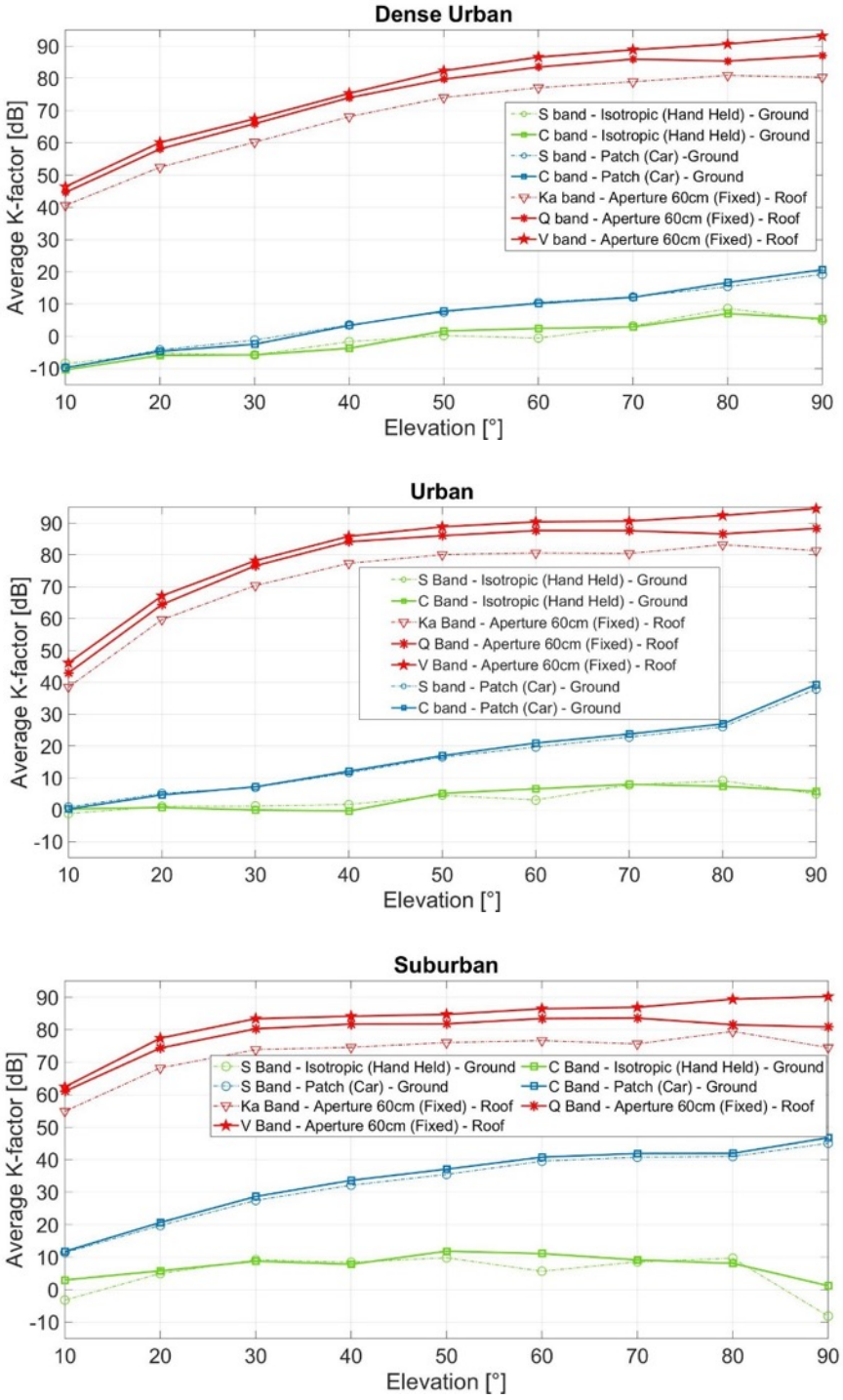

Figure 51: *Rice factor vs. satellite elevation at different frequency band and different use case*

According to ***Figure 51*** and ***Figure 52***, both Rice factor and delay spread are in general clearly affected by the occurrence of the LoS condition. This makes physical sense, as greater LoS probability entails the presence of a powerful, short-delayed received signal contribution with higher likelihood, that exactly contributes – on the average – to increase the Rice factor and to reduce the delay spread. In the framework of the considered RT simulations, two main factors have a clear impact on the LoS condition:

- The satellite elevation, as of course it gets easier visibility of the ground stations when it flies at higher elevation. Close to zenith (80°-90°), the Rice factor can be 20 to 30 dB greater than its value at the lowest elevation, whereas the delay spread can increase by 1 to 2 order of magnitude;
- The height of the ground station: if moved from street- to roof-level, the Rice factor increases by more than 40dB, whereas the delay spread reduces of 2/3 order of magnitude.

Antenna radiation pattern of the ground equipment has also importance, as a reduction of the beam width corresponds to a greater Rice factor and a lower delay spread. As a matter of fact, a greater directivity means a larger number of multipath components reaching the ground station antenna with out of its main radiation lobe, and therefore they are basically cut out from the multipath pattern. Since they usually correspond to long-delayed, diffused contributions, this results in greater Rice factor and lower delay spread. This is clearly shown by the comparison of the results achieved for the “hand-held” and “car” cases, that share the same band (C) and deployment (Ground), i.e. the difference is due to the radiation pattern only.

With reference to the frequency sensitivity, not surprisingly results for frequencies lower than 6 GHz (S and C band) are totally different from results achieved for the (sub-) millimeter band. It is worth noting that S and C bands basically yield the same values, i.e. they share the same propagation conditions. The same remark holds for the Q and the V bands, though to a lower extent. In comparison with the Ka band, the Rice factor at Q/V frequencies is 5-10dB greater, whereas quite light difference results for the delay spread.

Finally, ***Figure 51*** and ***Figure 52*** also show that Rice factor and delay spread also depend on the urban building density, in a way that is not simply straightforward. On the one hand, a reduction in the building density (i.e. moving from DU to U and SU scenario) corresponds to a larger LoS probability, that contributes to greater K values and lower DS values. On the other hand, a lower building density can more easily enable the existence of long-delayed, not negligible scattered contribution at the receiver side, that might result in lower K values and greater DS values. According to ***Figure 51*** and ***Figure 52***, the former effect prevails at the lower elevation (up to 40° approximately), whereas a clear trend can be hardly highlighted otherwise.

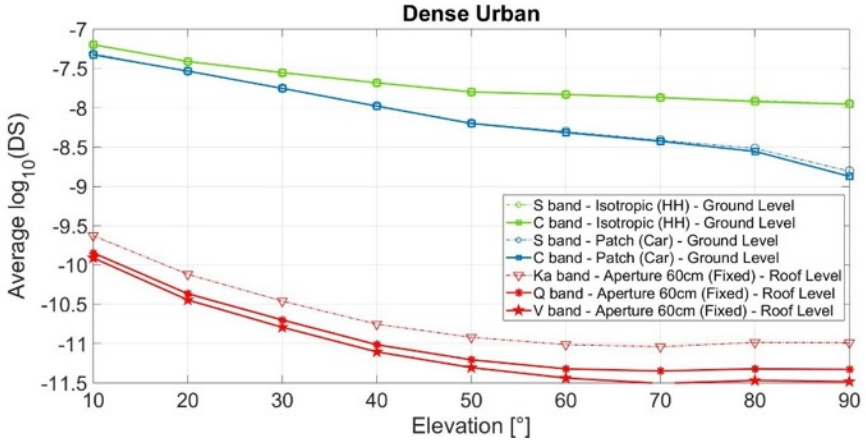

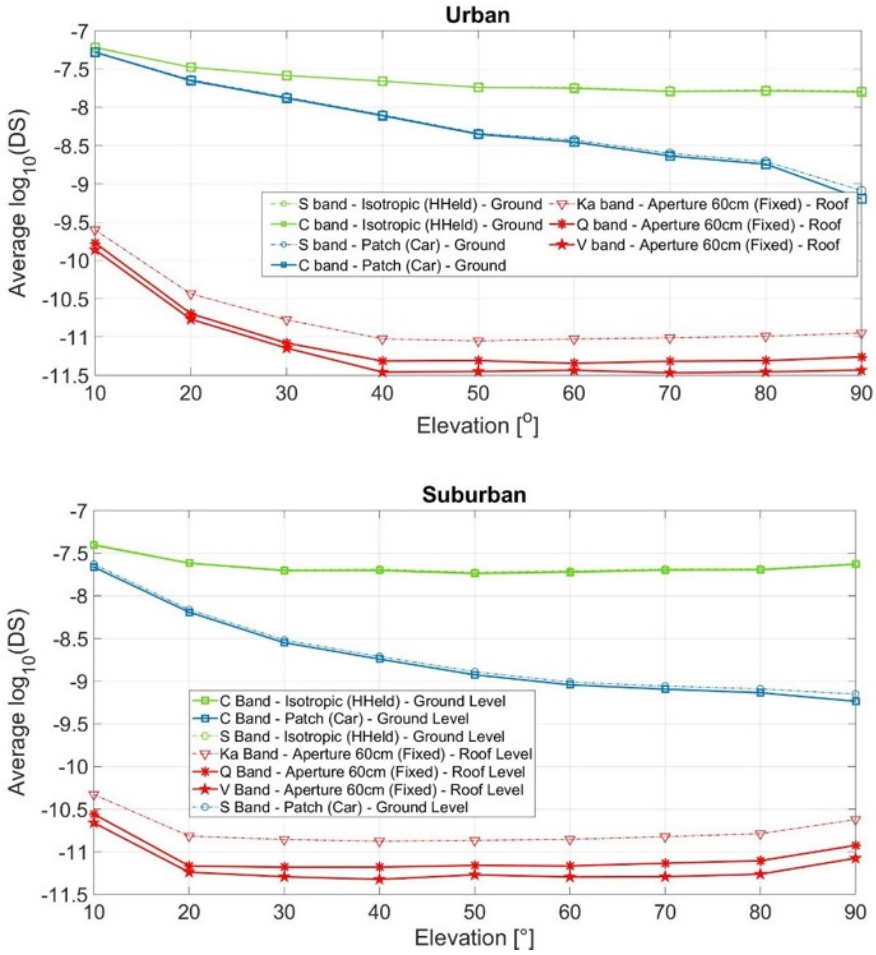

Figure 52: *Delay spread vs. satellite elevation for different frequency bands and different use case*

Considerations

Throughout the project, different 'families' of channel models were developed: i) a detailed urban/sub-urban/dense urban ray tracing modes following a 3GPP-like approach; ii) the data-driven models used for path loss prediction in D4.6; and iii) the path loss propagation framework adopted in D4.8 for coexistence studies.

The first one aims at defining the multipath effects triggered by the urban propagation environment on the Earth surface in terms of Rice factor and delay spread, considering different elevation and azimuthal angles. This analysis is independent of the satellite constellation, and it can be used to refine and validate the large-scale models in D4.8 for C and Q/V-bands, large-scale models used in practice for system evaluation of interference and coexistence management.

Regarding the second one, the propagation is split into two parts: i) satellite-to-a virtual site on the LoS line (modeled with free-space propagation), and ii) virtual site-to-UE (modeled with full ray tracing). The outputs are power-delay profiles (path losses and delays for each path), which are then used to build datasets for ML-based pathloss prediction in time.

Therefore, the Rice factor and the delay spread, computed with the ray tracing model developed in this deliverable, can be used on top of the RT rays to refine the small-scale

fading/channel dispersion in a subsequent link-level/channel model implementation (e.g., in MATLAB).

5 AI/ML BASED PHY FOR 6G-NTN

5.1 STATE OF THE ART OF AI APPLIED TO NTN

The evolution of wireless communication technologies has led to the conceptualization of 6G, which aims to provide ubiquitous connectivity, extremely high data rates, ultra-low latency, and massive device connectivity. NTNs, including satellite and aerial systems, are expected to play a crucial role in achieving these goals by providing wide-area coverage and addressing the limitations of terrestrial networks [34].
Artificial intelligence (AI) techniques are increasingly being recognized as essential tools for addressing the complex challenges posed by NTNs. AI's ability to learn from data and adapt in real-time makes it well-suited for dynamic and uncertain NTN environments. AI can enhance various aspects of NTN, from resource allocation and beam hopping to signal power prediction and ionospheric scintillation forecasting [35][36]. In particular, it is a versatile tool for handling the design of advanced waveform strategies at the lower layers of the protocol stack.
This survey will cover the general usage of AI in NTNs and focus on the lower layers, with particular attention to cross-layer and physical layer applications [38]-[100].

5.1.1 AI in communication systems

In wireless communications, AI is attracting interest because many problems involve complex, nonlinear relationships that are hard to model analytically. AI models can learn end-to-end mappings for a given waveform (for example, from received signals to decoded bits) or predict network behavior from environment data. In particular, AI can capture “intricate correlations among diverse network parameters”, making it a promising tool for the new challenges introduced by upcoming mobile communications standards [36][43]. For example, 6G use cases (augmented or virtual reality, holographic communications, Internet of Things, etc.) is expected to require extremely high data rates, ultra-low latency, and ubiquitous coverage [44]. Terrestrial networks alone struggle to meet these demands over all environments. Integrating satellite and aerial systems (NTNs) can provide wide-area coverage, but at the cost of addressing new problems like large propagation delays, strong Doppler shifts, and dynamic handovers [45]. AI’s ability to learn from data and adapt in real time makes it well-suited to these settings, e.g. by adapting link parameters or managing resources based on observed channel and traffic conditions.
The integration of AI and machine learning (ML) into communication systems has opened new avenues for enhancing network performance, efficiency, and reliability. These technologies are being applied across various layers of the communication stack, from the physical layer to the application layer.
In the core network and upper layers, ML has long been used for traffic prediction, network management, and self-organizing network (SON) functions. For example, operators use machine learning algorithms which can analyze traffic patterns and predict network congestion, enabling proactive resource allocation, load balancing, anomaly detection, and mobility management. This can significantly improve the quality of service (QoS) and user experience [38][39].
At the physical layer, AI can improve classical signal processing blocks. Traditional PHY algorithms (e.g., for channel estimation, synchronization, decoding) often rely on idealized models and may perform poorly under real-world impairments (nonlinearities, hardware imperfections, or unknown propagation effects). AI methods (e.g., neural networks) can learn to compensate for such impairments by training on data. For instance, deep neural demodulators or autoencoders can learn end-to-end mappings that implicitly handle channel distortions. Neural networks, for example, can learn to compensate for real-world impairments

and improve the accuracy of channel estimates. This is particularly beneficial in dynamic and non-linear environments, where traditional methods may fall short [38][40].
However, AI at the PHY layer also introduces challenges, such as real-time constraints and hardware limitations [37]. It is also hard to deploy very large models, and models must be robust to channel changes they weren't trained on.
In summary, AI and ML are revolutionizing communication systems by providing intelligent solutions to complex problems. Their ability to learn from data, adapt to changing conditions, and make real-time decisions makes them indispensable in the development of next-generation communication networks. As research and standardization efforts continue, the integration of AI and ML into communication systems is expected to deepen, paving the way for more efficient, reliable, and intelligent networks [46].

5.1.2 Choosing the right type of AI

The use of ML techniques is not always justified for all problems. 3GPP experts note that while AI can solve highly nonlinear, heuristic-rich problems effectively, it tends to be energy-hungry and may complicate analysis [47]. Data-driven or hybrid design approaches can be pertinent when one or many of the following conditions are met:

- Model-driven techniques are not applicable, either due to a model deficit (i.e., a sufficiently accurate model is unavailable) or due to an algorithm deficit (i.e., the known optimal algorithm is too complex for implementation). While both issues can be addressed with data-driven AI, the latter situation can also be handled by hybrid AI.
- Sufficiently large training and validation data sets exist or they can be created.
- The phenomenon being learned is stationary for a sufficiently long period of time[9]. Otherwise data-collection and learning steps become susceptible to overfitting or underfitting issues independent of the hypothesis class.
- The task does not have critical and formally provable performance requirements. For model-deficit situations a guarantee cannot be provided in general, and for algorithm-deficit cases guarantees need to be verified by numerical simulations and not by formal proof. It is important for data-driven AI that the task does not require justification on how the decision is made within the black-box nature of the trained machine. However, provable AI is a currently active research domain, given the practical importance of integrating critical functional and quantitative requirements on AI-based system functions. Evolutions may be expected on this topic in the future.

More details on the reasoning behind these criteria can be found in the tutorial [38]. Thus, a key focus is on balancing complexity and performance, and on incorporating AI as an assistant to traditional algorithms, through hybrid-AI strategy, wherever it yields gains by learning residual errors or by reducing algorithm complexity.

5.1.3 On the use of AI for 3GPP standards

3GPP has recognized the potential of AI and ML in enhancing wireless communication systems. 3GPP Release-18 includes study items on AI/ML for RAN, focusing on providing standards-based frameworks for data collection, model management, and AI/ML-assisted functions [47] [48]. In particular, 3GPP has prioritized AI integration by defining interfaces for collecting device data and delivering trained models, enabling localized decision-making (like closed-loop SON) without mandating specific algorithms. This reflects a trend toward "AI-

[9] There are some methods for performing ML in non-stationary environments but they require the use of advanced modelling and training techniques based on covariate shift adaptation. These techniques will not be dealt with in this report due to their complexity and we refer the reader to [45].

native" air interfaces and open RAN (O-RAN) architectures, where intelligence can be inserted at various network nodes.

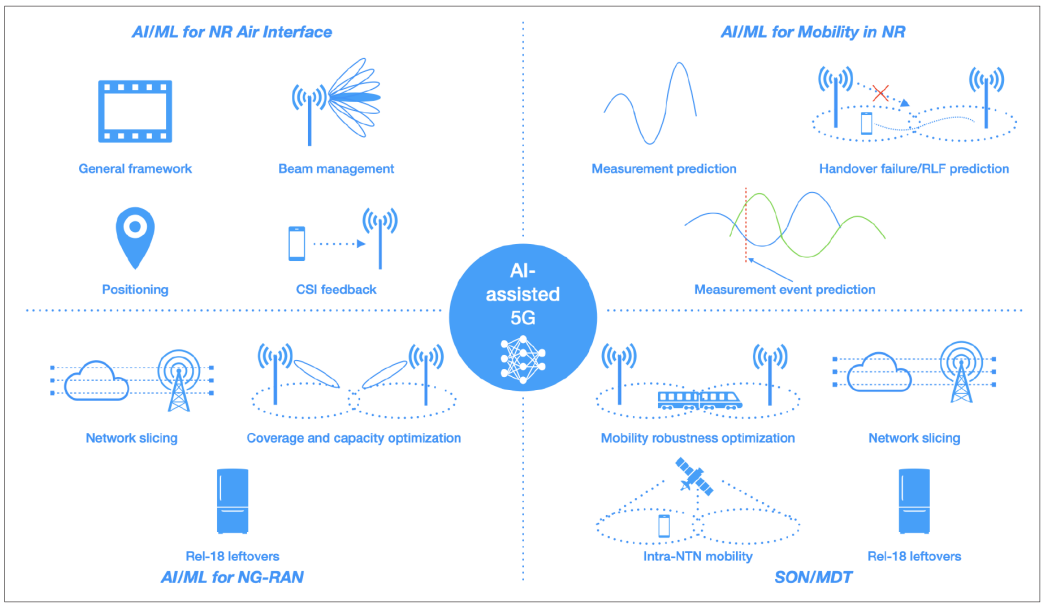

Figure 53: *Illustration of the key 3GPP Release 19 features related to AI-assisted 5G [48]*

Regarding network management, AI and ML is explored for improving energy saving, load balancing and mobility optimization among others. These involve optimizing resource allocation, predicting traffic patterns and managing user mobility. Reference [87] exposes the status of AI/ML related studies following the release 17, notably with the specifications in [88], involving many use case enhancements for data collection. With the release 18, investigations targeted more precisely the air interface through subjects like channel state information (CSI) enhancements, improved beam management and positioning (see [89]). Investigations on CSI prediction and compression are still ongoing with Release 19, in early 2025, as shown in Figure 53, however support for AI frameworks in life-cycle management, beam management and positioning has been effectively standardized [48].
Ongoing investigations for upcoming releases and 6G are numerous, and aim to expand AI/ML usage to federated learning and cross-layer integration. There are also various initiatives provided by independent actors and businesses such as DeepSig. This latter readily proposes solutions such as OmniPHY-5G which upgrades the RAN with neural networks at the physical layer for improved channel estimation and equalization performance [90]. These advances attest to the increased impact of AI/ML for next generation communication system design [91], however at this stage of technology, the computational complexity dimension of neural networks investigated in such schemes is often neglected. Although this might become less of an issue with the development of chips specialized for neural network processing, many of the technologies discussed above at least partially involve online training which constitutes an even more computationally intensive procedure.

5.1.4 On the role of AI in NTN

The high mobility of LEO satellites, the atmospheric volatility, and the complex interference patterns in integrated satellite-terrestrial systems create a "model-deficit" scenario. Here, data-driven techniques, particularly those based on DL, have demonstrated remarkable capabilities.

In particular, the dynamic nature of NTN channels, characterized by significant Doppler shifts and time-varying propagation paths, renders conventional channel estimation methods based on static assumptions inadequate. As reviewed, AI models, particularly recurrent neural

networks (RNNs) like LSTM and GRU, have proven highly effective.
AI has shifted the paradigm from reliance on costly ephemeris data to direct estimation from the received signal. Works like [69] and [72] have shown that neural networks can accurately predict Doppler shifts by learning the temporal patterns in CSI or RSRP measurements. This not only reduces signaling overhead but also enables faster and more adaptive synchronization, which is critical for maintaining link reliability in high-velocity LEO scenarios.

The long propagation delays in NTNs make CSI feedback obsolete by the time it reaches the transmitter. The surveyed works [58][59] demonstrate that by treating CSI as a time series, AI models can predict future channel states with impressive accuracy. The use of efficient architectures like GRU and Informer enables real-time prediction with low computational complexity, facilitating proactive link adaptation, such as AMC and beamforming adjustments, thereby maximizing spectral efficiency.
AI is not merely enhancing existing signal processing blocks but is also enabling the design of entirely new, end-to-end optimized communication systems. Autoencoder-based PHY designs, as explored in works like [73][99], can jointly optimize modulation, pulse shaping, and demodulation for specific NTN channel characteristics. This is particularly powerful for mitigating non-linearities and unmodeled hardware impairments, which are prevalent in satellite payloads. By learning an optimal mapping from bits to waveforms, these systems can achieve performance gains that are unattainable with modular, model-driven designs. For complex tasks like MIMO detection and equalization, a hybrid approach has emerged as a pragmatic solution. Instead of replacing the entire receiver with a black-box neural network, AI is used to augment specific algorithmic steps. For example, "deep unfolding" techniques, as seen in the OAMP-Net [80] and its variants, embed learnable parameters within iterative algorithms. This approach retains the structure and interpretability of model-based methods while leveraging DL to refine performance, bridging the gap between theoretical optimality and practical feasibility [95][96]. This is a crucial lesson for NTNs, where a complete lack of a model is rare, but imperfections are common.
Fourati and Alouini [35] provide a broad, foundational survey of AI applications in satellite communications. The paper dedicates a significant portion to a primer on AI, ML, deep learning (DL), and reinforcement learning (RL) before systematically reviewing their use in solving specific challenges. Its contribution lies in its extensive scope, addressing eleven distinct application areas including beam-hopping, anti-jamming, network traffic forecasting, channel modeling, telemetry mining, and remote sensing. Similarly, Mahboob and Liu [36] offers a contemporary analysis focused on AI's role in satellite-based NTNs for 6G.

5.1.4.1 AI the PHY layer of NTN air interface

At the PHY layer of most communications systems, operations at the baseband can often be modelled with high fidelity and model-based (near)-optimal receivers can be derived, such as the BCJR detector [78], MMSE turbo equalizers [79]. However, such algorithms can only be implemented if sufficient computational complexity, memory storage and induced processing latency are affordable for the target platform. Moreover, many algorithms, especially related to synchronization or estimation procedures require the transmission of additional probe signals, which reduces the system’s overall throughput.
The benefit of ML-based (data-based) AI is mainly for algorithm-deficit situations, for instance, when maximum likelihood (or maximum a posteriori) detection/decoding is too expensive for implementation. Model-deficit phenomena at PHY can rather appear at the front-end, on handling non-linearity, synchronization and channel/interference/jammer modelling issues. Such issues are common, for instance, for optical or molecular communications and for some wireless systems operating in the non-linear amplification regime.
It is common to seek AI for improving the wireless PHY layer receivers for data transmission [92] where the computational complexity of the near-optimal receivers are often prohibitive, and where the real-world transmission medium can incorporate some poorly modelled

phenomena. The application of emerging machine learning and deep learning techniques for mitigating these aspects gather a lot of attention [37]. For instance OMNIPHY-5G is a product of DeepSig which uses learning to enhance 5G compatible radio access networks with data-driven online AI techniques [93][94]. However it is also becoming more and more common to use AI for joint transmitter and receiver optimisation by learning the PHY-layer parameters of flexible waveforms.
Lower layers of NTNs for the 6G air interface poses many challenges that significantly affect both receiver design and waveform design aspects. AI techniques can enhance parameter estimation, waveform optimization, and demodulation, improving the overall performance and reliability of NTNs. This section explores the application of AI at the lower layers, focusing on parameter estimation and waveform optimization.

5.1.4.1.1 Parameter Estimation

Accurate parameter estimation is crucial for the efficient operation of NTNs, particularly in dynamic and heterogeneous environments. AI techniques have been applied to various parameter estimation tasks, including channel estimation with a focus on Doppler estimation and prediction.
Traditional least squares (LS) channel estimation techniques may struggle to cope with the complexities of NTN environments, such as high mobility, atmospheric phenomena and wideband propagation. AI can enhance estimation by learning channel statistics and compensating for real-world impairments, and such strategies have seen relative success in terrestrial networks and they have attracted considerable research effort.
For instance, in [61], the authors utilize a DNN with ReLUs to enhance channel estimation after an initial LS estimation in an OFDM system. They recognize that a linear MMSE estimator can be modulated as a modified LS estimator influenced by channel and noise statistics, prompting them to employ a DNN to learn this dependency. Consequently, a DNN using LS estimator inputs must also learn autocorrelation dependency of reference sequences. In principle, CNNs or transformer encoders can process pilot and non-pilot OFDM symbols jointly to refine channel estimates under nonlinear distortions. This technique is applied to better temporally interpolate the channel for the vehicular uses cases of IEEE802.11p system.
Another class of solutions for estimating time-varying channels in the frequency domain uses CNNs instead of fully connected networks. The channel frequency response, evolving over time, is treated as an image that the CNN de-noises or corrects. Reference [62] follows this approach, utilizing a proposed CNN network for image super-resolution tasks in an OFDM system. The CNN's input is an initial channel estimate obtained from pilots using the LS method and spline interpolation, achieving encouraging performance. However, the work trains and tests the neural network on the same statistical channel model, without investigating generalization to other channel models.
The paper [63] presents a method starting from an LS channel estimate, refining it and interpolating on a time-frequency OFDM grid to obtain the channel value corresponding to the data. The authors focus on the neural networks' interpolation capability for rapidly changing channels. They use a CNN for feature extraction, fed into a 6-stage Transformer. However, the learning phase details are absent, implying the same channel model (ETU) was used for both training and testing. Although the technique outperforms a LMMSE estimator, it does not demonstrate generalization to other channel profiles. Bit Error Rate (BER) performance indicates a substantial improvement in estimation error (MSE) translates to a minimal BER enhancement.
Several authors have explored hybrid structures using the attention mechanism without strictly following the infamous transformer architecture with attention-heads. Paper [64] addresses the same channel estimation and interpolation improvement problem as studied in [63], employing a transformer-type encoder with multi-head attention and a CNN structure with residual connections for the decoder. Notably, both transformer and residual CNN utilize layer normalization instead of batch normalization. Like previous studies, training and evaluation

occur on the same ETU channel profile, showing generalization based on SNR and Doppler but not on different profiles. The paper compares various models in terms of complexity, noting the proposed mixed model has over 100,000 parameters, with potential pruning of 10% without significant performance loss. However, the model remains complex for basic channel estimation and interpolation tasks.
Alternative structures use the traditional strategy of treating the channel response on a time-frequency grid as an image, where known pilot symbol positions are pixels and data symbols are “holes” to be estimated. Reference [65] employs a residual convolutional network with 53,000 parameters, achieving performance close to the LMMSE algorithm. This benchmark trains on a 3GPP Urban Micro-cell model and tests on Extended Pedestrian A and WINNERII A1, similar channels with minimal spread, suggesting easy generalization without significantly different profiles. In contrast, [66] proposes a smaller residual structure with 9,000 parameters, testing on EPA, ETU, and EVA channels, showing saturated MSE performance due to lack of generalization capability. Reference [67] optimizes and reduces neural network complexity for frequency domain channel estimation, using a large, diverse training set, including 3GPP channels above 6 GHz. Their residual structure with fully connected layers learns noise subtraction, presenting a hyper-parameter optimization study for Pareto optimal configurations. Variable quantization and pruning reduce model size significantly but only slightly lower complexity. Different networks per SNR sub-interval improve low SNR denoising gain but lack BER or PER impact details. The problem of generalizing to diverse channels remains open.

Similar developments have been emerging in recent years concerning NTN networks, where most of the effort is concentrated on the Doppler estimation.
For instance, authors in [68] propose a novel application of the Denoising Convolutional Neural Network (DnCNN) for channel estimation in massive Multiple-Input Single-Output (MISO) LEO satellite systems. The DnCNN architecture, originally designed for image denoising, comprises 17 convolutional layers, each followed by batch normalization and ReLU activation functions. This deep architecture, with residual connections, enables the network to effectively learn and subtract noise components from the input, enhancing the accuracy of channel estimation. Simulation results demonstrate that the DnCNN-based method outperforms traditional estimation techniques, particularly in scenarios with high Doppler shifts and rapid channel variations typical of LEO environments.

Doppler shifts introduced by the movement of satellites and aerial platforms can significantly impact signal quality in NTNs. AI techniques have been developed to estimate and predict Doppler shifts, enabling proactive compensation and synchronization. Instead of relying only on the satellite ephemeris or GPS, AI can directly estimate Doppler from signal patterns.
For example, deep networks have been shown to accurately estimate the time-varying Doppler offset from the received waveform, without explicit knowledge of satellite orbits. By learning from sequences of frequency-offset symbols, the model can predict the Doppler trend, enabling the receiver to re-synchronize more quickly. This data-driven approach cuts the need for frequent ephemeris updates, reducing overhead while achieving good synchronization.
Kim et al. [69] introduce a machine learning-based Doppler shift estimator (MLDSE) tailored for 5G high-speed train (HST) systems operating in the millimeter-wave band. Recognizing the challenges posed by significant Doppler shifts in such environments, the authors utilize reference signal received power (RSRP) measurements, which are consistently available from the mobile receiver. To address the one-to-many mapping issue between RSRP patterns and Doppler shifts, they design an RSRP ambiguity reducer (AR) that preprocesses the input data, enabling effective learning. The neural network architecture employed is a three-layer fully connected network, emphasizing low computational complexity suitable for real-time applications. Simulation results demonstrate that the MLDSE outperforms traditional estimators, such as LS and minimum mean square error (MMSE), in terms of accuracy and robustness, making it a promising solution for enhancing the reliability of 5G HST communications, which is a study case that can be extended to 6G LEO links.

In their 2021 study [70], Yoon et al. present a machine learning-based approach for Doppler spread estimation in OFDM systems operating under mixed-channel conditions, including varying Rician K-factors, azimuth angle of arrival (AOA) widths, and channel estimation errors. The authors design a neural network that utilizes averaged PSD sequences derived from channel state information (CSI) as input features. This preprocessing step enhances the quality of training data, leading to improved estimation accuracy. The neural network architecture comprises multiple layers optimized for regression tasks, although specific details regarding the number of layers and neurons are not explicitly provided in the paper. Simulation results demonstrate that the proposed method outperforms traditional approaches, such as those using channel frequency response (CFR) sequences, in terms of root mean square error (RMSE) across various signal-to-noise ratios (SNRs) and Doppler frequencies. This work underscores the potential of machine learning techniques in enhancing Doppler spread estimation for OFDM systems in complex wireless environments.
In [71], authors propose a deep learning-based method for predicting Doppler shifts in mobile communication systems. The authors employ a hybrid neural network architecture combining Convolutional Neural Networks (CNNs) and long short-term memory (LSTM) networks. The CNN layers are utilized to extract spatial features from the input data, while the LSTM layers capture temporal dependencies, enabling the model to learn complex patterns associated with Doppler shifts. This approach allows for accurate prediction of Doppler shifts without relying on pilot signals or training sequences, enhancing transmission efficiency. Simulation results demonstrate that the proposed method achieves high estimation accuracy and robustness in high-speed mobile scenarios, outperforming traditional estimation techniques. The study highlights the potential of integrating deep learning models, particularly CNN-LSTM architectures, in improving Doppler shift prediction for mobile communications. Finally, in the NTN context, Kim, Park, and Lee present a CNN-based approach for Doppler shift estimation in LEO satellite communications [72]. The authors design a CNN architecture tailored to process input features derived from received signal characteristics, enabling the model to learn complex patterns associated with Doppler shifts. The network comprises multiple convolutional layers, each followed by activation functions and pooling layers, facilitating hierarchical feature extraction. This deep learning-based method allows for accurate Doppler shift estimation without relying on traditional pilot signals, enhancing the efficiency of satellite communication systems. Simulation results demonstrate that the proposed CNN model achieves high estimation accuracy, outperforming conventional estimation techniques, particularly in scenarios with high mobility and dynamic channel conditions typical of LEO environments. The study underscores the potential of integrating deep learning models, especially CNNs, in improving Doppler shift estimation for satellite communications.

Extending these channel frequency response estimation techniques to F-OFDM could involve training AI models to account for the filtered sub-bands in F-OFDM and to Doppler shifts for each filtered sub-band. By learning the unique correlative characteristics of F-OFDM signals, this would enable more precise compensation and reducing inter-carrier interference provide more accurate estimates compared to conventional LS estimates.

5.1.4.1.2 OFDM Detection

In the broad sense, “detection” is computing probabilistic estimates on transmitted bits from received samples. Because optimal detection is often too computationally complex for practical use, the process is typically split into simpler, sub-optimal steps. These include "equalization," which converts a channel with interference into a simpler AWGN channel and "demapping" or sometimes “symbol demodulation” which is the detection process on binary labels performed on the symbols of this simplified channel. For OFDM transmissions, as in 3GPP standards, equalization is somewhat transparent through the use of DFT on received samples, when the channel’s time coherence is high enough, and when cyclic prefixes are sufficiently large. However, AI techniques have been investigated to improve OFDM detectors for cases where

these conditions are not met, or when the channel incorporates time-selectivity or non-linearity.

In reference [74], a DNN-based OFDM detector is proposed, with five layers. When there is a sufficient number of pilots (with regards to the delay spread), then this receiver operates similarly to the OFDM receiver with MMSE-based channel estimation. On the other hand, when there is a pilot deficiency, DNN-based detector operates significantly better, and similar observations are made for transmissions without cyclic prefix, and in presence of clipping and distortion effects, with several dBs of gains. The training is performed on a specific channel model, but it is claimed that the learned coefficients remain quite robust to changes in the power-delay profile.
Reference [75] compares three alternative neural network-based detection architectures for OFDM: a fully-connected DNN-based detector, a ComNet receiver, which makes a hybrid with LS estimator and detector with a few neural refinement layers, and a novel receiver called Switch-Net. ComNet outperforms other options when the validation channel is the same as the training channel, otherwise FC-DNN is more robust. However, Switch-Net makes a promising alternative where two NNs are trained for two different channels, and the validation receiver switches between the two NNs depending on a scalar parameter that is updated with online training.
In reference [76], another hybrid structure called, ComNet is proposed for OFDM systems, which combines classical LS channel estimation and zero-forcing (ZF) detection with two neural networks. The refinement network used for the LS is a one-layer fully connected network, with no activation function (i.e. a linear estimator), and two options are considered for the refinement network of ZF detection: two-layer fully connected network or a three-layer bidirectional LSTM network. Both variants are robust to channel and SNR variations, in particular training is performed under fixed SNR and the BER performance remains good at varying levels of SNR (although it could be further optimized). The receiver outperforms other alternatives when operating under nonlinear channels (clipping) or under CP deficiency.
In reference [85], an attention-based neural demapper is used for demodulating OFDM signals in the presence of a multipath channel and a very basic LMMSE channel estimator. It is shown that the use of a demapper based on convolutional transformer with multi-head attention enables significant improvements with respect to the baseline AWGN demapper and RNN-based demappers. The structure of the convolutional transformer consists in the use of separable convolutions, followed by batched normalization and multi-head attention with a residual connexion, also followed by another two layer ResNet with separable convolutions.

A MIMO detection system is investigated in reference [80], where the deep-learning network is built upon the OAMP algorithm, and called OAMP-Net, with the advantage of having only a few parameters, independent of the number of antennas. This is achieved by inserting two learnable scalar variables within OAMP, such that each one of them scales a different component of signals. Note that the considered OAMP-Net does not use the optimal implementation of OAMP, as it fails to use a divergent-free non-linear component. This structure is fast and easy to train, and it is able to follow channel variations, as long as the CSI is available.
The work [81] proposes a channel estimation strategy for mmWave MIMO systems by using learned denoising-based AMP (LDAMP) in which an iterative AMP-like algorithm uses a denoiser for estimating and removing the residual noise from the channel estimate. More specifically, the denoiser is implemented with a convolutional neural network (20 layers) which is trained to identify the residual Gaussian noise with an unknown noise level. The resulting channel estimator (10 LDAMP layers) competes with the state of the art AMP algorithms and it is predictable through state evolution.
In reference [82], the OAMP-Net of [80] is extended to OAMP-Net2, by incorporating two additional learnable parameters on the non-linear estimator (which now incorporates ability to remove the divergence of the estimator). The resulting detector is shown to significantly outperform OAMP and OAMP-Net in various configurations, especially in the high SNR regime

of low-order constellations, and in high-dimensional MIMO systems. Next, this structure is coupled with a data-based channel estimator in order to perform joint channel estimation and detection. The resulting structure is compared with OAMP (with data-based channel estimator) and it is able to bring additional gain for the detection threshold (performance comparison is in the uncoded regime).
In reference [83], a hybrid AI approach is used to design a CP-free OFDM receiver, by exploiting a DNN for refining the channel estimation and an unfolded OAMP-based algorithm (OAMP-Net) for carrying out detection within inter-block interference. The channel estimation DNN is simply a linear layer, and it is initialized by mimicking LMMSE channel estimation matrix, by exploiting the LS-based CSI, and then the weights of the matrix are trained to optimize MSE on channel estimation. For the unfolded OAMP implementation, the approach of [56] is used. Channel estimation performance is able to reach the one of the LMMSE estimator when continuous pilots are used and a gap in reachable MSE exists when considering a comb pattern. Reference [84] improves the receiver above by replacing the OAMP-Net with “improved ComNet based on expectation propagation (IComNet-EP)” which is simply EP algorithm with fixed damping factors, and no parameters to train, and it operates close to the ML performance with perfect CSI.
For example, deep convolutional networks have been designed as OFDM demodulators that jointly estimate the channel and demap symbols [53]. This paper presents a Deep Complex-valued Convolutional Neural Network (DCCNN) based OFDM receiver that recovers bitstreams from time-domain signals without relying on traditional DFT/IDFT transforms. The architecture consists of a DCCNN-based equalizer and demodulator, trained using a two-phase transfer learning scheme for improved convergence. The equalizer sub-module uses a series of complex dense layers and a 2D C-Conv layer to estimate the channel response. The network effectively processes complex signals using a CReLU activation function. In performance evaluations under multipath fading channels, the proposed DCCNN estimator is superior to traditional methods. Notably, in an Extended Typical Urban (ETU) channel, it outperforms the ALMMSE estimator by approximately 4.8 dB at an uncoded BER of 0.01. Although not yet standardized for NTN, such AI receivers could enable lower-power or lower-complexity implementation by replacing iterative DSP blocks with one forward network pass.

Extending these techniques to F-OFDM could involve designing neural networks that account for the filtered sub-bands and the unique characteristics of F-OFDM signals. By training AI models on F-OFDM-specific data, these receivers could provide more accurate channel estimation and equalization, enhancing the performance of F-OFDM in NTNs.
Finally, the reference [96] proposes two machine learning-based physical-layer receivers for DFT-s-OFDM to provide reliable soft bit estimates under power amplifier (PA) nonlinear distortion and phase noise. The primary architecture, a "full DFT-s CNN receiver," features a novel design with trainable layers both before and after the IDFT operation. It employs 11 ResNet blocks (6 before, 5 after the IDFT) and 64 parallel IDFT transformations to avoid bottlenecks, totaling approximately 703,000 trainable parameters. Evaluations at 28 GHz show significant gains. For QPSK, the full receiver increases uplink coverage by over 22.4% compared to a conventional LMMSE receiver. For 256-QAM, it outperforms the aforementioned ML receiver (iDeepRx [95]) by more than 5 dB at a BER of 1%. The key conclusion is that having learned layers on both sides of the IDFT is crucial for mitigating coexisting channel and hardware impairments effectively.

5.1.4.1.3 Waveform Optimization

Waveform optimization and demodulation are critical for achieving high spectral efficiency and reliable communication in NTNs. AI techniques have been applied to various waveform optimization tasks, including OFDM receiver design, sub-THz receiver design, and PAPR optimization.

As shown in reference [92] auto-encoder based PHY design is typically limited to the baseband modulation/detection stage (between a model-based encoder and a decoder), or for handling non-linearities between transmit pulse-shaping and receive synchronisation/downsampling stages. For standard wireless systems, this technique has been mostly used for constellation and filter design in the presence of interference (non-orthogonal access or electronic warfare). Another very interesting application is given in reference [78], which proposes to use an auto-encoder based transmitter and receiver for OFDM signals over a multipath channel, by imposing the use of an IFFT and a cyclic prefix insertion at the emitter, and the cyclic prefix removal and an FFT at the receiver. It is seen that imposing certain expert-knowledge can help the auto-encoder's performance, for instance by explicitly providing pilots for equalization (or by equalizing explicitly), otherwise a performance loss of 1-2dB is observed (but from a spectral efficiency point of view, the loss is lesser, as there are no need for pilots). It is also seen that the proposed method is also robust with respect to the CFO and to nonlinearities.
Similarly, the reference [99] explores end-to-end learning for OFDM systems in time- and frequency-selective fading channels. It proposes two pilotless communication schemes: one using learned superimposed pilots (SIPs) with QAM, and another that learns an optimized, zero-mean constellation. The core of the receiver is a CNN with five ResNet blocks. This architecture operates on entire frames, enabling it to learn tempo-spectral correlations. The key conclusion is that both pilotless schemes achieve a 7% higher throughput compared to a pilot-based baseline by eliminating the overhead of demodulation reference signals, but the impact on the computational complexity remains to be evaluated.

High PAPR in multi-carrier OFDM-like signals can stress power amplifiers on satellites and terminals, and high ACLR with such waveforms also cause spectral efficiency loss during resource allocation. Machine learning approaches have been proposed to design low-PAPR waveforms or clipping filters which can also limit out-of-band emissions. For example, one can train an autoencoder network to output a transmit waveform with bounded PAPR while preserving information, effectively learning an optimized pulse shaping filter. The survey in [77] sees considerable interest in autoencoder and DNN-based techniques for PAPR reduction in OFDM-like waveforms.
A notable strategy is used in reference [98], where the authors propose a ML framework to design frequency-domain spectrum shaping (FDSS) filters for PAPR reduction in DFT-s-OFDM systems. The core of the method is an end-to-end optimization of a 10th-order polynomial that models the filter taps. The coefficients of this polynomial are the trainable parameters, learned by minimizing a novel loss function that balances symbol error rate (SER), PAPR, and spectral shape. The results show significant improvements over conventional root-raised-cosine (RRC) filters. For instance, a learned filter can achieve a 2.3 dB PAPR gain (at a cost of 3 dB in SNR), while a constrained "zero-ISI" design yields a 0.5 dB PAPR gain with no SNR degradation. This data-driven approach provides a valuable benchmark for designing power-efficient waveforms. Moreover, autoencoder-style networks can optimize the entire OFDM chain (modulation mapping, pilot insertion, demodulation) end-to-end for a given channel distribution.

Such waveform optimization strategy has also been considered for single-carrier transmissions [100]. The latter work presents an end-to-end learning framework to jointly design a SC waveform, including its transmit/receive filters and constellation, alongside a NN receiver. The system maximizes an achievable information rate while constraining ACLR and PAPR. The receiver uses a 1D ResNet with four blocks; for multipath channels, a dense NN first processes pilot symbols to extract channel state information. On a 3GPP multipath channel, the learned waveform achieves a 10 dB lower ACLR and a 2 dB lower PAPR than an OFDM baseline, while offering competitive or higher information rates.
These optimization techniques can be naturally extended to F-OFDM through AI models tasked to determine the filters used in F-OFDM, reducing PAPR and out-of-band emissions and improving energy efficiency. Combining such filter design techniques along with AI-boosted F-OFDM receiver algorithms (e.g. synchronization, channel estimation and

equalization) can lead to solutions which can achieve end-to-end link optimization at PHY layer.

5.2 CHANNEL PREDICTION

5.2.1 Motivation

As it has been detailed from the above state of the art, the typical NTN impairments hamper the estimation and the knowledge of the CSI. Traditional channel estimation techniques rely on the frequent transmission of pilot symbols to enable accurate equalization of data symbols at the receiver. However, this approach reduces spectral efficiency by allocating a significant portion of available resources to pilots rather than data transmission. To address this limitation, deep learning-based channel prediction offers a promising alternative by leveraging past channel estimates to predict future channel states. Indeed, this is in line with the 3GPP activities on the application of AI to the radio access network (RAN), with channel prediction being identified as one of the key use cases [101]. This is of particular interest in the context of NTN, where the propagation channel exhibits complex dynamics on the one hand, but also predictable patterns on the other. In the context of OFDM-based NTNs, accurate channel prediction allows the system to alternate between pilot-assisted and pilot-free transmission slots, effectively halving the overhead associated with pilot symbols. Thus, the network can maintain link quality while freeing additional resources for data transmission, thereby improving overall throughput. Furthermore, the one-sided nature of channel prediction models is beneficial to uplink-oriented NTN systems, as no additional complexity is required at the transmitter. Several works have been carried out in the field of channel prediction in NTNs, with most of them focusing on MIMO systems, *e.g.*, [102]-[105], thus neglecting spectral variations of the propagation channel in exchange for spatial insights, or on the prediction of the path loss only, *e.g.*, [106]-[108]. The prediction of the channel frequency response (CFR) matrix in NTN systems has been studied in [109][110], posing the basis for this analysis. Operating at the physical layer, this activity complements the link quality prediction module reported in D4.6, which focuses on large-scale path loss prediction to support service satellite switching at higher layers: for this reason, a different dataset is here considered based on the following system model.

5.2.2 System model

An uplink transmission with CP-OFDM on the service link is here considered, with a full gNB implemented on board of a LEO satellite. The scheduling algorithm is assumed to allocate non-overlapping portions of the available uplink band to different UEs; in particular, it is here considered the case of $N_{SC} = 48$ subcarriers (*i.e.*, $N_{PRB} = 4$ PRBs) allocated to a reference user for data transmission on the PUSCH. Differently from the traditional PUSCH structure, it is assumed that pilot symbols are transmitted every other slot in order to reduce the pilot overhead (***Figure 54***): to obtain an estimate of the channel frequency response and therefore equalize the received symbols, channel estimation is carried out on regular, pilot-full slots, while channel prediction is applied on pilot-less slots based on the most recent slot's channel estimates. Intuitively, the channel estimates obtained through channel estimation are expected to be more accurate than those obtained through channel prediction, *e.g.*, due to the coherence time of the propagation channel. Nonetheless, it should be noted that some effects, *e.g.*, the phase drift due to the presence of residual Doppler, may be partially compensated through channel prediction. Given the considered frame structure, with a total of $N_{pilot}^{(slot)} = N_{SC} = 48$ pilot symbols being transmitted every two slots, the theoretical maximum throughput gain amounts to $\left(2N_{sym}^{(slot)} - 1\right) / \left[2\left(N_{sym}^{(slot)} - 1\right)\right] - 1 \approx 3.85\%$. It should be noted that further gains

may be achieved by further reducing the pilots transmission frequency: considering a periodicity of N_{slot}^{period} slots (*i.e.*, alternating one regular slot with $N_{slot}^{period} - 1$ pilot-less slots) the theoretical throughput gain can be generalized to $\left(N_{slot}^{period} N_{sym}^{(slot)} - 1\right) / \left[N_{slot}^{period} \left(N_{sym}^{(slot)} - 1\right)\right] - 1$, which asymptotically (*i.e.*, for $N_{slot}^{period} \to +\infty$) tends to $1/\left(N_{sym}^{(slot)} - 1\right) \approx 7.69\%$.

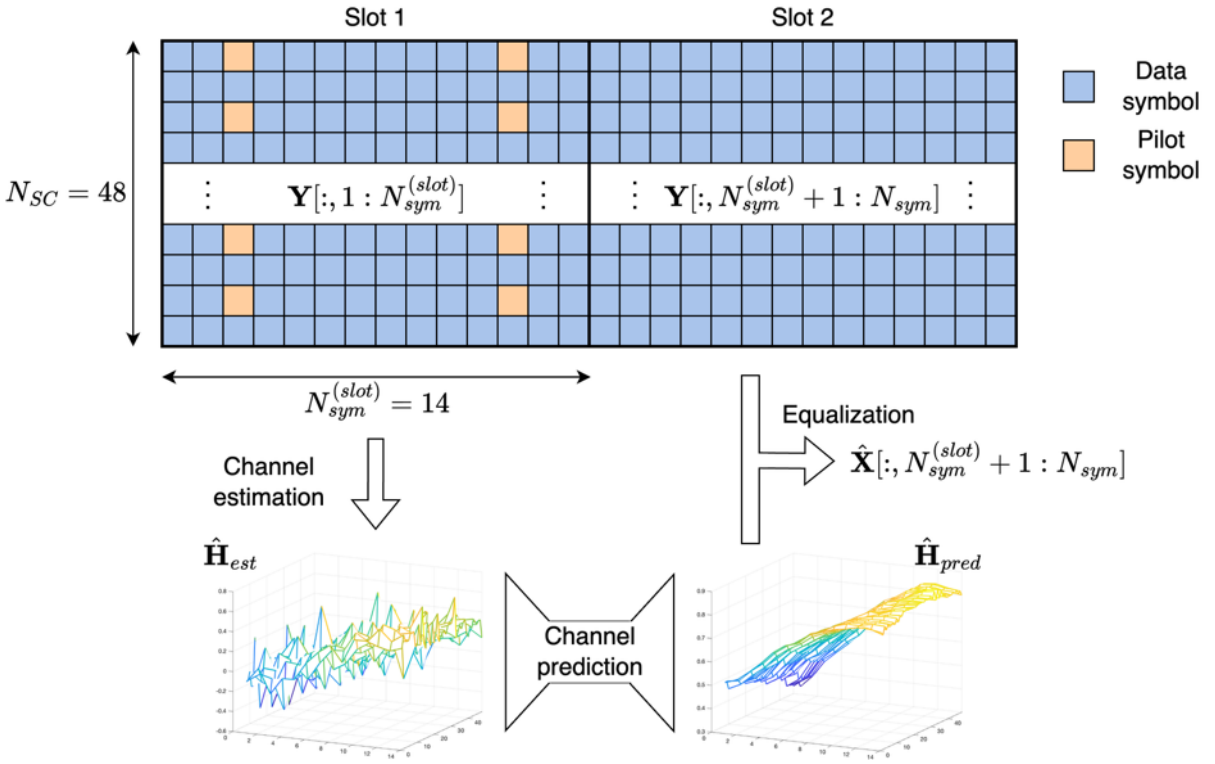

Figure 54: *Channel prediction framework.*

5.2.3 Deep learning models

Taking inspiration from computer vision, several deep learning architectures can be employed for channel prediction. Indeed, the CFR can be regarded as an image with two channels (real and imaginary part), where the height and the width of the image correspond to the frequency and temporal span of the considered resource grid, respectively. Thus, the input to the channel prediction models is a tensor of shape $\left[N_{sc}, N_{sym}^{(slot)}, 2, N_{batch}\right]$ obtained by stacking real and imaginary parts of the estimated CFR over each other. As an additional preprocessing step, the CFR is refined by using the demodulated symbols to estimate the channel at data symbols positions, thus introducing quantized errors in the received grid: this highlights potential inaccurate non-refined estimates as spikes in the CFR, thus improving the capabilities of the channel predictor. The fourth dimension of the input tensor, of size N_{batch}, allows multiple predictions to be carried out in parallel, *e.g.*, for transmissions on the same slot from different UEs. Given the considered system model, the output of all channel prediction models is a tensor of equal shape representing the stacked real and imaginary parts of the predicted CFR on the succeeding pilot-less slot.

5.2.3.1 Convolution-based Encoder-Decoder

The convolution-based encoder-decoder (CED) architecture aims at performing the channel prediction through the computation of a low-level compact representation of the input CFR (

Figure 55) [109]. In particular, a first encoding section is tasked with the extraction of the low-level features, employing 2-dimensional convolutional (Conv2D) layers with no padding and different stride values. Table 15 reports the complete list of the layer parameters. Given the input tensor's shape, at the output of the encoding section is a compact tensor of size $[8, 2, 14, N_{batch}]$ containing all the channel trends identified in the frequency and temporal domain in the input matrix. Based on the extracted features, the decoder builds the predicted CFR matrix, decompressing the compact low-level representation obtained by the channel encoder. For this task, Transposed Conv2D (TConv2D) layers are implemented: these layers apply rectangular filters to each element of the input tensor, effectively mirroring the compression carried out by Conv2D layers in the encoder. To minimize the checkerboard pattern that typically affects tensors reconstructed with TConv2D layers, the output tensor is smoothed with a Conv2D layer with "same" padding (*i.e.*, a Conv2D layer that preserves the tensor's size) using "replicate" pattern, i.e., the value of padding is equal to the value of the elements at the closest boundary of the tensor. Throughout the model, batch normalization (BN) layers are employed to maintain the data distribution under control and Leaky Rectified Linear Unit (LReLU) activation functions introduce non-linearities in the model.

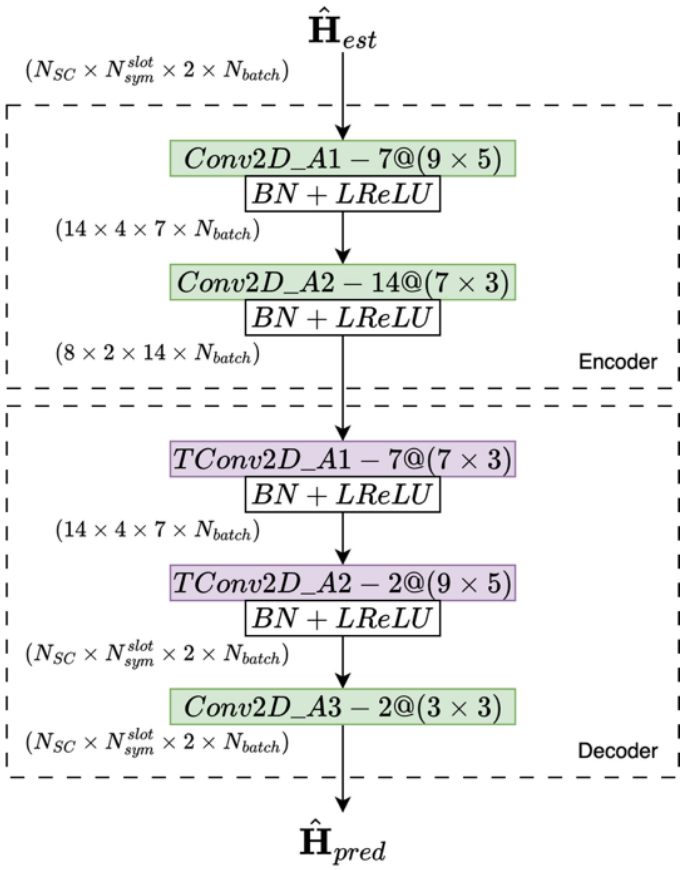

Figure 55: *Convolutional Encoder-Decoder architecture*

Table 15: *Layers parameters for CED architecture.*

Layer name	Kernels	Kernels size	Stride	Padding/Cropping
Conv2D_A1	7	[9, 5]	[3, 3]	0

Conv2D_A2	14	[7, 3]	[1, 1]	0
Conv2D_A3	2	[3, 3]	[1, 1]	"Same"
TConv2D_A1	7	[7, 3]	[3, 3]	0
TConv2D_A2	2	[9, 5]	[3, 3]	0

5.2.3.2 Hybrid CNN-LSTM

The Hybrid Convolutional Neural Network (CNN) –LSTM architecture takes inspiration from LinkNet [111], implementing skip connections in an encoding-decoding structure. Similarly to CED, it maintains Conv2D layers and TConv2D layers in an encoding and decoding section, respectively, while also introducing an LSTM layer dedicated to the prediction (***Figure 56***) [110]. The architecture Starting from the encoder, differently from the previous model, here a single Conv2D layer identifies complex patterns in time and frequency and adds them as features to the tensor. The frequency dimension is then flattened to the channel dimension, resulting in a tensor of size $[14,32,N_{batch}]$. The tensor is inverted on its temporal index, *i.e.*, the last sample of the tensor becomes the first, and vice versa: this is required in light of the LSTM-based prediction, as the sequential nature of such layer would make the channel estimates predicted over the first OFDM symbol depend on the first input sample, i.e., the most outdated one. On the opposite, the TimeFlip operation allows the LSTM to begin the prediction from the most recent sample to the most outdated one: effectively, the model learns and applies the inverse temporal trend of the CFR matrix. The LSTM layer can then carry out the prediction task, leveraging its recurrent nature to identify patterns in the extracted low-level features. In parallel, two skip connections with Conv2D layers, represented by dashed arrows, operate on higher-level features and directly on the input tensor, respectively, extracting information in support of the LSTM-based predictions. Similarly to CED, TConv2D layers are employed to restore the size of the output tensor, while a Conv2D layer with [3, 3] kernels acts as a smoothing filter for an improved CFR prediction accuracy. The skip connections are integrated in the decoder by means of addition layers, with LReLU-activated features coming from Conv2D layers in skip connections and TConv2D layers in the decoder section are summed together and then normalized with a BN layer. All layers' parameters are reported in ***Table 16***.

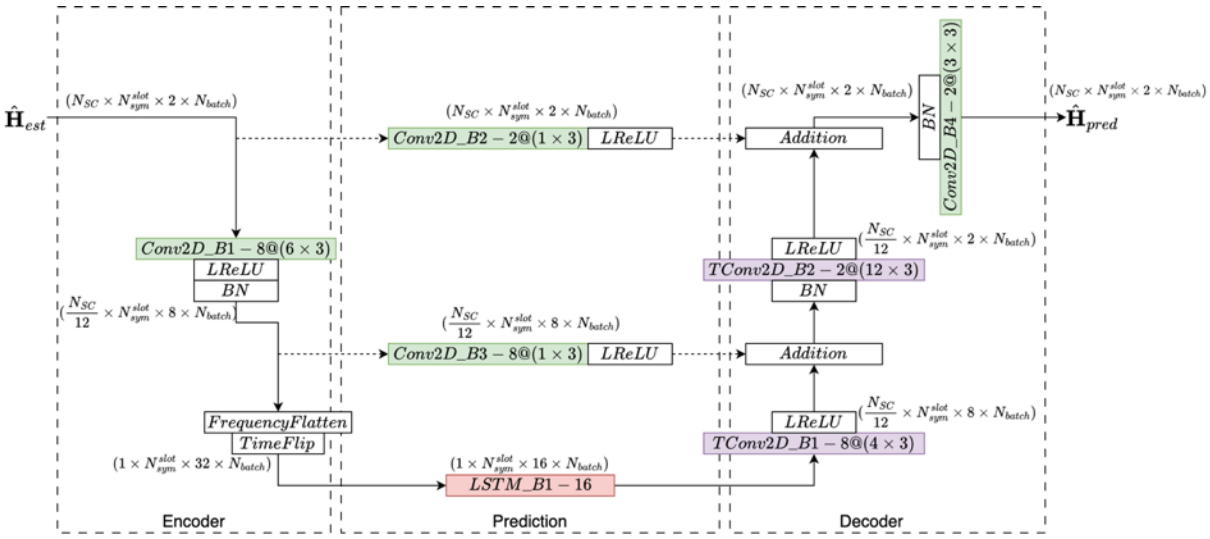

Figure 56: *Hybrid CNN-LSTM architecture*

Table 16: *Layers parameters in Hybrid CNN-LSTM architecture*

Layer name	Kernels/Cells	Kernels size	Stride	Padding/Cropping
Conv2D_B1	8	[6, 3]	[12, 1]	[0, 0, 1, 1]
Conv2D_B2	2	[1, 3]	[1, 1]	“Same”
Conv2D_B3	8	[1, 3]	[1, 1]	“Same”
Conv2D_B4	2	[3, 3]	[1, 1]	“Same”
LSTM_B1	16	N/A	N/A	N/A
TConv2D_B1	8	[4, 3]	[1, 1]	[0, 0, 1, 1]
TConv2D_B2	2	[12, 3]	[12, 1]	[0, 0, 1, 1]

5.2.3.3 Temporal Convolutional Network

Temporal convolutional networks (TCNs) have been proposed in [112] as a feed-forward alternative to recurrent neural networks, which have historically been the best choice for time series modeling tasks. In TCNs, a series of residual blocks with 1-dimensional convolutional (Conv1D, implemented by means of Conv2D layers with 1-dimensional kernels) layers is used to process an input time series. To increase the receptive field of the output samples, Conv1D layers in different residual blocks employ different a dilation factor, with the n-th block typically having dilation factor $d_n = 2^{(n-1)}, n \geq 1$. Furthermore, to let the model operate on continuous streams of data, TCNs typically employ causal convolutions, *i.e.*, padding is added before the first temporal element only instead of being distributed at the beginning and at the end of the sequence; however, given that CFRs are estimated slot-wise, we here consider regular convolutions. As in the previous two models, encoding and decoding sections are necessary

to maintain the computational complexity low. Thus, the overall structure of the model is similar to that of U-Net [113] (***Figure 57***). Differently from the previous two models, 2-dimensional Average Pooling (AvgPool) and 2-dimensional Average Unpooling (AvgUnpool) layers are employed at the encoder for compression and at the decoder for expansion, respectively. On the one hand, AvgPool layers act as averaging filters over the frequency-time dimensions, effectively reducing their input tensor size; on the other hand, AvgUnpool layers with size $[S_f, S_t]$ are implemented as a simple repetition of each frequency-time element by S_f times on the frequency dimension and S_t on the temporal dimension. Thus, Conv1D layers are the only trainable layers implemented, employing "same" padding to not affect the tensor size. As previously mentioned, the prediction is here taken care of by a TCN, which comprises of two Conv2D-based residual blocks. As for the Hybrid CNN-LSTM model, skip connections are also supporting the prediction based on features at different depths, with depth concatenation (DepthConcat), i.e., channel-wise concatenation, being used instead of addition layers. The parameters for the layers employed in the TCN architecture are reported in ***Table 17***.

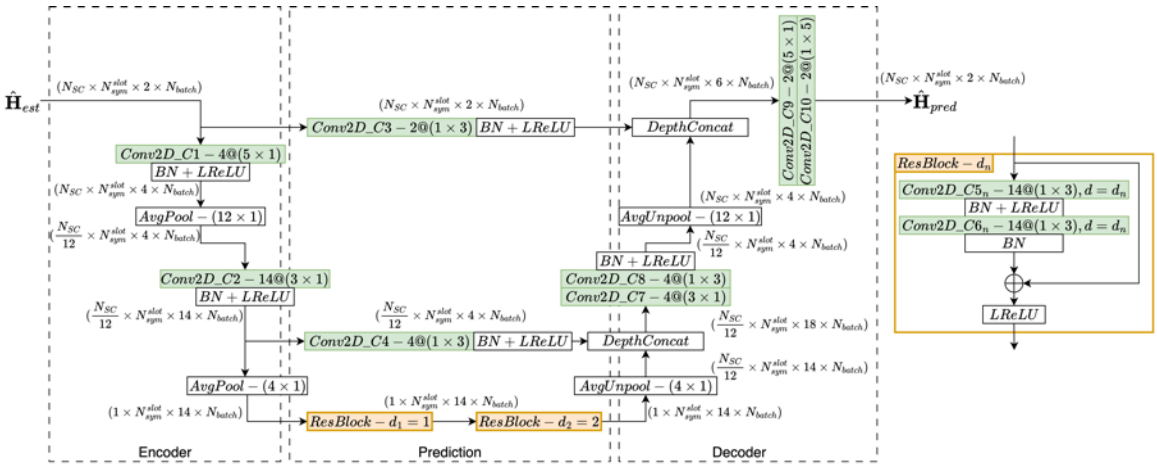

Figure 57: *TCN architecture*

Table 17: *Layers parameters in TCN architecture*

Layer name	Kernels/Cells	Kernels size	Stride	Dilation	Padding/Cropping
Conv2D_C1	4	[5, 1]	[1, 1]	1	"Same"
Conv2D_C2	14	[3, 1]	[1, 1]	1	"Same"
Conv2D_C3	2	[1, 3]	[1, 1]	1	"Same"
Conv2D_C4	4	[1, 3]	[1, 1]	1	"Same"
Conv2D_C5₁	14	[1, 3]	[1, 1]	1	"Same"
Conv2D_C6₁	14	[1, 3]	[1, 1]	1	"Same"
Conv2D_C5₂	14	[1, 3]	[1, 1]	2	"Same"
Conv2D_C6₂	14	[1, 3]	[1, 1]	2	"Same"

Conv2D_C7	4	[3, 1]	[1, 1]	1	"Same"
Conv2D_C8	4	[1, 3]	[1, 1]	1	"Same"
Conv2D_C9	2	[5, 1]	[1, 1]	1	"Same"
Conv2D_C10	2	[1, 5]	[1, 1]	1	"Same"

5.2.4 Models training

Each model is trained using an on-demand dataset, *i.e.*, the training process involves the generation of a new batch of synthetic data of N_{batch} samples during each epoch according to the system model described in Section 5.1.2; the generated data is then used to train the model for the current epoch (e.g., as in the popular library Sionna [114]). With this strategy, the risk of overfitting on a dataset is avoided, thus making validation unnecessary. On the opposite, the models may overfit to the inherent training data *characteristics*, *e.g.*, the channel model considered, including the LoS condition and the Doppler spread: for this reason, each model is separately trained on different propagation conditions and then tested on not only matching, but also mismatching channel models, thus assessing the generalization capabilities of the trained channel predictor. This also serves as an indicator of how well may the predictor be able to perform under realistic propagation conditions in a real world deployment; while 3GPP channel models are here used, ray tracing propagation models could also be considered to capture further real-world effects. The training loss function is the MSE, while the selected optimizer is the popular Adam algorithm [115]. Samples within a batch are generated at different E_b/N_0, whereE_b is the average energy per bit and N_0 is the noise power spectral density of the receiver: to lower the error floor typical of DL models in wireless communications, which arise due to the function approximation behavior of such algorithms, the E_b/N_0 value for the n-th generated data point γ_n is sampled from the range $\Gamma = [0, 1, \dots, 10]$ in dB with probability mass function $P_{\gamma_n}(i) = Prob\{\gamma_n = \Gamma(i)\} = i^2/\sum_{k=1}^{|\Gamma|} k^2$, *i.e.*, data at high E_b/N_0 is generated more often than under high noise conditions. Each model is trained using the following techniques:

- **L2 regularization**. This technique ensures that trainable weights do not diverge too much from 0, thus reducing overfitting. This is achieved by introducing a loss function penalization factor equal to the sum of the squared weights scaled down by a constant ϵ_R. Although overfitting is not an issue *per se* due to the continuous generation of data, if was observed that the models would still benefit from a low ϵ_R value rather than without implementing L2 regularization at all.
- **Learning rate warm-up**. Typical learning rate schedules foresee starting training with a large learning rate to quickly move from the initialization state towards a local minimum of the loss function. However, it has been observed that sometimes the training process benefits from starting with a very low learning rate λ_{min} and linearly ramping up to a large learning rate λ_{max} in a few training epochs T_w. This technique, called "learning rate warm-up", often helps in starting the gradient descent in a better direction: the general intuition behind this is that the direction for gradient descent may not be optimal at the beginning of the training process due to random weight initialization, thus leading to a great descent in a suboptimal direction when a large learning rate is implemented. On the opposite, a low starting learning rate can help in gaining momentum towards a more optimal direction over multiple training steps or epochs.

- **Learning rate cosine annealing with warm restarts**. This schedule lets the learning rate oscillate from a maximum value λ_{max} to a minimum value λ_{min} over the span of T_c epochs following a cosine trend as, *i.e.*, the learning rate at the *i*-th training epoch has value $\lambda(i) = \lambda_{min} + \frac{1}{2}(\lambda_{max} - \lambda_{min})\left(1 + cos\left(\frac{mod(i,T_c)}{T_c}\pi\right)\right)$. Conversely from cold restarts, the trainable weights are not reinitialized to small random values, possibly leading to other nearby local minima being reached during the following cycle of T_c epochs.
- **Early stopping**. Typically, training is interrupted after T_s epochs without a loss function improvement, with the model providing the best loss function value being restored. Given the cosine annealing schedule, which tends to provide loss function improvements at the end of a cycle (*i.e.*, when low learning rates are being used), we set T_s in terms of number of completed full cosine annealing cycles since the lowest loss function value was achieved.

Clearly, the benefits of these techniques are strongly dependent on the choice of the corresponding parameters. ***Table 18*** reports the list of the training parameters used in common to all models. The minimum and maximum learning rates, which are separately reported in ***Table 19***, were found to be impacted by the choice of the model architecture and the channel model; thus, they have been optimized separately based on the learning rate range test. In this test, a model is trained for a few epochs, starting from a very small learning rate and increasing the value each epoch up to a very large learning rate. Then, the loss function achieved at every epoch can be plotted as a function of the corresponding learning rate, resulting in a graph similar to that in ***Figure 58***. Optimal lower bounds for the learning rate are often where the learning rate starts decreasing, while upper learning rate bounds should be chosen before the loss function plateaus, maintaining a safety margin to avoid diverging too much during warm restarts.

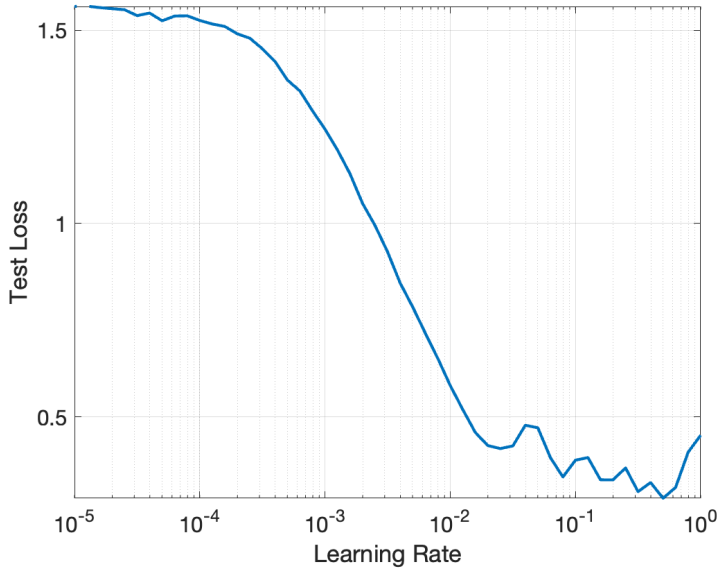

Figure 58: *Example of Learning rate range test plot (candidate learning rate lower and upper bounds would be 10^{-4} and $8 \cdot 10^{-3}$, respectively)*

Table 18: *Common training parameters*

Parameter	Value
Training batch size	$N_{batch} = 2048$

Maximum number of training epochs	8000
L2 regularization factor	$\epsilon_R = 10^{-6}$
Learning rate warm-up period	$T_w = 40$ epochs
Learning rate cosine annealing period	$T_c = 100$ epochs
Early stopping patience	$T_s = 3$ full cosine annealing cycles

Table 19: *Learning rate bounds*

Architecture	Training fading model	λ_{min}	λ_{max}
CED	NTN-TDL-D	10^{-4}	$8 \cdot 10^{-3}$
	NTN-TDL-A	10^{-4}	$5 \cdot 10^{-3}$
Hybrid CNN-LSTM	NTN-TDL-D	10^{-4}	$8 \cdot 10^{-3}$
	NTN-TDL-A	10^{-4}	$5 \cdot 10^{-3}$
TCN	NTN-TDL-D	10^{-4}	$5 \cdot 10^{-3}$
	NTN-TDL-A	10^{-4}	$3 \cdot 10^{-3}$

5.2.5 Evaluation results

All models were trained and evaluated in MATLAB considering the simulation parameters reported in ***Table 20***. The evaluation is carried out in two phases:

- Computational complexity analysis: the computational complexity of each model is evaluated in terms of Multiply-and-Accumulate units (MACs), reflecting the overall number of operations carried out in the prediction models, and in terms of trainable parameters, impacting the memory occupancy at the gNB. Based on the number of MACs, an estimate for the prediction latency is also inferred.
- MSE analysis: the MSE achieved by each model is evaluated for each E_b/N_0 test value. Based on this analysis, the best performing model is selected for further assessments.
- Throughput analysis: the throughput achieved by the selected model is evaluated under various propagation conditions, focusing on the generalization capabilities of the model to different fading characteristics and UE speeds from those used for training.

Table 20: *Simulation Parameters for channel prediction*

Parameters				Training	Test
TX	SCS			15 kHz	
	# PRBs			4	
	Data modulation			QPSK	
	Code rate			679/1024	
	Rv			0	
	# OFDM symbols			14	
	# DMRS symbols			2	
Channel	AWGN		SNR values	[0, 1, …, 9, 10] dB	[-1, 0.5, …, 7.5, 8] dB
	Fading channel	NTN TDL D/A	Delay spread	50ns	
			UE speed	5 km/h	[5, 30] km/h
			K factor	First tap K=11.707dB (NTN-TDL-D)	
	Impairments		Normalized Doppler on the SCS	Distributed as $\mathcal{N}(0, 7.8 \cdot 10^{-3})$[10]	
RX	Synchr.		Algorithm	Not considered	
	Channel Estimation		Algorithm	LS	
	Equalization		Algorithm	MMSE	

5.2.5.1 Computational complexity

The computational complexity of a single prediction (*i.e.*, no batching) is computed based on the architectures and parameters reported in Section 5.2.3, considering only trainable layers

[10] A standard deviation of $7.8 \cdot 10^{-3}$ ensures that the residual Doppler remains within 0.1 p.p.m. of a carrier frequency of 3.5 GHz 99.7% of the times (3σ rule) under the considered subcarrier spacing.

as the main contributors to the computational complexity. The number of MACs per layer can be assessed as follows [116]:

- Conv2D layers: assuming that the *i*-th Conv2D layer has $C^{(i)}$ kernels of size $[W_f^{(i)}, W_t^{(i)}]$ and is applied to a tensor of shape $\left[L_f^{(i)}, L_t^{(i)}, N^{(i)}\right]$ (neglecting the batch dimension), the corresponding number of MACs can be estimated as $MAC_{Conv2D} = L_f^{(i+1)} L_t^{(i+1)} N^{(i)} W_f^{(i)} W_t^{(i)} C^{(i)}$;
- TConv2D layers: assuming that the *i*-th TConv2D layer has $C^{(i)}$ kernels of size $[W_f^{(i)}, W_t^{(i)}]$ and is applied to a tensor of shape $\left[L_f^{(i)}, L_t^{(i)}, N^{(i)}\right]$ (neglecting the batch dimension), the corresponding number of MACs can be estimated as $MAC_{TConv2D} = L_f^{(i)} L_t^{(i)} N^{(i)} W_f^{(i)} W_t^{(i)} C^{(i)}$;
- LSTM layers: assuming that the *i*-th LSTM layer has $U^{(i)}$ hidden units and as many cells as the input/output sequences length $L_t^{(i)}$, the corresponding number of MACs can be estimated as $MAC_{LSTM} = L_t^{(i)} U^{(i)} \left(4N^{(i)} + 4U^{(i)} + 3\right)$.

Table 21 reports the number of MACs required to perform a single inference, the number of trainable parameters, and an estimate for the prediction latency for the three prediction models under evaluation. To perform a fair evaluation, the models were developed with the same target computational complexity, set to 160k MACs. Indeed, all models reported require an extremely low number of operations, which is necessary to meet the inference latency requirements of real-time wireless communications systems under the strict power requirements of LEO satellite payloads. Considering a negligible latency contribution for channel estimation, channel prediction should be carried out within the temporal duration of an OFDM slot, set here to $T_{slot} = 1\ ms$ according to the 5G numerology set for this assessment. In [117], the authors implemented a convolution-based DL model on a nano Unmanned Aerial Vehicle (UAV) for inference, showing that dedicated hardware accelerators can achieve high inference throughput even with strict power and size requirements: indeed, the hardware accelerator chosen by the authors consumes only 100mW of power and achieves an inference throughput of 139 inferences/s (equivalent to an inference latency of 7.19 ms/inference) with a model comprising 15 sequential Conv2D and pooling layers for a total of 1.1M MACs. Scaling down the inference latency with respect to the number of MACs required by each of the models considered here, a rough estimate for the channel prediction inference latency is obtained. Based on the reported figures, all models may be suitable for real-time and low-power inference. It should be noticed that no complexity reduction technique was implemented , *e.g.*, model pruning and weight quantization, which can further reduce a model's computational complexity and inference latency with minimal impact on its performance [118]. However, the number of MACs is not the only element affecting a model's inference latency. Deep models involve numerous sequential operations, which may increase the time taken by the hardware accelerator to process an input tensor through all layers. Considering only the main layers (Conv2D, TConv2D, LSTM, addition, and pooling), recalling that the LSTM layer in the Hybrid CNN-LSTM architecture can be unrolled to $N_{sym}^{(slot)} = 14$ sequential layers, the CED, Hybrid CNN-LSTM, and TCN architectures foresee 5, 20, and 14 sequential layers, respectively. In comparison, the model employed in [117] is based on 15 sequential layers. Thus, the real-world inference latency achieved by each model should be separately evaluated by means of a hardware implementation, which is out of the scope of this assessment. Nonetheless, the rough estimation provided here is a promising result in the direction of real-time inference in the context of channel prediction.

Table 21: *Number of MACs, trainable parameters, and inferred latency for each prediction model*

Architecture	MACs	Trainable parameters	Inferred latency
CED	160k	5.5k	1.05 ms
Hybrid CNN-LSTM	157k	5.8k	1.03 ms
TCN	155k	3.3k	1.01 ms

5.2.5.2 Mean squared error

Each model presented in Section 5.2.3 is evaluated by computing the MSE achieved on a test dataset of $4.1 \cdot 10^5$ samples per tested E_b/N_0 value. In this phase, the assessment focuses on the prediction accuracy considering the same propagation conditions as in the training dataset. ***Figure 59*** shows the MSE as a function of the E_b/N_0 for each trained model under the NTN-TDL-D (on the left) and the NTN-TDL-A (on the right) fading models considering a UE speed of 5 km/h. The TCN exhibits the best prediction accuracy out of the three considered models under NTN-TDL-D, crossing the 10^{-2} MSE threshold at 6 dB of E_b/N_0 (more than 2dB lower than the Hybrid CNN-LSTM model, while the CED architecture remains at a higher MSE level). On the non-LoS fading model NTN-TDL-A, the TCN is once again the best performing model at low E_b/N_0, while high E_b/N_0 ranges see all models perform approximately the same at under $3 \cdot 10^{-2}$ of MSE. It is also worth mentioning that the CED outperforms the Hybrid CNN-LSTM under NTN-TDL-A fading by 1 dB of E_b/N_0. Based on this, the TCN architecture is selected for the following evaluation phase.

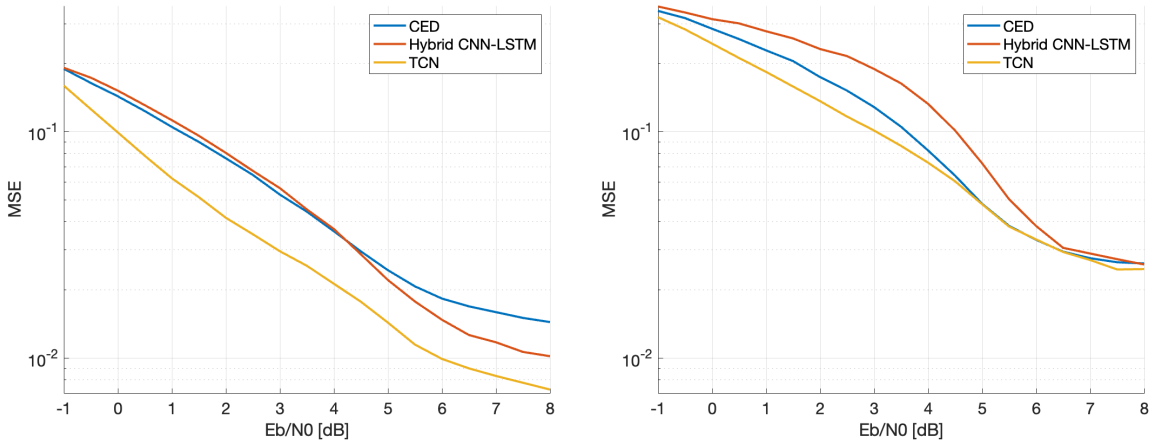

Figure 59: *MSE on NTN-TDL-D (left) and NTN-TDL-A (right) fading models as a function of the* E_b/N_0.

5.2.5.3 Throughput

5.2.5.3.1 Matching training/test propagation conditions

Figure 60 reports the average throughput achieved by the TCN model on an NTN link under propagation conditions matching to those considered during training. As a comparison, the

dashed curves report the throughput achieved without channel prediction, *i.e.*, considering channel estimation and regular slots only; the plots also report the theoretical gain achievable with prediction. On the NTN-TDL-D fading model, the prediction curve closely follows the estimation until 1 dB of E_b/N_0, where the latter starts approaching the saturation level. On the opposite, the increased available resources for data transmission result in an increased throughput with respect to the regular system, with the continuous curve approaching the theoretical maximum throughput with channel prediction (0.97 Mbps, corresponding to a 3.8% improvement over the regular system) at $E_b/N_0 = 5$ dB. Nonetheless, under these conditions channel prediction provides substantial gains at all E_b/N_0 working points over 1 dB, with the 0.80 Mbps threshold being passed with a 1.5 dB gain with respect to the estimation-based system. The less accurate predictions on the NTN-TDL-A fading model highlighted in the MSE assessment are reflected on the right-hand side of ***Figure 60***, showing a loss of under 0.5 dB at low E_b/N_0 under channel prediction with respect to the estimation-aided system; nonetheless, the gains of channel prediction appear evident from $E_b/N_0 = 3$ dB, despite their entity being smaller than the theoretical maximum.

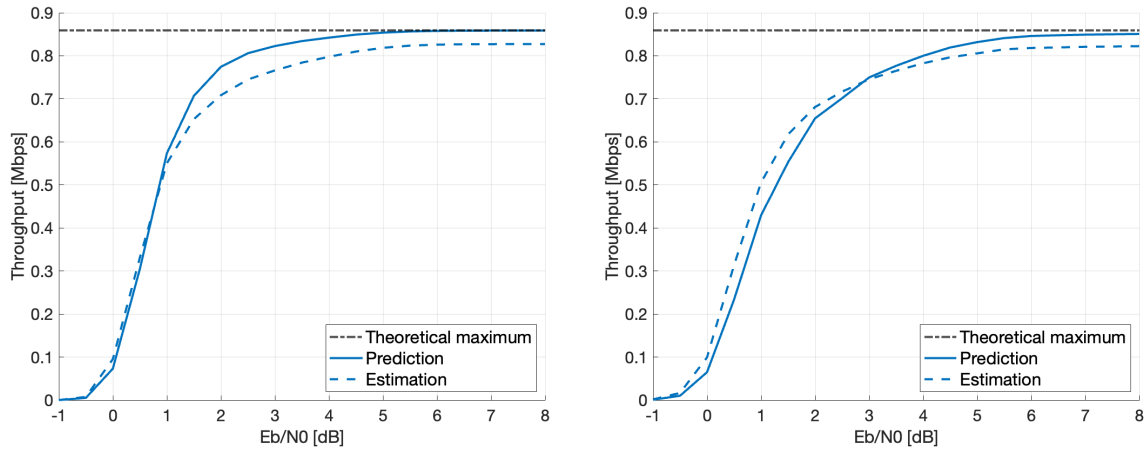

Figure 60: *Throughput achieved under matching training/test propagation conditions (test on NTN-TDL-D (left) and NTN-TDL-A (right), UE speed 5 km/h)*

5.2.5.3.2 Mismatching training/test UE speed

In this assessment, the pre-trained TCN models are tested under the same fading model as the one used for training, but at higher UE speed. Clearly, a larger UE speed results in a shorter channel coherence time and, consequently, a larger Doppler spread: therefore, the objective of this evaluation is to verify the generalization capabilities of the pre-trained models to perform predictions under more complex channel dynamics. The blue curves on the left-hand side of ***Figure 61*** show that, similarly to the case of matching training/test conditions (orange curves), the throughput in NTN-TDL-D fading under channel prediction follows a similar trend to that under channel estimation only. After 1 dB of E_b/N_0 the continuous curve surpasses the dashed curve, highlighting a throughput improvement: in particular, the prediction-based system reaches the 0.80 Mbps throughput mark at 4 dB of E_b/N_0, a 1.5 dB gain with respect to the estimation-based system. However, in non-LoS conditions (NTN-TDL-A) the channel dynamics are too complex for the prediction model to provide meaningful gains over the regular system; additionally, the poor estimation performance implies that low-accuracy estimates are fed to the prediction model, further impacting the accuracy of the predicted CFRs and, thus, the throughput gain.

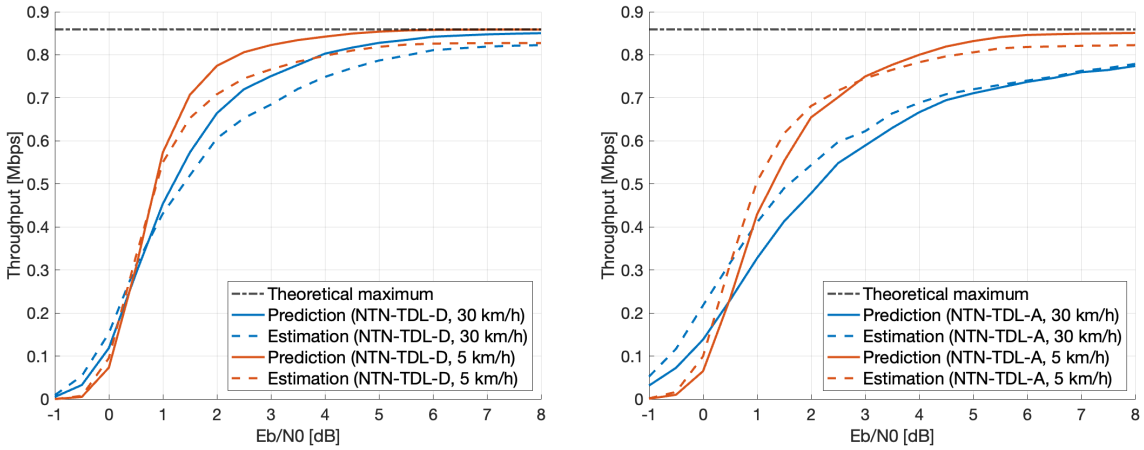

Figure 61: *throughput achieved under mismatching training/test ue speed (test on ntn-tdl-d (left) and ntn-tdl-a (right), ue speed 5 km/h and 30 km/h)*

5.2.5.3.3 Mismatching training/test fading model

Figure 62 reports the throughput achieved by the pre-trained TCNs considering a mismatch between training and test fading models. On the left-hand side, the plot shows the performance of the TCN trained on NTN-TDL-A and tested on NTN-TDL-D (blue curve): even with a fading model mismatch, the achieved throughput surpasses that with channel estimation at 2.5 dB of E_b/N_0, with the mismatch leading to a loss from the matched case (orange continuous curve) of 1 dB. On the opposite, when tested on NTN-TDL-A with fading model mismatch, the pre-trained TCN is not able to provide accurate channel estimates, leading to a severe throughput degradation. An interpretation for this behavior is that in presence of a strong LoS path in the training data (as in the case of the NTN-TDL-D fading model), the TCN is not able to accurately focus on the interactions between the low-power non-LoS multipath components, resulting in poor performance when the LoS path is absent.

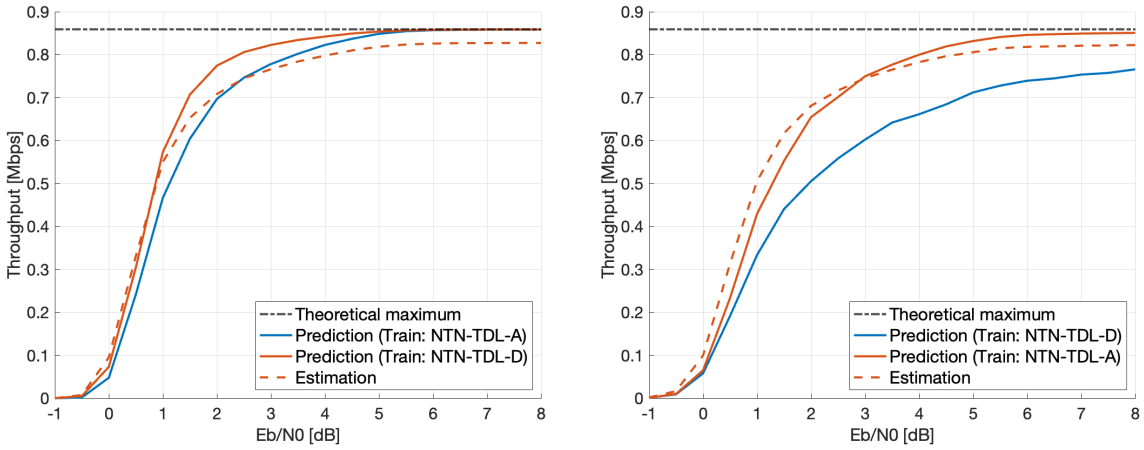

Figure 62: *Throughput achieved under mismatching training/test fading model (test on NTN-TDL-D (LEFT) and NTN-TDL-A (RIGHT), UE speed 5 KM/h)*

5.2.6 Conclusions and perspectives

This study focused on the application of AI as a means to improve the throughput in NTNs through uplink channel prediction. In the considered system model, additional resource elements are allocated to data transmission by avoiding the transmission of pilot symbols every other slot. Regular slots, *i.e.*, slots that carry pilots, can be equalized by means of channel estimation; the estimated CFR is then fed to the channel prediction model to obtain a CFR estimate to equalize the succeeding slot. Three architectures, namely the CED, Hybrid CNN-

LSTM, and TCN were trained and tested on a variety of propagation conditions, comparing the achieved MSE as a function of the E_b/N_0 and complexity aspects, including an initial assessment of the real time inference feasibility with low power accelerators. As a result of this comparison, the TCN architecture was selected to carry out additional assessments on the achieved throughput, including the generalization capabilities of the pre-trained TCNs under different propagation conditions (fading model, UE speed) from those used in the training phase. Simulation results revealed that a peak 3.8% throughput gain can be achieved under the NTN-TDL-D and NTN-TDL-A fading models with <0.5 dB losses with respect to traditional system models. Furthermore, consistent throughput gains can also be observed when testing the TCN on the NTN-TDL-D fading model with a user equipment speed of 30 km/h, regardless of the training fading model (NTN-TDL-D or NTN-TDL-A) and the lower training UE speed (5 km/h). On the opposite, the pre-trained TCN cannot provide throughput gains under NTN-TDL-A at higher UE speed; furthermore, the model is not able to generalize well to the non-LoS channel model when trained on LoS conditions. ***Table 22*** summarizes these findings by reporting the throughput gain achieved through channel prediction as a percentage of the throughput achieved by the benchmark estimation-based system. Notably, in some cases, a reduction in throughput gain can be observed with an increase in Eb/N0. When this occurs, the gain surpasses 3.85% (*i.e.*, the theoretical maximum achievable gain threshold) and the accuracy of predicted CFRs is, intuitively, better than that of estimated CFRs: this highlights not only the model's prediction capabilities at low Eb/N0, but also its ability in compensating for residual effects on the estimated channel matrix (*e.g.*, phase shifts due to the residual carrier frequency offset).

Table 22: *Throughput gain with channel prediction, expressed as a percentage of the estimation-based throughput*

Training fading model	**Test fading model**	**Test v_{UE}**	**Eb/N0 [dB]**		
			4 dB	6 dB	8 dB
NTN-TDL-D	NTN-TDL-D	5 km/h	5.57%	3.87%	3.81%
		30 km/h	7.22%	3.86%	3.37%
	NTN-TDL-A	5 km/h	-15.5%	-9.65%	-6.87%
NTN-TDL-A	NTN-TDL-A	5 km/h	2.21%	3.40%	3.45%
		30 km/h	-3.21%	-0.42%	-0.62%
	NTN-TDL-D	5 km/h	3.12%	3.77%	3.78%

While the considered system model assumes the transmission of a pilot-less slot every other slot, further throughput gains can be achieved by further reducing the pilots transmission periodicity, *i.e.*, inserting multiple pilot-less slots. To maintain high prediction accuracy, prediction models which outputs temporally span multiple slots should be avoided. Instead, updated channel information can be indirectly fed in the prediction process using iterative prediction techniques, where the CFR at each slot is obtained by means of prediction based on the refined CFR at the preceding slot; the refinement step employs the demodulated symbols as pilots, introducing updated information on the current slot's CFR, thus potentially reducing the propagation of CFR errors. Nonetheless, the phase coherency across

consecutive slots should be ensured, triggering the transmission of regular slots (*i.e.*, containing pilot symbols) to re-establish a highly accurate CFR through channel estimation whenever the prediction accuracy falls under a certain threshold (*e.g.*, using the bit error rate as a metric): thus, multi-slot prediction requires several dedicated assessments to ensure its feasibility under various conditions. Furthermore, more in general, hardware implementations of the channel predictors should be developed to assess the real-world inference latency and verify the real time feasibility of the considered models under strict power constraints. Finally, as the predictors are trained on synthetic data, real-world studies should assess the generalization capabilities of the models to real-world propagation effects that may not have arisen from the synthetic tests reported here.

5.3 OPTIMIZATION OF BACKOFF INDICATOR FOR RANDOM ACCESS IN 5G NON-TERRESTRIAL NETWORKS USING DEEP REINFORCEMENT LEARNING

5.3.1 Introduction

The random access (RA) procedure is a fundamental component of 5G NR systems, serving as the primary mechanism for UE to establish initial connections, synchronize with the network, and request uplink resources. Efficient execution of this procedure is essential to ensure reliable connectivity, particularly in dense or delay-sensitive environments. In conventional terrestrial networks, RA performance is primarily influenced by factors such as user density, preamble collisions, and network configuration parameters. Among these, the backoff indicator (BI) plays a critical role in regulating retransmission timing following failed access attempts, directly affecting network access delay and collision probability.

In NTN, the importance of efficient random access becomes even more pronounced. The unique characteristics of NTN, such as long propagation delays, large coverage footprints, and high mobility, impose additional constraints on access timing and contention resolution. Unlike terrestrial networks, where round-trip times are typically below one millisecond, NTN links may experience delays exceeding tens of milliseconds, making rapid and reliable access granting essential to maintain service continuity and reduce connection setup latency. Inefficient backoff control in such environments can result in excessive waiting times.

Recent research on RA optimization for LEO satellite networks and massive Internet of Things (IoT) scenarios has evolved from traditional model-based schemes to learning-driven approaches. Foundational surveys [119][120] distinguish between non-learning estimators and ML-based methods, emphasizing the latter's capacity to adapt to complex, time-varying traffic and long-term optimization. Several works [121][122] propose enhancements to backoff and preamble allocation strategies using reinforcement learning (RL). Protocol learning via Multi-Agent Deep Reinforcement Learning (MADRL) has been proposed, with emergent schemes like emergent Random Access Channel protocol (eRACH) [123] and Satellite-RACH (S-RACH) [124] demonstrating decentralized, model-free access coordination using locally observable information. Hybrid frameworks such as Q-learning-enhanced Diversity Slotted Compressive Random Access Control (QDCC) and Adaptive Frame Length QDCC (AFL-QDCC) [125] integrate compressive sensing (CS) with Q-learning to exploit sparsity, although their reliance on fixed frame structures and replica-based access can reduce performance under dense contention. In addition, deep Dyna-reinforcement learning approaches [126] have been proposed to combine model-based and model-free strategies, enabling predictive RA control while improving sample efficiency and reducing learning time in satellite IoT networks. Meanwhile, traffic prediction has been addressed using Long Short-Term Memory (LSTM) and Recurrent Neural Network (RNN)-based supervised learning, often decoupled from access control via frameworks like Decoupled Learning Strategy (DLS), which improve modularity but introduce latency in adaptation. Notably, the work by Kim et al. [122] on backoff indicator tuning via Deep Deterministic Policy Gradient (DDPG) exhibits instability, as the learned policy tends to inflate delay under high congestion. Similarly, Gupta et al. [121] propose predictive backoff and beam-aware planning, but their rule-based mechanisms lack the flexibility and adaptability of learned policies. The cooperative variant eRACH-Coop [123] improves coordination through inter-agent communication, although this introduces overhead and reduces fairness. Overall, while these studies lay a strong foundation, they often fall short in balancing throughput and delay. In contrast, this work focuses on the optimization of BI in 5G NR NTN environments using reinforcement learning techniques. The proposed framework aims to minimize access delay while maintaining low collision rates, ensuring that UEs are granted access rapidly in a

LEO satellite system. Through simulation and numerical analysis, the study evaluates the performance of adaptive BI optimization compared with conventional fixed-parameter configurations, demonstrating the potential of AI-driven control to enhance access efficiency in NTN networks.

5.3.2 Random access procedures steps

As detailed in TS 38.321, RA procedure enables UE to establish initial communication with the gNB through a four-message handshake sequence . The process begins with MSG1, where the UE transmits a randomly selected preamble on the Physical Random-Access Channel (PRACH) to request access. Upon successful detection, the gNB responds with MSG2, known as the Random-Access Response (RAR), which provides timing advance, uplink grant, and an optional BI to regulate retransmission behavior for unsuccessful UEs. The UE then sends MSG3, a scheduled transmission carrying its identity and connection request using the allocated resources. Finally, the gNB completes the procedure with MSG4, which resolves contention by confirming the successful UE identity and finalizing access. In specific configurations, such as for prioritized or delay-sensitive UEs, a two-step RA procedure may be used instead, consisting only of MSG1 and MSG2. This variant reduces latency by bypassing contention resolution and identity transmission and is typically applied to UEs with configured grant or special access profiles. The UEs with unsuccessful RA proceed for the preamble retransmission after waiting a random time that is selected in the range of the BI.

According to table 7.2-1 in TS 38.321, BI field is 4 bits wide and the BI index value 0-13 maps to explicit BI values in milliseconds as defined in Table 23.

Table 23: *BI values as given in Table 7.2-1 in TS 38.321*

BI index	BI value (ms)
0	5
1	10
2	20
3	30
4	40
5	60
6	80
7	120
8	160
9	240
10	320
11	480
12	960
13	1920

When a UE receives an RAR containing a BI subPDU, it applies the following rule (TS 38.321, clause 5.1.4):

Preamble_backoff = BI value from table 1× scaling factor

The scaling factor is configured by the RRC signaling to provide prioritization and defaults to one if not explicitly set. If no BI is included in the RAR, the UE sets the BI to zero.

5.3.3 Reinforcement Learning approach

As previously highlighted, *BI* plays a critical role in regulating retransmission timing following failed access attempts. Its configuration directly influences key network performance metrics such as access delay and collision probability. Also, the fact that static or heuristic BI configurations cannot adapt efficiently to time-varying traffic load, for instance, consistently selecting the smaller BI value may lead to surge in excessive collision, which in turn increases the overall access delay. Conversely, opting for larger BI value may reduce the likelihood of collisions but causes UEs to experience longer waiting times before reattempting RA.

Given the nature of the problem, it exhibits a sequential decision-making nature under uncertainty, where each decision (BI selection) influences future network states and outcomes. Therefore, this problem can be effectively modeled as Markov Decision Process (MDP), where the system evolves through discrete-time steps *t,* which in this case through random access opportunities (RAOs).

Within this MDP framework, the agent observes the current state s^t from state space $\mathbb{S}$ ($s^t \in \mathbb{S}$) and selects an action a^t from action space $\mathbb{A}$ ($a^t \in \mathbb{A}$). After executing action a_t, the agent receives a reward r^t and moves to the next new state$s^{t`}$. This process continues iteratively until terminal state is reached. The agent's behavior is governed by policy $\pi(a^t|s^t)$, which defines the mapping from a given state to a specific action. The main objective of the agent is to learn a policy that maximizes the cumulative (discounted) reward.

Given the discrete nature of action space and to learn the effective policy, DRL based Q learning framework is adopted. The overall framework is illustrated in Figure 63.

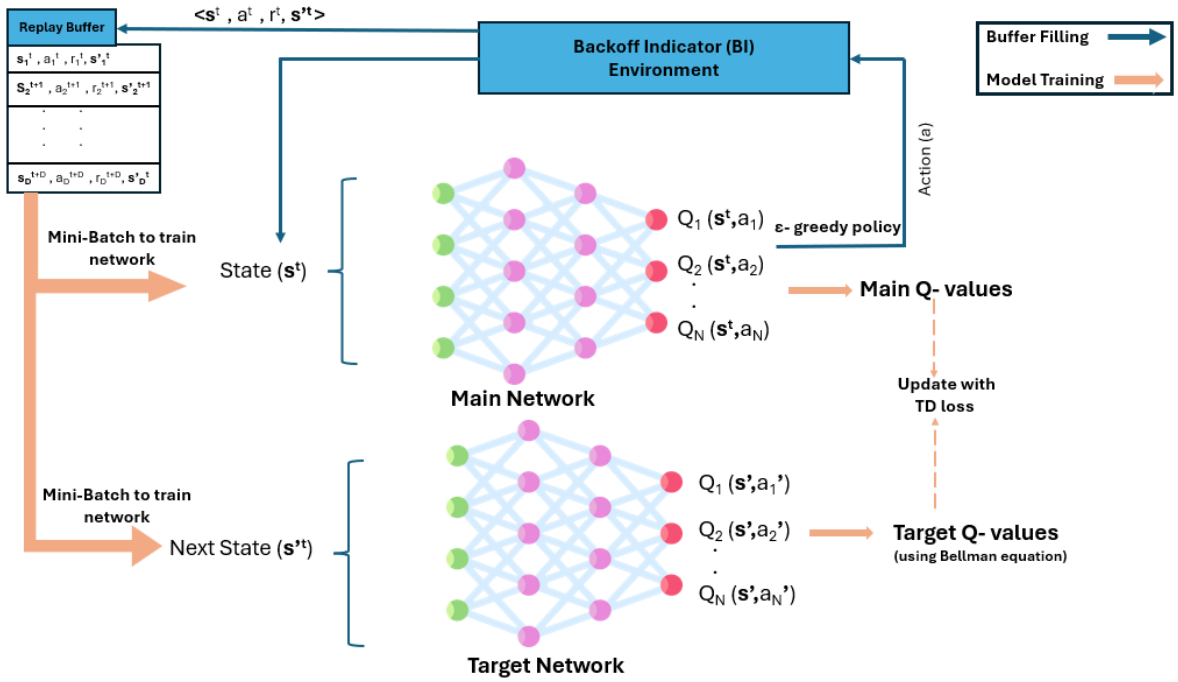

Figure 63: *DRL framework for adaptive BI selection*

The adopted DRL mechanism is as follows:

1. The framework employs two deep neural networks (DNNs) i.e. a main network and a target network, where the latter is an identical replica of the former. These networks map the local state vector to Q-values of all possible actions. The number of input

neurons equals the dimensionality of state space while the number of output neurons corresponds to size of action space $\mathbb{A}$.

2. In addition to DNNs, a replay buffer with a fixed memory capacity *D* is maintained to store the agent's experience at each time step *t* in the form of tuple $\langle s^t, a^t, r^t, s'^t \rangle$. The replay buffer enables randomized samples of past experiences, thereby improving training stability and reducing correlation among consecutive samples. To initialize the model training, it is required to have sufficient samples stored in the replay buffer.
3. Initially, a step size is defined, and a random action is executed to obtain the initial state at first step, which serves as the input to main network.
4. Subsequently, the agent adopts an ε-greedy policy for action selection, where, at each step, a random action is chosen (exploration) with probability ε or the action corresponding to maximum Q-value (exploitation) with probability $1-\varepsilon$. The chosen action is then applied to *BI Environment,* yielding a reward r^t and the next state s'^t . The resulting experience tuple $\langle s^t, a^t, r^t, s'^t \rangle$ is then stored in the replay buffer until a sufficient number of experiences are accumulated for training.
5. For model training, a random mini-batch of size *F* is sampled from replay buffer*,*

    a. The minibatch of current state vector s^t is fed into to the main network to obtain the predicted Q-values for all actions.

    b. The mini-batch of next state vector s'^t is fed to the target network to obtain the Q-values by choosing an optimal action value function i.e. $max_a Q(\boldsymbol{s'}, \boldsymbol{a'})$ and use this into Bellmen equation given below to finally estimate the target Q-values.

$$Q^*(s', a) = r + \gamma \, max \, Q_{target}(s', a') \quad , \gamma \in [0,1)$$

    Where r is the reward from minibatch and γ is the parameter to prioritize the future reward.

6. Finally, the temporal difference (TD) loss between the target and predicted Q-values is calculated and minimized through backpropagation, thereby updating the parameters of main network. This process interactively repeated until the specified number of episodes.
7. The target network parameters are periodically synchronized with those of the main network using soft updates to stabilize training.

5.3.4 Handling DRL model non-observable metrics in 3GPP-compliant deployments

The state variables used in the analytical formulation—such as the number of UEs whose Backoff Indicator (BI) expires in the current RAO ($R_{\text{users}}(t)$), the number of UEs still in backoff ($W_{\text{users}}(t)$), the number of new arrivals ($N_{\text{users}}(t)$), and the number of collided users ($C(t)$) provide an accurate description of the system dynamics; however, they are not all directly observable at the gNB in a 3GPP-compliant deployment. BI handling is a fully UE-local procedure. The NR specifications do not require nor allow UEs to report their remaining backoff, BI expiration time, or "ready" status to the network. As a result, the exact values of $R_{\text{users}}(t)$ and $W_{\text{users}}(t)$ cannot be known at the base station.

In practical implementations, one may replace these unobservable quantities with estimated values $\hat{R}(t)$ and $\widehat{W}(t)$ derived from gNB-observable signals. A suitable estimator can be constructed by maintaining a backlog distribution over remaining backoff intervals (quantized in RAO units). This approach is consistent with well-established RACH load inference methods based on maximum-likelihood estimation of idle/singleton/collision statistics [127], pseudo-Bayesian backlog tracking under bursty arrivals [128], and recent ML-based extensions that address massive-access regimes [129]. In this setting, knowing the total number of contending UEs and the probability distribution of their backoff intervals (normally uniform) allows us to estimate how many UEs have reached a backoff of zero and are ready to transmit, as well as how many remain in nonzero backoff. The evaluation is carried out by keeping a log of the number of users that experienced a collision at each RAO together with the backoff interval selected by the algorithm at that instant. At any later time, the probability that a collided user is ready to transmit is determined by whether its initially chosen backoff interval would have expired exactly at that time. Only those users whose backoff matches the elapsed time since their collision are considered ready; users with shorter backoffs would have already attempted transmission earlier, while those with longer backoffs are still waiting. By repeating this probability check across all groups of collided users and using the BI value that was in effect when they selected their counters, we obtain an estimate of the number of active users ready to transmit at the current RAO. These estimated variables preserve the structure of the original proposed model while ensuring compatibility with the standard.

A similar consideration applies to the estimation of new arrivals $N_{\text{users}}(t)$. Perfect prediction is generally infeasible, especially under sudden traffic bursts, but one may replace $N_{\text{users}}(t)$ with a practical estimate $\widehat{N}(t)$. The reinforcement-learning controller does not require exact future arrivals; rather, it benefits from a reasonable estimate whose stochastic variation is naturally handled during training. This aligns with existing RACH estimation frameworks where only aggregate backlog evolution is predicted, without requiring per-UE state information.

Finally, while the exact number of collided UEs $C(t)$ is partially hidden, the gNB can observe singleton and collided preambles through PRACH processing, and these observations provide a meaningful basis for estimating the number of collision-involved UEs. Although the resulting estimate $\hat{C}(t)$ carries some uncertainty, such uncertainty is typical in RACH load estimation and has been shown to be adequate for driving adaptive control mechanisms [3]–[5]. The reinforcement-learning model can therefore operate effectively with $\hat{C}(t)$ rather than its true value. Future extension of the proposed framework will consider developing optimized estimation modules that tightly integrate backlog tracking, BI-aware inference, and arrival prediction to improve the realism of learning-based random access control schemes.

5.3.5 Simulation results

To map this DRL framework defined above onto the adaptive BI problem, the model uses the five attributes as *states* for each time step *t* such as, $s^{\mathrm{t}} = \{R^t_{users}, W^t_{user}, N^t_{users}, A^t_{users}, C^{t-1}\} \in \mathbb{R}$, where R^t_{users} denotes the set of *ready users* whose BI becomes 0 at the current RAO and prepared to reattempt RA, W^t_{user} represents users that are still waiting with *BI>0* , N^t_{users} indicates the predicted number of new users expected to perform RA during current time slot *t*, A^t_{users} corresponds to the total number of active users in the current slot, including both R^t_{users} and W^t_{user} *and* C^{t-1} denotes the number of collided users in the previous time slot.

Given the state's representation described above, the state vector is defined as $\boldsymbol{s_t} \in \mathbb{R}^{1\times 5}$.

5.3.5.1 Action Space

The action space $\mathbb{A}$ consists of discrete BI values taken from Table 23. Specifically, the first eight BI values from 5 to 120 are selected, as larger values would lead to excessive delays in RAOs for users.

5.3.5.2 Reward Function

The reward function integrates three components:

1) Accumulative Collision (C_t): represents the number of users that experienced collisions during the current step t.
2) Mean Access Delay (D_t): Denotes the average time delay experienced by users, measured from their first RA attempt until successful access.
3) Penalty (P_t): Corresponds to the remaining waiting time for users already assigned a BI before they can reattempt RA after the current step. This penalty encourages the agent to balance between minimizing collisions and avoiding excessive delays, rather than favoring a single objective.

Two waiting factors, α and β, are introduced to control the trade-off between collision minimization and future access delay. The overall reward function is expressed as:

$$r = -\alpha C^t - D^t - \beta P^t$$

5.3.5.3 Model Training

After defining the state representation, action space, and reward function, the model is trained using the hyperparameters listed in Table 24.

Table 24: *Hyperparameters used for DRL-based adaptive BI model training*

Parameters	Values
Number of Hidden Layers	2
No. of neurons	64
Replay Memory Size	5000
Batch Size	64
Target Network Update	Soft Update (0.01)
Learning Rate	1e-4
Epsilon Decay	0.9817
Step Size	50
γ	0.99
Episodes	150
No. Of Preambles	48
Monto Carlo Trials	500

The training process is organized into steps and episodes. During the model training, the agent iteratively interacts with the established BI *Environment*, exploring actions at each time step, returning the reward and observing next state. Over the episodes, this process enables the agent to converge towards strategies that maximize long-term objective, as can be seen in TD loss in Figure 64 and Episode reward in Figure 65. As shown in Figure 64, the TD loss represents the difference between the main Q-network and the target Q-network. The loss begins to stabilize after approximately 2000 steps, indicating that the Q-network has started to align with the target network's expectations. However, as seen in Figure 65, the agent continues exploring and refining its policy during this stage.

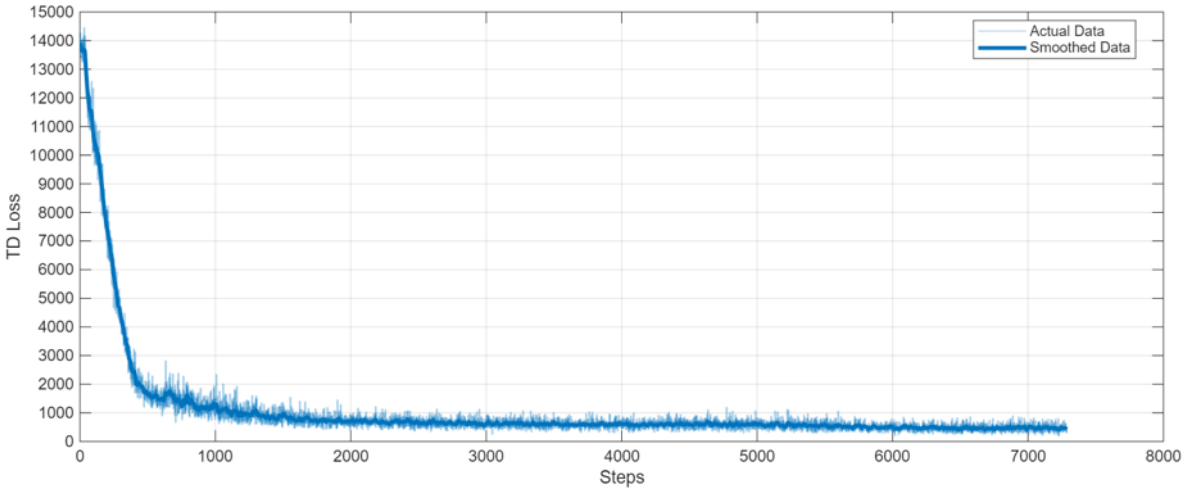

Figure 64: *TD loss during DRL training*

The episode reward is defined as the average of the step rewards across all steps within an episode. Initially, the episode reward is approximately –200, reflecting the agent's early exploration phase. As training progresses and the epsilon value decays, the reward gradually improves. After around 100 episodes, the reward stabilizes as the agent increasingly exploits the learned policy through greedy action selection.

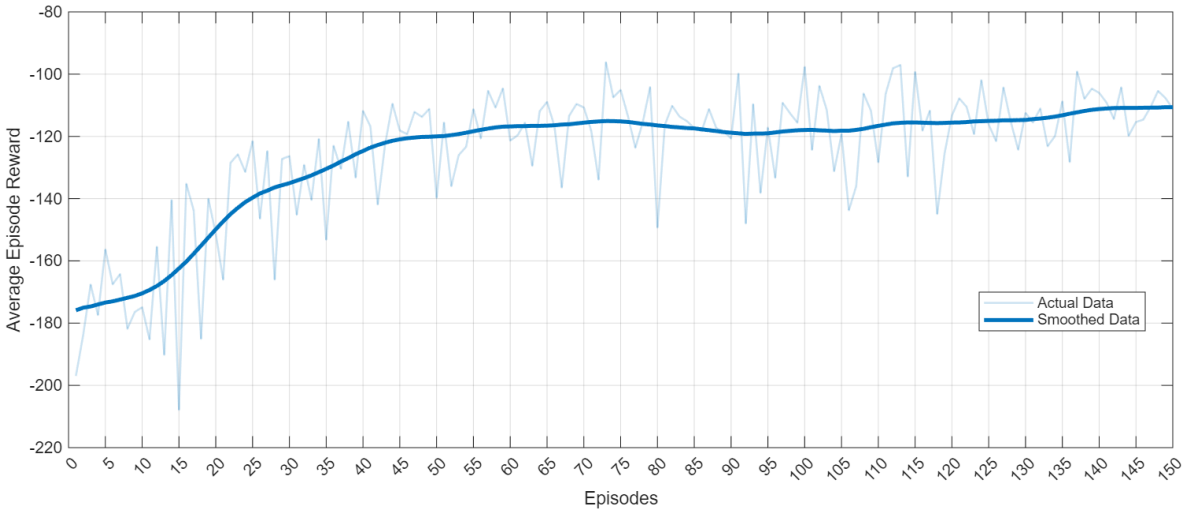

Figure 65: *Episode reward progression during DRL training*

5.3.5.4 Model Inference and performance evaluation

Model inference is conducted to evaluate the trained agent's performance using several key performance indicators (KPIs):

- **Reward:** As defined in Section 5.3.5.2
- **Served Ratio:** The percentage of users successfully served out of the total number of users within an episode (step size = 50).
- **Average Delay:** The mean waiting time from a user's first RA attempt until successful completion during an episode (step size), measured in terms of RAOs. The actual time delay depends on the interval between consecutive RAOs; to obtain the true delay in real time, the reported average delay should be multiplied by the

RAO periodicity. For example, if the RAO periodicity is 120 milliseconds, the real average delay is the reported value multiplied by 120 milliseconds..

- **Pending Delay:** The expected minimum waiting time for active users whose BI extends beyond the final time slot considered in the simulation, measured in terms of RAOs. This value represents a lower bound on the actual delay, as these users will only be able to reattempt RA outside the simulation window in future time slots.

The performance of the proposed DRL-based adaptive BI approach is evaluated against fixed BI schemes under two user density scenarios: 1000 users and 1500 users. The results in Table 25 and Table 26 demonstrate that the DRL model achieves a superior balance between reward, served ratio, average delay, and pending delay, compared to static BI configurations.

Table 25: *Performance comparison of DRL-based adaptive BI versus fixed BI schemes for 1000 users*

BI	Reward	Served Ratio (%)	Average Delay (RAO)	Pending Delay (RAO)
DRL	-113.96	86.86	2.9246	7.9750
5	-153.38	85.99	3.5864	1.1295
60	-175.57	73.15	2.6648	20.56
120	-290.64	69.76	1.3340	48.24

Table 26: *Performance comparison of DRL-based adaptive BI versus fixed BI schemes for 1500 users*

BI	Reward	Served Ratio (%)	Average Delay (RAO)	Pending Delay (RAO)
DRL	-275.6825	54.36	3.2080	6.2276
5	-880.30	22.87	3.1229	1.2479
60	-222.39	58.42	3.7390	20.6445
120	-327.45	56.21	1.9260	48.1820

As for the 1000 user's scenario, the proposed DRL approach achieves the highest overall reward (–113.96), indicating more efficient learning and better trade-off management among collision minimization, access delay reduction, and resource utilization. The served ratio (86.86%) is slightly higher than that of BI=5 (85.99%), but the improvement in reward demonstrates that DRL achieves this with a better balance of delay and collision handling. The average delay (2.9246) of the DRL model is moderate compared to fixed schemes as the average delay is higher than BI=120 (1.3340) but significantly lower than BI=5 (3.5864). This indicates that while the DRL model avoids the excessive waiting times of small BI values, it also mitigates the long idle periods caused by large BI settings. The pending delay (7.9750) shows that the DRL scheme maintains a reasonable lower-bound waiting time for active users. Although higher than BI=5 (1.1295), it is much smaller than BI=120 (48.24), confirming that DRL dynamically adapts the BI to balance serving ongoing users and providing fair opportunities for new arrivals. It is important to note that for BI = 5 (1.1295), this represents a theoretical lower bound; in practice, higher collision rates would increase the actual pending delay significantly. Hence, the DRL agent demonstrates adaptive decision-making, maintaining high service ratios with efficient delay management, resulting in the best overall reward performance among all schemes.

As the network load increases from 1000 to 1500 users, the performance of the DRL-based approach demonstrates graceful degradation compared to the fixed BI schemes, reflecting their adaptability under heavier traffic conditions. Although the overall reward decreases from –113.96 to –275.68 and the served ratio drops from 86.86% to 54.36%, this decline is significantly smaller than the deterioration observed in the fixed BI configurations, In particular, the served ratio under BI = 5 falls sharply to 22.87%, while BI = 60 and BI = 120 show declines

of about 15% and 13%, respectively, compared with the 32% drop observed for DRL.. The average delay under DRL increases moderately (from 2.92 to 3.21 RAOs), while the pending delay decreases (from 7.97 to 6.23 RAOs), indicating that the agent dynamically adjusts the BI to balance contention resolution and waiting times.. In contrast, static BI values either cause severe congestion (small BI) or which remain high across both load levels. This consistent relative performance across user loads confirms that the DRL framework is more resilient, scalable, and capable of maintaining a balanced trade-off between delay and collision rates in dense network environments.

5.3.6 Conclusions

This study presented a DRL-based adaptive BI optimization framework to enhance the RA procedure in 5G NR NTN environments. By formulating the BI configuration task as an MDP, the proposed approach enables dynamic, context-aware adjustment of BI values in response to varying network states. Unlike static or heuristic BI configurations, the DRL agent learns an optimal policy that minimizes access delay while maintaining a low collision probability. Simulation results demonstrated that the proposed DRL framework outperforms fixed BI schemes across different user densities. For both 1000 and 1500 users, the DRL model consistently achieved the highest overall reward, and a balanced trade-off between served ratio and delay performance,, effectively managing contention without introducing excessive waiting time. As network load increased, the DRL approach exhibited smooth and predictable performance degradation, confirming its adaptability, robustness, and scalability compared to static configurations. The results validate that intelligent BI control via DRL can significantly improve RA efficiency in LEO-based NTN systems. Future work may explore multi-agent DRL to further enhance RA optimization under complex network conditions.

6 HYBRID AUTOMATIC REPEAT REQUEST IN 6G NTN

In terrestrial networks, data transmission reliability is typically ensured through the use of hybrid-automatic repeat request (HARQ)protocol. However, the adaptation of HARQ in satellite networks is not straight forward mainly due to the non-negligible round-trip time (RTT) that satellite communications experience due to the long distance between the users and the satellite [130]. HARQ over NTN may experience stalling as a result of its stop-and-wait behavior, during which data transmission is paused while awaiting feedback from the receiver. In the following chapter, we describe the HARQ protocol and the enhancements agreed upon in 3GPP to enable more efficient HARQ operation in NTN networks. We analyze the HARQ protocol under different feedback configurations. In particular, we propose and investigate the performance of the HARQ protocol combined with maximum-distance separable (MDS) codes in an NTN scenario with a partial feedback configuration.

6.1 HARQ OVERVIEW

Since the introduction of 3G, the retransmission of missing or erroneous data units has been primarily managed by the HARQ mechanism at the medium access control (MAC) layer. This process is further supported by the radio link control (RLC) layer, which provides additional retransmission functionality to enhance reliability [131].

HARQ consists in the combination of two techniques, forward error correction (FEC) with automatic repeat request (ARQ) to enhance data transmission reliability. Upon receiving data, the system performs error correction. If the data is successfully decoded, an acknowledgment (ACK) message is sent to the transmitter, confirming successful reception. However, if decoding fails, a negative acknowledgement (NACK) message is sent, triggering a retransmission process.

Two different retransmission methods can be implemented: chase combining (CC) and incremental redundancy (IR).

- Chase combing: this method retransmits the same data unit, meaning that each retransmission is identical to the original. Undecoded data units are buffered, and the receiver applies maximal ratio combining (at PHY layer) between retransmissions to enhance the SNR, improving the probability of successful decoding.
- Incremental redundancy: instead of repeating the same data, each retransmission includes additional redundancy units, which combined to the original data unit help the FEC decoder in reconstructing the original data.

The basis for the hybrid ARQ implemented in modern terrestrial communications is based on multiple stop-and-wait protocols, each operating on a single transport block (data unit). In a stop-and-wait protocol, the transmitter stops and waits for an ACK after each transmitted transport block. An HARQ process cannot be reused for a new transmission until the feedback for the previous transmission is received. To maintain efficiency, multiple stop-and-wait processes are operated in parallel, allowing the transmitter to send data to one process while waiting for the ACK from another. The number of parallel processes supported is determined by the RTT.

In 5G terrestrial networks, HARQ supports 16 parallel processes [117], benefiting from a negligible RTT that ensures correct and efficient implementation.

6.1.1 HARQ NTN in 3GPP

The significantly increased RTT in satellite communications presents a major challenge for the correct execution of the HARQ process compared to terrestrial networks. The propagation delay in satellite networks depends on the satellite orbit and elevation angle ε. Examples of RTT for LEO satellites are shown in ***Table 27*** [132]. The large RTT not only increases the latency but also raises the memory requirement of the HARQ process. This impacts both the performance and the system requirements.

Table 27: *Example of RTT for different orbits*

Satellite Orbit	Payload type	Min RTT [ms] ε= 90°	Max RTT [ms] ε =10°
LEO 600 km	Regenerative	4	13
LEO 600 km	Transparent	8	26
LEO 1200 km	Regenerative	8	21
LEO 1200 km	Transparent	16	42

To enhance the applicability of HARQ in NTN, several significant studies have been proposed and discussed, contributing to 3GPP TR 38.811. Notably, two key decisions have been approved

- First, the number of parallel HARQ processes has been extended to 32, which may be sufficient for some NTN scenarios, such as communication with LEO satellites. However, this increase may still be insufficient to accommodate the longer RTT in GEO satellite scenarios [133]
- The second decision involves disabling feedback, allowing transmissions to continue without the HARQ process waiting for an ACK/NACK signal. The enabling/disabling feedback is configurable on a per UE and HARQ process basis [134][135].

These agreements represent a first step toward improvements. They cannot, however, guarantee the proper operation of the protocol across all satellite constellations.

6.2 STUDY CASE: HARQ OVER LEO

We consider an NTN scenario involving a LEO satellite and a UE. The LEO satellite is assumed to have a regenerative payload. The UE employs time division multiplexing, which prevents it from transmitting and receiving simultaneously, whereas the LEO operates in full-duplex frequency division mode allowing it to transmit and receive at the same time.

Our analysis focuses on the downlink channel, where the satellite is required to reliably transmit data to the device. The transmission is carried out using TBs of equal size and duration: t_{TB} =1 ms with each TB representing a separate HARQ transmission process. As agreed in Release 17, $N_p = 32$ supported processes are assumed to mitigate stop-and-wait due to RTT and to maintain a continuous transmission flow.

The propagation time of a TB to reach the receiver depends on the distance between the UE and the LEO, and is denoted by: t_{prop}. Each TB experiences independent Rayleigh fading. The channel amplitude is h , assumed to be constant over each block. This results in a varying SNR denoted by Γ , computed as:

$$\Gamma = \frac{h^2 P}{\sigma^2}$$

where $h^2 P$ is the received power and σ^2 is the Gaussian noise power. The random variable Γ follows an exponential distribution, with probability density function,

$$f_\Gamma(x) = \frac{1}{\overline{\Gamma}} \exp\left(-\frac{x}{\overline{\Gamma}}\right),\ x > 0 \text{ and } f_\Gamma(x) = 0,\ x \leq 0$$

where $\overline{\Gamma}$ is the average SNR.

TBs are protected by a channel code with rate R and each block is successfully decoded when $\log_2(1+\overline{\Gamma}) \geq R$. From this, we can also define the decoding threshold:

$$\gamma_{th} = 2^R - 1.$$

We then define the probability of decoding a TB as

$$P_{dec}(\Gamma, \gamma_{th}) = \Pr\{\Gamma \geq \gamma_{th}\} = \int_{\gamma_{th}}^{\infty} f_\Gamma(x)\, dx = e^{-\frac{\gamma_{th}}{\overline{\Gamma}}}.$$

For simplicity, we refer to $P_{dec}(\Gamma, \gamma_{th})$ as P_{dec}. It is assumed that the satellite continuously transmits data during its visibility windows, denoted by W_{tx}, within which transmissions occur of TB new processes are transmitted over the transmission windows W_{tx}, of which TB_{succ} are successfully received.

When feedback is enabled, the UE transmits an ACK or NACK message to the satellite, indicating the outcome of the last TB reception. The feedback duration is indicated with t_{FB}.

6.2.1 Modeling Approach

We present three different HARQ approaches considered. For an easy comparison between schemes, HARQ is assumed to be non-adaptive meaning that there is no change in the modulation, coding or bandwidth. A truncated HARQ scheme is also assumed where the maximum number of retransmissions is set to r_{max}.

We compare the performance under the following configurations: feedback is enabled for all processes, feedback is disabled for all processes, and feedback is partially enabled, with the proposed MDS-HARQ scheme applied.

6.2.1.1 HARQ Feedback Enabled

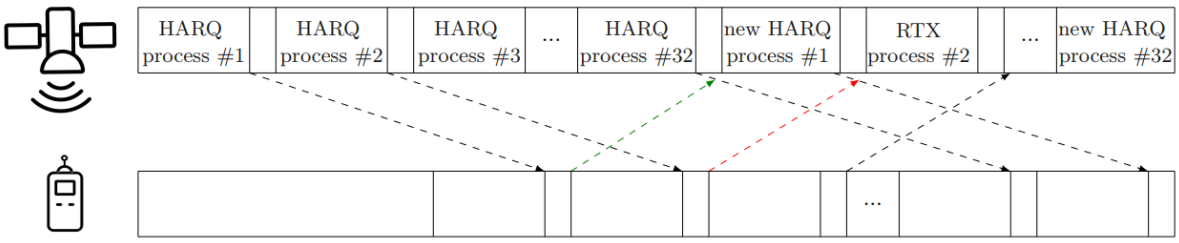

Figure 66: *HARQ scheme with feedback enabled*

In the feedback enabled configuration illustrated in ***Figure 66***, the satellite transmits N_p processes, a process is transmitted by means of a transport block. The UE attempts to decode each HARQ process upon reception. When the UE successfully decodes the i-th process, it sends an ACK, prompting the scheduler to allocate a new TB for the i-th HARQ process. If decoding fails, due to severe fading affecting the received block, the UE sends a NACK and

stores the received TB. The satellite then retransmits an identical replica of the failed TB. The UE applies combination between the stored and the retransmitted block using maximum ratio combining (MRC) and attempts decoding again. If decoding fails again, the information is preserved and incrementally updated with each subsequent retransmission. This process continues iteratively until successful decoding is achieved or the maximum number r_{max} of retransmissions is reached.

The SNR after maximum ratio combining of *i* retransmissions is given by: $\Gamma_{MRC} \geq \gamma_{th}$

where h_l denotes the channel amplitude of the l-th retransmission.

Transmission is successful when $\Gamma_{MRC} \geq \gamma_{th}$.

6.2.1.2 HARQ Feedback Disabled

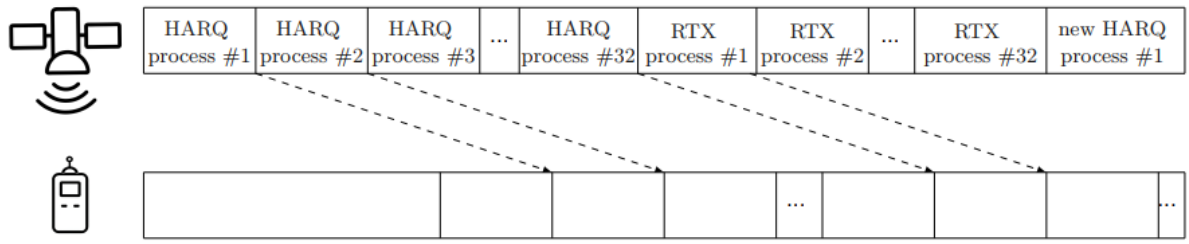

Figure 67: *HARQ scheme with feedback disabled*

In the feedback disabled configuration, as illustrated in ***Figure 67***, the UE attempts to decode each received TB upon reception. Unlike the feedback enabled case, no ACK/NACK is sent to the satellite. Consequently, the satellite blindly transmits a predetermined number r_{max} of retransmissions for each TB.

If the initial decoding attempt fails, the UE employs MRC to combine the received retransmissions, thereby enhancing the probability of successful decoding. However, in cases where the UE successfully decodes a TB before all r_{max} retransmissions are received, the remaining transmissions result in unnecessary use of spectral and energy resources.

6.2.1.3 MDS-HARQ Partial Feedback

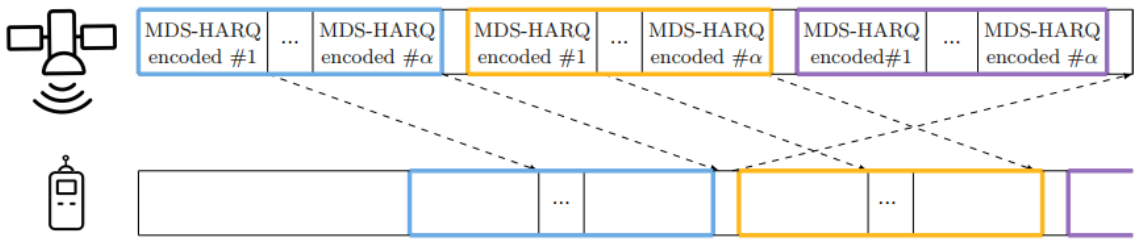

Figure 68: *MDS-HARQ scheme with partial feedback*

A possible implementation of MDS-HARQ is illustrated in Figure 68.

The proposed MDS-HARQ partial feedback scheme constructs N encoded blocks from n original processes using a MDS(N, n) code, providing the satellite with (N, n) redundant blocks

for potential retransmissions. To fairly compare this scheme with respect to the others, we assume that the number of encoded blocks is $N = n\, r_{max}$.

This coding enables reliable reconstruction of the original n processes at the UE from any n successfully received out of the N encoded TB.

The procedure of the scheme can be described as follows: the satellite encodes a group of

$n \leq N_p$ processes into N encoded blocks, and transmits $\alpha \geq n$ of them to the device, as illustrated in the figure, where colors refer to different encoding processes. Feedback is received after $\alpha + N_p$ processes, indicating whether the group of n processes has been successfully reconstructed. If decoding fails, additional blocks from the remaining $N - \alpha$ redundancy are transmitted until success or until all blocks have been sent.

An enhanced feedback mechanism may additionally be employed, specifying the number of failed transmissions and enabling the LEO to transmit the corresponding redundancy proactively.

The main advantage of the scheme is two-fold: first, it reduces the amount of feedback required by a factor of n ; second, it allows the transmission of predetermined redundancy in advance, improving reliability and efficiency.

Note that unlike the conventional HARQ schemes, the MDS-HARQ proposed does not rely on combining techniques at the receiver.

In this context, we investigate the following feasible MDS-HARQ scheme implementations:

i. a feedback-based scheme, in which the satellite transmits α TB without redundancy and receives a single feedback message for the encoded group. Based on this feedback, either a retransmission is performed or new encoded processes are transmitted.

ii. a feedback-free scheme, in which the satellite transmits α TB with a priori redundancy based on the average number of TB required for successful decoding, eliminating the need for any feedback exchange.

iii. a feedback-based smart scheme similar to (i), assuming that the NACK contains information on the number of unsuccessful TB. Upon reception of the NACK, the corresponding number of blocks is transmitted.

6.2.2 Numerical Results

In our first set of results, we compare the throughput, block error rate, and delay for three schemes: HARQ with feedback enabled, HARQ with feedback disabled, and MDS-HARQ. In this setting, we assume that the MDS-HARQ encodes $n = 32$ processes into $N = n + r_{max}$ encoded transport blocks. A total of $\alpha = 32$ encoded blocks are transmitted, and feedback is sent after the reception of the last block.

For all the results, we consider unitary power $P = 1$ and a code rate of $R = \frac{1}{3}$.

We set the feedback time to $t_{FB} = 0.125$ ms, which is one-eighth of the TB duration $t_{TB} = 1$ ms. The propagation time is set to $t_{prop} = 6$ ms and the visibility window to $W_{tx} = 50 \cdot 10^4$ TB, which defines the simulation duration.

In Figure 69 the throughput is shown as a function of the SNR per bit for HARQ with feedback enabled, HARQ with feedback disabled, and MDS-HARQ, for one and four repetitions. Here, a throughput of zero indicates that none of the transmitted processes are successfully received, while a throughput of one indicates the best performance, where the maximum transmittable processes in the visibility window are correctly received.

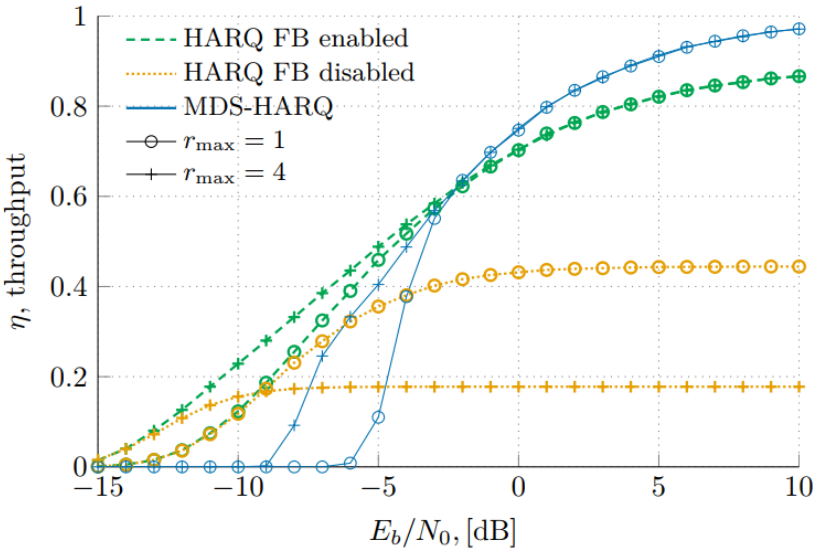

Figure 69: *Throughput as a function of Eb/N0 for HARQ with feedback enabled, with feedback disabled and for MDS-HARQ for r_max = 1, 4 retransmissions*

From the plot, we can identify two distinct performance regimes. At very low SNR, from -15 dB to -3 dB, traditional HARQ with feedback outperforms MDS-HARQ. This is because at low SNR, performing maximum ratio combining over retransmissions is highly effective, allowing the receiver to accumulate enough signal energy to successfully decode the transmitted blocks. In the higher SNR regime, from -3 dB to 10 dB, MDS-HARQ shows superior throughput, as it reduces the number of feedback rounds and ensures successful reception as soon as a sufficient number of encoded blocks are received, improving transmission efficiency. The performance of HARQ with feedback disabled is degraded because time resources are wasted in blind retransmissions, where decoding has already succeeded and new processes cannot be allocated. Finally, we note that only at low SNR values (below -3 dB) does the difference between one and four repetitions significantly affect the performance of HARQ with feedback enabled and MDS-HARQ. At higher SNRs, a single retransmission is sufficient to achieve high throughput.

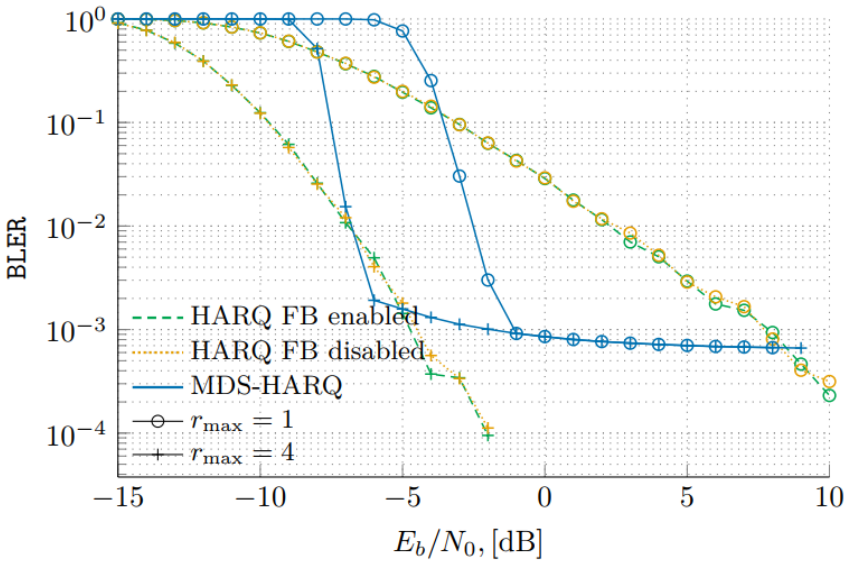

Figure 70: *Block error rate as a function of Eb/N0 for HARQ with feedback enabled, with feedback disabled and for MDS-HARQ for r_max = 1, 4 retransmissions*

In ***Figure 70***, the block error rate is shown as a function of SNR for HARQ with feedback enabled, HARQ with feedback disabled, and MDS-HARQ, for one and four retransmissions. As expected, the block error rate improves with increasing SNR. For a fixed number of retransmissions, the performance of HARQ with feedback enabled and feedback disabled coincides. This is because both schemes achieve decoding once the accumulated energy from retransmissions is sufficient, which on average occurs after the same number of retransmissions, regardless of whether feedback is present. In contrast, MDS-HARQ with four retransmissions can achieve lower block error rates at low SNR by allowing successful recovery once a sufficient number of encoded blocks are received.

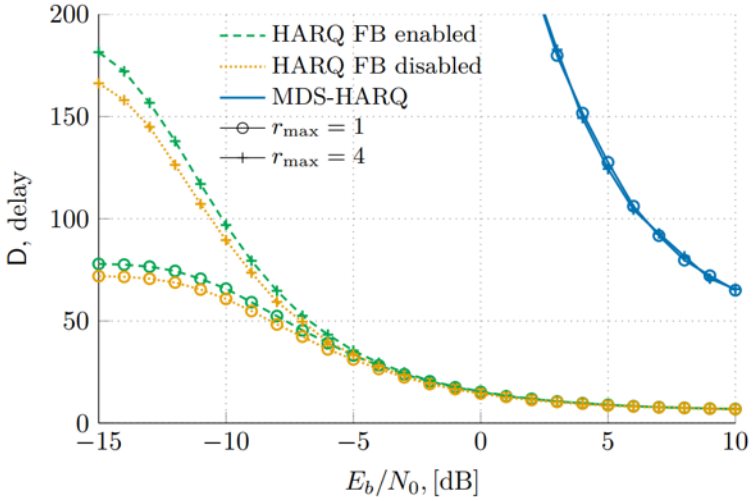

Figure 71: *Delay as a function of Eb/N0 for HARQ with feedback enabled, with feedback disabled and for MDS-HARQ for r_max = 1, 4 repetitions*

In ***Figure 71***, the delay is shown as a function of SNR for HARQ with feedback enabled, HARQ with feedback disabled, and MDS-HARQ, for one and four retransmissions. HARQ, both with and without feedback, consistently outperforms the MDS-HARQ scheme. Furthermore, for SNR values above -5 dB, the performance is nearly identical across all schemes, since a single retransmission is sufficient and decoding occurs at the same time in both feedback-enabled and feedback-disabled cases.

MDS-HARQ is penalized in terms of delay because the receiver must wait to decode the entire group of processes; in the case of retransmissions, additional blocks must be received before decoding can occur. To reduce this delay, alternative implementations of MDS-HARQ are proposed and evaluated.

In subsequent figures (shown in ***Figure 72***), three different implementations of MDS-HARQ are compared: standard MDS-HARQ, MDS-HARQ with smart feedback, and MDS-HARQ with traditional feedback. The results show that the smart feedback configuration outperforms the previous implementations in terms of block error rate and delay, while achieving comparable throughput. Compared to traditional HARQ schemes, the smart feedback implementation demonstrates superior performance in terms of reliability. Specifically, at SNR values above -3 dB with four retransmissions and above -1 dB with a single retransmission, MDS-HARQ with smart feedback achieves negligible block error rates, significantly outperforming conventional HARQ approaches.

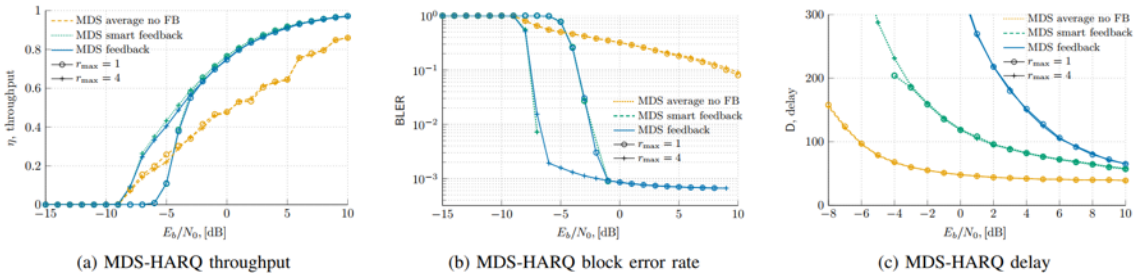

(a) MDS-HARQ throughput (b) MDS-HARQ block error rate (c) MDS-HARQ delay

Figure 72: *MDS-HARQ implementation comparision: (a) MDS-HARQ throughput, (b) feedback MDS-HARQ block error rate, and (c) MDS-HARQ DELAY*

However, MDS-HARQ continues to suffer from higher delays due to the need to decode the entire group of blocks collectively. Implementing the average number of transmitted blocks without feedback is not convenient, as channel variability can lead to under- or over-transmission. Fewer blocks than necessary may be sent, resulting in decoding failures, while more blocks than required increase delay and reduce efficiency. Feedback-based MDS-HARQ adjusts the number of transmitted blocks according to actual channel conditions.

Finally, the performance of MDS-HARQ with smart feedback is evaluated for different numbers of encoded processes: 8, 15, 24, and 32, as represented in ***Figure 73***. At high SNR values, throughput is essentially independent of the number of processes. In the intermediate SNR range, a slightly better performance is observed for 8 processes when only one retransmission is allowed. For block error rate, different numbers of processes exhibit similar behavior, with a slight gain for 32 processes in some cases. Lower numbers of processes improve delay, since the probability of successful decoding is higher when fewer blocks are involved.

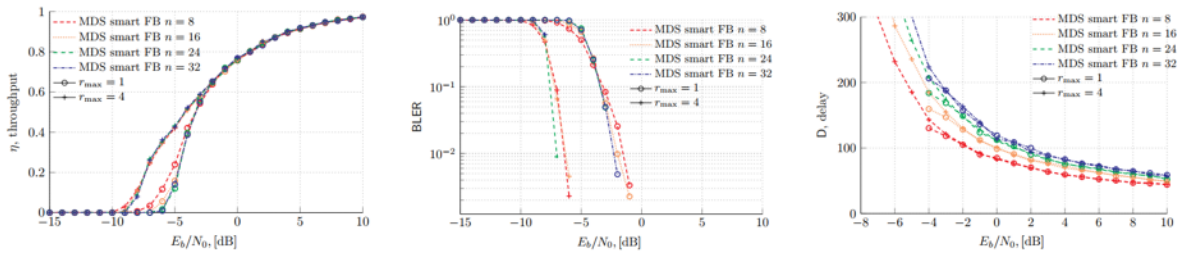

(a) Throughput (b) Block error rate (c) Delay

Figure 73: *MDS-HARQ IMPLEMENTATION comparision: (a) MDS-HARQ throughput, (b) feedback MDS-HARQ block error rate, and (c) MDS-HARQ DELAY*

Overall, alternative HARQ configurations offer advantages in applications where delays can be tolerated. MDS-HARQ is also scalable for broadcasting to multiple users: retransmissions do not need to be dedicated to specific users, as any additional encoded packet can be useful to all recipients. Future work will evaluate MDS-HARQ in multi-user scenarios, exploring potential improvements.

6.2.3 HARQ for light indoor communications

HARQ protocol implemented with MRC can be very effective for indoor communications, particularly in scenarios where the penetration loss is high. From both the investigated model and the results, it is observed that even with just four repetitions, the energy accumulated from retransmissions is often sufficient to successfully decode some transport blocks (even at low SNR, such as –15dB), highlighting how MRC can exploit repeated transmissions to overcome the signal attenuation and channel impairments. By increasing the number of repetitions when necessary, the protocol can further enhance performance, improving both reliability and throughput.

Based on the observed results, HARQ offers a flexible and practical solution for challenging indoor environments. In particular, adapting the number of retransmissions allows the system to maintain robust communication even under difficult propagation conditions.

6.2.4 Conclusion and future perspective

In this chapter, the performance of HARQ protocol in NTN under different feedback configurations and introduced the MDS-HARQ approach as an effective compromise between reliability and efficiency. The proposed scheme reduces feedback overhead and improves throughput compared to fully disabled feedback, while maintaining competitive reliability performance. Simulation results demonstrated that MDS-HARQ over NTN, particularly with the smart feedback mechanism, achieves significant gains in block error rate and throughput at moderate-to-high SNR values, confirming its suitability for next-generation satellite systems where feedback is costly or delayed. Moreover, the results indicate that the studied HARQ, when properly adapted, can support communications even in challenging propagation environments such as indoor communications, achieving 90% successful decoding at SNR levels as low as –10 dB. Even lower SNRs can be supported by increasing the maximum number of allowed retransmissions. Overall, the study carried out in section 6 highlights the potential of HARQ schemes to adapt and to enhance communication efficiency and robustness in NTN scenarios.
The novel HARQ study conducted in this project, particularly for the partial feedback configuration, provides valuable insights that can guide future enhancements to the 3GPP standard. Indeed, these results serve as a reference for improving the efficiency and reliability of the HARQ in NTN networks, supporting better performance across different satellite constellations and deployment scenarios.

7 SYNCHRONIZATION ANALYSIS

This section is dedicated to the analysis, design, and assessment of algorithms to allow the downlink and uplink synchronization during the initial access without the GNSS. Before delving into their description, a brief overview of the initial access is provided.

7.1 OVERVIEW OF THE INITIAL ACCESS

The 5G initial access procedure enables a UE to establish a connection with a base station (gNB). It is illustrated in ***Figure 74***.

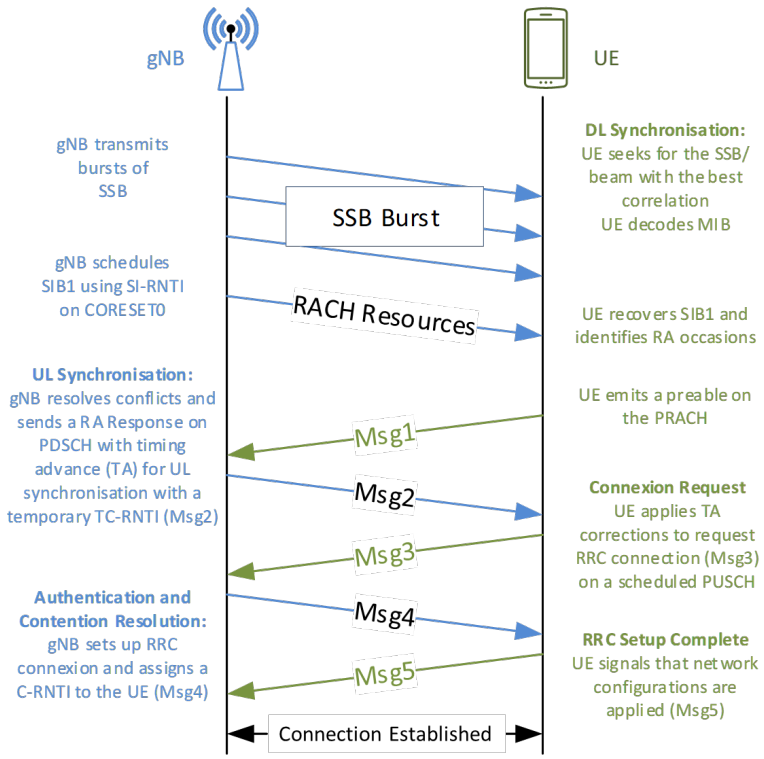

Figure 74: *Flow diagram of the initial access procedure of a terminal into a 5G-NR CELL*

Cell search procedure is used by the UE to acquire time and frequency synchronization within a cell and detects the Cell ID of that cell. The process begins with downlink synchronization Both synchronization signals primary synchronization signal (PSS) and secondary synchronization signal (SSS) are used by UE to acquire the downlink synchronization of the network, which comprises the following procedures: frequency synchronization, slot synchronization, frame synchronization, and cell ID detection. The PSS is used for initial symbol boundary, CP, sub frame boundary, and initial frequency synchronization to the cell. The SSS is used for radio frame boundary identification. PSS and SSS together are used for the detection of physical layer Cell ID (PCI). Synchronization signals (SS) and the physical broadcast channel (PBCH) channel are packed as a single block that always moves together. They are jointly referred to as a SS block or SSB. Through the PBCH, the UE decodes system information (MIB and SIB1) needed to proceed.

Other synchronization mechanisms are defined, e.g., for radio link monitoring, transmission timing adjustments and timing for cell activation/deactivation. To accommodate the large Doppler shift in LEO/MEO–based NTN Satellite systems, beam-specific pre-compensation of common frequency shift can be applied to the signal in the DL, which can be conducted with respect to a reference point (RP) (e.g., the spot beam center) such that the DL signal received at this RP is appeared to have zero Doppler shift from the satellite movement. This solution was a potential enhancement extensively discussed during the study and normative phases of NR NTN support. It is observed via simulations that for DL initial synchronization, with common frequency offset compensation on the DL service link, robust performance can be provided by the SSB design in Rel-15/16 in case of GEO and LEO. However, the DL initial synchronization is also possible on NGSO radio link without pre-compensation of the frequency offset and no issues have been identified based on Rel-15/16 NR design. Only additional complexity is needed at UE receiver to achieve robust DL initial synchronization performance based on Rel-15. Therefore, NR NTN SI concluded that no further enhancement on the SSB is needed to support NTN. Moreover, during the NTN normative phase, it was agreed that DL frequency compensation by gNB for the service link Doppler is not supported in Release 17.

Next, the UE initiates uplink synchronization through the 4-step Random Access Channel (RACH) procedure. The UE transmits a randomly selected preamble (msg1). The gNB responds with a random-access response (RAR, msg2), which provides a critical Timing Advance (TA) command for uplink alignment and a temporary identifier (TC-RNTI).

By adjusting the TA for each device appropriately, the network can manage the timing of the signals that the base station receives from those devices. Devices that are located further away from the base station experience greater propagation delays and therefore must initiate their uplink transmissions slightly earlier than those that are closer to the base station, as demonstrated in ***Figure 75***.

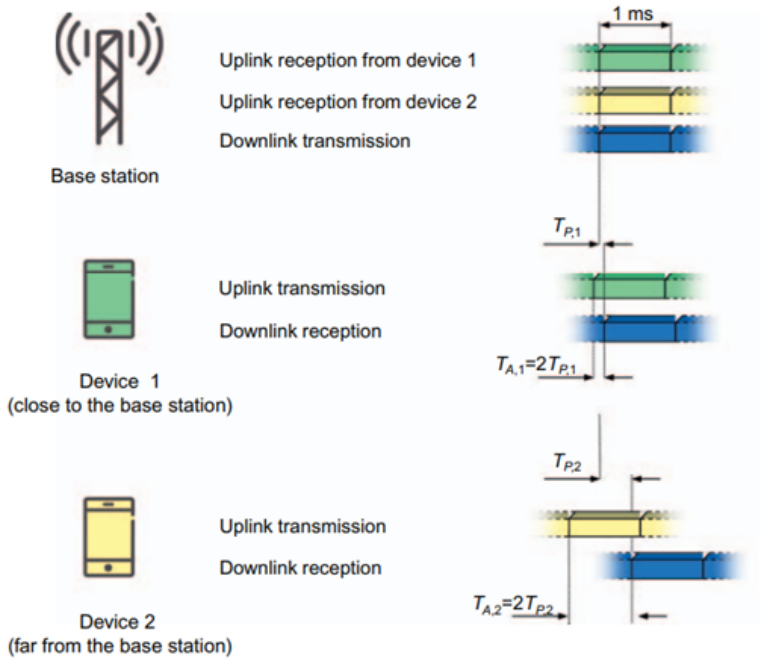

Figure 75: *Representation of the TA concept*

Finally, an RRC connection is established. The UE uses the provided TA to send an RRC Connection Request (msg3). The procedure typically concludes when the gNB sends a contention resolution message (msg4), assigning the UE a permanent identifier (C-RNTI). This entire process is often enhanced by beamforming, where each SSB in a burst is transmitted in a different direction, allowing the UE to identify and select the optimal beam to improve spectral efficiency.

In NR, uplink transmission from all UEs within a serving cell shall be synchronized when received at the Base Station reception point: Inter-symbol interference shall be avoided and thereby all uplink transmissions shall be received with a time spread, which is less than the duration of the CP. The uplink timing of each individual UE is controlled by the base station With MAC message. This is mainly applicable to the physical uplink shared channel (PUSCH), physical uplink control channel (PUCCH), and sounding reference signal (SRS). In NR TN, the PRACH can only use a fixed timing offset because the UE transmits the PRACH preambles before the gNB is able to provide any timing adjustment. The TA refers to the negative offset between the start of a given DL frame as observed by the UE and the start of the corresponding frame in the UL. The TA applied by the UE is given by the following formula:

$$T_{TA} = (N_{TA} + N_{TA,offset})T_c$$

With $T_c = 1/(480000 \cdot 4096)$.

For initial access, random-access procedure is used in order for UE to achieve Uplink synchronization and obtain the resource for RRC Connection Request message. Initial access procedure is triggered by the UE by transmitting a random access PRACH preamble with $N_{TA} = 0$, then the UE receives its first timing advance command (TAC) within the RAR message. Within the TAC, a set of 12 bits is used to indicate a TA value from 0 to 3846. The UE uses this value to calculate NTA as follows:

$$N_{TA} = T_{TA} \cdot 16 \cdot \frac{64}{2^{\mu}}$$

With μ indicating the subcarrier spacing. At PRACH preamble transmission $N_{TA} = 0$. $N_{TA,offset}$ is provided in SIB1 and it was specified to ensure that a UL radio frame finishes before the start of the subsequent DL radio frame.

Considering the large RTT in satellite radio link, it is clear that the value of TA in the TAC during initial is far from sufficient. Further, the high delay drift in case of non-GEO satellites can be a problem for TA control in Connected state and solutions have been specified in 3GPP Release 17 to meet the challenges related to large RTT and timing drift: NTN UE shall support the uplink time pre-compensation and frequency pre-compensation, timing relationship enhancements and a set of other NTN essential features, e.g., timers extension in MAC/RLC/PDCP layers and RACH adaptation to handle long RTT and introduction of several higher layer parameters and NTN specific SIB (i.e., SIB19) to assist the UE in uplink time and frequency synchronization. For uplink time synchronization in NR NTN access, the UE should perform the uplink time pre-compensation. To this aim, the UE is assisted by its GNSS and by the network. The network broadcasts assistance information in SIB19 in the serving NTN cell, including ephemeris information and higher layer Common-TA-related parameters. The UE shall acquire a valid GNSS position as well as assistance information before and during connection to an NTN cell. Then, the UE calculates UE-specific TA corresponding to the RTT on the service link, based on its GNSS-acquired position and the serving satellite ephemeris.

If Common-TA-related parameters are indicated, the UE calculates common TA corresponding to any common delay, e.g., RTT on the feeder link, according to the parameters provided by

the network. UE considers common TA as 0 if these parameters are not provided. The UE performs the pre-compensation of the calculated TA in its uplink transmissions, including PRACH preamble transmissions and uplink transmissions during the RRC CONNECTED state.

For TA update in RRC CONNECTED state, combination of both open-loop (i.e., UE autonomous TA estimation, and common TA estimation) and closed-loop (i.e., received TA commands in RAR message or MAC CE) is supported. 3GPP Release 17 specified the following formula for TA calculation that shall be applied by NTN UEs for PRACH preamble transmission and in RRC CONNECTED state:

$$T_{TA} = (N_{TA} + N_{TA,offset} + N_{TA,adj}^{common} + N_{TA,adj}^{UE}) \cdot T_c$$

Where, $N_{TA,adj}^{common}$ is a network-controlled common TA, and may include any timing offset deemed necessary by the network (e.g., feeder link delay) and $N_{TA,adj}^{UE}$ is UE self-estimated TA to pre-compensate for the service link delay. It is computed by the UE based on UE position and serving satellite-ephemeris-related higher-layers parameters if configured. These parameters (shown in Figure 76) are autonomously updated by the UE (i.e., open-loop TA control), while N_{TA} is updated via closed-loop TA control.

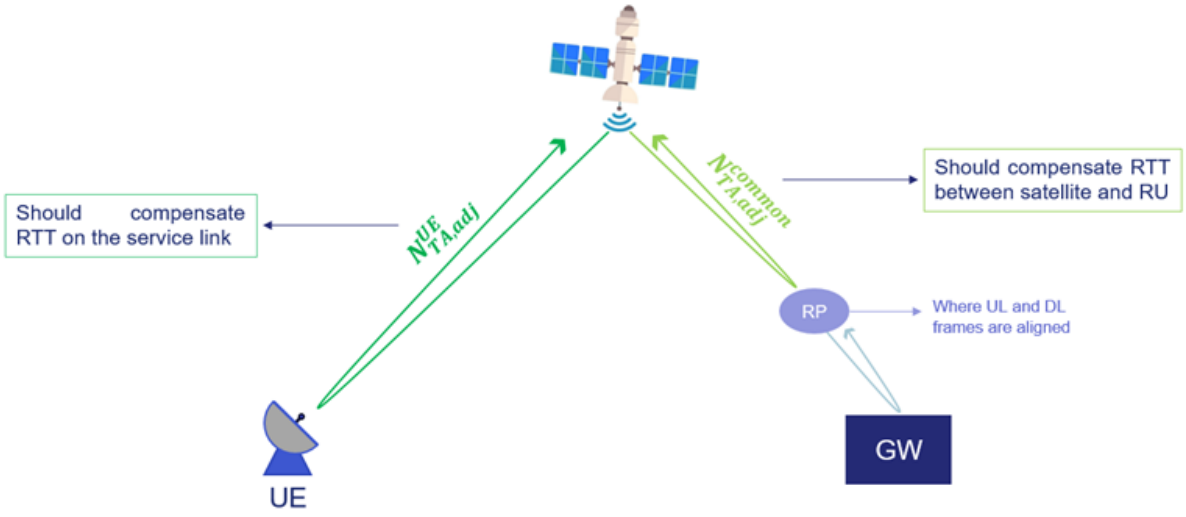

Figure 76: *Representation of $N_{TA,adj}^{common}$ and $N_{TA,adj}^{UE}$*

The 3GPP has defined the initial transmission timing error for the UE, which shall be less than or equal to $\pm T_{e\_NTN}$ where the timing error limit value T_{e_NTN} is specified in ***Table 28***

Table 28: *Timing error limit from 3GPP 38.188 requirements (Section 7.1C.2 for fixed VSAT)*

Frequency Range	SCS of UL signal (kHz)	Te_NTN	Half of CP duration
FR2	60	4,23.10-7 s	5,85.10-7 s
	120	2,44.10-7 s	2,85.10-7 s

FR1	30	7,17.10-7 s	1,17.10-6 s

Regarding the frequency estimation performance, the mean value of basic measurements of UE modulated carrier frequency shall be accurate to within **± 0.1 PPM** observed over a period of 1ms of cumulated measurement intervals compared to the carrier frequency received from the NR gNB, as shown in ***Table 29***.

Table 29: *3GPP 38.101 requirements (cf 6.4.1)*

Carrier Frequency	SCS of UL signal (kHz)	Tolerated frequency offset (kHz)	% of SCS
30 GHz	60	3	5
	120	3	2,5
14,5 GHz	30	1,45	4,8

7.2 GNSS FREE OPERATIONS

UEs compatible with releases 17/18/19 and supporting NTN access are expected to be equipped with GNSS. These UEs should support uplink time and frequency pre-compensation based on their GNSS-acquired position. The GNSS availability is therefore essential for NTN access due to its necessity for physical layer operations. Additionally, GNSS availability may be useful for higher layer procedures such as location-based conditional handovers.

However, GNSS information in UE may be

- temporarily unavailable;
- or available but degraded, leading to a reduction in GNSS position accuracy

These occurrences are becoming more and more common and result in a 3GPP NTN service that is not very robust.

The main reasons include:

- Potential occurrence of GNSS jamming, leading to denial of service. Figure 77 shows the map of the GNSS jamming.
- Potential occurrence of GNSS spoofing and other effects (e.g., poor geometry, local blockages, solar storm activity or simply increased GNSS measurement period to save UE power) beyond the control of the satellite network operator, leading to incorrect/inaccurate location calculation and position fix at the UE side, resulting in an out-of-sync condition;
- UE possibly being in an adverse environment where NTN access is possible but GNSS signal is too weak, due to the difference in link budget margin between both systems.

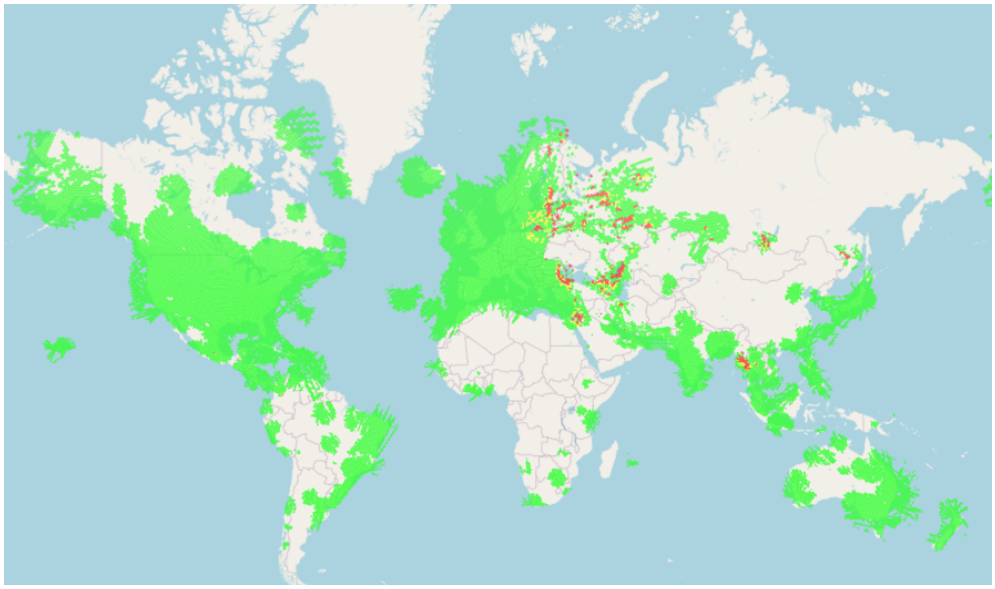

Figure 77: *GNSS jamming map from ADS-B receivers (GPSJAM.ORG)*

Moreover, the dependency on the GNSS system renders the 3GPP NR NTN system less resilient, as it relies on an external third-party system. While previous releases primarily focused on introducing NTN support within 3GPP specifications, the Release 20 should aim to enhance resilience by reducing dependence on GNSS [137]. This involves supporting GNSS-resilient operation, thereby allowing the system to function efficiently even in scenarios where GNSS is temporarily unavailable or compromised.

Referring to the previous paragraph, it is clear that GNSS resilient operations have many impacts on the NR-NTN procedures. Indeed, when UE is either in connected or idle modes, both time and frequency synchronization are essential to allow the system to properly work. The first impacted operation is the uplink (UL) synchronization, when the UE is in idle mode. When in connected mode, the acquired synchronization should be kept. Notably, the UE should be able to update the TA, partially alone by means of the open loop control [136], and the k_{mac} parameter (essential for scheduling).

7.3 DOWNLINK SYNCHRONIZATION

7.3.1 Introduction

The primary challenge for initial access in 5G NTN stems from the combination of the higher carrier frequencies and the significant orbital velocity of LEO satellites. This synergy results in extreme Doppler shifts and rapid frequency variations that far exceed those seen in lower bands, reaching values nearing ± 850 kHz for a carrier frequency of 37 GHz in Q/V-band for instance. These large frequency misalignments severely hamper a terminal's ability to perform the critical initial access procedure: the detection of the Physical Cell ID from PSS/SSS contained within the SSB. The performance of this process needs to be evaluated not only by the probability of non-detection (PND) (also known as probability of missed detection) but also by practical receiver constraints such as computational complexity and the probability of false alarm (PFA).

To address these challenges, this study develops and details a comprehensive framework to simulate and analyze the initial DL synchronization process for a 5G NTN system operating in the Q/V band. The methodology involves establishing a channel model compliant with existing

3GPP specifications adapted to the system parameters used in the 6G-NTN project, defining and evaluating robust receiver algorithms, and proposing a two-stage hierarchical synchronization strategy to manage the high Doppler dynamics inherent to LEO scenarios. The goal is to provide recommendations for algorithm design that can ensure reliable network access in these demanding future operating bands.

The remainder of this section is organized as follows. First, the next sub-sections detail the system model by discussing the waveform parameters and operating hypotheses. Afterwards, the considered circular orbit channel model is explained, and equations for channel characteristics such as the propagation delay or the Doppler shift are given. Following sections discuss in detail the proposed receiver architecture and the motivation behind different design parameters. Finally, the numerical results are analyzed to extract concluding remarks from this study.

7.3.2 System Model

7.3.2.1 NTN architecture

The simulation framework is founded upon the 3GPP TR 38.811 [11] Deployment Scenario D4, which specifies a non-geostationary satellite platform operating at a 600 km altitude with Earth-fixed beams, compliant with the scenarios and the constellation developed in the 6G-NTN project under WP3.

This scenario utilizes a frequency division duplex (FDD) scheme with bandwidths up to 800 MHz and assumes an NTN Architecture A4, where the space-borne platform directly serves Relay Node terminals, effectively placing gNB functionality on the satellite. Terminals are defined as very small aperture terminals (VSAT) or relay nodes, which may be fixed or mounted on moving platforms such as aircraft traveling at speeds up to 1000 km/h.

The corresponding network architectures from TR 38.811 [11] are reproduced in ***Figure 78*** and ***Figure 79***.

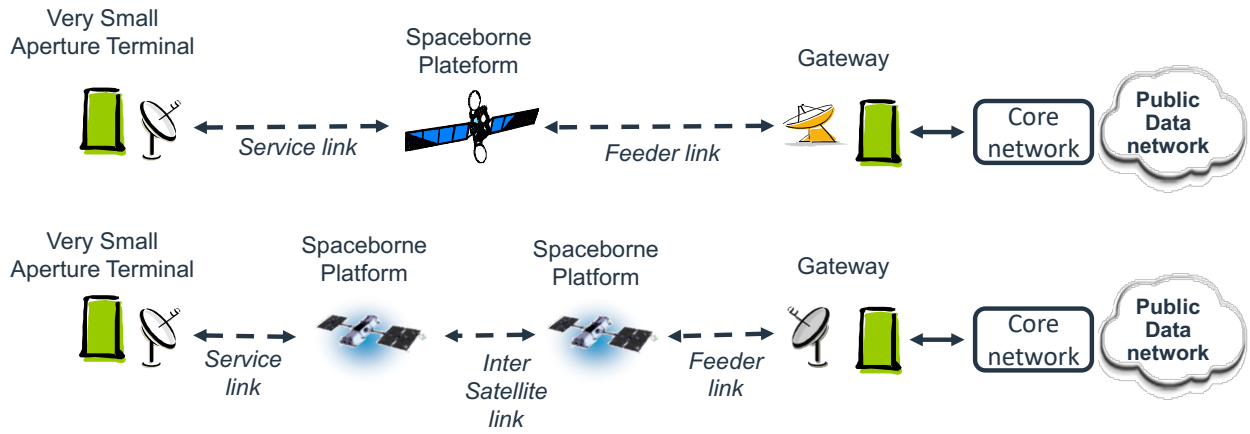

Figure 78: *considered 3gpp satellite access network architectures with a service link provided by onboard gnb on satellite and vsat type terminal, for operating in frequency bands above 6 ghz allocated to fixed and mobile satellite services (reproduced from figure)*

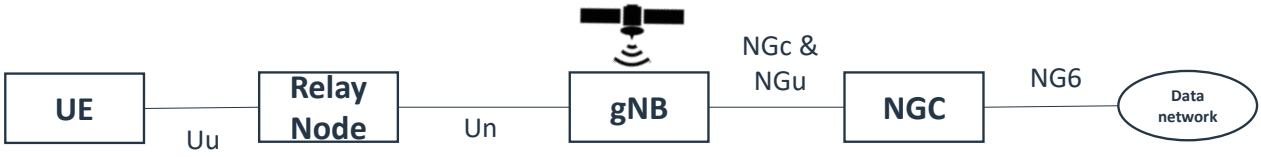

Figure 79: *Considered NTN access network serving a terrestrial relay node (VSAT) with a satellite/aerial gNB (reproduced from Figure 4.7-4 of* ***ERROR! REFERENCE SOURCE NOT FOUND.****)*

While this scenario is originally thought out for Ka-band scenario with a DL carrier at around 20 GHz, in this study higher frequencies will be considered as explained below.

7.3.2.2 Frequency and bandwidth parameters

This study focuses on a forward-looking scenario using the Q/V frequency band, with WP3/WP4 assumptions considering DL at 37 GHz and UL at 47 GHz. This frequency range is above the currently standardized NTN bands such as the S/L-bands (n256, n255, n254) or the Ka-band (n512, n511, n510) as described in clause 5.2 of TS 38.101-5 [3].

Table 30: *Maximum transmission bandwidth configuration in FR2-NTN, reproduced from ts 38.101-5* ***Error! Reference source not found.***

SCS (kHz)	50 MHz	100 MHz	200 MHz	400 MHz
	N_{RB}	N_{RB}	N_{RB}	N_{RB}
60	66	132	264	N/A
120	**32**	66	132	264

A DL carrier frequency at 37 GHz is considered. Hence, being in the FR2-NTN configuration, the maximum transmission bandwidth is defined as in the Table 5.3.2-2 of 5.2 of TS 38.101-5 [3], as reproduced above (***Table 30***). For the purpose of analyzing the synchronization process, a representative channel bandwidth of 50 MHz is selected. This configuration supports a maximum of 32 RB, which is sufficient to accommodate the 20 RBs required by the SSB. The choice of a 120 kHz SCS, corresponding to numerology $\mu = 3$, balances the number of available resource blocks and the synchronization complexity, by putting the maximum Doppler shift of $\pm\ 850$ kHz, in a range of ± 7 subcarrier offset.

7.3.2.3 5G NR waveform configurations

An OFDM signal over the range of 20 to 32 RBs at 120 kHz SCS can be handled by a sample rate of 61.44 MHz and an IFFT-length of 512. At numerology 3, this results in frames consisting of 80 slots, each consisting of 14 OFDM symbols under a 'Normal' CP configuration. Indeed, the cyclic prefix in this setup consists of 68 samples every 56 OFDM symbols, and of 36 samples otherwise.

In this configuration, there can be up to 64 SSBs within a 5ms burst, whose OFDM symbol positions are given by $l = \{4,8,16,20\} + 28 \cdot n$, with $n \in \{0, \dots 3,5, \dots 8,10, \dots 13,15, \dots 18\}$, according to TS 38.213 [144], each carrying the PSS, SSS, and the PBCH.

For a totally agnostic user terminal, there are three possible PSSs, identified with $N_{ID}^{(2)} = 0,1,2$ and for a given value of $N_{ID}^{(2)}$, there are 336 possible SSSs (hence there are 1008 unique SSS sequences when PSS is not fixed), denoted by $N_{ID}^{(1)} = 0, \dots ,335$. During the initial access phase, the UE needs to identify these sequences in order to compute the cell ID through $N_{ID}^{cell} =$

$3N_{ID}^{(1)} + N_{ID}^{(2)}$. The PSS and SSS in each SSB remain the same, as they are solely determined by the N_{ID}^{cell}. On the other hand, PBCH and its Demodulation Reference Signal (DMRS) depend also on the SSB index i_{SSB} along with the cell ID N_{ID}^{cell}. Hence the UE needs also to identify the correct i_{SSB} index on the SSB that it synchronizes in order to have the correct DMRS sequence among the N_{SSB} possibilities. In this configuration $N_{SSB} \leq 64$. Note that in order to demodulate PBCH and to decode the Master Information Block (MIB), PBCH has to be descrambled with the correct N_{ID}^{cell} and i_{SSB}.

For the purpose of this study, the use of 5G frames that only contains SSBs is considered to focus on the DL synchronization performance, in other terms, it is an empty traffic model. A key aspect to be considered at the transmitted SSBs is the power allocation policy for the PSS, SSS and PBCH. Indeed, as PSS and SSS use a smaller bandwidth of 127 subcarriers, and as the OFDM symbols accommodating them within the SSB possesses respectively 113 and 17 empty resource elements, these signals can be amplified in order to normalize the expected value of the time domain signal power and to optimize the receiver SNR.

In the case of the considered empty traffic model, the power scaling coefficients of PSS, SSS and PBCH are set as $\beta_{PSS} = \frac{240}{127} \cdot \frac{N_{RB}}{20}$, $\beta_{SSS} = \frac{144}{127} \cdot \frac{N_{RB}}{20}$ and $\beta_{PBCH} = \frac{N_{RB}}{20}$, by leveraging the use of empty resources to increase the SSB's power. In an alternative scenario, where the OFDM symbols containing the SSB would also have to accommodate other traffic (e.g. PDSCH for system information), then these power allocation parameters would have to limit normalize the signal within the 20 RBs of the SSB with parameters $\beta_{PSS} = \frac{240}{127}$, $\beta_{SSS} = \frac{144}{127}$ and $\beta_{PBCH} = 1$.

This optimized power allocation is crucial for achieving reliable detection at the low SNR explored in sub-section 7.3.4.

7.3.3 NTN channel model

7.3.3.1 Geometrical and orbital model

For the LEO satellite channel behavior, a geometric propagation model is considered (***Figure 80***), inspired from the figure 6.3-1 of TR 38.811 [11], where the Earth is assimilated to a sphere and the satellite follows a circular orbit on the Oxy plane.

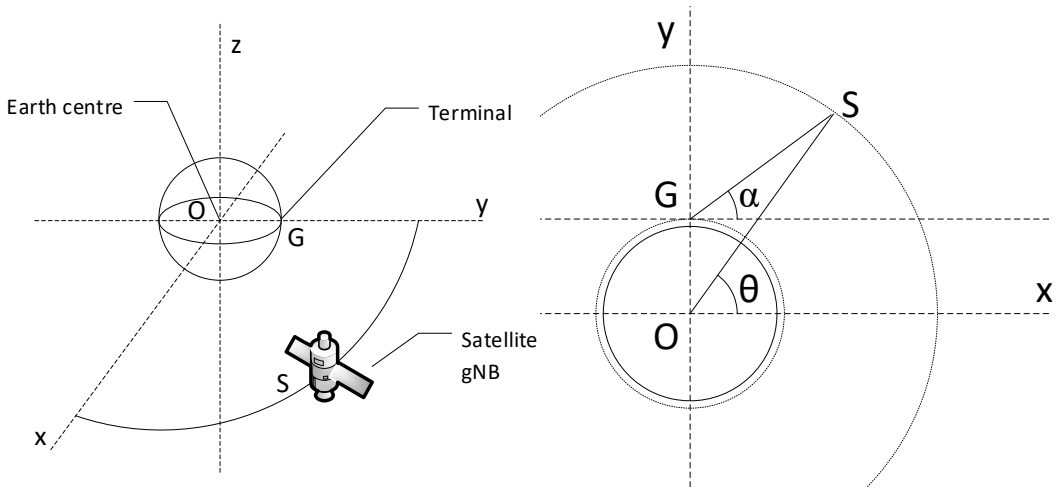

Figure 80: *geometry of the circular orbit and spherical earth model for ntn propagation channel*

We consider that the ground station/user terminal G is located at the coordinate $\boldsymbol{p_G} = (x_G, y_G, z_G) = (0, R_E + h_G, 0)$ where R_E is the Earth radius of 6371 km and h_G is the altitude of

the ground station/user terminal (locally, around G, we assume that the Earth radius is $R = R_E + h_G$). Let us also consider the satellite S's position, with an altitude of h_S and a latitude of θ, defined with respect to the Oxz plane, then $\boldsymbol{p_S} = (x_S; y_S; z_S) = \big((R_E + h_S)\cos(\theta)\,; (R_E + h_S)\sin(\theta)\,; 0\big)$. Let us define the relative altitude of the satellite as $H = h_S - h_G$, the relative position vector from G to S as $\boldsymbol{r}_C = \boldsymbol{p_S} - \boldsymbol{p_G}$ and the elevation of the satellite, with respect to G, as the angle α_G from the unit vector $(1, 0, 0)$ at point G, to the vector $\boldsymbol{r}_C$. Consequently, the slant range, which directly impacts the path loss, is defined as

$$d_C = \|\boldsymbol{r}_C\| = \frac{R + H}{\sin\left(\frac{\pi}{2} + \alpha\right)} \sin\left(\frac{\pi}{2} - \theta\right) = \sqrt{(R + H)^2 + R^2 - 2R(R + H)\cos\left(\frac{\pi}{2} - \theta\right)}.$$

By using these two expressions of the slant range d_C, one can establish the following one-to-one relationships between d_C, θ and α_G:

$$d_C = \sqrt{(R + H)^2 + R^2 - 2R(R + H)\sin\theta} = \sqrt{R\sin^2\alpha_G + H^2 + 2HR} - R\sin\alpha_G,$$

$$\alpha_G = \operatorname{acos}\frac{(R + H)\cos\theta}{\sqrt{(R + H)^2 + R^2 - 2R(R + H)\sin\theta}},$$

$$\theta = \operatorname{asin}\frac{R\cos^2\alpha_G + \sin\alpha_G\sqrt{(R\sin\alpha_G)^2 + 2RH + H^2}}{(R + H)}.$$

Finally, in order to incorporate the dynamics of the satellite movement, considering the third law of Kepler, the latitude of the satellite evolves as $\theta = \theta_0 + \omega_S t$ depending on time t, for a given initial latitude of θ_0, and with the angular velocity being defined as $\omega_S = \sqrt{GM_E/(R_E + h_0)^3}$.

7.3.3.2 Channel dynamics and Doppler model

With the model above, the propagation delay is given as

$$\tau_{prop} = \frac{d_C}{c} = \frac{\sqrt{(R + H)^2 + R^2 - 2R(R + H)\sin\theta}}{c},$$

with $c = 299792458$ m/s being the speed of light. Then the delay rate of the channel can be computed as

$$\frac{\partial\tau_{prop}}{\partial t} = -\frac{\omega_S R(R + H)}{c}\frac{\cos\theta}{\sqrt{(R + H)^2 + R^2 - 2R(R + H)\sin\theta}}.$$

Similarly, considering the Doppler frequency generated by the movement of the satellite is given by

$$f_D = \|\vec{\boldsymbol{v}}_{\boldsymbol{S,G}}\|\frac{f_c}{c}\cos\theta_p$$

where $\vec{v}_{S,G}$ is the relative speed of the satellite with respect to the NTN terminal and θ_p is the angle between direction of arrival (DoA) of the signal (i.e., vector $\boldsymbol{r}_C$) and $\vec{v}_{S,G}$. The relative speed vector is given as

$$\vec{\boldsymbol{v}}_{\boldsymbol{S,G}} = \vec{\boldsymbol{v}}_{\boldsymbol{S}} - \vec{\boldsymbol{v}}_{\boldsymbol{G}} = \frac{\partial\boldsymbol{p_S}}{\partial t} - \frac{\partial\boldsymbol{p_G}}{\partial t},$$

by considering that the terminal is static, to investigate first the impact of satellite movement, we have

$$\vec{\boldsymbol{v}}_{\boldsymbol{S,G}} = \frac{\partial \boldsymbol{p_S}}{\partial t} = (-\omega_S(R+H)\sin(\theta)\,;\,\omega_S(R+H)\cos(\theta)\,;\,0),$$

and $\left\|\vec{\boldsymbol{v}}_{\boldsymbol{S,G}}\right\| = \omega_S(R+H)$. Then the computation of the relative angle θ_p is given by

$$\begin{aligned}\theta_p &= \cos^{-1}\frac{\langle \vec{\boldsymbol{v}}_{\boldsymbol{S,G}}, \boldsymbol{r}_C\rangle}{\left\|\vec{\boldsymbol{v}}_{\boldsymbol{S,G}}\right\|\|\boldsymbol{r}_C\|}\\ &= \cos^{-1}\frac{-(R+H)\cos(\theta)\,\omega_S(R+H)\sin(\theta) + \big((R+H)\sin(\theta)-R\big)\omega_S(R+H)\cos(\theta)}{\omega_S(R+H)\sqrt{(R+H)^2+R^2-2R(R+H)\sin\theta}}\\ &= \cos^{-1}\frac{-R\cos(\theta)}{\sqrt{(R+H)^2+R^2-2R(R+H)\sin\theta}}.\end{aligned}$$

Thus, inserting this expression into the Doppler frequency formula, the Doppler shift generated by the satellite movement in this setup is given by

$$f_D = \frac{f_c}{c}\frac{-\omega_S R(R+H)\cos(\theta)}{\sqrt{(R+H)^2+R^2-2R(R+H)\sin\theta}}.$$

The corresponding Doppler rate at any time instant is computed by computing the derivative $\frac{\partial f_D}{\partial t}$.

To use this model effectively, the desired initial elevation angle $\alpha_{G,\text{init}}$ is provided as an input, which can be used to compute the corresponding initial latitude θ_0. Then the instantaneous latitude evolution is generated through $\theta = \theta_0 + \omega_S t$, which can be used to evaluate instantaneous values of α_G, d_C, τ_{prop} and f_D and their derivatives, through the formulae above.

Figure 81 illustrates the characteristics of a LEO orbit profile for $h_S = 600$km and $h_G = 0$ km for a carrier frequency $f_c = 37$ GHz.

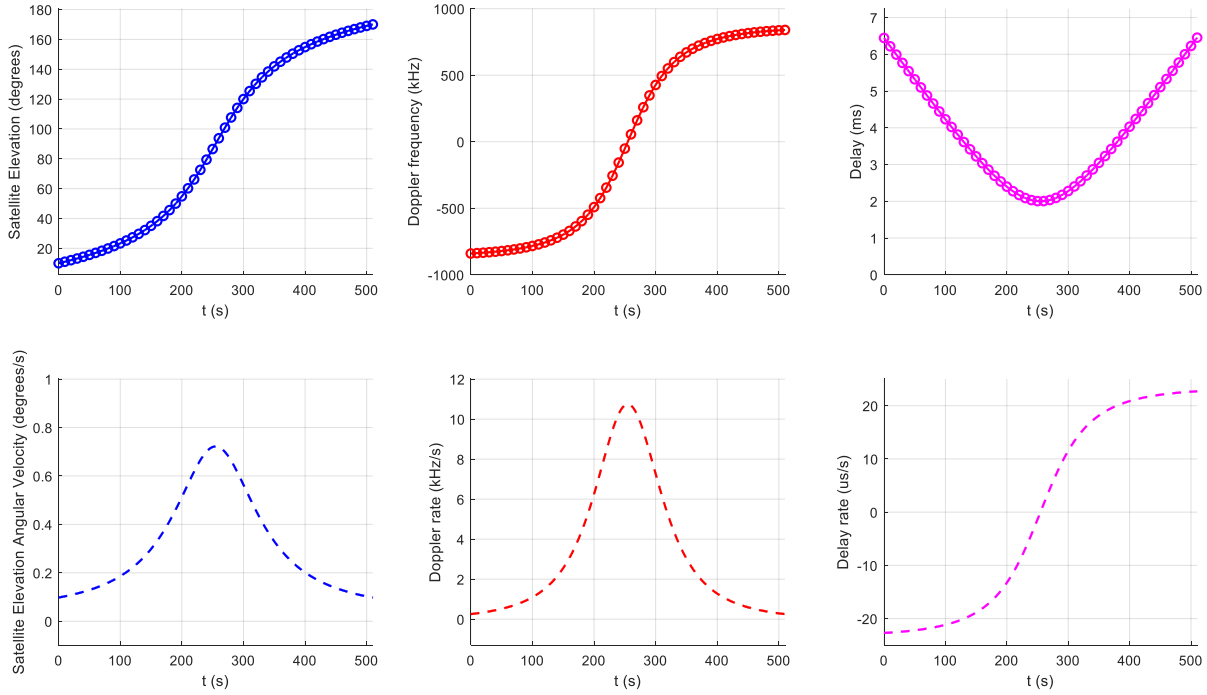

Figure 81: *Evolution of propagation parameters of a signal at 37 GHZ carrier frequency, transmitted from a satellite on a circular orbit of 600 km altitude on the oxy plane*

7.3.4 Receiver Design

7.3.4.1 Initial Access Problem Formulation

This study investigates the behavior of the initial DL synchronization step over the NTN channel where the propagation delay and the Doppler shifts are orders of magnitude higher that the values seen in conventional terrestrial use cases. The considered simulation setup is illustrated in ***Figure 82***.

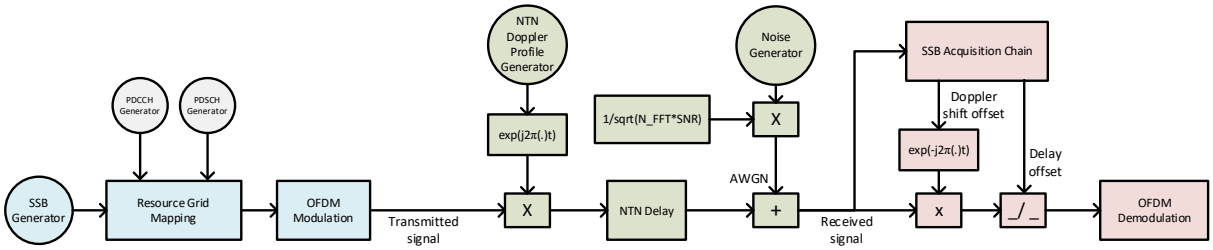

Figure 82: *Simulation setup for evaluating downlink synchronization in NTN channels*

The remainder of this subsection discusses the design of the SSB Acquisition Chain block, which will enable correcting the initial Doppler shift and delay offset of the received signal. In future work, algorithms inspired by this initial detection module could be used for the tracking phase, once the connection is established.

The generic framework of such a synchronization algorithm consists of:

- a set of N_{ref} reference signals to be used for detection, in its simplest form, in this context, it can be a PSS signal, it can be the burst of PSS signals, it can be similarly

a SSS signal or a set of SSS signals, or it can be a combination of PSS and SSS signals,

- in the general case when the Cell ID is unknown, there are different candidate reference sequences to be tested. For a set of reference signals consisting only of PSS signals there at most 3 candidates, for a set of reference signals including SSS, there can be up to 1008 candidates. However using the underlying properties of PSS and SSS, and using any additional architectural hypotheses on the beam and cell organization, the number of tentative references N_{ID} can be smaller.
- a listening window T_w over which a useful signal is expected, with its first sample being $n_0 \in [0, T_w F_{samp}]$, where F_{samp} is sampling rate,
- a set of M_{DC} Doppler cases over which the useful signal is scanned for, explicitly defined by a Doppler frequency step Δf_D, and the maximum expected Doppler frequency $f_{D,max}$, such that the case m corresponds to the frequency $f_m = m\Delta f_D$ with the integer $m \in \left[-\frac{M_{DC}}{2}, \frac{M_{DC}}{2}\right]$ with $M_{DC} = 2\left\lceil \frac{f_{D,max}}{\Delta f_D} \right\rceil + 1$.
- a criterion $C(n, m)$ which is used to locate the best sampling instant n_0 and the best Doppler case m_0,
- a threshold c_{th} to tune the false-alarm probability.

The listening window should be chosen to cover at least N_{ref} SSB bursts, in addition to the expected amount of delay incertitude. It also has to leverage receiver complexity (e.g., battery consumption for a terminal) and the maximum initial acquisition latency. For ground stations with high processing capabilities, one can use very large listening windows with a good amount of buffering for real-time processing during the initial acquisition. On the other hand, for the user terminals, it is rather smarter to listen to small chunks of signals, and in case of non-detection, the listening window can be shifted with incremental time-offsets, in order to align with the reference signals, depending on the SSB transmission periodicity of the system. This concept is illustrated in ***Figure 83***, where the SSB burst periodicity is of 20 ms, and the terminal uses a listening window of 5 ms (which is already very high, but chosen for practical for illustrative purposes), and the at each SSB periodicity, the terminal shifts its listening window by an additional 5 ms.

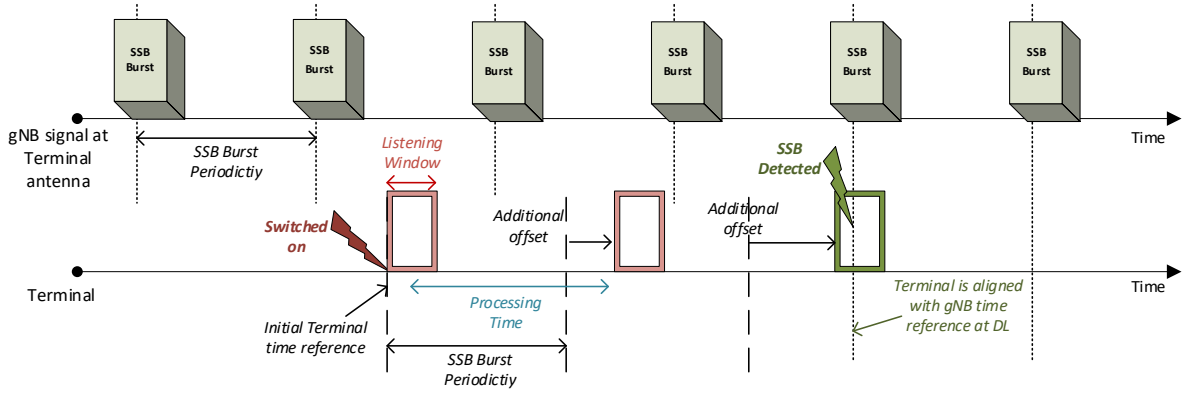

Figure 83: *Initial acquisition with time-shifted listening windows*

7.3.4.2 Fundamental Detection Criteria

In this study, two criteria are considered for reference detection and tracking: the normalized cross-correlator (XCORR) and the generalized likelihood ratio test (GLRT) algorithms.

Let us consider that there are N_{ref} reference sequences of length K_{ref}, located at samples p_l, $l = 1, \dots N_{ref}$ of the transmitted signal, and denoted $r_{k,l}[i_{id}], k = 1, \dots, K_{ref}$, with $i_{id} = 1, \dots, N_{ID}$ being the number of candidate reference signals. Let us denote the received signal x_k, and introduce the Dopplerized reference sequence $r_{k,l,m}[i_{id}] = r_{k,l}[i_{id}] \cdot e^{\frac{j2\pi f_m k}{Fsamp}}$, with $f_m = m\Delta f_D$ and $m = -\frac{M_{DC}}{2}, \dots, \frac{M_{DC}}{2}$.

The expression of these criteria are as follows [140][141]:

$$C_{\mathrm{XCORR}}(n, m, i_{id}) = \frac{1}{N_{ref}} \sum_{l=1}^{N_{ref}} R_{d,l}[i_{id}]^{-1} \hat{R}_{xr,n,l,m}[i_{id}],$$

$$C_{\mathrm{GLRT}}(n, m, i_{id}) = R_d[i_{id}]^{-1} \sum_{l=1}^{N_{ref}} \hat{R}_{xr,n,m}[i_{id}]^* \hat{R}_{x,n}^{-1} \hat{R}_{xr,n,m}[i_{id}],$$

where the auto-correlation corresponding to the l^{th} reference signal position of x_k and $r_{k,l}[i_{id}]$ are given by $\hat{R}_{x,n} \triangleq \sum_{l=1}^{N_{ref}} \sum_{k=1}^{K_{ref}} x_{n+p_l+k} x_{n+p_l+k}^*$ and $R_d[i_{id}] \triangleq \sum_{l=1}^{N_{ref}} \sum_{k=1}^{K_{ref}} r_{k,l}[i_{id}] r_{k,l}^*[i_{id}]$, and the cross-correlation between them is $\hat{R}_{xr,n,m}[i_{id}] \triangleq \sum_{l=1}^{N_{ref}} \sum_{k=1}^{K_{ref}} x_{n+p_l+k} r_{k,l,m}^*[i_{id}]$. Note that, in order to reduce the sensitivity to noise, these quantities have been computed over N_{ref} references, which has an averaging effect over time.

In the considered single-antenna scenario, these two criteria yield the same peak, but they still have different sensitivity to the frequency errors, and different false alarm distributions. Hence Doppler case sizes and the false-alarm threshold depend on the choice of criterion. Moreover, the GLRT criterion naturally incorporates a noise variance estimator, which has two major advantages:

- it yields a constant false alarm rate (CFAR) detector, hence the false alarm detection can be performed through a constant threshold,
- it can enhance detection performance if the received signal is filtered down to the bandwidth of the reference signal, which is the case of PSS and SSS signals, compared to the bandwidth of the OFDM grid. This aspect will be discussed in the next paragraph.

On the other hand, the GLRT requires much more computational complexity, compared to the XCORR.

7.3.4.3 Doppler Case Analysis

In Figure 84, the behavior of the criteria above as a function of residual frequency error is plotted for different number of SSBs used for the criterion computation ($N_{ref} = 1,2,3,4$), and for the case of using PSS/SSS only (left side of ***Figure 84***) versus PSS and SSS (right side of ***Figure 84***).

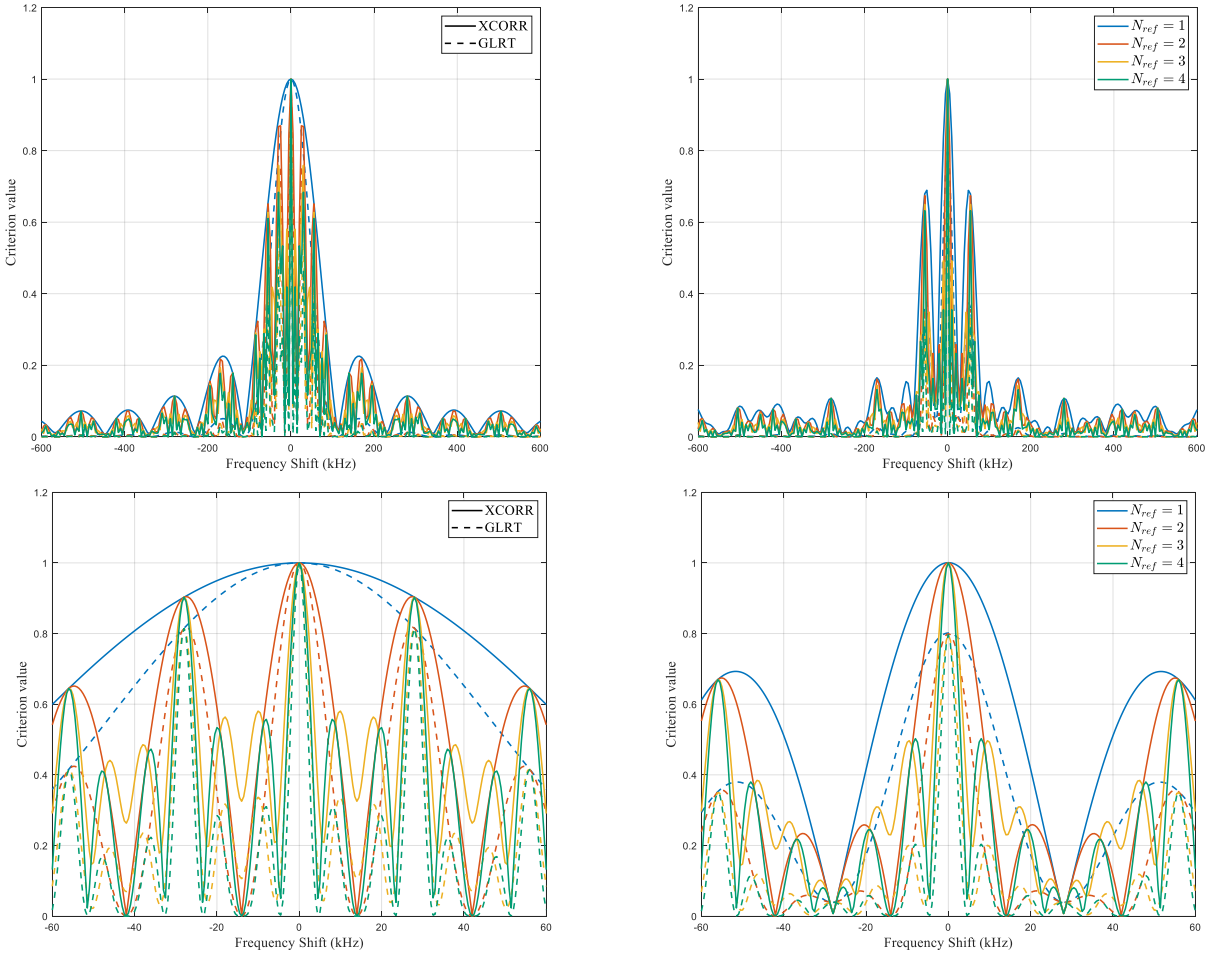

Figure 84: *Comparison of XCORR and GLRT criteria as a function of frequency shift, for $N_{ref} = 1, \ldots 4$ reference sequences, with a PSS or SSS sequence at left, or with a PSS and SSS sequence at right*

The first major observation is that the use of a single PSS as a reference yields to widest correlation peak, which is an attractive shape for an initial coarse acquisition of time and frequency, from a computational complexity point of view. The use of both PSS and SSS, with possibly multiple SSBs yield much more selective correlation peaks, with multiple ambiguities, which can be used in a second step, to further refine the delay and Doppler offset estimates, on smaller search windows.

In the following, the dimensioning of the number of Doppler cases M_{DC} is discussed quantitatively, through the analysis of the Doppler step Δf_D and the maximum Doppler shift $f_{D,max}$.

The sensitivity of these criteria can be used to select the desired Doppler step Δf_D, which determines the search resolution, by computing the value of the frequency offset which causes a phase shift $\Delta\varphi_{\text{MAX}} = 60°$ on the received signal. Indeed as $\cos(60°) = 0.5$, such a limit on phase shift ensures that reference signal's sign remains consistent over the correlation window, ensuring that these criteria remain approximately close to their peak, despite the residual frequency offset. Thus we have

$$\Delta f_D \triangleq \frac{\Delta\varphi_{\text{MAX}}}{2\pi\left(p_{N_{ref}} - p_1 + K_{ref}\right)} F_{samp},$$

and values of the Doppler case resolution is given in Table 31 for different reference signal configurations. In the case of PSS and SSS the sample offset between the PSS and SSS is added to the denominator, to keep the frequency variation constant. These values loosely

determine the region around the peak where either XCORR or GLRT remain above a value of 0.8-0.9.

Table 31: *Approximate Doppler case resolution of the XCORR or GLRT criteria, as a function of number of reference sequences, for references that consist either of PSS or SSS, or of PSS and SSS*

Δf_D	$N_{ref} = 1$	$N_{ref} = 2$	$N_{ref} = 3$	$N_{ref} = 4$
PSS or SSS only	18.69 kHz	3.74 kHz	1.44 kHz	1.1 kHz
PSS and SSS	6.23 kHz	2.67 kHz	1.25 kHz	0.98 kHz

The maximum value of the Doppler offset is obtained by combining the expected maximum local oscillator impairments $\Delta_{LO,UE}$ and $\Delta_{LO,gNB}$, the maximum terminal speed $v_{MAX,UE}$, and the peak Doppler frequency $f_{Dopp,Sat}$ caused by the satellite orbit. Hence

$$f_{D,max} = \left(\Delta_{LO,UE} + \Delta_{LO,gNB} + \frac{v_{MAX,UE}}{c}\right) f_c + f_{Dopp,Sat}.$$

According to TS 38.101-5 [3], $\Delta_{LO,UE} = 0.1$ppm and according to TS 38.108 [142] $\Delta_{LO,gNB} = 0.05$ppm, while $v_{MAX,UE} = 1000$km/h in the worst-case aircraft scenario from the deployment 4 scenario of TR 38.811 [11]. Finally for carrier frequency $f_c = 37$ GHz with 600 km orbit, the maximum Doppler shift caused by the satellite is $f_{Dopp,Sat} = 852$kHz, through the evaluations on the NTN channel in the previous subsection. Combining these values yield $f_{D,max} = 892$kHz.

Hence the number of Doppler cases needed to cover the maximum possible Doppler shift with various reference signal configurations is provided in Table 32.

Table 32: *Approximate number of required Doppler cases to detect a 3GPP 5G NR signal with no intiial guess in a Q-band NTN channel with OnBOARD LEO gNB at 600 km altitude*

N_{DC}	$N_{ref} = 1$	$N_{ref} = 2$	$N_{ref} = 3$	$N_{ref} = 4$
PSS or SSS only	97	479	1241	1623
PSS and SSS	289	671	1429	1823

Given the high number of frequencies to test, we propose to split the detection phases in two, with the first stage consisting in PSS only correlations with a single reference SSB over the whole Doppler case range, and the second stage in using a combined PSS and SSS correlations over a smaller Doppler offset range. After the first stage, we can remove the ambiguity on $N_{ID}^{(2)}$ and get the frequency error below 2×18.69 kHz by compensating the frequency corresponding to the peak of the criterion. Then we can compute a new set of Doppler cases with $f_{D,max,2} = 18.69$ kHz, which yields the much affordable number of Doppler cases $N_{DC,2}$ in ***Table 33***.

Table 33: *Approximate number of required Doppler cases for fine detection stage, over the reduced range of +- 18.69 kHz for refining Doppler shift estimation*

$N_{DC,2}$	$N_{ref} = 1$	$N_{ref} = 2$	$N_{ref} = 3$	$N_{ref} = 4$
PSS and SSS	7	11	27	35

7.3.4.4 False Alarm Probability Analysis

An equally important aspect of these criteria is their false alarm detection behavior. If these criteria are used without any checks, they might detect peaks even in the absence of a useful signal, which is undesirable for optimizing the battery consumption. Thus, a threshold η to

discard potential false detections is required, and it has to be turned to achieve a desired rate of false alarm.

Denoting the presence of signal as $\mathcal{H}_1$ and absence of the signal as $\mathcal{H}_0$, the false alarm probability of these criteria are characterized [140][141] as

$$\mathbb{P}(C_{\mathrm{XCORR}}(n,m,i_{id}) > \eta \mid \mathcal{H}_0) = \exp\left(-\eta \frac{E_s}{\sigma_n^2}\right),$$

$$\mathbb{P}(C_{\mathrm{GLRT}}(n,m,i_{id}) > \eta \mid \mathcal{H}_0) = (1-\eta)^{L_{ref}-1},$$

where $E_s = \mathrm{tr}(R_d)$, σ_n^2 is the AWGN noise variance and L_{ref} is the total number of reference samples, which in our case is $L_{ref} = N_{ref}N_{sym}$ with N_{sym} being the CP-extended OFDM symbol length, in the case where PSS or SSS signal is used as a reference signal. In the case where both PSS and SSS is used, $L_{ref} = 2N_{ref}N_{sym}$

Hence, the use of XCORR requires a noise variance estimator, either over the empty subcarriers, or through another heuristic method when the gNB is absent, whereas GLRT has a much simpler PFA expression for tuning the threshold, as it is independent of the SNR.

7.3.4.5 Proposed Two-Stage Synchronization Architecture

Based on the preliminary analyses of detection criteria, this paragraph discusses the selected SSB Acquisition Chain architecture, illustrated in ***Figure 85***.

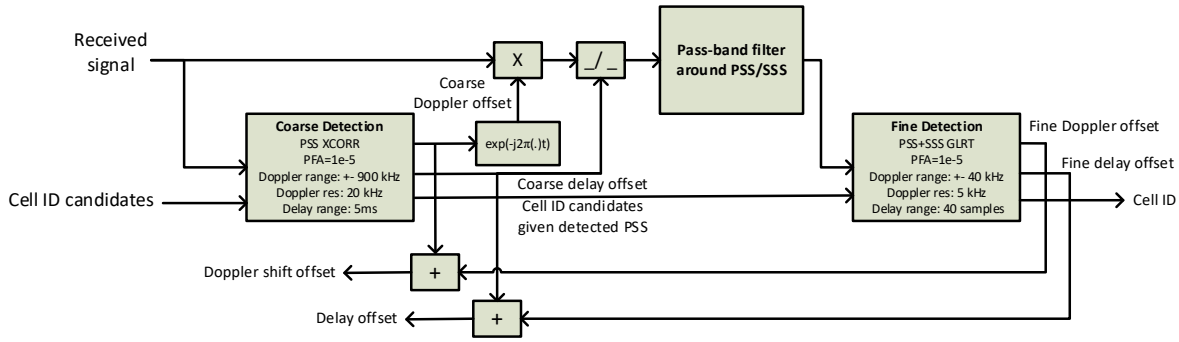

Figure 85: *Proposed receiver architecture*

As revealed through the Doppler case analysis, it is preferable to combine an initial coarse detection stage based solely on the PSS as a reference, with a second fine detection stage based on both PSS and SSS, over possible multiple SSBs, for further refining the Doppler shift estimation quality, while keeping a moderate complexity.
Specifically, the first stage can be carried out with the XCORR criterion, which has the advantage of complexity, especially when implemented through an FFT-based algorithm, as it has to cover a wider range of delay offset and Doppler offset ranges. This stage needs to test the received signal against the three PSS sequences, one for each of candidate values of $N_{ID}^{(2)} = 0,1$ and 2.
Next, we propose the use of pass-band filtering stage between the coarse and fine detection stages, with a bandwidth just enough to accommodate PSS and SSS signals, which can improve the selectivity of the GLRT criterion that can be used in the fine detection stage. In this second stage, there can be up to 336 PSS and SSS sequences to be used for identifying the cell ID at the initial search. Moreover, network/system design can restrict this set, for instance geographically, or if the modem is attempting a reconnection after a signal loss, this search set can be much smaller.

It is also important to note that the use of the pass-band filter changes the computation of the PFA with relation to the threshold for GLRT, as the noise within the signal bandwidth is no longer white. In this case, it can be empirically shown that $\mathbb{P}(C_{\text{GLRT}}(n,m,i_{id}) > \eta \mid \mathcal{H}_0) \approx (1-\eta)^{(L_{ref}-1)\frac{N_{sc,\text{filt}}}{512}}$ where $N_{sc,\text{filt}}$ is the pass-band bandwidth of the filter.
The effective parameters of the coarse and fine detection modules are as follows:

- the coarse detection step operates over 91 Doppler cases, from -900 kHz to 900 kHz with 20 kHz steps (rounding up the estimated value of 18.69 kHz), and the detection threshold is set such that a PFA of 10^{-5} is achieved. The receiver is assumed to know the true noise variance for this threshold computation. This first stage can operate over a listening window of 5 ms.
- the pass-band filter is a finite impulse filter designed with the Parks-McClellan technique, with passband ripple of less than 0.1 dB and a stop band attenuation of -40 dB, with pass-band limited to ± 63 subcarriers and stop-band starting from $\pm$ 70 subcarriers. This yields a 155-tap impulse response with approximately 75-tap delay, which is compensated at the filtering stage,
- the fine detection step operates over 17 Doppler cases, from -40 kHz to 40 kHz (a factor of 2 is added to the previous analysis to ensure no peak is missed) with 5 kHz steps, and the detection threshold is set such that a PFA of 10^{-5} is achieved. This stage seeks the peak within ± 20 samples of the peak detected by the coarse detector.
- the fine detection can use $N_{ref} = 1, \dots N_{SSB}$ couples of PSS and SSS as a reference signal, when $N_{ref} = 1$, the Doppler step remains $\Delta f_D = 5$ kHz, however $N_{ref} = 2, \Delta f_D = 2.5$ kHz and for $N_{ref} = 4, \Delta f_D = 1$ kHz. Naturally, the number of Doppler cases increase accordingly.

7.3.5 Numerical Results

7.3.5.1 Simulation Setup

For the numerical simulation, within the scope of hypotheses considered in the paragraphs above, the following are assumed:

- the SSB burst consists of $N_{SSB} = 4$ blocks,
- the NTN channel is simulated for an elevation of $\alpha_G = 10°, 30°, 45°$ and $90°$,
- in order to limit the simulation length, the signal delay with respect to the receiver is set uniformly randomly up to 0.2 ms, corresponding to over 12200 samples of delay. Accordingly the search range of the coarse detection algorithm is limited down to 0.5 ms instead of 5 ms for simulation purposes.
- 10000 Monte Carlo snap-shots of the received signal are simulated.

Note that the argument for the limitation of the delay search range, or even the Doppler search range has also a practical basis, as there are pre-compensation techniques, at the satellite side, for reducing the synchronization complexity at the terminal, as illustrated in Figure 86 [145].

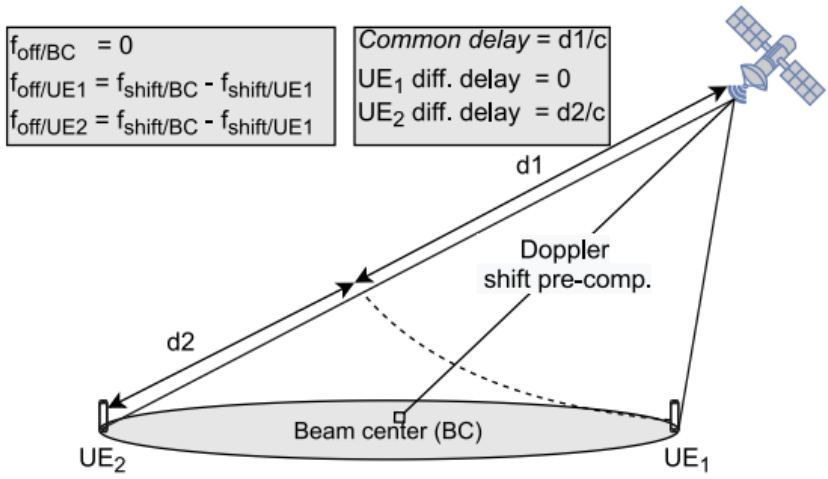

Figure 86: *Doppler and delay pre-compensation strategy for NTN*

7.3.5.2 Single SSB Detection: Coarse vs. Fine Stage Performance

Evaluating the probability of detection at the output of the coarse detection stage and the fine detection stage reveals that the satellite elevation has less than 0.5 dB impact on the detection performance. Indeed, for a target probability of non-detection (PND) of 10^{-2}, PSS detection is achieved for a SNR within -11.5 dB and -11.3 dB. Similarly the cell ID detection (PSS and SSS) at the fine detection stage is achieved with a PND of 10^{-2} for a SNR of within -9.5 dB and -9.0 dB.
This behavior is illustrated as the probability of detection in the linear domain in FIGURE 87 and as the PND in the log-domain in the FIGURE 88.

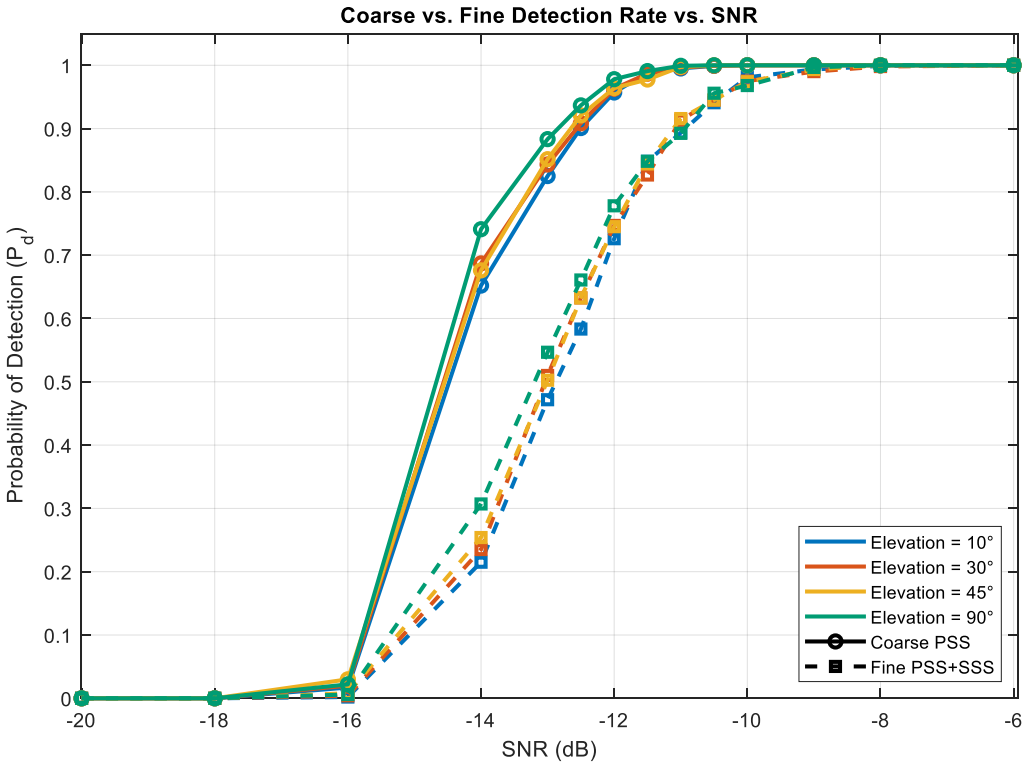

Figure 87: *Estimated probability of detection of $N_{ID}^{(2)}$ (coarse) and of N_{CellID} (fine)*

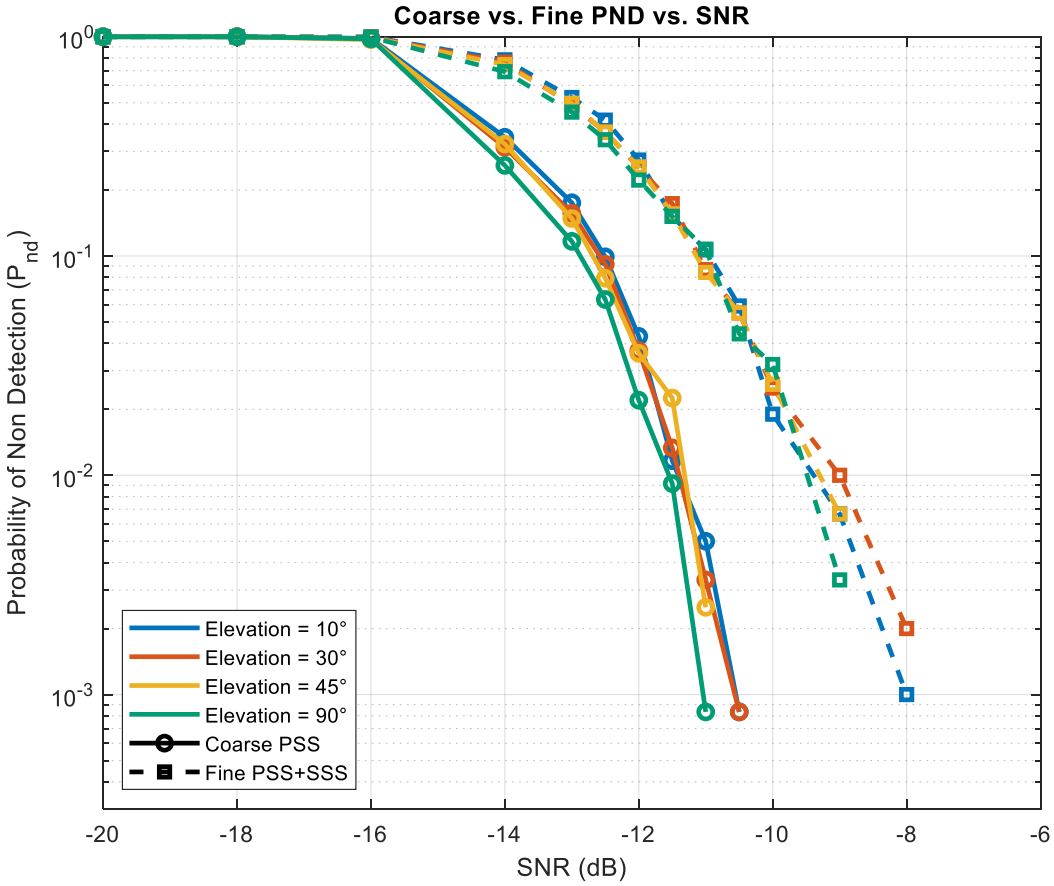

Figure 88: *Estimated probability of non-detection of $N_{ID}^{(2)}$ (coarse) and of N_{CellID} (fine)*

The precision of the detection algorithms by evaluating the root mean square error (RMSE) of the delay estimate and the Doppler estimate, among the samples which have been detected successfully. These metrics have been plotted in the FIGURE 89 below.

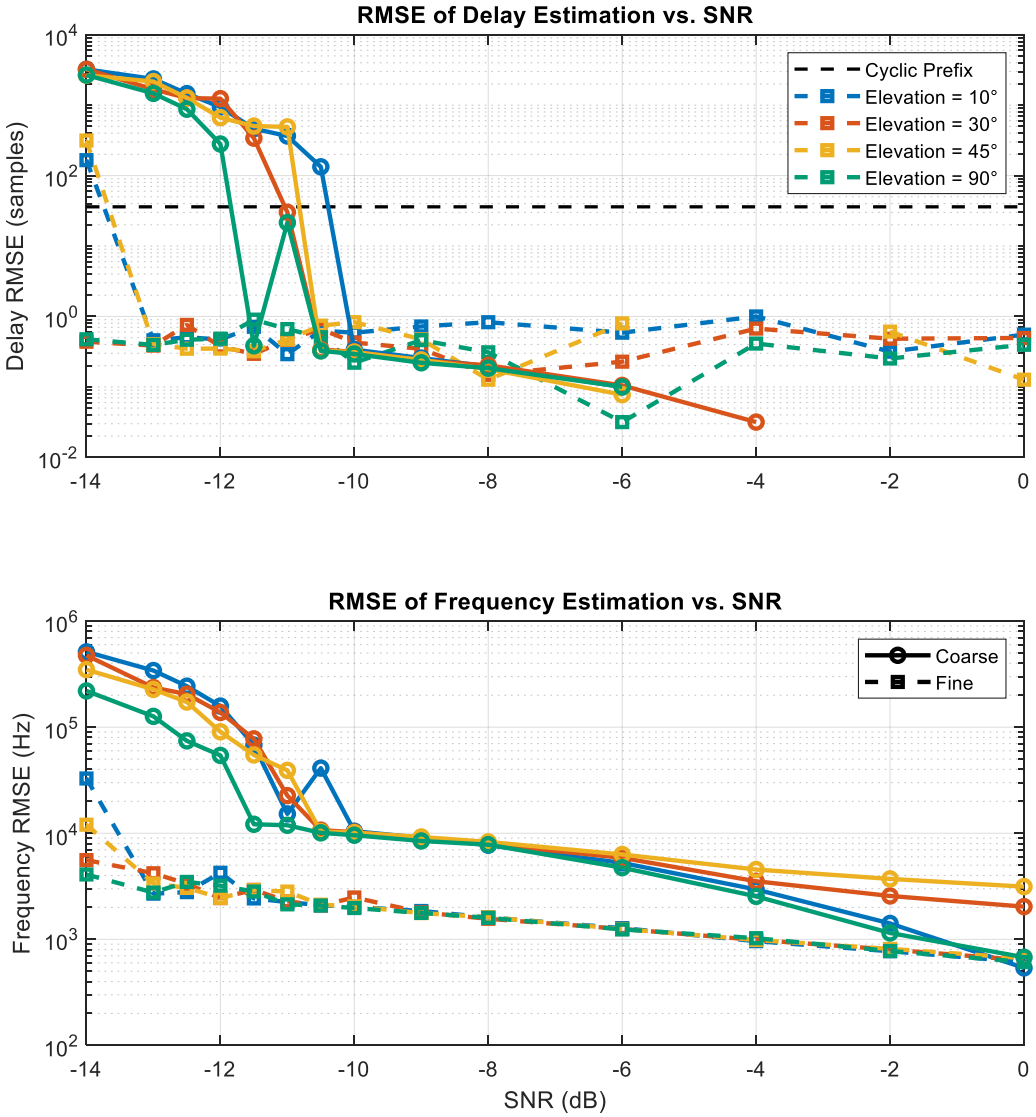

Figure 89: *Estimated RMSE of delay and Doppler shift*

Notice that the fine detection stage brings a significant improvement over the Doppler frequency estimation RMSE, with less than 1 kHz, i.e. 0.03 ppm of error above -6 dB. The fine detection is slightly perturbed when considering the delay estimation, due to parasitic peak shifts likely caused by the pass-band filter, however as the number of errors are very small for 1000 Monte Carlo trials, the value of delay offset RMSE is not precise above -8 dB. Nevertheless, these errors of less than a sample in average, remains much lower than the CP length, which ensures successful synchronization.

7.3.5.3 Multiple SSB Detection

The synchronization performance of this received could be improved by increasing the complexity of the fine detection stage, by using more than a single SSB as the reference signal, with $N_{ref} = 2$ or $N_{ref} = 4$. ***Figure 90*** illustrates the PND averaged over different elevations for different number of N_{ref} sequences used in the fine detection stage. It can be seen that the PND of cell ID detection reaches the PND of PSS detection from the coarse stage, with an effective gain of around 2 dB to achieve a PND of 10^{-3}. Indeed, $N_{ref} = 2$ is sufficient to reach this performance gain.

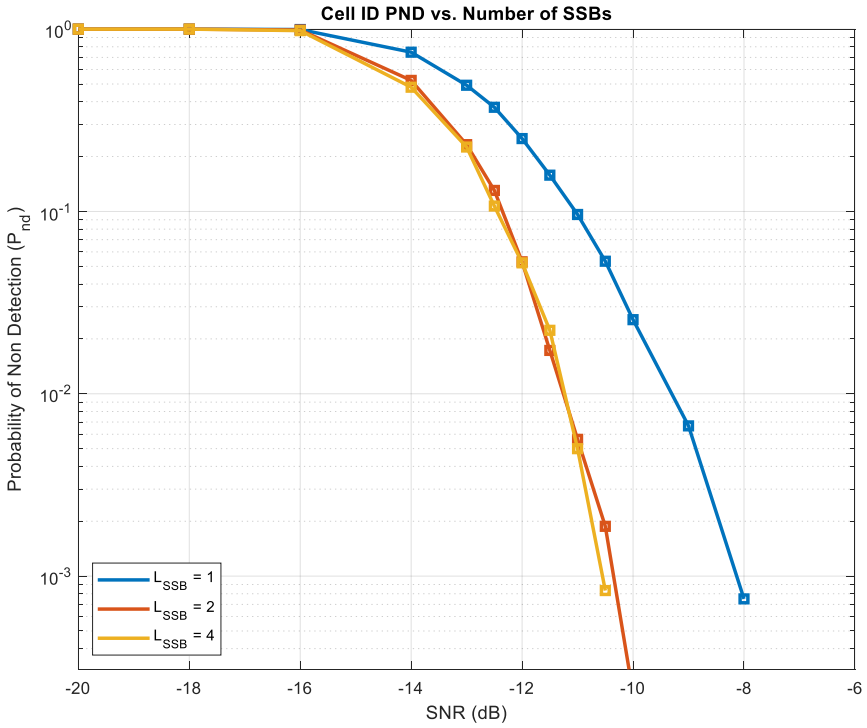

Figure 90: *Probability of non-detection for more than one SSBs*

This advantage of multiple-SSB detection can also be seen from a fixed SNR perspective, as a certain percentage of gain the detection rate, as illustrated in ***Figure 91***.

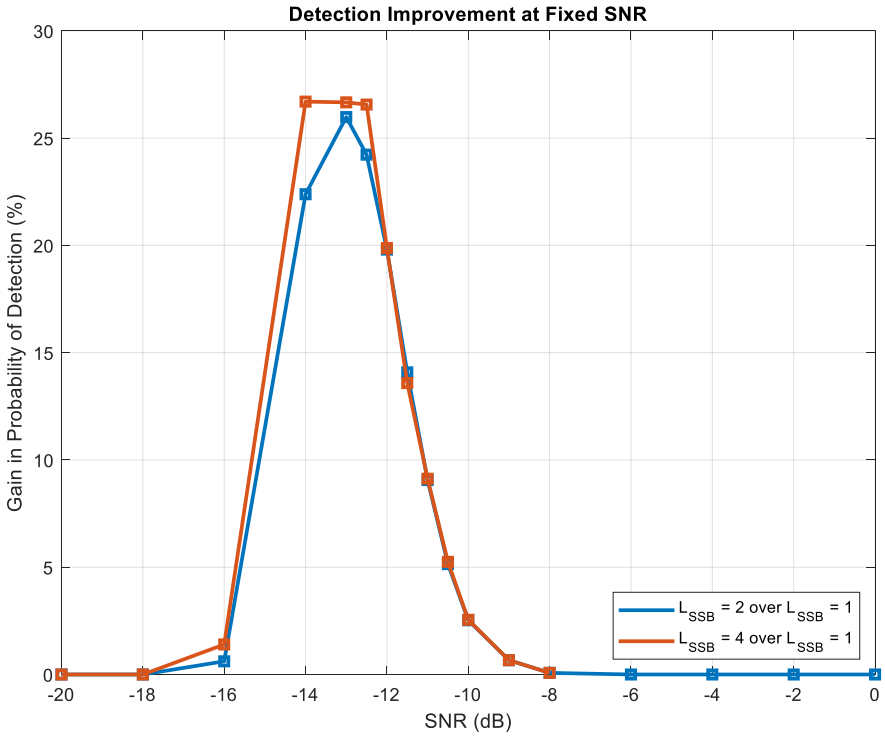

Figure 91: *Improvement in the rate of detection for more than one SSBs at fixed SNRs*

Hence the use of 2 SSBs for the fine detection stage can bring either 2 dBs (i.e. 58%) improvement on the detection SNR (or equivalently in the required transmit power at the satellite), or as a gain of between 10-25% between -15 and -11 dB SNR region.

The RMSE of the delay and Doppler estimates is also evaluated and plotted in the FIGURE 92, where it is noted that while there is not much improvement on the delay estimate, the Doppler shift estimate is significantly improved, reaching a RMSE of about 0.003 ppm for an SNR of -8 dB and $N_{ref} = 4$.

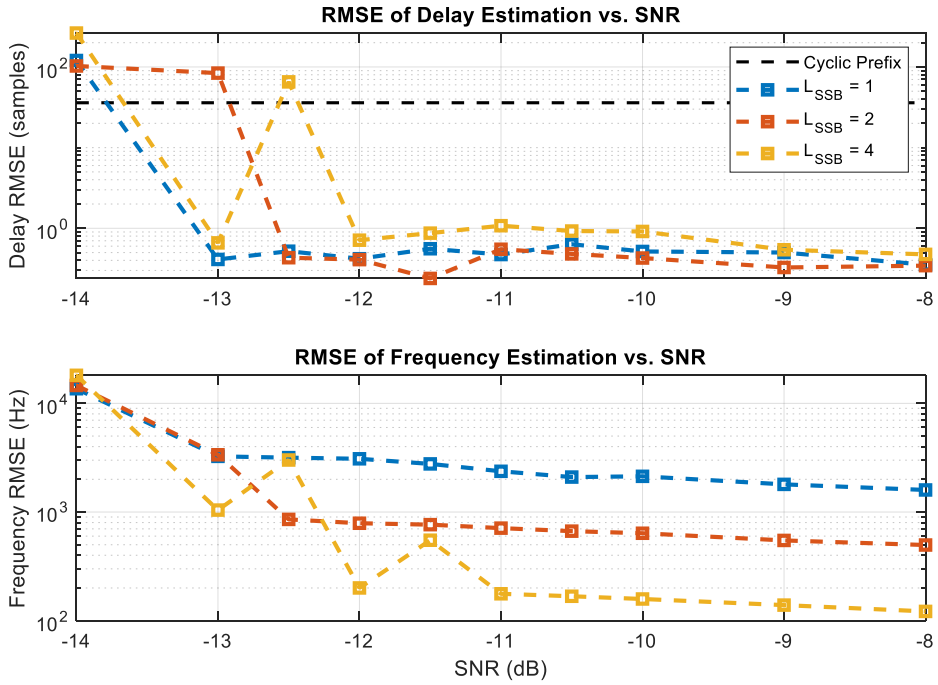

Figure 92: *Estimated RMSE of delay and doppler shift for multiple Ssbs*

This finding highlights a critical design trade-off, demonstrating that a significant 2 dB performance gain is achievable by doubling the reference signal length, while further increases (e.g., to $N_{ref} = 4$) yield no significant returns. A configuration using $N_{ref} = 2$ therefore represents a compelling balance between performance and computational load for a practical terminal implementation of this architecture, unless more precision on the Doppler shift estimate is needed for other reasons.

7.3.6 Conclusion and Perspectives

This study addressed the critical challenge of initial downlink synchronization for 5G NTN systems operating in the future Q/V-band. The combination of high carrier frequencies and the orbital dynamics of LEO satellites creates extreme Doppler shifts approaching ± 850 kHz, which poses a significant hurdle for standard signal acquisition procedures. To overcome this, we designed and evaluated a two-stage hierarchical synchronization strategy tailored to these demanding conditions. The proposed architecture first performs a wide, computationally efficient coarse search using a PSS-based cross-correlator followed by a highly selective fine synchronization stage that leverages both PSS and SSS with a GLRT-based criterion for improved accuracy.

Numerical simulations confirmed the viability of this approach. The fine detection stage was shown to significantly improve Doppler estimation, achieving a RMSE of less than 1 kHz at an SNR of -6 dB. Our results also revealed that while satellite elevation has a small impact on

detection performance, the number of SSBs used in the fine stage is critical. Coherently combining just two SSBs was sufficient to achieve a 2 dB performance gain, effectively closing the gap between coarse PSS detection and reliable Cell ID acquisition. This finding presents a flexible option to achieve trade-off between performance and complexity for practical receiver design.

Future work could extend this framework to the connected-mode tracking phase and investigate the combined impact of Doppler with other channel impairments prominent in the Q/V band, such as atmospheric scintillation and rain fade. There can be also further investigations on the receiver architecture, to improve the PND of the coarse detection step, which may lead to further improvements at low SNR operation.

7.4 UPLINK SYNCHRONIZATION

In this section, we address two solutions to allow the UE uplink synchronization without the GNSS. The first one aims to identify the most suitable signal for the calculation of the UE position during the downlink synchronization. Indeed, if the UE knows its own position along with the satellite ephemeris by means of the SIB 19, it can pre-compensate delay and Doppler shift, as it currently happens in Rel.19. Therefore, minimal modifications to the standard are envisioned. This analysis applies to CP-OFDM. The second analysis concerns the assessment of the robustness of the random-access scheme, in particular it focuses on a new preamble design for OTFS.

7.4.1 Comparison between SSB and PRS

In the following sections of this document, we aim to evaluate the performance of two candidate signals to allow the computation of the UE position during the initial access, before the uplink synchronization. The comparison is done in terms of their autocorrelation properties. This analysis is essential to determine the intrinsic capability of each signal to enable accurate estimation of two key parameters: the exact time of arrival and the carrier frequency. It is worth mentioning that in the current standard PRS is not a broadcast signal.

Assessing these candidates through their autocorrelation properties is only a partial approach, and it is important to keep in mind that full synchronization—necessary for range determination—relies on additional information, particularly the exact transmission time of the signal. In practical scenarios, this timing reference is often unknown or difficult to acquire, which means that our evaluation does not address all the challenges associated with achieving true synchronization at the satellite level for accurate range and RTT calculations. Nevertheless, this represents a first step in the process and allows us to eliminate signals that are fundamentally unsuited for these applications.

7.4.1.1 5G NR signal ranging performance and associated procedures

7.4.1.1.1 Ambiguity function

The ambiguity function can be seen as a 2D autocorrelation function including the Doppler shift. For the present case, the approximation of the narrow-band ambiguity function will be used according to the following equation. Indeed, the Doppler effects on the signal $s(t)$ are neglected and only phase effects are taken into account, which is reasonable for low ratios of Doppler on the total bandwidth of the signal.

$$\chi(\tau,\nu) = \int_{-\infty}^{+\infty} s(t).s^*(t-\tau)e^{i2\pi\nu t}dt$$

Note that the ideal ambiguity function is a Dirac in both delay and Doppler domain at 0.0. Time/frequency relations allows to rewrite the autocorrelation function as inverse Fourier transform of the signal power spectral density:

$$\chi(\tau) = s(t) * s^*(-t) = \mathcal{F}^{-1}\{S(f)S^*(f)\} = \mathcal{F}^{-1}\{|S^2(f)|\}$$

Knowing that inverse Fourier transform of a rectangular function is a cardinal sinus, the ambiguity function may be seen as dual cardinal sinus over delay and Doppler. Indeed, the first nulls are placed at 1/BW and 1/Tint where BW is the total signal bandwidth (rectangular function in the frequency domain) and Tint the integration time (rectangular function (slots) in the time domain).

7.4.1.1.2 Positioning Reference Signal (5G PRS)

PRS works by providing time-stamped reference signals at known locations, enabling devices to measure signal characteristics like time of arrival or signal strength from multiple base stations. These measurements are then processed (often using techniques such as Time Difference of Arrival or Angle of Arrival) to accurately estimate the device's position.

Figure 93 illustrates the influence of the two parameters studied in this part, K_{comb} and the number of OFDM symbols, on PRS resource element allocation.

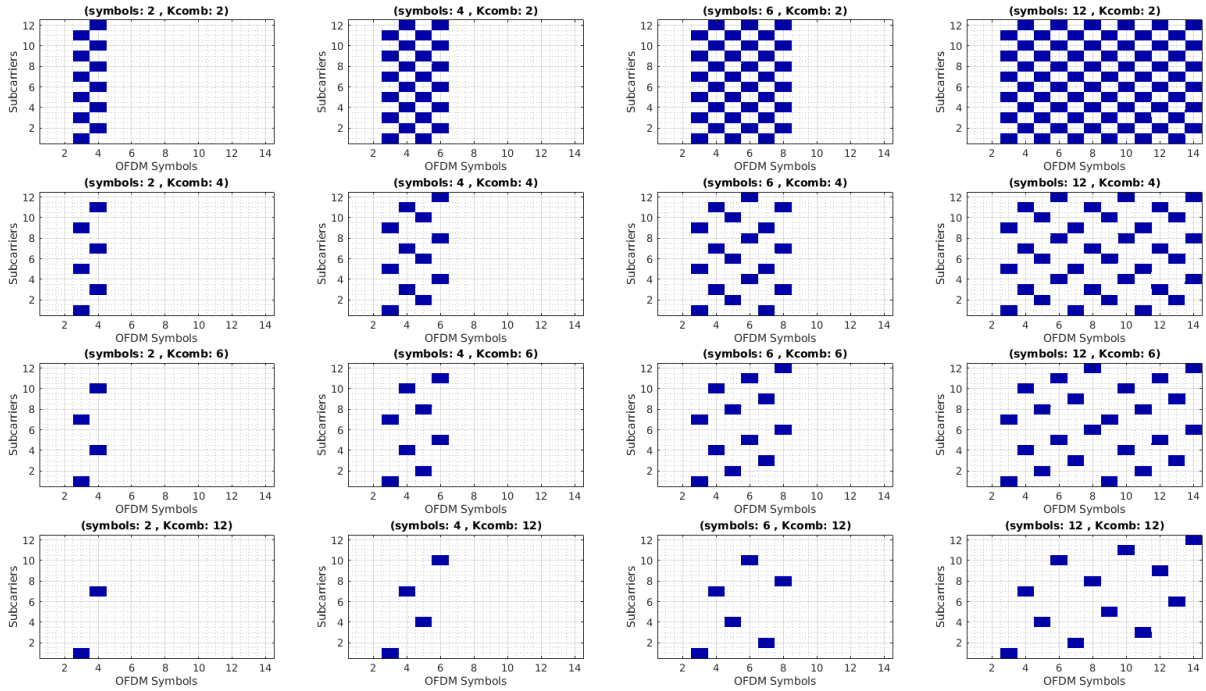

Figure 93: *PRS resource element allocation as a function ok K_comb and number of symbols*

The auto and intercorrelation properties of the PRS signal are explored in the following part where the main simulation parameters used are recalled in

Table ***34***.

Table 34: *Carrier and PRS simulation configuration*

Carrier	**Spacing**	**30kHz**		**PRS**	N_{symb}	**12**
	NSizeGrid	20 PRB			K_{comb}	2
	Slot	2			PRS id	10, 11

To give rough orders of magnitude, still simplistic, with respect to typical GNSS systems performances including standard processing's, the final user position error is about one order of magnitude below the actual signal correlation resolution, e.g., GPS C/A, correlation resolution is 300m while the final user position is below 30m. Targeting 1m of final user error position in the frame of 5G positioning would suggest a correlation resolution of about 10m corresponding to ~20 PRB for μ=3 or ~80 PRB for μ=1 (~30MHz of total signal bandwidth).

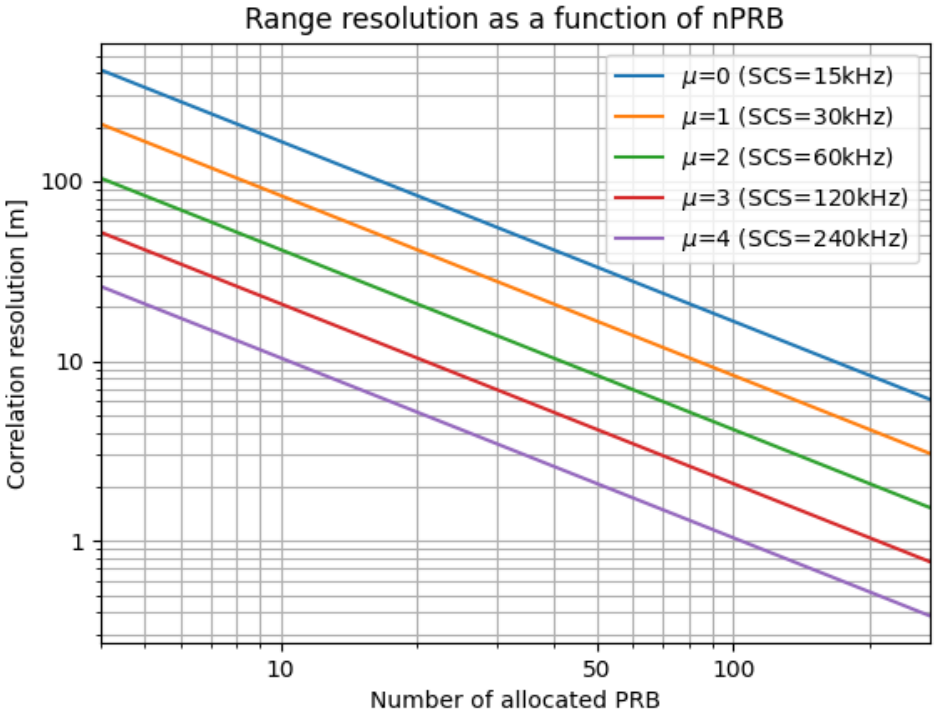

Figure 94: *Correlation resolution as a function of PRB*

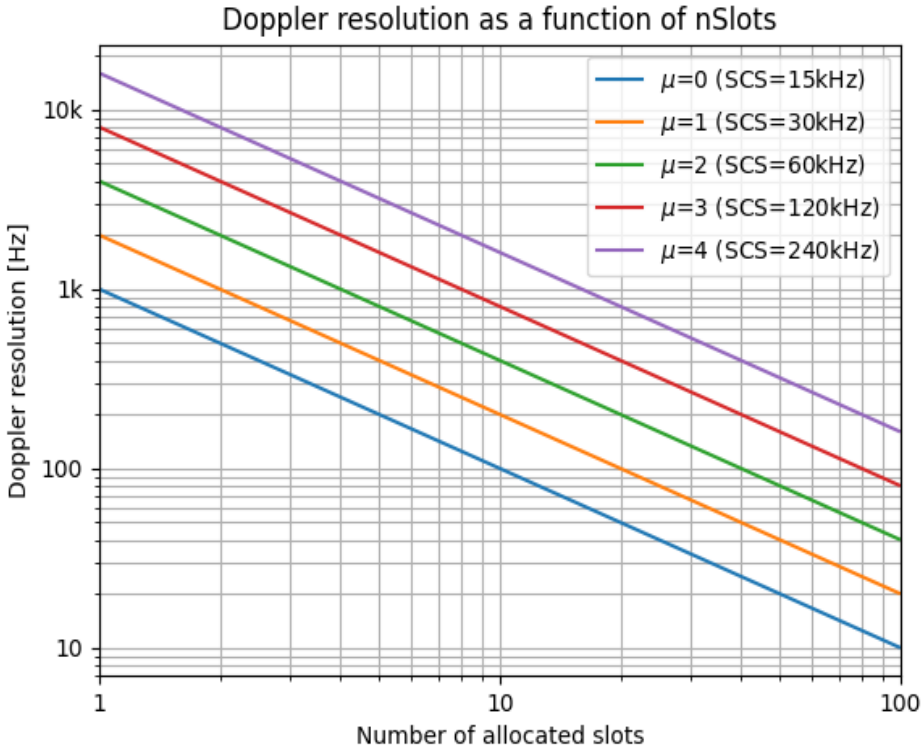

Figure 95: *Doppler resolution as a function of the number of PRS SLOTS*

A zoom on the auto correlation function (Figure 96) in the Doppler space highlights significant correlation side lobes, about -15dB in the present configuration but reaching up to -0.3dB in other configurations. The side lobe amplitude is function of the N_{symb}, basically the higher the number of symbols, the higher the randomness between the sub-sequences (due to the resource element mapping function), the lower the correlation side lobes correlation.

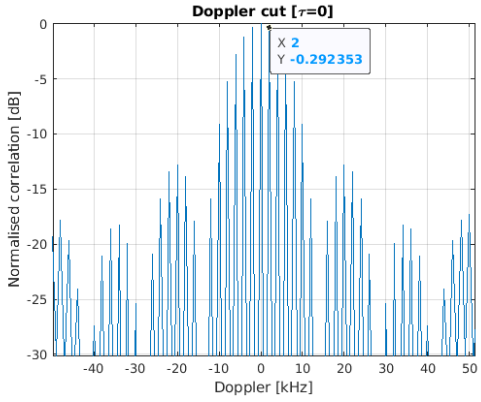

Figure 96: *worst case doppler side lobe correlation for N_symb =2, K_comb =2*

Table 35: *Carrier and PRS simulation configuration for ambiguity function*

Carrier	**Spacing**	**30kHz**		**PRS**	N_{symb}	**2;4;6;12**
	NSizeGrid	8 PRB			K_{comb}	2;4;6;12
	Slot	1			PRS id	10

Figure 97 explores the side lobes of the PRS waveform in the joint delay/Doppler space. The ambiguity function is representative of a typical acquisition of the signal as it would be performed in a navigation context by a receiver, ie search the signal by blind correlating received signal with local replica in both delay and Doppler spaces. Figure 97 represents the ambiguity function as a function of PRS configuration regarding K_{comb} and number of symbols as detailed in the table above. Each image is a 2D zoomed version of the search grid where the auto correlation main lobe is at the center (0 μs delay, 0 kHz Doppler).

First, there is a presence of correlation side lobes in each image, , as high as -3dB with regard to the maximum of the autocorrelation. The side lobe number is function of both K_{comb} and N_{symb} parameters. As already mentioned, the higher the number of symbols, the lower the Doppler side lobes replicas are. Regarding delay/Doppler side lobes, one can figure out that the side lobe replicas always cancel itself for the null delay beam, even in dense side lobe configurations. The side lobe positions over de delay space is function of K_{comb} as follow:

$$\tau\,[s] = \pm n.\frac{12}{K_{comb}}.\frac{1}{PRB_{BW}[Hz]}$$

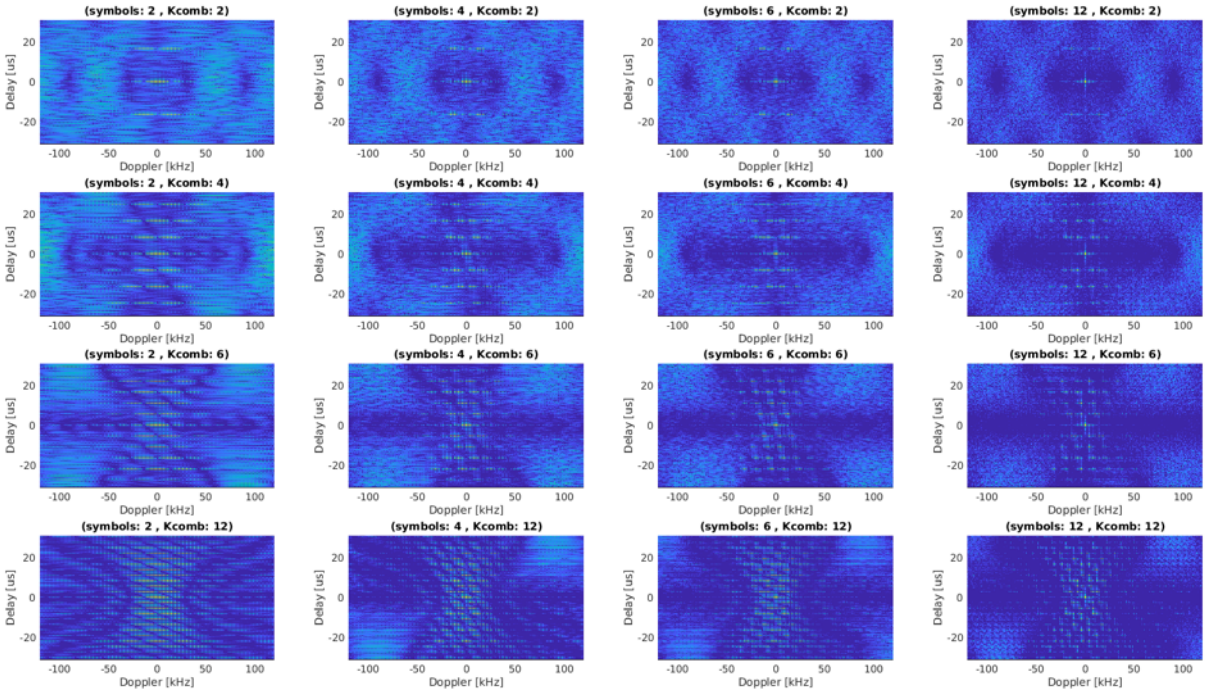

Figure 97: *PRS AMbiguity function as a function of K_comb and number of symbol*

Finally, Figure 98 and Figure 99 show that inter-correlation performances are still met with no major side lobes in the inter-correlation delay/doppler profile.

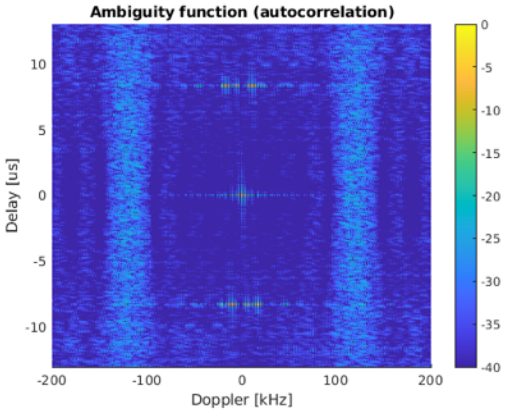

Figure 98: *Ambiguity function for autocorrelation (K_comb=4, N_symb=4)*

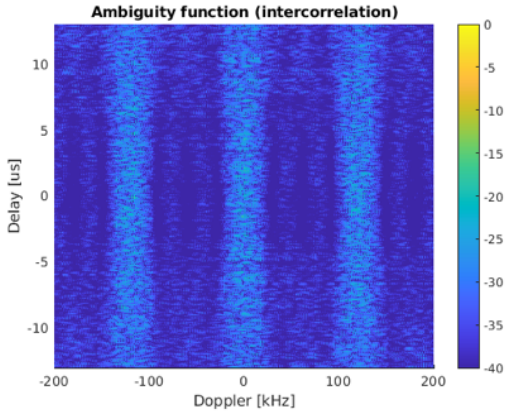

Figure 99*: Ambiguity function for inter-correlation (k_comb=4, n_symb=4)*

To make a parallel with navigation waveforms, continuous waves (time) with continuous spectrum (frequency) are typically used. As a side note, BOC (Binary offset carrier) modulations play with spectrum continuity/discontinuity to locally enhance correlation resolution at the expense of correlation side lobes to be discriminated. The 5G grid by construction introduce many discontinuities in time and frequency that reveals in the correlation process. To mimic GNSS waveforms and avoid correlation side lobes, K_{comb} =1 (all frequencies) and N_{symb}=14 (all slots) should be introduced in the standard. Another strategy to reduce pattern coherency introduced by K_{comb} could be to introduce pseudo random puncturing algorithms of PRS resource elements to break the artificial coherency and restore randomness in the pattern.

In conclusion, the PRS waveform is very versatile with many advantages regarding total signal bandwidth, time repetition or OFDM symbol density. However, the coherent structure of the PRS resource element allocation breaks the randomness of the waveform introducing critical side lobes in the ambiguity function out of the correlation process. A proper theoretical Fourier analysis of the correlation function is still to be performed to understand and predict how and where the side lobes appear as a function of the resource element mapping. Finally two possible workaround could be investigated to- mitigate PRS side lobes: extend current configurations to continuous waveform introducing K_{comb}=1, N_{symbol}=14 into 5G standard, use puncturing algorithms on top of resource element allocation to break Kcomb coherency and recover randomness properties.

7.4.1.1.3 Synchronization Signal Block

A similar study was conducted on the SSB, and more mainly on the use of the PSS and the SSS. The SSB pattern repeats from 5ms to 160ms even if the most common interval is 20ms. SSB allows to establish Downlink Synchronization. It is composed of Primary and Secondary Synchronization Signals and PBCH (shown in ***Figure 100***).

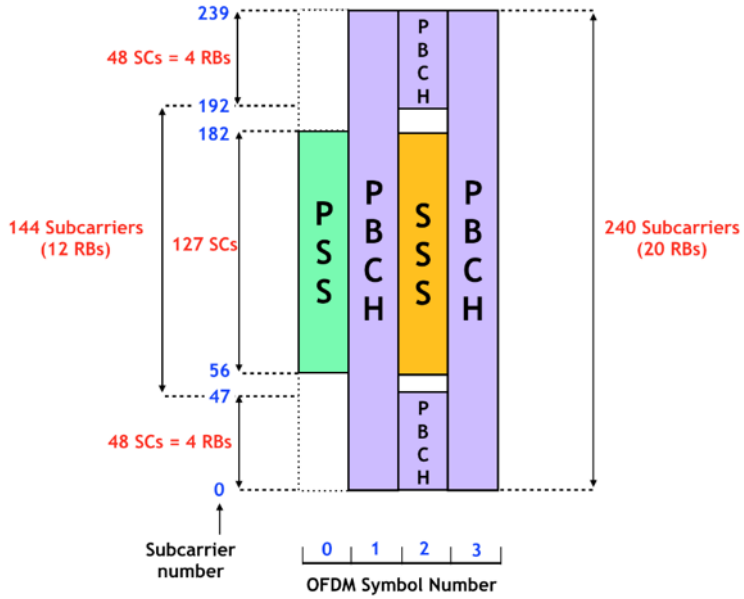

Figure 100: *5G-NR SSB Block*

In the following, the self and inter ambiguity function (Figure 101 and Figure 102) along with the autocorrelation in delay (Figure 103) and Doppler domain (Figure 104) and the cross-correlation function (Figure 105) of the synchronization signals with two different cell-id are shown.

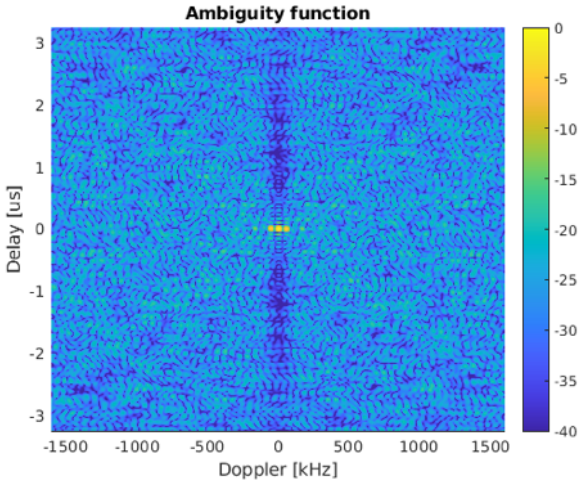

Figure 101: *PSS/SSS SELF ambiguity function*

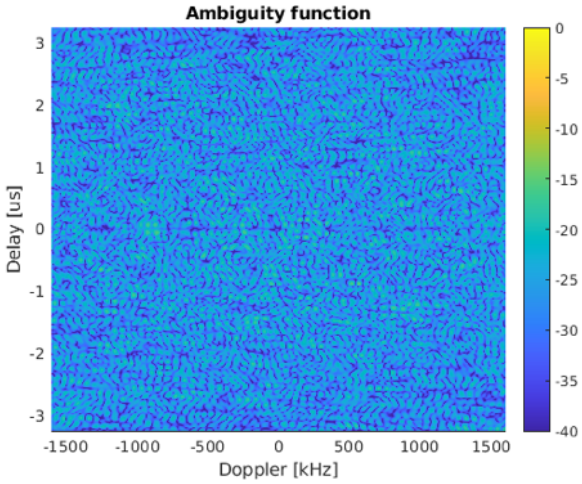

Figure 102: *PSS/SSS Inter-Ambiguity function*

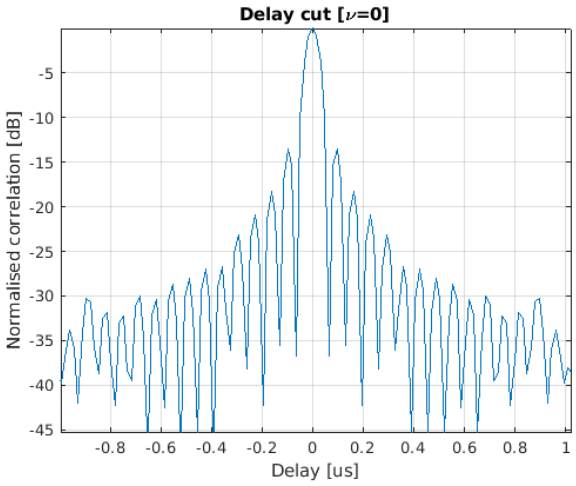

Figure 103: *zoom on autocorrelation in delay domain*

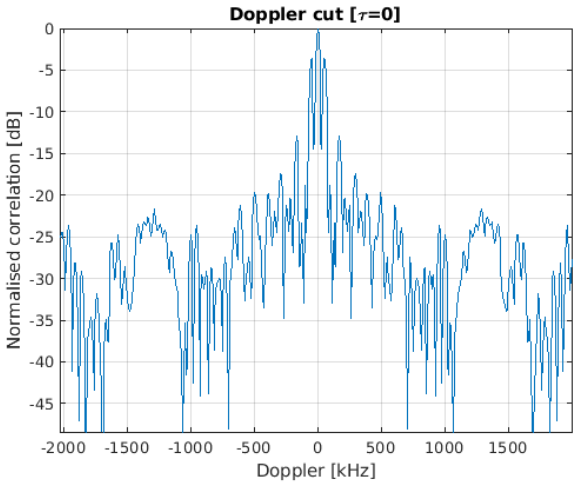

Figure 104: : *zoom on autocorrelation in doppler domain*

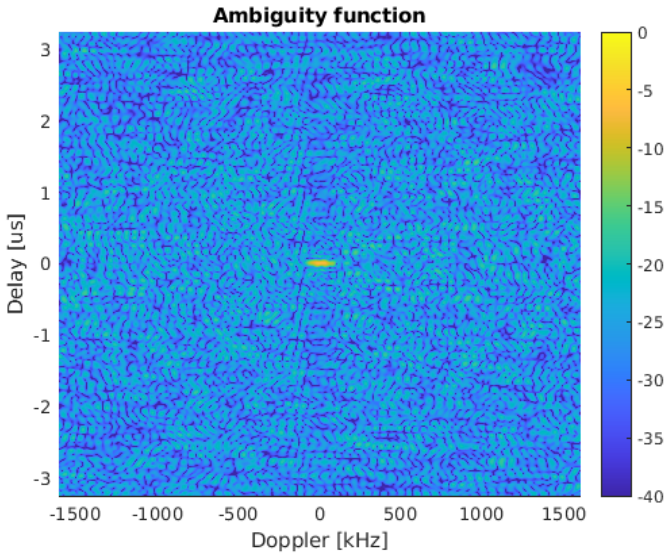

Figure 105: *Cross correlation (cell_id=10 vs cell_id =13) resulting from pss repetition*

7.4.1.2 Conclusion

The use of PRS has the advantage of having a flexible configuration (24 to 272 PRB, repetitions over time slots and possibility to adjust the density of RE within a PRB).

However, there are also many points limiting or even blocking its use:

- On the side of the waveform used, the repetitive/coherent patterns of the PRS RE allocation introduced by the parameters K_{comb} and N_{symb} breaks the randomness of the waveform and introduce critical side lobes in the ambiguity function.
- On the 5G protocol side, as the sending of the PRS is not systematic, it is necessary that the UE is already registered on the network before being able to use PRS. This aspect invalidates this solution for the initial network access procedure.
- At the system level and considering the total error budget, even using the full PRS bandwidth (400MHz), it would not improve other significant error posts such as SV clock or ephemeris, accurate phase center of the transmitting active antenna, SV live steering…

Some enhancements could improve its suitability:

- From a waveform point of view side lobe cancellation is a priority:
  - Introduce K_{comb} = 1 and N_{symb} = 14 values so that 5G PRS signal can be configured as a continuous waveform which would limit the correlation side lobes.
  - Introduce a code puncturing algorithm to break the RE allocation coherency introduced by K_{comb} /N_{symb} and restore the pseudo randomness property of the waveform.
- From a protocol point of view avoid 5G PRS configuration exchanges between gNB and UE could be achieved by reserving some PRS configuration/tuning and broadcasting such signal without connexion.
- From a system point of view, keep in mind that infinite precision on range estimation does not guarantee infinite precision on positioning and all error posts should remain of the same order of magnitude.

In terms of correlation properties, the use of **SSB** seems to be most promising than the use of PRS. First of all, PSS/SSS are 127 chip long m-sequence which are broadcasted by gNB and accessible immediately by the UE who must systematically acquire these signals to enter the network. Furthermore, the amplitude of the signal corresponds to usual GNSS order of magnitudes (3 to 30MHz bandwidth, neither to high nor too low).

The only negative point is the fact that the PSS is very redundant (there are only 3 sequences) which requires the terminal to identify the SSS in order to remove any ambiguity.

7.4.2 An OTFS-based random Access scheme for GNSS Independent operation in NTN

The standardized random-access signal that is specified in [146] consists of a CP and a preamble, which is modulated into DFT-s-OFDM waveform. The preamble is generated by concatenating identical Zadoff Chu (ZC) sequences to facilitate detection in the low SNR

regime. The CP is used to achieve a circular structure and prevent the interference from previous slots. Remarkably, the CP is dimensioned according to the maximum cell radius and the delay spread. In NTN, the CP is used to handle the residual timing offset (TO) that is induced by imperfect compensation. Reliable preamble detection requires the TO and the CFO to be less than the CP duration and half the SCS, respectively. Otherwise, pseudo-correlation peaks arise, leading to timing ambiguities and ultimately to erroneous detection. The preamble formats defined in the standard offer different tolerance levels for time and frequency misalignments. A large SCS is beneficial to mitigate CFO effects, but it reduces CP duration, making the system more sensitive to TO. As the authors have shown in [147], the available formats are not able to deal with the time and the frequency misalignment that result from an erroneous compensation in LEO satellite systems.

The main challenge in extending the radio access capabilities stems from the trade-off between TO and CFO detection ranges. Previous studies have explored two different approaches to achieve a balanced solution. The efforts focus on enhancing detection algorithms and preamble formats to mitigate the adverse effects of: i) large CFO in configurations with narrow SCS, or ii) large TO in configurations with wide SCS. These schemes rely on the fact that small and high SCSs are able to handle large TO and large CFO values, respectively.

Several solutions have been proposed to enhance robustness against CFO with a reduced SCS, such as those in [148][149][150][151][152][153][154][155][156]. The superposition of ZC sequences with different root indices is an effective approach to combat the adverse effects of CFO, as discussed in [148][149][150]. Another promising method to eliminate the impact of CFO is the concatenation of ZC sequences with multiple roots, as shown in [151][152][153]. The work in [154] and [155] introduce a detection algorithm that is designed to mitigate CFO impairments, by using the differential correlation metric. However, it is important to remark that the detector exhibits a trade-off between complexity and timing estimation performance. In [156], the detector counteracts the CFO by performing multiple hypotheses of discrete CFO candidates with a resolution of 1.25 kHz. The main drawback is the limited capacity for scalability, as the number of hypotheses grows with the magnitude of the CFO, which has an impact on the complexity of the detector. The schemes presented in [148][149][150][151][152][153][154][155][156] resolve timing and frequency ambiguities by using multiple root ZC sequences for preamble generation. This, however, reduces the overall efficiency of the preamble generation method, as well as the random access capacity.

The common approach to extend the TO detection range is based on cascading ZC sequences and implementing two-step detection algorithms. The aim of employing two detection steps is to sequentially estimate fractional and integer delays. Typically, fractional and integer delay components are computed with respect to the length of a single ZC sequence. The rationale behind this factorization is to reduce the search space. Upon performing the detection, the total delay can be estimated, taking into account the compound effects of fractional and integer delays. It is important to note that the two-step detection approach inherently suffers from uneven performance between fractional and integer delay estimation, as well as from error propagation between the two stages.

In the literature, several preamble designs implement the two-step detection scheme to achieve a large TO detection range, e.g., [145][147][157][158][159]. The solutions proposed in [147][157]are based on concatenating a single root ZC sequence with various cyclic shifts. In contrast, the method in [158] interleaves two ZC sequences, which could be generated from the same ZC root index, following a predefined pattern. Remarkably, the solutions addressed in [147][157][158] depart from the standardized preamble generation method described in [146]. To minimize the impact on the standard, the authors in [159] have shown the effectiveness of repeating a single root ZC sequence with a single shift in estimating large TOs. An improved preamble design is presented in [145], which outperforms the schemes in

[147][157][158][159] by eliminating the CP. Nevertheless, this preamble is constructed by using two ZC root sequences. Although this design reduces overhead, it limits the number of available ZC sequences and, consequently, reduces the random access capacity. As previously discussed, this limitation is also observed in [148][149][150][151][152][153][154][155][156].

Recently, some works have emphasized the importance of the waveform design on the random access scheme, e.g., [160][161][162]. In [160][161], the superior performance of the filterbank multicarrier modulation (FBMC) over DFT-s-OFDM is shown. In this regard, FBMC exhibits much lower OoB emissions and achieves lower missed detection probability (MDP) in presence of CFO. Nonetheless, the detector implemented in [160] is very demanding in terms of computational effort. The complexity burden comes from the sliding window approach, which is adopted to search for all possible TO values. The complexity is reduced in [161], but the resulting scheme provides similar TO and CFO detection ranges as the standard preamble formats specified in [146]. In contrast, the solution devised in [162] resorts to OTFS modulation to allocate high-power pilots in the DD domain. The detector estimates the delay from the pilot shift in the delay domain. To enable multi-user access, the pilots shall be transmitted in different Doppler bins. By separating the pilots according to the maximum frequency shift, the OTFS-based random access offers high robustness to the CFO. However, in the presence of large TO and CFO values, the number of available access patterns becomes limited. This constraint can significantly increase the probability of collision events, resulting in performance degradation.

Despite the remarkable features of FBMC and OTFS, the schemes devised in [160][161][162] exhibit limitations when applied to GNSS-free random access systems, especially to accommodate large TO and CFO.

To the best of our knowledge, existing preamble designs address large TO and CFO by either appending long CP blocks or employing multiple ZC root sequences. This observation highlights that a key challenge for future designs is the development of preamble structures that can effectively mitigate these impairments, which are inherent to the GNSS-independent operation, by using only a single ZC root sequence and minimal CP overhead.

The enhancement proposed here is based on the modulation of ZC sequences into OTFS. The use of OTFS is endorsed due to its effectiveness in achieving reliable communications in doubly-selective channels, as demonstrated in [163][164]. Therefore, OTFS is regarded as ideally suited to high-mobility scenarios, including those encountered in LEO satellite communications.

OTFS can be implemented by applying the Heisenberg transform at the transmitter and the Wigner transform at the receiver. This structure enables OTFS to be realized on the basis of OFDM. In recent works, a formulation of OTFS using the discrete Zak transform (DZT) has been provided, as detailed in [165]. Compared to the overlay structure, reduced complexity is offered by the DZT-based implementation, and the application of pulse-shaping techniques is facilitated. Motivated by these advantages, the DZT-based OTFS (DZT-OTFS) modulation is adopted in this work.

The main contributions of the proposed work can be summarized as follows:

- A novel random access signal design is proposed, in which the preamble is modulated into the DZT-OTFS waveform. The preamble is generated by concatenating identical ZC sequences. Efficient use of resources is enabled by employing a single ZC root index, allowing for a high level of commonality with 5G NR. A notable property of the proposed format is that circularity is exhibited at the receiver, even in the presence of large time offsets, without the requirement for long

CP blocks. In fact, the CP can be entirely omitted or minimized to accommodate the maximum expected delay spread.

- A DD domain input-output relation for the proposed random access scheme is derived. This relation is used to characterize the impairments affecting the received preamble. To facilitate the representation of delays exceeding the length of a single ZC sequence, a dual system is introduced.
- A preamble detection scheme tailored to the DZT-OTFS random access signal is designed to operate in the DD domain. Unlike conventional two-step detection methods, fractional and integer delay components are jointly estimated by the proposed scheme using a fixed detection window. No additional search steps are required by this joint estimation approach. Furthermore, the structure of the received signal is exploited by the algorithm to enable coherent combination of the received sequences, thereby maximizing the desired signal strength.

7.4.2.1 System model

As illustrated in ***Figure 106***, the service is provisioned by LEO satellites that divide the coverage area into multiple beams. In the proposed architecture, the satellites are integrated into the RAN. More precisely, we focus on satellites that are equipped with payloads capable of hosting a full gNB operating in FR2. Therefore, direct satellite connectivity is enabled without relying on terrestrial infrastructure.

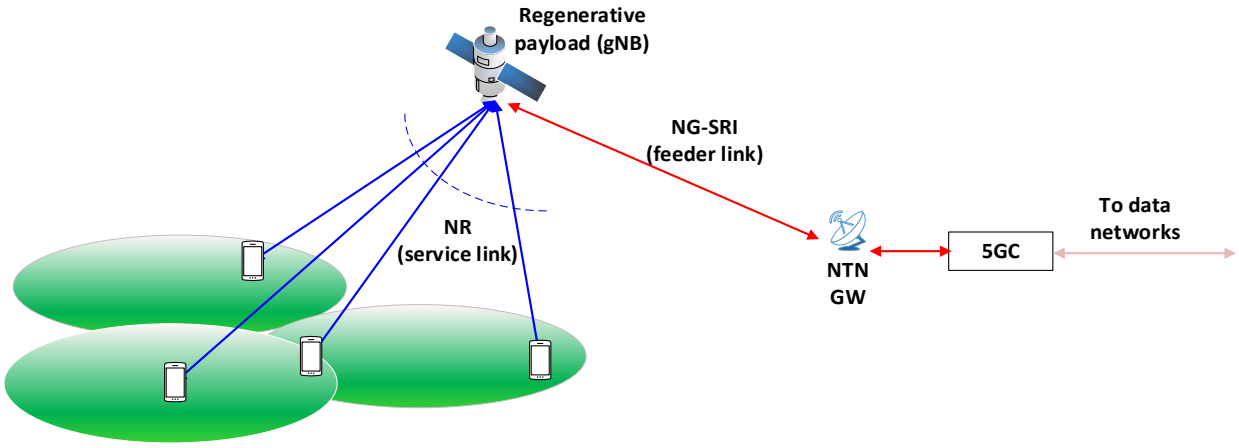

Figure 106: *Satellite regenerative architecture*

To transition from the idle to the connected state, the UE should perform the cell search and initiate the RAP. Upon achieving downlink synchronization and acquiring the cell identity, the UE selects a random-access occasion to transmit a preamble signal, which constitutes the first step of the RAP. To ensure that the UE is received in the time and frequency resources dedicated to PRACH, the UE adjusts the timing and the carrier frequency according to the RTT delay and the UL Doppler frequency shift experienced in the satellite link. This pre-compensation mechanism takes as inputs the location of the UE and a valid version of the satellite ephemeris, which is acquired from the SIB19. In the presence of user positioning errors, the transmitted preamble will be time and frequency misaligned at reception. The resulting TO and CFO depend on the accuracy of the positioning information. In this work, the working assumption is that the true coordinates lie within a circular uncertainty region of radius R_ϵ. The concept is illustrated in ***Figure 107***, where the reference point (RP) corresponds to the true coordinates. The operating frequency, the orbit and the user positioning error will dictate the magnitude of the TO and the CFO. It shall be noticed that any displacement at high

elevation angles leads to high CFO and low TO. At low elevation angles, the offsets follow an opposite trend, so that the position error translates into high TO and low CFO values.

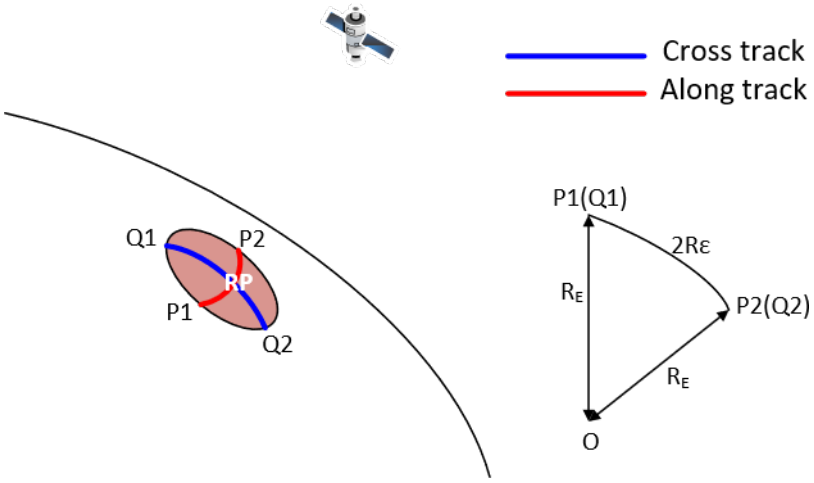

***Figure 107**: Geographic location uncertainty*

The detailed formulation of the DZT-OTFS system model, satellite channel, transmitter and receiver architecture are detailed in Appendix-A. Here we highlight the core principles relevent to the preamble design.

7.4.2.2 Preamble design

Building upon the system model introduced in Section 7.4.2.1 and Appendix-A, this section addresses the DZT-OTFS random access signal design. The objective is to enable reliable detection in the presence of large delays. Following similar design principles to those in 5G NR, the proposed scheme concatenates identical ZC sequences. However, unlike the standard, the preamble symbols are modulated in the DD domain. Hence, the OTFS frame is defined by

$$Z_x[l,k] = x_u[l] = e^{-j\frac{\pi u l(l+1)}{M}}, \qquad (7.4.2.2.1)$$

for $0 \leq k \leq N-1$. Notice that a ZC sequence of length M is mapped into the delay domain and is repeated along the Doppler domain. The root index u is selected from the set $\{1, \cdots, M-1\}$. To characterize the time domain signal, it is useful to recall that $\sum_{n=0}^{N-1} e^{j\frac{2\pi}{N}ni} = 0$, for $i \in \mathbb{Z}^+$ and $N \geq 2$. Invoking this property, the sequence that is obtained after executing the IDZT processing becomes

$$x[n] = \begin{cases} \sqrt{N} e^{-j\frac{\pi u n(n+1)}{M}} & n = 0, \cdots, M-1 \\ 0 & \text{otherwise.} \end{cases} \qquad (7.4.2.2.2)$$

This structure offers enhanced energy efficiency by transforming the CP into a zero-padding (ZP) operation. Another remarkable property is that $x[n-a] = x[(n-a)_{MN}]$, for $0 \leq a < M(N-1)$ and $0 \leq n \leq MN-1$. To take advantage of this circularity at the receiver, the channel delay τ_0 shall not exceed $(N-1)T$. When this constraint is satisfied, the CP block can be minimized or omitted entirely, since its main purpose is to prevent the leakage from already synchronized signals that are transmitted in previous slots. Hence, the duration of the CP block should be just dimensioned only to cover the maximum expected channel delay spread, without accounting for user positioning uncertainties or additional propagation delays. Under

this assumption, the normal CP length L_{CP} defined in 5G NR can be used as a reference. Consequently, the total burst duration becomes $(L_{\text{CP}} + 2Q + NM)\frac{T}{M}$.

Interestingly, the study in [166] proposes modifications to reduce the normal CP durations in NTN scenarios. This work is motivated by the low-frequency selectivity typically observed in satellite communication channels. The analysis highlights that these adaptations could significantly reduce the overhead in future standard releases.

At the other end of the link, the global response is defined by DD input-output relation. In this section, we will show that the expression can be generalized for $0 \leq a_0 < (N-1)M$, provided that the sequences are arranged in the DD domain according to Eq. 7.4.2.2.1. The first step is to express the integer delay offsets as $a_0 = q_M \times M + r_M$, where the quotient and the remainder are, respectively, given by $q_M = \lfloor \frac{a_0}{M} \rfloor$ and $r_M = (a_0)_M$, with $0 \leq q_M < N-1$ and $0 \leq r_M < M$. The second step is to consider the equivalence of the circular convolution in the delay domain.

Closely analyzing Eq. 1 7.4.2.2.1 and Eq. 7.4.2.2.2, it can be verified that

$$x[(n - q_M \times M)_{MN}] \Leftrightarrow Z_x[l,k]e^{-j\frac{2\pi}{N}kq_M}. \qquad (7.4.2.2.3)$$

In notation terms, Eq. 7.4.2.2.3 denotes that the signal on the left (right) is the IDZT (DZT) of the signal on the right (left).

Using this insight, we define a dual system that maintains the same original input-output relation, while simplifying the treatment of delay offsets. The corresponding block diagram is illustrated in Figure 108.

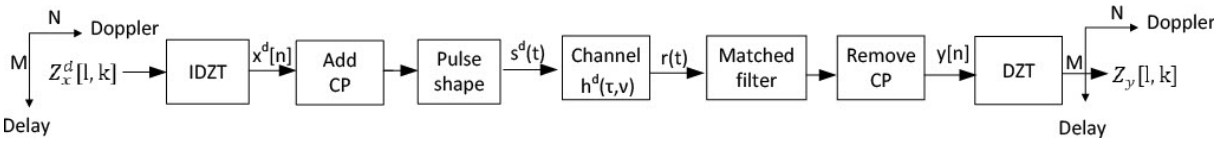

Figure 108: *Dual DZT-OTFS transmitter and receiver block diagram*

The difference lies in the treatment of timing errors. Under this alternative view, the dual channel response is represented by

$$h^d(\tau,\nu) = h_0^d \delta\left(\tau - \tau_0^d\right)\delta\left(\nu - \nu_0^d\right),$$

with

$$h_0^d = h_0 e^{-j\frac{2\pi(k_0+\kappa_0)}{N}q_M} \qquad \tau_0^d = \frac{r_M + \alpha_0}{\Delta_f M} \qquad \nu_0^d = \nu_0.$$

Here, the offset $q_M \times M$ is not induced by the channel, but it is instead deliberately embedded at the transmitter. Accordingly, the transmitted sequence in the dual system is given by

$$x^d[l+Mm] = \frac{1}{\sqrt{N}}\sum_{k=0}^{N-1} Z_x^d[l,k]e^{j\frac{2\pi}{N}km},$$

where

$$Z_x^d[l,k] = Z_x[l,k]e^{-j\frac{2\pi}{N}kq_M}. \qquad (7.4.2.2.4)$$

After transmission through the channel defined by $h^d(\tau,\nu)$, the received signal can be expressed as

$$y[n] = \sum_{i=-L}^{L} \beta[i]x^d[(n-i-r_M)_{MN}]e^{-j\frac{2\pi(k_0+\kappa_0)}{N}q_M} \times e^{j\frac{2\pi(k_0+\kappa_0)}{MN}(n-i-r_M)} + w[n].$$

For notational simplicity, we adopt the dual system representation. Under this formulation, the DD domain output is given by

$$Z_y[l,k] = e^{-j\frac{2\pi(k_0+\kappa_0)}{N}q_M} \sum_{i=-L}^{L} \beta[i]Z_{y_i}[l,k] + Z_w[l,k],$$

where the DD input-output relation for each multipath tap is expressed as

$$Z_{y_i}[l,k] = \sum_{m=0}^{N-1}\sum_{q=0}^{M-1} Z_x^d[q,m]Z_{i+r_M}^{\tau}[l-q,k]Z_{k_0+\kappa_0}^{\nu}[q,k-m]. \qquad (7.4.2.2.5)$$

To simplify the notation, it is assumed that $0 \le i + r_M \le M-1$. In the next section, we will demonstrate that the proposed detection algorithm can be effectively developed based on the formulation in Eq. 7.4.2.2.3.

$$Z_{y_i}[l,k] = \begin{cases} \frac{e^{-j\frac{2\pi}{N}k}}{\sqrt{N}} \sum_{m=0}^{N-1} Z_x^d[(l-i-r_M)_M, m]Z_{k_0+\kappa_0}^{\nu}[(l-i-r_M)_M, k-m] & \text{if } 0 \le l < i+r_M \\ \frac{1}{\sqrt{N}} \sum_{m=0}^{N-1} Z_x^d[(l-i-r_M)_M, m]Z_{k_0+\kappa_0}^{\nu}[(l-i-r_M])_M, k-m] & \text{if } i+r_M \le l \le M-1 \end{cases}$$

(7.4.2.2.6)

7.4.2.2.1 Preamble detection

The objective of this section is to design a preamble detector specifically tailored to the format introduced in Section 7.4.2.1. It will be shown that the delays experienced by each transmission can be easily inferred from the detected preambles. To design the detection algorithm, we build upon the model described in Section 7.4.2.2 and Appendix-A. In this regard, the detector takes as input the signal $Z_y[l,k]$, defined in Eq. 7.4.2.2.5 which reveals that the DD domain output is affected by inter-delay and inter-Doppler interference. The key insight is summarized in the following proposition.

Proposition 1. If the ZC sequence is arranged in the DD domain according to Eq. 7.4.2.2.4, then the interfering terms in the Doppler domain add constructively.

The mathematical details that lead to the proof of Proposition 1 are provided hereinafter. For a given delay index l and a Doppler shift $\nu_0 = b/NT$, the following equivalence can be established:

$$\sum_{m=0}^{N-1} \frac{1}{\sqrt{N}} Z_x^d[l,m] Z_b^v[l,k-m]$$
$$= \frac{x_u[l] e^{j\frac{2\pi}{MN}bl}}{N} \sum_{m=0}^{N-1} e^{-j\frac{2\pi}{N}mq_M} \sum_{i=0}^{N-1} e^{j\frac{2\pi}{N}(b-k+m)i}$$
$$= x_u[l] e^{j\frac{2\pi}{MN}bl} e^{j\frac{2\pi}{N}(b-k)q_M}.$$

An immediate consequence of Proposition 1 is that the summation in Eq. 7.4.2.2.6 can be eliminated. Applying this result, we can define a new system equation, namely,

$$Z_y[l,k] = \sum_{i=-L}^{L} \beta\,[i] x_{uk}[(l-i-r_M)_{2M}] \times e^{j\frac{2\pi}{MN}(k_0+\kappa_0)l} e^{-j\frac{2\pi}{N}kq_M} + Z_w[l,k].$$

To characterize the phase rotation in $l = 0, \cdots, i + r_M$, we establish a periodization of the extended signal

$$x_{uk}[l] = \begin{cases} x_u[l] & 0 \le l \le M-1 \\ e^{-j\frac{2\pi}{N}k} x_u[l] & M \le l \le 2M-1, \end{cases}$$

which is made up of two concatenated ZC sequences. The key parameters of the prevous equations are q_M and r_M, which have been defined to express the total delay as $a_0 = q_M \times M + r_M$. Hence, the objective of the detector is to find the signature of the transmitted preamble by jointly searching over $0 \le q_M < N-1$ and $0 \le r_M \le M-1$. Upon detecting the presence of the preamble, the detection algorithm shall return a two-dimensional index. Next, the detector will provide an estimate of the delay, which can be unambiguously derived from the selected index.

The analysis is initially restricted to scenarios where the offsets span this range $0 \le i + r_M \le M-1$. The rest of the cases where the indices may not be confined within that interval will be examined and addressed in subsequent analyses.

Assuming the working hypothesis $0 \le i + r_M \le M-1$, the decision variable for preamble detection is computed as

$$\rho_v(\mu,\gamma) = \left| \sum_{k=0}^{N-1} \sum_{l=0}^{M-1} e^{j\frac{2\pi}{N}k\gamma} \frac{Z_y[l,k]}{MN} x_{vk}^*[(l-\mu)_{2M}] \right|^2 = \frac{1}{|MN|^2} |C_v(\mu,\gamma)|^2 + \eta_v(\mu,\gamma), \quad (7.4.2.2.7)$$

where the correlation term is

$$C_v(\mu,\gamma) = \sum_{k=0}^{N-1} \sum_{i=-L}^{L} \sum_{l=0}^{M-1} \beta\,[i] e^{j\frac{2\pi}{N}k(\gamma-q_M)} \times x_{vk}^*[(l-\mu)_{2M}] x_{uk}[(l-i-r_M)_{2M}] e^{j\frac{2\pi(k_0+\kappa_0)}{MN}l}. \quad (7.4.2.2.8)$$

The noise component in last equation is defined by $\eta_v(\mu,\gamma)$, where the variable v denotes the root index of the candidate ZC sequence. The standard approach is to use 64 ZC sequences to generate the preamble set. To account for all possible delay and Doppler shifts, the decision

variable in the last equation is evaluated over the ranges $0 \leq \mu \leq M-1$ and $0 \leq \gamma < N-1$. Since the identical ZC sequence is transmitted across the Doppler domain, the decision variable results from the coherent accumulation process. It is important to remark that, in OFDM systems, coherent combination of sequences is not possible in the presence of CFO, due to the accumulated phase rotation across each multicarrier symbol. Consequently, conventional detection methods for repeated sequences in OFDM rely on non-coherent accumulation, as shown in [159][167].Thanks to the specific characteristics of OTFS, the detector devised in this section can coherently combine the received signals across the Doppler domain, enabling more effective computation of the decision variable.

Detailed discussion of the practical implementation, computational complexity and correlation analysis are available in Appendix-B.

7.4.2.2.2 Peak search and parameter estimation

The detector is able to characterize the signature of the transmitted preamble by solving

$$\{\hat{u}, \hat{r}_M, \hat{q}_M\} = \underset{\upsilon,\mu,\gamma}{\operatorname{argmax}} \mathrm{P}(\rho_\upsilon(\mu,\gamma) \geq r_{\mathrm{th}}). \qquad (7.4.2.2.9)$$

The distinctive feature of this approach is that r_M and q_M are jointly estimated. The common approach is to separately estimate these two parameters that define the delay. Several examples can be found in [145][147][157][159]. The consequence of carrying out sequential processing is that errors are propagated. Hence, the estimation of r_M may become the performance bottleneck. In this regard, a small deviation in r_M could lead to a wrong decision in q_M, as shown in [159]. The joint detection proposed here addresses this issue by accounting for the dependencies between the parameters.

The criterion that drives the parameter estimation in Eq. 6.3.9 is based on finding the index that exhibits the highest peak value. The magnitudes that are above the detection threshold will be classified as peak values. The parameter r_{th} is computed to comply with the false alarm probability, which is defined by

$$P_{\mathrm{FA}} = \mathrm{P}(\eta_\upsilon(\mu,\gamma) \geq r_{\mathrm{th}}).$$

Bearing in mind the statistical information provided in Section 7.4.2.2.1 and the closed-form expression Eq. 7.4.2.2.4, we can resolve that the noise component can be formulated as $\eta_\upsilon(\mu,\gamma) = \frac{1}{MN}\chi^2(2)$. The term $\chi^2(n)$ is used to represent a chi-square distribution with n degrees of freedom. The equation that relates P_{FA} to r_{th} is derived according to [168] as

$$P_{\mathrm{FA}} = 1 - \left(1 - e^{-\frac{r_{\mathrm{th}} MN}{2}}\right)^M.$$

It is important to note that the detection process defined by Eq. 7.4.2.2.9 can be impaired by the leakage effect resulting from the fractional delay. This is clearly when $\alpha_0 = \pm 0.5$. In such cases, it is highly likely that two adjacent indices, such as μ^* (the true peak) and its neighbors $\mu^* \pm 1$, may both be declared as peaks. Without corrective measures, the detector may incorrectly identify a neighboring index as the true peak.

Although the impact on the estimation accuracy is not significant, we propose a low complexity solution to refine the estimates. The approach is based on evaluating the power imbalance between the correlation peaks observed at μ^* and $\mu^* \pm 1$. If the difference is relatively small, e.g., less than 25 %, then the outcome is the average of the peak positions. The resulting index becomes $\mu^* \pm 0.5$. The sign of the additive term depends on whether the fractional delay is

positive or negative. Notice that the proposed method improves the resolution, without resorting to complex techniques such as fractionally spaced sampling receivers.

To sum up, the detection scheme envisaged in this section benefits from joint detection and coherent signal combining. Nevertheless, the scheme suffers from distortion in the presence of fractional delays. To understand which is the dominant effect, some numerical results are presented in the next section.

7.4.2.3 Numerical results and discussion

In this section, numerical simulations are presented. We first analyze the PAPR and the frequency confinement of the transmitted signal, and then the MDP is computed. To achieve a high level of commonality with 3GPP, 64 ZC sequences are formed following the procedure specified in (3GPP; Technical Specification Group Radio Access Network; NR;)[146] for FR2. To shape the preamble symbols, we have employed the square-root raised cosine filter with a roll-off factor of 10% and finite support in the time domain. To confine the energy of the burst within a short interval, the pulse spans $20\frac{T}{M}$, which is parameterized by setting $2Q = 20$.

In the scenario under study, we focus on LEO satellite systems with regenerative capabilities. Hence, the RTT delay, and the Doppler frequency shift exclude feeder link impairments. The system and orbit parameters are gathered in Table 36.

Table 36: *System and orbit parameters*

Frame size	N = 4, M = 139
DD resolutions	T = 16.67μs, ∆f = 60 kHz
PRACH bandwidth	B = 8.34 MHz
Frequency band	Q/V
Satellite altitude	600 km
Minimum elevation angle	30º

To ensure that the preamble is received within the allocated RACH resources, a pre-compensation mechanism is autonomously applied by the UE. Given the low delay spread in satellite channels, preamble arrival differences mainly arise from UE positioning errors. Based on that, it is assumed that already synchronized signals virtually do not interfere with the received preambles. Accordingly, the CP length is set to zero. Nevertheless, to ensure reliable detection, the duration of both the preamble and the guard time shall be larger than the residual delay. Following this rationale and bearing in mind the design principles described before, the delay should not exceed $(N-1)T$. Accordingly, the guard time is equal to $(N-1)T$. The details are provided in Table 37.

Table 37: *PRACH Parameters*

	OTFS	**OFDM [159]**	**OFDM [145]**

Preamble length	T/M (M + 2Q)	N T	(N + 1)T
CP length	0	(N-1)T	0
Guard time	(N-1)T	(N-1)T	(N-1)T
Detection window	NT	NT	2NT
Number of roots	1	1	2
Detection algorithm	One Step CA	Two-step NCA	Two-step CA
Detector time resolution	$\frac{1}{512\Delta_f}$	$\frac{1}{512\Delta_f}$	$\frac{1}{512\Delta_f}$

Following the methodology outlined in (Caus & Shaat, PRACH Signal Design and Detection for LEO Satellite Systems with Imperfect UE Positioning, 2024), we compute the maximum TO and CFO values that result from UE positioning errors. The corresponding results are represented in Figure 109 as a function of the radius of the uncertainty region R_ϵ. The timing and frequency offsets are characterized by the parameters τ_0 and ν_0. Under the proposed configuration, preamble detection is feasible as long as $0 \leq \tau_0 < (N-1)T$ and $-\Delta_f/2 \leq \nu_0 \leq \Delta_f/2$). Evaluating these conditions for the parameters used in this section, it follows that the uncertainty region should not exceed $R_\epsilon = 4.3$ km.

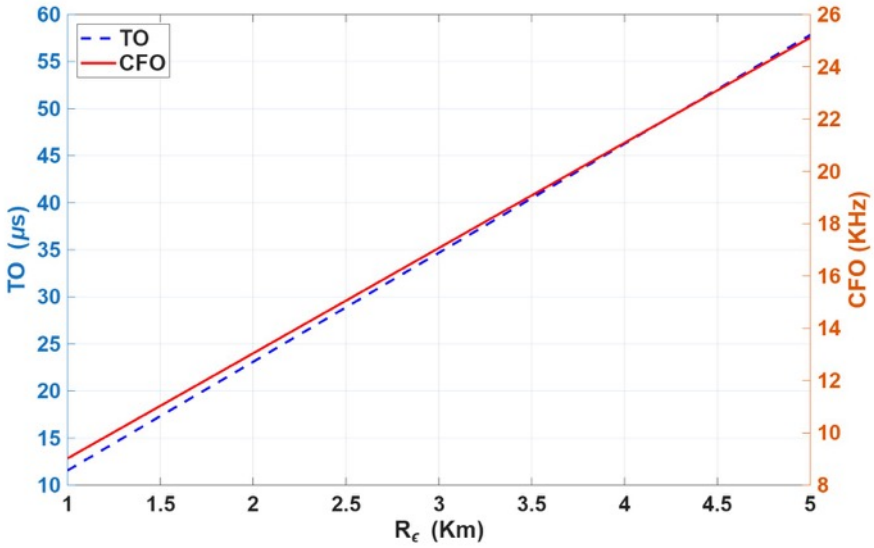

***Figure 109**: Maximum TO and CFO values as function of Rϵ.*

As a benchmark, we have considered the solutions proposed in [145][159]. Both schemes modulate ZC sequences using DFT-s-OFDM. Analogously to the method described in this work, the preamble provided in [159] is obtained by concatenating N identical ZC sequences.

The main difference stems from the fact that a CP block of length $(N-1)T$ is needed to achieve a circular structure at reception. To estimate the delay, the detector uses a fixed detection window of length NT, which is precisely the preamble duration. The random access signal structure is enhanced in [145] by removing the CP. Interestingly, the preamble is constructed by using two ZC root sequences. The resulting preamble spans $(N+1)T$. At reception, the signal does not exhibit circularity. Hence, to capture the preamble samples, the detection window should cover all possible delays. Accordingly, the window length should be at least $2NT$. Concerning the detection algorithm, both schemes resort to the two-step design, where fractional and integer delay components are separately estimated. However, a clear distinction shall be made between the techniques regarding the computation of the decision variable. The solution conceived in [159] performs non-coherent accumulation (NCA). By contrast, the authors in [145] rely on coherent accumulation (CA). The specific characteristics of each design are described in Table 37. From here onwards, we will refer to OFDM NCA and OFDM CA to identify the techniques described in [159] and [145], respectively. Based on the values gathered in Table 37, we can conclude that OFDM-based designs require a considerably larger amount of resources to transmit and receive the preamble than the proposed scheme.

7.4.2.3.1 Peak-to-average power ratio

This subsection focuses on evaluating the envelope fluctuation of the random access signals. To this end, we have represented in Figure 110 the CCDF of the PAPR. The sequences are generated by considering all ZC root indices. As Figure 110 shows, OTFS demonstrates a slightly better PAPR performance compared to OFDM. These results indicate that, in OTFS modulation schemes, the power amplifier efficiency will not differ significantly from that of OFDM.

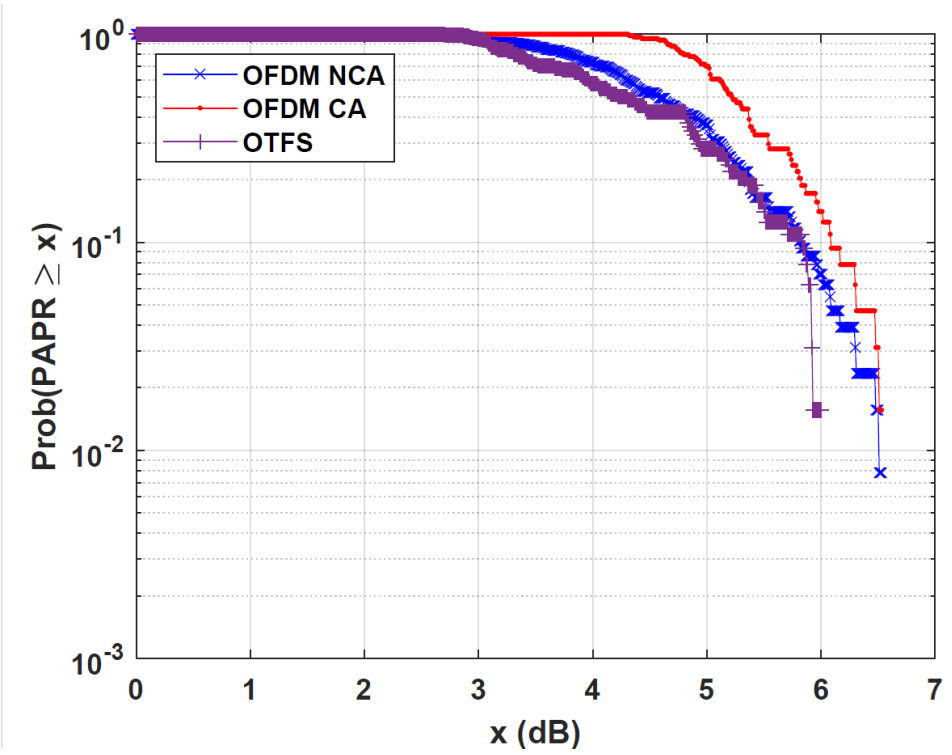

Figure 110: *CCFD of PAPR of random access signals*

7.4.2.3.2 Frequency response

In this subsection, we aim at evaluating the spectral leakage suppression outside the PRACH bandwidth. To evaluate the frequency domain information, Figure 111 depicts the PSD in a 60 MHz bandwidth. For the sake of clarity, the highest spectral peak is normalized to 0 dB. An interesting result is that the PSD decays faster in OFDM NCA than in OFDM CA. This can be attributed to the CP that is transmitted in OFDM NCA, which extends the rectangular pulse that is used to shape the subcarrier signals. Hence, by increasing the CP length, the subcarrier signals become narrower in the frequency domain, reducing OoB emissions. However, the overhead is significantly increased. By contrast, thanks to pulse shaping, OTFS can improve the spectrum confinement with a moderate overhead. By increasing the duration of the prototype pulse, which is controlled by the variable Q, OTFS exhibits much higher stopband attenuation than OFDM.

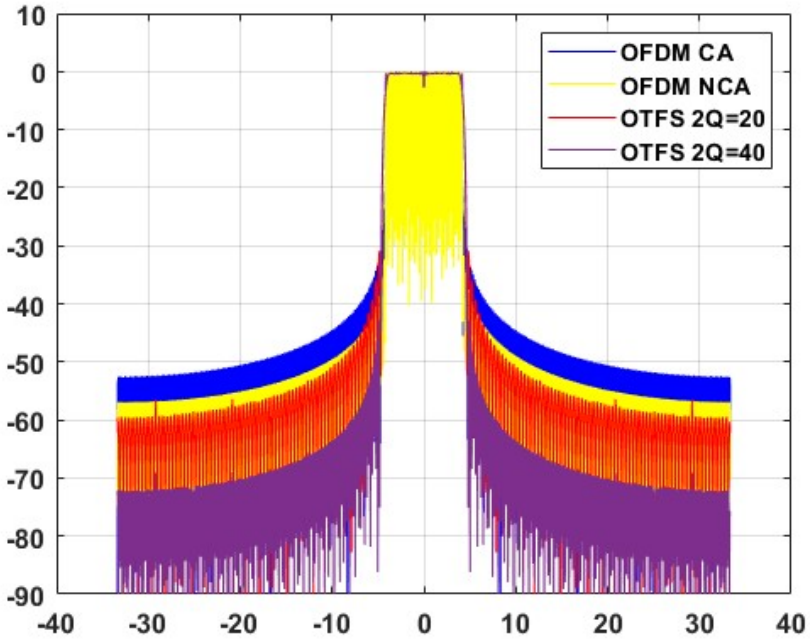

Figure 111: *PSD of random access signals*

7.4.2.3.3 Missed detection probability

To complete the performance analysis, we evaluate the MDP versus SNR. The transmission goes through the channel model previously defined (also see Appendix-A). Hence, the SNR is a function of the satellite channel gain, the power of the symbols and the power of the noise, i.e., SNR $= |h_0|^2 \mathbb{E}\{|Z_x[l,k]|^2\}$. The events that lead to an erroneous detection include: 1) the detection of a different preamble than the one that was sent, 2) not detecting a preamble at all or 3) correct preamble detection but with the wrong timing estimation. Specifically, a timing estimation error is declared if the magnitude of the error exceeds $\frac{1}{M\Delta_f}$. We consider that N_U users are simultaneously accessing the network in a single random access occasion. In alignment with the PRACH study cases defined in [169] (3GPP; Technical Specification Group Radio Access Network;), we consider $N_U = 1{,}2$. All detection schemes that are assessed in this section are configured to ensure a false alarm probability of $P_{\text{FA}} = 10^{-3}$.

Numerical results are provided in Figure 112 and Figure 113 for the uncertainties associated with $R_\epsilon = 4.3$ km. In such a case, as Figure 109 shows, the maximum time misalignment is

given by 49.72 μs. The preamble designs specified in Table 37 tolerate up to 50 μs. As far as the delay is concerned, all the contenders are well suited to deal with the impairments that result from erroneous positioning. In the proposed scenario, the TO is uniformly drawn from $[0,50]$ μs, to cover all possible delays. The CFO is fixed to either 0 or 15 kHz, to respectively model ideal and extreme conditions.

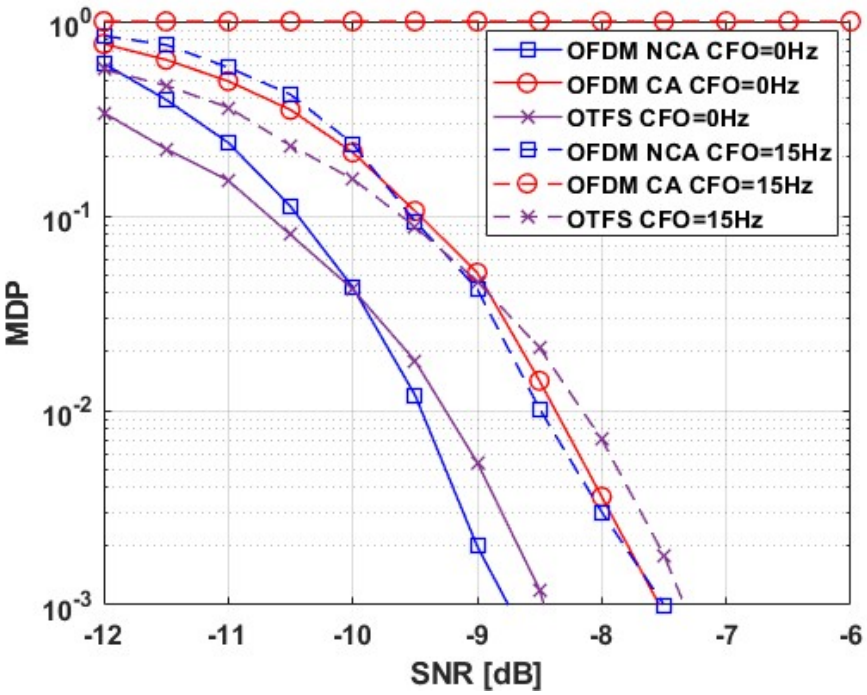

Figure 112: *MDP versus SNR for N_U =1*

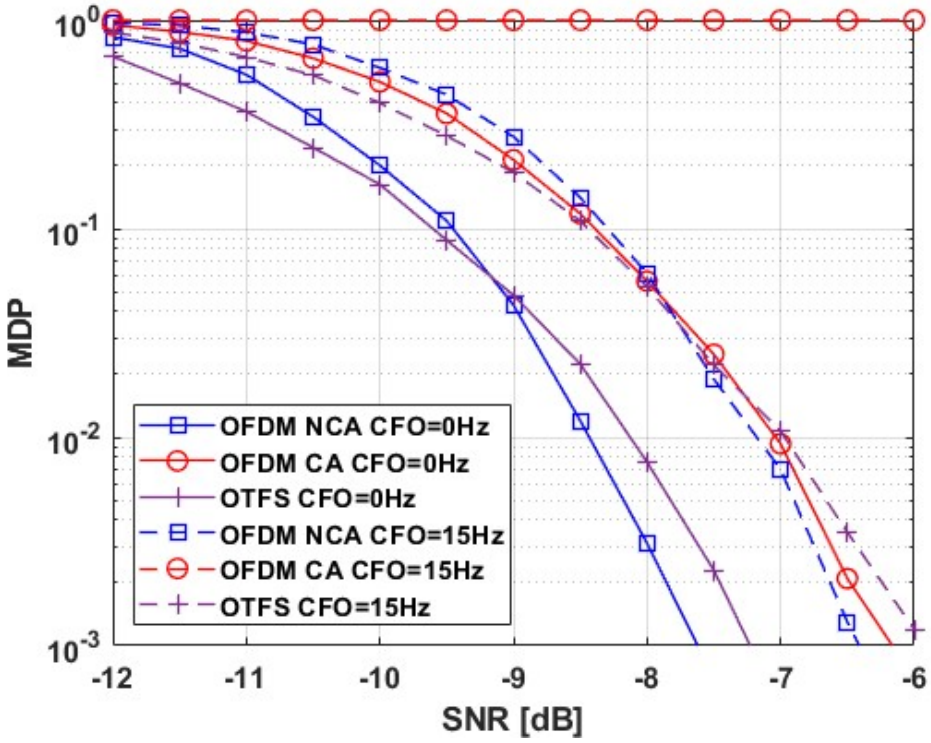

Figure 113: *MDP versus SNR for N_U=2*

The curves depicted in Figure 112 illustrate that OTFS and OFDM NCA achieve comparable performance in terms of preamble detection and delay estimation. The performance gap is limited to a maximum of 0.5 dB. This result indicates that the proposed detector effectively mitigates the adverse effects of fractional delays on OTFS. Moreover, unlike OFDM NCA, OTFS prevents the energy wastage that implies transmitting the CP. As a result, the energy required to transmit the OTFS-based preamble is reduced by a factor $1 + (N - 1)/N$ compared to its OFDM NCA counterpart. Consequently, the implementation of OFDM NCA comes at the cost of increasing energy consumption by 2.43 dB. Additionally, it is observed that OFDM CA exhibits poor performance under the evaluated conditions. To understand this result it is essential to note that the size of the detection window determines the number of noise samples that are accumulated. Given that OFDM CA employs the largest detection window, it follows that the noise energy at the detector input will be maximized.

It is obvious that the MDP increases significantly as the CFO approaches $\Delta_f/2$. As shown in Figure 112, OTFS and OFDM NCA achieve comparable robustness to the CFO. However, it is important to note that OFDM CA is considerably more sensitive to the CFO than the other two schemes. As previously discussed, when OFDM is used as the modulation scheme, the presence of CFO prevents coherent combination of the received sequences for preamble detection. Consequently, OFDM CA fails to support random access under such conditions, as illustrated in Figure 112.

Figure 113 shows the MDP in the scenario where two users are simultaneously requesting access in the same time-frequency resources. The analysis focuses on the case where users pick different preambles, thus avoiding collisions. As expected, with the increase in the number of active UEs, the MDP increases as well. This effect arises from the lack of orthogonality among preambles, which are generated from different root sequences. The curves in Figure 113 indicate that inter-user interference degrades the performance of all schemes to a similar extent.

8 CONCLUSION

D4.5 is the last version of the deliverable on the unified and data-driven air interface for 6G NTN, whose primary purpose is to provide guidance related to the design of the flexible waveform for 6G NTN systems based on the outcomes of the evaluation of a set of waveforms identified by the project as potential candidates for the NTN component of 6G.

Deliverable D4.1 identified a set of potential waveforms for 6G NTN (i.e., CP-OFDM, DFT-s-OFDM, BF-OFDM, WOLA-OFDM, UFMC, F-OFDM, BF-OFDM, and OTFS) and provided their preliminary performance evaluation in terms of PAPR, PSD with and without HPA amplification, and BER/BLER with and without phase noise and interference introduced by in-band distortions (caused by the HPA) and frequency selective channels. Building upon this foundation, deliverable D4.5 extended the analysis by assessing the candidate waveforms under additional KPIs and by developing and testing advanced solutions to enable robust system operation under typical NTN impairments, such as high propagation delays and Doppler shifts.

The work was organized into three main activities.

i. Waveform analysis and comparative evaluation.

Robustness to time and frequency synchronization errors.

The main conclusion of this analysis is that, under these two KPIs, WOLA-OFDM offers a good alternative to CP-OFDM. Indeed, focusing on the robustness to frequency synchronization errors, as evidenced, DFT precoding and some filtered waveform variants (i.e., BF-OFDM and F-OFDM) exhibit a minor degradation in their robustness relative to CP-OFDM due to the impact of the additionally observed ICI and filter dispersion, respectively; unlike UFMC, which suffers more significantly from its further constraining noise enhancement limitation. On the contrary, WOLA observes a slightly improved robustness associated with the improved phase continuity between symbols of the windowing, overlapping, and adding operations. Looking at the robustness to time synchronization errors, filtered OFDM variants differ more significantly from the legacy CP-OFDM among the considered alternatives, especially around the CP protection window boundaries. Indeed, the time dispersion of filtering/windowing techniques causes a tapering of the effective CP protection window boundaries. As a result of such tapering, the performance detriment is softened around the CP window of protection at the expense of a reduction of the region with zero degradation. OTFS with one CP per OTFS block provides similar performance to that of CP-OFDM in terms of robustness to frequency synchronization errors Its inherent flexibility in defining the CP placement improves resilience to time synchronization errors.

Based on the studies on robustness to synchronization errors, it can be concluded that WOLA offers a good alternative to CP-OFDM.

In-band distortion and out-of-band emission measurements.

Numerical results, in terms of total degradation and adjacent channel leakage ratio, show that a low PAPR proves key in driving both in-band distortion and out-of-band emissions. On the contrary, a high PAPR requires a large backoff for the same level of requirements, which further reduces the power amplifier efficiency. Notably, it was observed that the total degradation (TD) reduction leveraged by filtered

waveform variants and OTFS relative to CP-OFDM at 30 dB of ACLR requirements is half of that in the case of the PAPR-reduced DFT-s-OFDM variant (1 dB instead of 2 dB of TD reduction), despite its larger out-of-band emissions prior to amplification. Therefore, it was concluded that filtering techniques must be considered secondary to low PAPR techniques for simultaneous in-band and out-of-band emissions reductions at such ACLR requirements. Indeed, the WOLA variant becomes an attractive alternative to complex filtering from this standpoint as well, providing the benefits of low intrinsic out-of-band emissions via modest windowing, overlapping, and adding operations.

Assessment of the number and configuration of demodulation reference signals.

Focusing on CP-OFDM, considering the trade-off with spectral efficiency, two DMRS symbols per slot are sufficient to compensate for frequency offset in the considered scenarios; however, DMRS cannot correct the misalignment of symbol timing and sampling points at the receiver. Indeed, results show that increasing the number of DMRS symbols improves BER under large frequency offsets; however, adding more than two DMRS symbols per slot does not yield further improvement. The impact of different DMRS patterns on BER performance under different time offsets was investigated. Results indicate that increasing the number of DMRS symbols does not improve BER.

Regarding OTFS, results with an impulsive pilot, surrounded by a number of zeros equal to the number of DMRS used for CP-OFDM, show that the greater the number of zeros around the pilot, the greater is the equivalent power of the pilot, better is the estimation of frequency offset. However, it comes at the expense of high PAPR. The length of the guard symbols depends on the length of the channel impulse response. The pilot can be exploited also to estimate the time offset.

Scoring of the candidate waveforms.

The results produced in both D4.1 and D4.5 have been merged to compare the waveforms. The analyses show that there is no waveform better than CP-OFDM in all KPIs. On the contrary, each waveform exhibits distinct trade-offs relative to the evaluated technical metrics.

Assessment of DFT-s-OFDM PAPR in multi-user multi-beam scenario.

The numerical analysis highlighted the fundamental limitation of single-carrier precoding schemes in multi-beam NTN systems.

In the single-user single-beam scenario, DFT precoding remains the most cost-effective technique, among the ones considered in this deliverable, for improving TD and ACLR. Therefore, we completed the study by assessing the performance of two PAPR reduction methods for the relevant NTN case of multiple users in the downlink. The PAPR reduction performance of DFT-s-OFDM and PTS-enhanced DFT-s-OFDM were analyzed over frequency and space division multiplexing. The results show the PAPR advantage of DFT-s-OFDM over CP-OFDM rapidly collapses with increasing multiuser load in all multiplexing schemes and their orders (either frequency multiplexing, space multiplexing, or their combination). The PAPR reduction benefit of the DFT precoding waveform variant decreases by more than two-thirds as the number of users increases from one to five (1 dB from 3 dB obtained over a single user). Alternatively, the considered PTS-enhanced DFT-s-OFDM scheme manages to sustain a low PAPR with the number of users multiplexed in the frequency domain for a single beam, but fails to sustain it over

more than one beam. Particularly, owing to the challenge in operating PTS across beams, the PAPR improvement of PTS-enhanced DFT-s-OFDM stays well under 1 dB relative to conventional DFT-s-OFDM above one beam. In view of the reliance of modern payload architecture on beamforming and active antenna systems, the obtained results underscore the relevance of research towards techniques that allow for sustaining a low PAPR under many simultaneously active beams. This study complements the previous one by addressing the impact of multiuser multiplexing on PAPR performance, which helps to understand the behavior of DFT-s-OFDM and its variants under realistic multiuser NTN scenarios.

ii. Definition of wireless propagation models for NTN within the new frequency bands addressed in the project (i.e., C, Q, and V bands) by means of ray tracing simulations of specific scenarios.

Ray tracing (RT) results showed that the wireless channel in the C band basically keeps the same properties it has in the S band, and the same holds between the Q and the V band, though to a slightly lesser extent.

Since free space loss increases proportionally to the square of the frequency, it can be easily computed at any frequency of interest. The evaluation of additional loss due to atmospheric gases and rain can rely on recommendations released by ITU. With reference to scintillation effects, tropospheric scintillations mostly affect the Q and V bands, but it is important just at very low elevation angles, whereas ionospheric scintillation is known to be a possible threat at lower communication frequencies, but in C band it is actually quite light. In case the ground equipment is located indoor, building entry loss must be also considered, thus making indoor wireless coverage a more challenging task compared to the outdoor case. Not surprisingly, the entry loss is greatly affected by the percentage of building walls covered in glass. It is also worth pointing out that much heavier attenuation must be expected in modern buildings where infrared reflecting glass is often used to to improve the buildings energy efficiency, to the extent that it may result in an especially harsh problem for indoor wireless coverage in NTN.
Since the forthcoming NTNs are expected to complement terrestrial cellular networks to create a single, integrated communication infrastructure, satellites (or UAVs and HAPs) will provide wireless connectivity also to (mobile) terrestrial users at street level in (dense) urban environment, where NLoS propagation conditions in general occur with greater probability compared to standard ground equipment placed at building roof level or in open, rural areas. Therefore, multipath propagation may represent an issue to take into consideration. The intensity of multipath effects can be evaluated by means of several parameters. Rice factor and delay spread have been in particular investigated by means of ray tracing simulations carried out in different urban scenarios, at different frequencies and elevation angles, and for different radiation patterns of the ground antenna. Results show that both Rice factor and delay spread are in general clearly affected by the occurrence of the LoS condition. In particular, satellite elevation and height of the ground station represent the main factors affecting the LoS condition. With reference to the antenna pattern, a reduction of the beam width entails a larger number of multipath components reaching the ground station antenna out of its main radiation lobe, and this results in greater Rice factor and lower delay spread.

iii. Design and assessment of advanced solutions for the 6G NTN air interface.

AI-based 6G NTN air interface.

- By designing a deep learning-based channel predictor to alternate between pilot-assisted and pilot-free transmission slots, it is possible to achieve consistent throughput gains.

  Indeed, in the considered system model, additional resource elements were allocated to data transmission by avoiding the transmission of pilot symbols every other slot. Regular slots, i.e., slots that carry pilots, were equalized by means of channel estimation; the estimated channel frequency response is then fed to the channel prediction model to obtain a channel frequency response estimate to equalize the succeeding slot. While the considered system model assumes the transmission of a pilot-less slot every other slot, further throughput gains can be achieved by further reducing the pilots transmission periodicity, i.e., inserting multiple pilot-less slots. To maintain high prediction accuracy, prediction models which outputs temporally span multiple slots should be avoided. Instead, iterative prediction techniques can be considered, where the channel frequency response (CFR) at each slot is obtained by means of prediction based on the refined CFR at the preceding slot, where the refinement step employs the demodulated symbols as pilots to reduce the propagation of CFR errors. Furthermore, hardware implementations of the channel predictors should be developed to assess the real-world inference latency and verify the real time feasibility of the considered models under strict power constraints.

- The DRL-based adaptive backoff index (BI) optimization framework is able to enhance the RA procedure in 6G NTN environments. By formulating the BI configuration task as a missed detection probability (MDP), the proposed approach enables dynamic, context-aware adjustment of BI values in response to varying network states. Unlike static or heuristic BI configurations, the DRL agent learns an optimal policy that minimizes access delay while maintaining a low collision probability.

Review and modification of the HARQ mechanism.

The maximum-distance separable hybrid automatic repeat request (MDS-HARQ) approach offers an effective compromise between reliability and efficiency.

The proposed scheme reduces feedback overhead and improves throughput compared to fully disabled feedback, while maintaining competitive reliability performance. Simulation results demonstrated that MDS-HARQ over NTN, particularly with the smart feedback mechanism, achieves significant gains in block error rate and throughput at moderate-to-high SNR values, confirming its suitability for next-generation satellite systems where feedback is costly or delayed. Moreover, the results indicate that the studied HARQ, when properly adapted, can support robust communications even in challenging propagation environments such as indoor communications, being able to achieve successful decoding even at SNR levels as low as –15 dB. Overall, this study highlights the potential of HARQ schemes to adapt and to enhance communication efficiency and robustness in NTN scenarios. The novel HARQ study conducted in this project, particularly for the partial feedback configuration, provides valuable insights that can guide future enhancements to the 3GPP standard. Indeed, these results serve as a reference for improving the efficiency and reliability of the HARQ in NTN networks, supporting better performance across different satellite constellations and deployment scenarios.

Assessment and adaptation of the downlink and uplink synchronization procedures during the initial access to work without GNSS.

- The downlink synchronization procedure has been modified by including 2 SSB for the fine detection, leading to an improvement of 10-25% of the signal detection probability between -15 and -11 dB SNR region.

  To achieve such improvement, a two-stage hierarchical synchronization strategy has been designed and assessed. The proposed architecture first performs a wide, computationally efficient coarse search using a PSS-based cross-correlator followed by a highly selective fine synchronization stage that leverages both PSS and SSS with a generalize likelihood ratio test (GLRT)-based criterion for improved accuracy. The fine detection stage was shown to significantly improve Doppler estimation, achieving a RMSE of less than 1 kHz at an SNR of -6 dB. Results revealed that while satellite elevation has a small impact on detection performance, the number of SSBs used in the fine stage is critical. Coherently combining just two SSBs was sufficient to achieve a 2 dB performance gain, effectively closing the gap between coarse PSS detection and reliable Cell ID acquisition. This finding presents a flexible option to achieve trade-off between performance and complexity for practical receiver design. This framework could be extended to the connected-mode tracking phase.

- For the uplink synchronization procedure, two different solutions have been proposed considering two distinct waveforms:

  - CP-OFDM: SSB and PRS have been compared as candidate solutions to allow the computation of the UE position after the downlink synchronization. The PRS proves to be a good candidate, due to its flexibility. However, it is not a broadcast signal. In addition, modifications should be made, such as introducing K_comb = 1 and N_symb= 14 values, so that this signal can be configured as a continuous waveform, which would limit the correlation side lobes. SSB seems to be more promising than the use of PRS. However, PSS is very redundant (there are only 3 sequences) which requires the terminal to identify the SSS to remove any ambiguity.

  - OTFS: the design of a preamble based on identical ZC sequences modulated into a delay–Doppler domain OTFS waveform ensures more reliable random-access success under challenging synchronization conditions.

    Unlike traditional OFDM-based designs, which employ long cyclic prefixes and sequential detection methods vulnerable to error propagation, the proposed approach presents a single-step joint detection algorithm capable of simultaneously estimating both fractional and integer delays. Analytical derivations and simulation results demonstrate that the proposed DZT-OTFS preamble structure achieves performance comparable to advanced OFDM-based schemes in terms of MDP and PAPR, while delivering notable enhancements in spectrum containment and overhead reduction. By eliminating the need for long cyclic prefixes, the design significantly improves energy efficiency and simplifies receiver processing. Furthermore, the DZT-OTFS scheme exhibits enhanced tolerance to CFO compared with OFDM approaches that employ coherent accumulation, thereby ensuring more reliable random access under challenging synchronization conditions.

It is worth emphasizing that the waveforms were compared considering both C-band and Q/V band frequency bands, with a bandwidth spanning from 5 to 50 MHz, according to the scenario. Moreover, the simulated hardware (e.g., definition of the HPA) and channel impairments (such as time and frequency offsets) were selected to ensure consistency with the reference scenarios defined in the 6G-NTN project.

As high-level conclusions, the analysis shows that each waveform exhibits distinct trade-offs relative to the evaluated technical metrics, suggesting that the waveform selection shall also take into consideration other metrics, such as satisfaction of coexistence requirements between TN and NTN, backward compatibility with 5G waveforms, , and, in particular, the possibility of harmonizing TN and NTN configurations to limit complexity. Indeed, a harmonized waveform design can lead to simplified base station and UE implementations with a single architecture optimized for both TN and NTN, enabling cost-effective and scalable deployments in 6G. Furthermore, a harmonized waveform allows seamless handovers, maintaining service continuity as the UE moves between network domains.

Based on the analyses performed in this project, UNIBO, TASF, TH-SIX, CTTC, and DLR prepared and submitted the technical contribution to 3GPP RAN1 Meeting #122bis [170], co-signed also by the European Space Agency.

Finally, it is worthwhile noticing that the analysis and conclusions of the 6G-NTN project on the waveforms for 6G NTN align with the decision taken by 3GPP to select as a baseline CP-OFDM and DFT-s-OFDM and to further investigate improvements for the NTN component.

REFERENCES

[1] 3GPP TS 38.108; “NR; Satellite Access Node radio transmission and reception”, v19.2.0 (2025-10)

[2] 3GPP TS 36.108 “Evolved Universal Terrestrial Radio Access (E-UTRA); Satellite Access Node radio transmission and reception” v19.1.0 (2025-10)

[3] 3GPP TS 38.101-5 “NR; User Equipment (UE) radio transmission and reception; Part 5: Satellite access Radio Frequency (RF) and performance requirements”, v19.0.0 (2025-03)

[4] 3GPP TS 36.102 “Evolved Universal Terrestrial Radio Access (E-UTRA); User Equipment (UE) radio transmission and reception for satellite access” v19.1.0 (2025-10)

[5] M. Li, Y. Rui and Z. Bu, Fourier Transform Based Transmission Systems for Broadband Wireless Communications, Rijeka, Croatia: IntechOpen, 2011.

[6] 6G-NTN, “D4.1 - Report on unified and data driven air-interface for 6G-NTN (1st version)”

[7] R. Zayani, Y. Medjahdi, H. Shaiek and D. Roviras, "WOLA-OFDM: A Potential Candidate for Asynchronous 5G," in 2016 IEEE Globecom Workshops, Washington, DC, USA, 2016.

[8] Y. Liu et al., "Waveform Design for 5G Networks: Analysis and Comparison," in IEEE Access, vol. 5, pp. 19282-19292, 2017.

[9] 3GPP TS 38.211 “NR; Physical channels and modulation v19.1.0”

[10] George, Geordie, et al. "5G new radio in nonlinear satellite downlink: A physical layer comparison with DVB-S2X." 2021 IEEE 4th 5G World Forum (5GWF). IEEE, 2021.

[11] 3GPP TR 38.811, “Study on New Radio (NR) to support non-terrestrial networks” (Rel. 15), September 2020.

[12] A. Maltsev, A. Lomayev, A. Khoryaev, A. Sevastyanov and R. Maslennikov, “Comparison of Power Amplifier Non-Linearity Impact on 60 GHz Single Carrier and OFDM Systems,” in 7th IEEE Consumer Communications and Networking Conference, Las Vegas, NV, USA, 2010.

[13] R. Gerzaguet et al., "The 5G candidate waveform race: a comparison of complexity and performance." EURASIP Journal on Wireless Communications and Networking 2017.1 (2017): 13.

[14] R. Gerzaguet et al., "Comparison of promising candidate waveforms for 5G: WOLA-OFDM versus BF-OFDM," 2017 International Symposium on Wireless Communication Systems (ISWCS), Bologna, Italy, 2017, pp. 355-359, doi: 10.1109/ISWCS.2017.8108139.

[15] D. Demmer, R. Gerzaguet, J. -B. Doré, D. Le Ruyet and D. Kténas, "Block-filtered OFDM: A novel waveform for future wireless technologies," 2017 IEEE International Conference on Communications (ICC), Paris, France, 2017, pp. 1-6, doi: 10.1109/ICC.2017.7997061.

[16] Farhang, Arman, et al. "Low complexity modem structure for OFDM-based orthogonal time frequency space modulation." *IEEE wireless communications letters* 7.3 (2017): 344-347.

[17] K. Anwar, A. Priantoro, M. Saito, T. Hara, M. Okada and H. Yamamoto, “On the PAPR reduction for wavelet based transmultiplexer,” in *IEEE International Symposium on Communications and Information Technology, 2004. ISCIT 2004.*, Sapporo, Japan, 2004.

[18] K. Xu and D. L. Jones, “PAPR REDUCTION FOR BEAMFORMING OFDM VIA CONSTELLATION-BEAM,” in *2009 Conference Record of the Forty-Third Asilomar Conference on Signals, Systems and Computers*, Pacific Grove, CA, USA

[19] C. A. Schmidt, M. Crussière and J. F. Hélard, “Digital Beamforming with PAPR Reduction: An Approach for Energy Efficient Massive MIMO,” in *2020 IEEE 91st Vehicular Technology Conference (VTC2020-Spring)*, Antwerp, Belgium, 2020

[20] A. R. M. Ismail, M. Guenach, A. Bourdoux and H. Steendam, “PAPR Reduction in Single Carrier Modulation at Sub-THz Band,” in *Globecom 2024*, Cape Town, South Africa, 2024.

[21] N. Dinur and D. Wulich, “Peak-to-average power ratio in high-order OFDM,” *IEEE Transactions on Communications,* vol. 49, no. 6, 2001.

[22] T. Sravanti and N. Vasantha, “Precoding PTS scheme for PAPR reduction in OFDM,” in *2017 International Conference on Innovations in Electrical, Electronics, Instrumentation and Media Technology (ICEEIMT)*, Coimbatore, India, 2017.

[23] 6G-NTN, “D3.3 - Software defined payload and its scalability“

[24] E. Lutz et al., “The Land Mobile Satellite Communication Channel-Recording, Statistics, and Channel Model”, IEEE Trans. on Veh. Tech, vol. 40, No. 2, May 1991, pp. 375-386, DOI: 10.1109/25.289418

[25] J. Huang, Y. Cao, X. Raimundo, A. Cheema, S. Salous, “*Rain Statistics Investigation and Rain Attenuation Modeling for Millimeter Wave Short-Range Fixed Links*”, IEEE Access, vol. 7, pp. 156110-156120, October 2019, doi: 10.1109/ACCESS.2019.2949437;

[26] A.D. Panagopulos, P-D M. Arapoglou, P.G. Cottis, “*Satellite Communications at Ku, Ka, and V bands: Propagation Impairments and Mitigation Techniques”*, IEEE Comm. Surveys & tutorials, vol. 6, No. 3, pp. 2-14, Third Quarter 2004, doi: 10.1109/COMST.2004.5342290;

[27] Rec. ITU-R P.676-11: “Attenuation by atmospheric gases”;

[28] Rec. ITU-R P.618-14, “Propagation data and prediction methods required for the design of Earth-space telecommunication systems”, August 2023;

[29] Rec. ITU-R P.531-15, “Ionospheric propagation data and prediction methods required for the design of satellite networks and systems”, August 2023;

[30] ETSI TR 38.901, “Study on channel models for frequencies from 0.5 to 100 GHz”, April 2022;

[31] E.M. Vitucci, V. Degli Esposti, F. Mani, F. Fuschini, M. Barbiroli, M. Gan, C. Li, J. Zhao, Z. Zhong , “Tuning Ray Tracing for Mm-wave Coverage Prediction in Outdoor Urban Scenarios”, Radio Science, vol. 54, no. 11, pp. 1112-1128, November 2019, DOI: 10.1029/2019RS006869;

[32] V. Degli Esposti, F. Fuschini, E. Vitucci, G. Falciasecca, “Measurement and modelling of scattering from buildings”, IEEE Transactions on Antennas and Propagation, vol. 55, No. 1, January 2007, pp. 143-153, DOI: 10.1109/TAP.2006.888422;

[33] H.L Bertoni, “Radio Propagation for Modern Wireless Systems”, Prentice Hall, 2000;

[34] A. Guidotti *et al.*, "The path to 5G-Advanced and 6G Non-Terrestrial Network systems," *2022 11th Advanced Satellite Multimedia Systems Conference and the 17th Signal Processing for Space Communications Workshop (ASMS/SPSC)*, Graz, Austria, 2022, pp. 1-8, doi: 10.1109/ASMS/SPSC55670.2022.9914764.

[35] F. Fourati and M.-S. Alouini, "Artificial intelligence for satellite communication: A review," *Intell. Converg. Netw.*, vol. 2, no. 3, pp. 213–243, Sep. 2021, doi: 10.23919/ICN.2021.0015.

[36] S. Mahboob and L. Liu, "Revolutionizing future connectivity: A contemporary survey on AI-empowered satellite-based non-terrestrial networks in 6G," *IEEE Commun. Surveys Tuts.*, vol. 26, no. 2, pp. 1279–1321, 2nd Quart., 2024, doi: 10.1109/COMST.2023.3347145.

[37] A. Zappone, M. Di Renzo and M. Debbah, “Wireless networks design in the era of deep learning: model-based, AI-based or both?”, *arXiv:1902.02647*, 2019.

[38] O. Simeone, “A very brief introduction to machine learning with applications to communications systems”, *IEEE Transactions on Cognitive Communications and Networking*, vol. 4, no. 4, Dec. 2018.

[39] D. Gündüz, P. de Kerret, N. D. Sidiropoulos, D. Gesbert, C. R. Murthy, M. van der Schaar, “Machine learning in the air”, *IEEE Journal on Selected Areas in Communications*, vol. 37, no. 10, Oct. 2019.

[40] A. Balatsoukas-Stimming and C. Studer, “Deep unfolding for communications systems: a survey and some new directions”, *arXiv:1906.05774*, 2019.

[41] M. Pereyra, P. Schniter, E. Chouzenoux, J.-C. Pesquet, J.-Y. Tourneret, A. O. Hero III, S. McLaughlin, “A survey of stochastic simulation and optimization methods in signal processing”, *IEEE Journal of Selected Topics in Signal Processing*, vol. 10, no. 2, Mar. 2016.

[42] A. Krizhevsky, I. Sutskever, G. E. Hinton, “ImageNet classification with deep convolutional neural networks”, *Advances in Neural Information Processing Systems*, vol. 25, pp. 1097-1105, 2012.

[43] A. Bakambekova, N. Kouzayha and T. Al-Naffouri, "On the Interplay of Artificial Intelligence and Space-Air-Ground Integrated Networks: A Survey," in *IEEE Open Journal of the Communications Society*, vol. 5, pp. 4613-4673, 2024, doi: 10.1109/OJCOMS.2024.3429198.

[44] C. -X. Wang et al., "On the Road to 6G: Visions, Requirements, Key Technologies, and Testbeds," in *IEEE Communications Surveys & Tutorials,* vol. 25, no. 2, pp. 905-974, 2nd Quart 2023, doi: 10.1109/COMST.2023.3249835.

[45] M. M. Azari et al., "Evolution of non-terrestrial networks from 5G to 6G: A survey," *IEEE Commun. Surveys Tuts.*, vol. 24, no. 4, pp. 2633–2672, 4th Quart., 2022, doi: 10.1109/COMST.2022.3199901.

[46] B. Al Homssi et al., "Artificial intelligence techniques for next-generation massive satellite networks," *IEEE Commun. Mag.*, vol. 62, no. 4, pp. 66–72, Apr. 2024, doi: 10.1109/MCOM.004.2300277.

[47] "Artificial Intelligence and Machine Learning in 3GPP Networks," 3rd Generation Partnership Project, Feb. 19, 2025. [Online]. Available: https://www.3gpp.org/news-events/3gpp-news/ai-ml-2025

[48] X. Lin, "The Bridge Toward 6G: 5G-Advanced Evolution in 3GPP Release I9,"

in *IEEE Communications Standards Magazine,* vol. 9, no. 1, pp. 28-35, March 2025, doi: 10.1109/MCOMSTD.0001.2300063.

[49] M. Huang, J. Chen and S. Feng, "Synchronization for OFDM-Based Satellite Communication System," in *IEEE Transactions on Vehicular Technology*, vol. 70, no. 6, pp. 5693-5702, June 2021, doi: 10.1109/TVT.2021.3069580.

[50] T. E. Humphreys, P. A. Iannucci, Z. M. Komodromos and A. M. Graff, "Signal Structure of the Starlink Ku-Band Downlink," in *IEEE Transactions on Aerospace and Electronic Systems*, vol. 59, no. 5, pp. 6016-6030, Oct. 2023, doi: 10.1109/TAES.2023.3268610.

[51] V. Dalakas, P. T. Mathiopoulos, F. Di Cecca and G. Gallinaro, "A Comparative Study Between SC-FDMA and OFDMA Schemes for Satellite Uplinks," *in IEEE Transactions on Broadcasting*, vol. 58, no. 3, pp. 370-378, Sept. 2012, doi: 10.1109/TBC.2012.2193494.

[52] L. Zhang, A. Ijaz, P. Xiao, M. M. Molu and R. Tafazolli, "Filtered OFDM Systems, Algorithms, and Performance Analysis for 5G and Beyond," in *IEEE Transactions on Communications*, vol. 66, no. 3, pp. 1205-1218, March 2018, doi: 10.1109/TCOMM.2017.2771242.

[53] B. Adoum, K. Zoukalne, M. Idriss , A. Ali, A. Moungache and M. Khayal, “A Comprehensive Survey of Candidate Waveforms for 5G, beyond 5G and 6G Wireless Communication Systems”. *Open Journal of Applied Sciences*, vol. 13, pp. 136-161, 2023. doi: 10.4236/ojapps.2023.131012.

[54] Y. İ. Demir, A. Yazar, and H. Arslan, "Waveform Management Approach With Machine Learning for 6G Systems," in *IEEE Transactions on Network and Service Management*, vol. 21, no. 5, pp. 5432–5444, Oct. 2024, doi: 10.1109/TNSM.2024.3407017.

[55] R. Giuliano and E. Innocenti, "Machine learning techniques for non-terrestrial networks," *Electronics*, vol. 12, no. 3, p. 652, Jan. 2023, doi: 10.3390/electronics12030652.

[56] W. Usaha and J. A. Barria, "Reinforcement learning for resource allocation in LEO satellite networks," *IEEE Trans. Syst., Man, Cybern. B, Cybern.,* vol. 37, no. 3, pp. 515–527, Jun. 2007, doi: 10.1109/TSMCB.2007.894670.

[57] X. Hu et al., "Dynamic beam hopping method based on multi-objective deep reinforcement learning for next generation satellite broadband systems," *IEEE Trans. Broadcast.*, vol. 66, no. 3, pp. 630–646, Sep. 2020, doi: 10.1109/TBC.2019.2960940.

[58] G.-Y. Chang, C.-K. Hung, and C.-H. Chen, "A CSI prediction scheme for satellite-terrestrial networks," *IEEE Internet Things J.,* vol. 10, no. 9, pp. 7774–7785, May 2023, doi: 10.1109/JIOT.2022.3207582.

[59] Ding, Junhao, and Zhiyong Luo. "Informer-CSI predict CSI for non-terrestrial networks." *Journal of Physics: Conference Series*. Vol. 2849. No. 1. IOP Publishing, 2024.

[60] S. Liu et al., "Pattern-Aware Intelligent Anti-Jamming Communication: A Sequential Deep Reinforcement Learning Approach," in *IEEE Access*, vol. 7, pp. 169204-169216, 2019, doi: 10.1109/ACCESS.2019.2954531.

[61] A. K. Gizzini, M. Chafii, A. Nimr, and G. Fettweis, “Deep learning based channel estimation schemes for ieee 802.11p standard,” *IEEE Access*, vol. 8, pp. 113 751–113 765, 2020.

[62] X. Ru, L. Wei and Y. Xu, "Model-Driven Channel Estimation for OFDM Systems

Based on Image Super-Resolution Network," *2020 IEEE 5th International Conference on Signal and Image Processing (ICSIP),* pp. 804-808, Nanjing, China, 23-25 Oct. 2020. Available: http://arxiv.org/abs/1911.13106

[63] Z. Chen, F. Gu and R. Jiang, "Channel Estimation Method Based on Transformer in High Dynamic Environment," *2020 International Conference on Wireless Communications and Signal Processing (WCSP),* pp. 817-822, 2020.

[64] D. Luan and J. Thompson, “Attention based neural networks for wireless channel estimation," arXiv preprint, *arXiv:2204.13465*, April 2022.

[65] L. Li, H. Chen, H. -H. Chang and L. Liu, "Deep Residual Learning Meets OFDM Channel Estimation," in *IEEE Wireless Communications Letters*, vol. 9, no. 5, pp. 615-618, May 2020.

[66] D. Luan and J. Thompson, “Low complexity channel estimation with neural networks solutions," arXiv preprint, *arXiv:2201.09934v1*, January 2022.

[67] M. v. Lier, A. Balatsoukas-Stimming, H. Corporaal and Z. Zivkovic, "OPTCOMNET: Optimized Neural Networks for Low-Complexity Channel Estimation," in *Proc. of ICC 2020 - 2020 IEEE International Conference on Communications (ICC)*, pp. 1-6, June 2020.

[68] M. J. Kang, J. H. Lee, and S. H. Chae, "Channel estimation with DnCNN in massive MISO LEO satellite systems," in *Proc. 2023 14th Int. Conf. Ubiquitous Future Netw. (ICUFN),* 2023, pp. 825–827, doi: 10.1109/ICUFN57871.2023.10267890.

[69] T. Kim et al., "RSRP based Doppler shift estimator using machine learning in high-speed train systems," *IEEE Trans. Veh. Technol.*, vol. 70, no. 1, pp. 371–380, Jan. 2021, doi: 10.1109/TVT.2020.3038814.

[70] E. Yoon, S. Kwon, U. Yun, and S.-Y. Kim, "Doppler spread estimation based on machine learning for an OFDM system," *Wireless Commun. Mobile Comput.*, vol. 2021, Article ID 6678992, 2021, doi: 10.1155/2021/6678992.

[71] T. Ngo, B. T. Kelley, and P. Rad, "Deep learning based prediction of Doppler shift for mobile communications," in *Proc. 2021 Telecoms Conf. (ConfTELE)*, 2021, pp. 1–6, doi: 10.1109/ConfTELE50222.2021.9435472.

[72] S. Kim, J. Park, and C. Lee, "CNN-based Doppler shift estimation for low earth orbit satellites," in *Proc. 2022 37th Int. Tech. Conf. Circuits/Syst., Comput. Commun. (ITC-CSCC),* 2022, pp. 1–3, doi: 10.1109/ITC-CSCC55564.2022.9894810.

[73] J. Ji, N. P. Tran, Z. Xiong, K. Zhu, and T. Q. S. Quek, "Deep Complex-valued Convolutional Learning for Waveform OFDM Receiver Design," in *Proc. IEEE Wireless Communications and Networking Conference (WCNC)*, Milan, Italy, Mar. 2025, pp. 1–6, doi: 10.1109/WCNC61545.2025.10978276.

[74] H. Ye, G. Ye Li and B.-H. Juang, “Power of Deep Learning for Channel Estimation and Signal Detection in OFDM Systems”, *IEEE Wireless Communications Letters*, vol. 7, no. 1, Feb. 2018.

[75] P. Jiang, T. Wang, B. Han, C.-K. Wen, S. Jin and G. Ye Li, “Artificial Intelligence-aided OFDM Receiver: Design and Experimental Results”, *arXiv preprint, 1812.06638*, Dec. 2018.

[76] X. Gao, S. Jin, C.-K. Wen and G. Ye Li, “ComNet: Combination of Deep Learning and Expert Knowledge in OFDM Receivers”, *IEEE Communications Letters*, vol. 22, no. 12, Dec. 2018.

[77] A. Felix, S. Cammerer, S. Dörner, J. Hoydis and S. ten Brink, “OFDM-Autoencoder for End-to-end Learning of Communications Systems”, *Proceedings of IEEE SPAWC*, Kalamata, Greece, 2018.

[78] L. Bahl, J. Cocke, F. Jelinek and J. Raviv, “Optimal decoding of linear codes for minimizing symbol error rate”, IEEE Transactions on Information Theory, vol. 20, no 2, Mar. 1974.

[79] M. Tüchler and A. C. Singer, “Turbo Equalization: an Overview”, *IEEE Transactions on Information Theory*, pp. 920-952, Feb. 2011.

[80] H. He, C.-K. Wen, S. Jin and G. Ye Li, “A model-driven deep learning network for MIMO detection”, *Proceedings of the IEEE GlobalSIP*, Anaheim, CA, USA Nov. 2018.

[81] H. He, C.-K. Wen, S. Jin and G. Ye Li, “Deep learning-based channel estimation for beamspace mmWave Massive MIMO Systems”, *IEEE Wireless Communications Letters*, vol. 7, no. 5, Oct. 2018.

[82] H. He, C.-K. Wen, S. Jin and G. Y. Li, “Model-Driven Deep Learning for Joint MIMO Channel Estimation and Signal Detection”, *arXiv preprint, 1907.09439*, Jul. 2019.

[83] J. Zhang, C.-K. Wen, S. Jin and G. Ye-Li, “Artificial Intelligence-aided Receiver for a CP-free OFDM System: Design, Simulation and Experimental Test”, *IEEE Access*, May 2019.

[84] J. Zhang, X. Yang, C.-K. Wen, X. Li and S. Jin, “Improved ComNet based on Expectation Propagation for CP-Free OFDM System“, *Proceedings of IEEE/CIC ICCC*, Changchun, China, Aug. 2019.

[85] A. Michon, F. A. Aoudia and K. P. Srinath, "Convolutional Self-Attention-Based Multi-User MIMO Demapper," in *Proc. of ICC 2022 - IEEE International Conference on Communications*, Seoul, Korea, Republic of, 2022, pp. 2621-2626.

[86] 3GPP TS 38.300: “5G; NR; NR and NG-RAN Overall description; Stage-2”, v17.2.0.

[87] Juan Montojo, “AI/ML for NR Air Interface”, Rapporteur for RAN1-led study on AI/ML, Qualcomm Inc., Available: https://www.3gpp.org/technologies/ai-ml/nr.

[88] 3GPP TR 37.817: “E-UTRA and NR; Study on enhancement for Data Collection for NR and EN-DC”, v17.0.0.

[89] 3GPP TR 37.817; “E-UTRA and NR; Study on Artificial Intelligence (AI)/Machine Learning (ML) for NR air interface”, v18.0.0.

[90] T. O’Shea, T. Zhang, V. Zakharchenko, “White Papier: Amplifying 5G vRAN Performance with Artificial Intelligence & Deep Learning”, DeepSig, Intel Corporation, 2022.

[91] C. You, Y. Cai, Y. Liu, M. Di Renzo, T. M. Duman, A. Yener, A. L. Swindlehurst, “Next Generation Advanced Transceiver Technologies for 6G and Beyond”, *arXiv:2403.16458*, Mar. 2024.

[92] S. Dörner, S. Cammerer, J. Hoydis, and S. t. Brink, “Deep learning based communication over the air”, *IEEE Journal of Selected Topics in Signal Processing*, pp. 132-143, Feb. 2018.

[93] B. Hilburn, T. O’Shea, T. Roy and N. West, “DeepSig: Deep Learning for Wireless Communications”, Web: https://devblogs.nvidia.com/deepsig-deep-learning-wireless-communications/, Aug, 2018.

[94] "OMNIPHY-5G: Enhancing 5G RAN Performance with Machine Learning", Web: https://www.deepsig.io/omniphy-5g , Visited: 06/01/2020.

[95] W. Qi, C. Ye, D. J. Korpi, C. Gong, Y. Jin, and T. Yang, "iDeepRx Enabled 100 Gb/s DFT-s-OFDM Data Transmission Over 220 GHz Testbed," in *Proc. IEEE International Conference on Communications (ICC)*, Rome, Italy, May 2023, pp. 3684–3689, doi: 10.1109/ICC45041.2023.10278696.

[96] Pihlajasalo, D. Korpi, T. Riihonen, J. Talvitie and M. Valkama, "Machine Learning Physical-Layer Receivers for DFT-s-OFDM," in *IEEE Transactions on Vehicular Technology*, doi: 10.1109/TVT.2025.3556843.

[97] B. S. de C. da Silva, V. D. P. Souto, R. D. Souza, and L. L. Mendes, "A Survey of PAPR Techniques Based on Machine Learning," *Sensors*, vol. 24, no. 6, p. 1918, Mar. 2024. doi: 10.3390/s24061918.

[98] F. Carpi, S. Rostami, J. Cho, S. Garg, E. Erkip and C. J. Zhang, "Learned Pulse Shaping Design for PAPR Reduction in DFT-s-OFDM," 2024 *IEEE 25th International Workshop on Signal Processing Advances in Wireless Communications (SPAWC),* Lucca, Italy, 2024, pp. 406-410, doi: 10.1109/SPAWC60668.2024.10694070.

[99] F. Ait Aoudia and J. Hoydis, "End-to-End Learning for OFDM: From Neural Receivers to Pilotless Communication," in *IEEE Transactions on Wireless Communications*, vol. 21, no. 2, pp. 1049-1063, Feb. 2022, doi: 10.1109/TWC.2021.3101364.

[100] F. Ait Aoudia and J. Hoydis, "Waveform Learning for Next-Generation Wireless Communication Systems," in *IEEE Transactions on Communications*, vol. 70, no. 6, pp. 3804-3817, June 2022, doi: 10.1109/TCOMM.2022.3164060.

[101] 3GPP, 'TR 38.843 - Study on artificial intelligence (AI)/machine learning (ML) for NR air interface (Release 18)'. 2024.

[102] M. Ying, X. Chen, Q. Qi, and W. Gerstacker, 'Deep Learning-Based Joint Channel Prediction and Multibeam Precoding for LEO Satellite Internet of Things', *IEEE Trans. Wireless Commun.*, vol. 23, no. 10, pp. 13946–13960, Oct. 2024, doi: 10.1109/TWC.2024.3406952.

[103] Y. Zhang, A. Liu, P. Li, and S. Jiang, 'Deep Learning (DL)-Based Channel Prediction and Hybrid Beamforming for LEO Satellite Massive MIMO System', *IEEE Internet Things J.*, vol. 9, no. 23, pp. 23705–23715, Dec. 2022, doi: 10.1109/JIOT.2022.3190412.

[104] Y. Zhang, Y. Wu, A. Liu, X. Xia, T. Pan, and X. Liu, 'Deep Learning-Based Channel Prediction for LEO Satellite Massive MIMO Communication System', *IEEE Wireless Commun. Lett.*, vol. 10, no. 8, pp. 1835–1839, Aug. 2021, doi: 10.1109/LWC.2021.3083267.

[105] J. Wang *et al.*, 'A Lightweight Channel Prediction Network for UAV-LEO Satellite Communications', *IEEE Wireless Commun. Lett.*, vol. 14, no. 1, pp. 113–117, Jan. 2025, doi: 10.1109/LWC.2024.3489677.

[106] B. De Filippo, R. Campana, A. Guidotti, C. Amatetti, and A. Vanelli-Coralli, 'Cell-Free MIMO in 6G NTN with AI-predicted CSI', in *2024 IEEE 25th International Workshop on Signal Processing Advances in Wireless Communications (SPAWC)*, Lucca, Italy: IEEE, Sep. 2024, pp. 631–635. doi: 10.1109/SPAWC60668.2024.10694298.

[107] C. Cui, W. Jing, Z. Lu, and X. Wen, 'Attention Aided Channel Prediction Scheme

For Satellite-Terrestrial Networks', in *2024 IEEE 35th International Symposium on Personal, Indoor and Mobile Radio Communications (PIMRC)*, Valencia, Spain: IEEE, Sep. 2024, pp. 1–5. doi: 10.1109/PIMRC59610.2024.10817356.

[108] O. Abbasi and G. Kaddoum, 'Channel Aging-Aware LSTM-Based Channel Prediction for Satellite Communications', *IEEE Netw. Lett.*, vol. 6, no. 3, pp. 183–187, Sep. 2024, doi: 10.1109/LNET.2024.3444495.

[109] B. De Filippo, C. Amatetti and A. Vanelli-Coralli, "Channel Prediction in 6G Non-Terrestrial Networks With Deep Learning: a Physical Layer Analysis," *2025 IEEE International Conference on Machine Learning for Communication and Networking (ICMLCN)*, Barcelona, Spain, 2025, pp. 1-6, doi: 10.1109/ICMLCN64995.2025.11140545.

[110] B. De Filippo, C. Amatetti and A. Vanelli-Coralli, "Uplink OFDM Channel Prediction with Hybrid CNN-LSTM for 6G Non-Terrestrial Networks," *2025 Joint European Conference on Networks and Communications & 6G Summit (EuCNC/6G Summit)*, Poznan, Poland, 2025, pp. 7-12, doi: 10.1109/EuCNC/6GSummit63408.2025.11037085.

[111] A. Chaurasia and E. Culurciello, 'LinkNet: Exploiting encoder representations for efficient semantic segmentation', in *2017 IEEE Visual Communications and Image Processing (VCIP)*, St. Petersburg, FL: IEEE, Dec. 2017, pp. 1–4. doi: 10.1109/VCIP.2017.8305148.

[112] S. Bai, J. Z. Kolter, and V. Koltun, 'An Empirical Evaluation of Generic Convolutional and Recurrent Networks for Sequence Modeling', Apr. 19, 2018, *arXiv*: arXiv:1803.01271. doi: 10.48550/arXiv.1803.01271.

[113] O. Ronneberger, P. Fischer, and T. Brox, 'U-Net: Convolutional Networks for Biomedical Image Segmentation', May 18, 2015, *arXiv*: arXiv:1505.04597. doi: 10.48550/arXiv.1505.04597.

[114] J. Hoydis *et al.*, *Sionna*. (2022). [Online]. Available: https://nvlabs.github.io/sionna/

[115] D. P. Kingma and J. Ba, 'Adam: A Method for Stochastic Optimization', Jan. 30, 2017, *arXiv*: arXiv:1412.6980. doi: 10.48550/arXiv.1412.6980.

[116] P. Freire, S. Srivallapanondh, A. Napoli, J. E. Prilepsky, and S. K. Turitsyn, 'Computational Complexity Evaluation of Neural Network Applications in Signal Processing', Mar. 10, 2024, *arXiv*: arXiv:2206.12191. doi: 10.48550/arXiv.2206.12191.

[117] L. Lamberti *et al.*, 'Distilling Tiny and Ultrafast Deep Neural Networks for Autonomous Navigation on Nano-UAVs', *IEEE Internet Things J.*, vol. 11, no. 20, pp. 33269–33281, Oct. 2024, doi: 10.1109/JIOT.2024.3431913.

[118] J. Guo, J. Wang, C.-K. Wen, S. Jin, and G. Y. Li, 'Compression and Acceleration of Neural Networks for Communications', *IEEE Wireless Commun.*, vol. 27, no. 4, pp. 110–117, Aug. 2020, doi: 10.1109/MWC.001.1900473.

[119] N. Jiang, Y. Deng, and A. Nallanathan, "Traffic prediction and random access control optimization: Learning and non-learning-based approaches," *IEEE Communications Magazine*, vol. 59, no. 3, pp. 16–22, 2021.

[120] C. Zhang, C. Zhang, W. Xia, R. Huang, H. Zhu, and Y. Huang, "Learning or non-learning: Effective access traffic prediction in random access," in *Proc. IEEE International Workshop on Radio Frequency and Antenna Technologies (iWRF&AT)*, 2024, pp. 180–185.

[121] H. Gupta, N. Srivastava, and L. Borman, "Optimized RACH procedure for low

earth orbit (LEO) satellites in non-terrestrial networks (NTN)," in *Proc. IEEE SPACE Conference*, 2025.

[122] J. Kim, C. You, and H. Park, "Optimization of reinforcement learning-based backoff indicator for 5G NR random access procedure," in *Proc. IEEE ICTC*, 2023, pp. 299–303.

[123] J.-H. Lee, H. Seo, J. Park, M. Bennis, and Y.-C. Ko, "Learning emergent random access protocol for LEO satellite networks," *IEEE Transactions on Wireless Communications*, vol. 22, no. 1, pp. 257–272, 2023.

[124] J.-H. Lee, H. Seo, J. Park, M. Bennis, Y.-C. Ko, and J. Kim, "Random access protocol learning in LEO satellite networks via reinforcement learning," in *Proc. IEEE VTC Spring*, 2022.

[125] F. Jiang, S. Ma, T.-Y. Yin, Y. Wang, and Y.-J. Hu, "An access control scheme combining Q-learning and compressive random access for satellite IoT," *IEEE Communications Letters*, vol. 27, no. 11, pp. 3008–3012, 2023.

[126] X. Liu, H. Zhang, K. Long, A. Nallanathan, and V. C. M. Leung, "Deep Dyna-reinforcement learning based on random access control in LEO satellite IoT networks," *IEEE Internet of Things Journal*, vol. 9, no. 16, pp. 14818–14828, 2022.

[127] L. Tello-Oquendo *et al.*, "Efficient Random Access Channel Evaluation and Load Estimation in LTE-A with Massive MTC," *IEEE Transactions on Vehicular Technology*, vol. 68, no. 2, pp. 1998 2002, Feb. 2019.

[128] G.-Y. Lin, S.-R. Chang, and H.-Y. Wei, "Estimation and Adaptation for Bursty LTE Random Access," *IEEE Transactions on Vehicular Technology*, vol. 65, no. 4, pp. 2560–2577, Apr. 2016.

[129] A. O. Elmeligy *et al.*, "Load Estimation in a Two-Priority mMTC Random Access," arXiv:2405.14667, 2024.

[130] A. Guidotti, A. Vanelli-Coralli, M. Conti, S. Andrenacci, S. Chatzinotas, N. Maturo, B. Evans, A. Awoseyila, A. Ugolini, T. Foggi, L. Gaudio, N. Alagha, and S. Cioni, "Architectures and key technical challenges for 5g systems incorporating satellites," IEEE Transactions on Vehicular Technology, vol. 68, no. 3, pp. 2624–2639, 2019.

[131] E. Dahlman, S. Parkvall, and J. Sköld, 4G: LTE/LTE-Advanced for Mobile Broadband. Amsterdam, Netherlands: Academic Press, 2011.

[132] G. Prasad, V. R. Chandrika, L. Lampe and G. Vos, "Enhanced Hybrid Automatic Repeat Request Scheduling for Non-Terrestrial IoT Networks," in IEEE Open Journal of the Communications Society, vol. 4, pp. 2802-2814, 2023.

[133] 3GPP, "Study on New Radio (NR) to Support Non-Terrestrial Networks (Release 15)," 3GPP TR 38.811, V15.4.0, Jul. 2020. [Online]. Available: https://www.3gpp.org/DynaReport/38811.htm

[134] S. Cioni, X. Lin, B. Chamaillard, M. El Jaafari, G. Charbit, and L. Raschkowski, "Physical layer enhancements in 5G-NR for direct access via satellite systems," International Journal of Satellite Communications and Networking, vol. 41, no. 3, pp. 262–275, 2023.

[135] "Solutions for NR to support non-terrestrial networks (NTN)," 3GPP, Technical Report TR 38.821, Dec. 2019, https://www.3gpp.org/DynaReport/38821.htm.

[136] G. A. Medina-Acosta et al., "3GPP Release-17 physical layer enhancements for LTE-M and NB-IoT," IEEE Commun. Standards Mag., vol. 6, no. 4, pp. 80–86,

Dec. 2022.

[137] 3GPP, “RP-251863 – Study on GNSS resilient NR-NTN operation”, 2025

[138] M. M. Azari et al., "Evolution of Non-Terrestrial Networks From 5G to 6G: A Survey," in *IEEE Communications Surveys & Tutorials*, vol. 24, no. 4, pp. 2633-2672, Fourthquarter 2022, doi: 10.1109/COMST.2022.3199901.

[139] S. Liu et al., "LEO Satellite Constellations for 5G and Beyond: How Will They Reshape Vertical Domains?," in *IEEE Communications Magazine*, vol. 59, no. 7, pp. 30-36, July 2021, doi: 10.1109/MCOM.001.2001081.

[140] Steven M. Kay, Fundamentals of Statistical Signal Processing: Detection theory, Prentice-Hall PTR, 1998, ISSN 1050-2769.

[141] Sonja Hiltunen, Pascal Chevalier, Titouan Petitpied, “New insights into time synchronization of MIMO systems without and with interference”, *Signal Processing*, Volume 161, 2019, Pages 180-194, ISSN 0165-1684, https://doi.org/10.1016/j.sigpro.2019.03.001.

[142] 3GPP TS 38.108; “3GPP; TS Group RAN; NR; UE radio transmission and reception; Part 5: Satellite access RF and performance requirements”, v19.0.0.

[143] H. Chougrani, S. Kisseleff, W. A. Martins and S. Chatzinotas, "NB-IoT Random Access for Nonterrestrial Networks: Preamble Detection and Uplink Synchronization," in *IEEE Internet of Things Journal*, vol. 9, no. 16, pp. 14913-14927, 15 Aug.15, 2022, doi: 10.1109/JIOT.2021.3123376.

[144] 3GPP TS 38.213; “3GPP; TS Group RAN; NR; Physical layer procedures for control (Release 18)”, v18.6.0.

[145] J. Zhu, Y. Sun and M. Peng, "Timing Advance Estimation in Low Earth Orbit Satellite Networks," *Timing Advance Estimation in Low Earth Orbit Satellite Networks,* vol. 73, no. 3, p. 4366–4382, 2024.

[146] 3GPP TS 38.211 ‘NR Physical channel and modulation’ v18.2.0 (2024-03)

[147] M. Caus and M. Shaat, "PRACH Signal Design and Detection for LEO Satellite Systems with Imperfect UE Positioning," in *27th International Workshop on Smart Antennas (WSA)*, 2024.

[148] G. Cui, Y. He, P. Li and W. Wang, "Enhanced Timing Advance Estimation With Symmetric Zadoff-Chu Sequences for Satellite Systems," IEEE Communications Letters, vol. 19, no. 5, p. 747–750, 2015.

[149] S. Huang, L. Zhao, M. Jiang and W. Liu, "Improved Preamble Detection and Round-Trip Delay Estimation for Random Access in High-Mobility Airborne Communication Systems," in IEEE/CIC International Conference on Communications in China (ICCC), 2019.

[150] S. Li and H.-M. Chen, "Design of Large Doppler Shift Mitigation in NTN Scenarios Through a Paired Index Based PRACH Transmission Scheme," in IEEE Wireless Communications and Networking Conference (WCNC), 2025.

[151] C. Zhang, W. Cao, Z. Yang, K. Tian and N. Zhang, "Random Access Preamble Design for Large Frequency Shift in Satellite Communication," in IEEE 2nd 5G World Forum (5GWF), 2019.

[152] C. Zhang, W. Cao, N. Zhang, K. Tian and R. Li, "Root Pair Selection for Two-root Random Access Preamble," in IEEE 93rd Vehicular Technology Conference (VTC2021-Spring), 2021.

[153] T. A. Khan and X. Lin, "Random Access Preamble Design for 3GPP Non-

terrestrial Networks," in 2021, IEEE Globecom Workshops (GC Wkshps).

[154] L. Zhen, T. Sun, G. Lu, K. Yu and R. Ding, "Preamble Design and Detection for 5G Enabled Satellite Random Access," IEEE Access, vol. 8, p. 49873–49884, 2020.

[155] L. Zhen, A. K. Bashir, K. Yu, Y. D. Al-Otaibi, C. H. Foh and P. Xiao, "Energy-Efficient Random Access for LEO Satellite-Assisted 6G Internet of Remote Things," IEEE Internet of Things Journal, vol. 8, no. 7, p. 5114–5128, 2021.

[156] H. Chen, P. Wang, S. Li, S. Lin, Z. Wang and C. Fang, "A Novel Preamble Design for 5G Enabled LEO Non-Terrestrial Networks," in GLOBECOM 2022 – IEEE Global Communications Conference, 2022.

[157] L. Zhen, H. Qin, B. Song, R. Ding, X. Du and M. Guizani, "Random Access Preamble Design and Detection for Mobile Satellite Communication Systems," IEEE Journal on Selected Areas in Communications, vol. 36, no. 2, pp. 280-291, 2018.

[158] Y. Chen, S. Huang and M. Jiang, "Preamble Design and Detection Based on Sequence Selection Pattern for Random Access in Non-Terrestrial Networks," IEEE Communications Letters, vol. 28, no. 10, p. 2357–2361, 2024.

[159] M. Caus, X. Artiga, M. Shaat and A. Guidotti, "GNSS Independent Random Access Schemes for Beam Hopping Satellite Systems," in 29th European Wireless Conference (European Wireless 2024), 2024.

[160] M. Caus, A. I. Pérez-Neira, J. Bas and L. Blanco, "New Satellite Random Access Preamble Design Based on Pruned DFT-Spread FBMC," IEEE Transactions on Communications, vol. 68, no. 7, p. 4592–4604, 2020.

[161] M. Caus and A. I. Pérez-Neira, "FBMC-Based Random Access Signal Design and Detection for LEO Base Stations," IEEE Transactions on Wireless Communications, vol. 22, no. 3, p. 2156–2170, 2023.

[162] A. K. Sinha, S. K. Mohammed, P. Raviteja, Y. Hong and E. Viterbo, "OTFS Based Random Access Preamble Transmission for High Mobility Scenarios," IEEE Transactions on Vehicular Technology, vol. 69, no. 12, p. 15078–15094, 2020.

[163] Hadani, R., et.al., “Orthogonal Time Frequency Space Modulation,” in IEEE Wireless Communications and Networking Conference, 2017.

[164] P. Raviteja, K. T. Phan, Y. Hong and E. Viterbo, "Interference Cancellation and Iterative Detection for Orthogonal Time Frequency Space Modulation," IEEE Transactions on Wireless Communications, vol. 17, no. 10, pp. 6501-6515, Oct. 2018.

[165] F. Lampel, A. Alvarado and F. M. Willems, "On OTFS Using the Discrete Zak Transform," 2022.

[166] N. Mazzali, S. Cioni and A. Ginesi, "Cyclic Prefix Reduction for 5G Non-Terrestrial Networks," in 12th Advanced Satellite Multimedia Systems Conference, 2025.

[167] S. Sesia, I. Toufik and M. Baker, "Random Access," in LTE – The UMTS Long Term Evolution: From Theory to Practice, Wiley, 2011, pp. 371-406.

[168] C. Rohde, N. Alagha, R. D. Gaudenzi, H. Stadali and G. Mocker, "Super-framing: A Powerful Physical Layer Frame Structure for Next Generation Satellite Broadband Systems," International Journal of Satellite Communications and Networking, vol. 34, no. 3, pp. 413-438, 2016.

[169] 3GPP; Technical Specification Group Radio Access Network;, "Solutions for NR to Support Non-Terrestrial Networks (NTN) (Release 16)," 3GPP TR 38.821.

[170] Thales, UNIBO, CTTC, DLR, ESA, ”R1-2506905 Discussion on waveform for 6GR air interface”

APPENDIX-A: OTFS SYSTEM AND RECIEVER MODELLING

AA.1 Transmitter

During the attachment procedure, the UE performs the PRACH processing. A schematic representation of the transmitter and the receiver block diagram is depicted in ***Figure 114***.

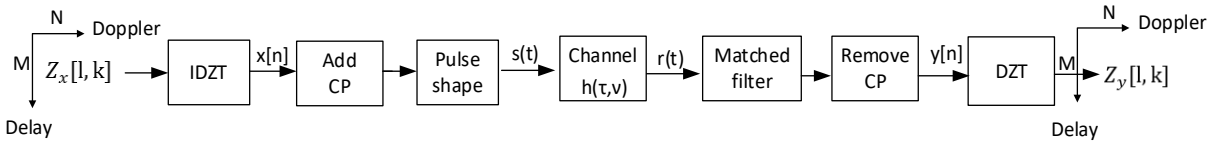

Figure 114: *DZT-OTFS transmitter and receiver block diagram*

In the first step, the UE maps MN preamble symbols into the DD plane, forming the matrix $Z_x[l,k]$. Here $l = 0,\cdots,M-1$ and $k = 0,\cdots,N-1$ denote the delay and the Doppler indices, respectively. The resolutions are given by $\frac{1}{M\Delta_f}$ for delay and $\frac{1}{NT}$ for Doppler. In this work, we restrict the analysis to the case of critical sampling, i.e., $\Delta_f T = 1$. The DD domain symbols are transformed into the time domain by applying the inverse DZT (IDZT), yielding the sequence

$$x[l+Mm] = \frac{1}{\sqrt{N}}\sum_{k=0}^{N-1} Z_x\,[l,k]e^{j\frac{2\pi}{N}km},$$

for $l = 0,\cdots,M-1$ and $m = 0,\cdots,N-1$. To achieve a circular structure and avoid interference from previous slots, a CP of length L_{CP} is appended at the beginning of the discrete-time sequence. At the output of the CP block, the sequence can be expressed as

$$x_c[n] = \begin{cases} x[(n)_{MN}] & n = -L_{\text{CP}},\cdots,MN-1 \\ 0 & \text{otherwise.} \end{cases}$$

The operation of a modulo n is represented by $(a)_n$. Then, the sequence $x_c[n]$ is shaped by the Nyquist filter $p(t)$, yielding a continuous time signal defined by

$$s(t) = \sum_{n=0}^{MN+L_{\text{CP}}-1} x_c\,[n-L_{\text{CP}}]p\left(t-n\frac{T}{M}\right).$$

The transmit pulse is defined for the symbol interval $\frac{T}{M}$ and spans a time duration of $2Q\frac{T}{M}$. The interval over which the pulse has support is defined such that $2Q \ll M$.

AA.2 Satellite channel model

This section models the impairments of the LEO satellite link. It must be underlined that in high-frequency bands, where directional antennas are needed, e.g., the Ka band, the multipath effect is usually weak. In such a case, the satellite channel is dominated by the LoS component. Thus, in the scenario under study, environmental

effects are not the primary source of signal degradation. Rather, the origin is the erroneous time and frequency compensation that results from the user position uncertainties. Bearing this in mind, the DD channel response is modeled as

$$h(\tau,\nu) = h_0\delta(\tau-\tau_0)\delta(\nu-\nu_0).$$

The link is characterized by the channel coefficient h_0, the delay τ_0, and the Doppler shift ν_0. It is important to remark that the offsets τ_0, ν_0 are directly induced by inaccuracies in the UE positioning. Adopting the model proposed in , the channel coefficient is formulated as

$$h_0 = \sqrt{\frac{G_{\text{UE}}G_{\text{SAT}}}{P_L K_B T_{\text{sys}} B}}\, e^{j\frac{2\pi}{\lambda}d_{\text{SAT-UE}}}.$$

The magnitude of the channel depends on typical gains and losses, i.e., the satellite antenna gain G_{SAT}, the UE antenna gain G_{UE}, the path loss P_L, the Boltzmann constant K_B, the bandwidth B and the system noise temperature T_{sys}. The satellite antenna gain is assumed to be constant over the uncertainty region. The phase term depends on the carrier wavelength λ and the slant range $d_{\text{SAT-UE}}$.

The time and the frequency misalignment are represented as a function of the DD resolutions as

$$\tau_0 = \frac{a_0+\alpha_0}{\Delta_f M} \qquad \nu_0 = \frac{k_0+\kappa_0}{TN},$$

where $a_0, k_0 \in \mathbb{Z}$ represent the integer components and $\alpha_0, \kappa_0 \in (-0.5, 0.5]$ are the fractional shifts.

AA.3 Receiver

The received signal is given by

$$\begin{aligned} r(t) &= \int_\tau \int_\nu h(\tau,\nu)s(t-\tau)e^{j2\pi\nu(t-\tau)}d\tau d\nu + w(t) \\ &= h_0 s(t-\tau_0)e^{j2\pi\nu_0(t-\tau_0)} + w(t). \end{aligned}$$

Since the channel is normalized to the noise variance, the additive noise $w(t)$ follows a white Gaussian stochastic model with unit power spectral density. As shown in ***Figure 114***, the received signal is passed through the matched filter, whose output is given by

$$y(t) = r(t) \star p^*(-t) = \int_\tau r(\tau)p^*(\tau-t)d\tau.$$

Sampling the output every $\frac{T}{M}$ seconds, we get $y\left((n+L_{\text{CP}})\frac{T}{M}\right) = y[n]$, for $n = 0, \cdots, MN-1$. Notice that the received signal is sampled with an offset of $L_{\text{CP}}\frac{T}{M}$ to discard the CP.

Assuming that the communication bandwidth is much larger than the maximum Doppler frequency shift, i.e., $M\Delta_f \gg \nu_0$, the following approximation holds

$$\int_{\tau} p\left(\tau - \tau_0 - n\frac{T}{M}\right) e^{j2\pi\nu_0(\tau-\tau_0)} p^*(\tau - t)d\tau \approx$$
$$e^{j2\pi\nu_0 n\frac{T}{M}} \int_{\tau} p\left(\tau - \tau_0 - n\frac{T}{M}\right) p^*(\tau - t)d\tau.$$

After further derivations, the received sequence becomes

$$y[n] = \sum_{m=0}^{MN+L_{\text{CP}}-1} h_0 R_p\left((n + L_{\text{CP}} - m)\frac{T}{M} - \tau_0\right) \times$$
$$x_c[m - L_{\text{CP}}] e^{j2\pi\nu_0 m\frac{T}{M}} + w[n],$$

where $R_p(t) = p(t) \star p^*(-t)$. Due to the Nyquist orthogonal transmission, the noise samples are independent and identically distributed (i.i.d.) random Gaussian variables, i.e., $w[n] \sim \mathcal{CN}(0,1)$.

Since the energy of $R_p(t)$ is concentrated around its main beam, only $2L + 1$ terms significantly contribute to interference, with $2L + 1 \ll MN$. Based on this premise, we can simplify the last equation as

$$y[n] = \sum_{i=-L}^{L} \beta[i] x_c[n - i - a_0] e^{j\frac{2\pi(k_0+\kappa_0)}{MN}(n-i-a_0)} + w[n]. \quad \text{(AA.1)}$$

To ease the analytical tractability, we define the coefficients that result from the fractionally spaced sampling by

$$\beta[i] = h_0 \times e^{j2\pi\nu_0 L_{\text{CP}}\frac{T}{M}} \times R_p\left((i - \alpha_0)\frac{T}{M}\right).$$

AA.4 Integer delay

When the delay is an integer multiple of the sampling period ($\alpha_0 = 0$), CP transmission results in a circular structure, and Eq. AA.1 simplifies to

$$y[n] = \beta[0] x[(n - a_0)_{MN}] e^{j\frac{2\pi(k_0+\kappa_0)}{MN}(n-a_0)} + w[n].$$

AA.5 Fractional delay

If fractional delays are present ($\alpha_0 \neq 0$), interference arises from negative and positive indices, i.e., $-L \leq i \leq L$. In this case, Eq. AA.1 is approximated to

$$y[n] \approx \sum_{i=-L}^{L} \beta[i] x[(n - i - a_0)_{MN}] e^{j\frac{2\pi(k_0+\kappa_0)}{MN}(n-i-a_0)} + w[n].$$

The equality holds true if the input sequence is defined as

$$x_c[n] = \begin{cases} x[(n)_{MN}] & n = -L_{\text{CP}}, \cdots, MN + L_{\text{CS}} - 1 \\ 0 & \text{otherwise.} \end{cases}$$

Note that, the received signal will exhibit circularity only if a cyclic suffix (CS) of length L_{CS} is appended to the transmitted sequence. However, to minimize overhead, CS is omitted in this work.

Regardless of the presence of fractional delays, the next step at the receiver is to apply the DZT to $y[n]$, yielding

$$Z_y[l,k] = \frac{1}{\sqrt{N}} \sum_{m=0}^{N-1} y\,[l+mM] e^{-j\frac{2\pi m}{N}k}, \qquad \text{(AA.2)}$$

for $l = 0, \cdots, M-1$ and $k = 0, \cdots, N-1$. Considering the mathematical framework developed in , the DD input-output relation can be expressed in the form of

$$Z_y[l,k] = \sum_{i=-L}^{L} \beta\,[i] Z_{y_i}[l,k] + Z_w[l,k],$$

where

$$Z_{y_i}[l,k] = \sum_{m=0}^{N-1} \sum_{q=0}^{M-1} Z_x\,[q,m] Z^{\tau}_{i+a_0}[l-q,k] Z^{v}_{k_0+\kappa_0}[q,k-m].$$

It is important to emphasize that the model considers the most general case, where the channel introduces fractional delays. Analogously to Eq. AA.2, $Z_w[l,k]$ denotes the DZT of the noise sequence $w[n]$. Since the DZT is a unitary transform, the statistical information of the noise is kept unchanged in the DD domain. Thus, the noise samples are independent and identically distributed as follows, $Z_w[l,k] \sim \mathcal{CN}(0,1)$. To complete the model, the DD spreading functions are formulated as

$$Z^{\tau}_a[l,k] = \frac{1}{\sqrt{N}} \sum_{m=0}^{N-1} \delta\,[l-a+Mm] e^{-j\frac{2\pi}{N}mk}$$

$$Z^{v}_b[l,k] = \frac{1}{\sqrt{N}} e^{j\frac{2\pi}{MN}bl} e^{j\frac{\pi}{N}(N-1)(b-k)} \frac{\sin\left(\pi(b-k)\right)}{\sin\left(\frac{\pi}{N}(b-k)\right)}.$$

An important aspect to highlight is that OTFS imposes constraints on time and frequency offsets to ensure reliable detection. As detailed in , the time and frequency misalignments are generally assumed to be bounded by $\tau_0 < T$ and $-\Delta_f/2 < \nu_0 < \Delta_f/2$. In the proposed model, these constraints translate into $a_0 < M$ and $-\frac{1}{2} < \frac{k_0+\kappa_0}{N} < \frac{1}{2}$. In the next section, we propose a new preamble structure specifically designed to handle scenarios with larger delays, that is, when $a_0 > M$.

APPENDIX-B: PRACTICAL IMPLEMENTATION AND ANALYSIS OF THE CORRELATION

Practical implementation

It is noteworthy to mention that the variable defined in Eq. 6.3.7 is the result of combining N circular convolutions. Therefore, $\rho_\upsilon(\mu,\gamma)$ can be efficiently implemented using IDFT and DFT blocks. To reduce the computational complexity, the sizes of DFT and IDFT blocks can be selected as a power of 2. The schematic view of the detector is shown in Figure 115.

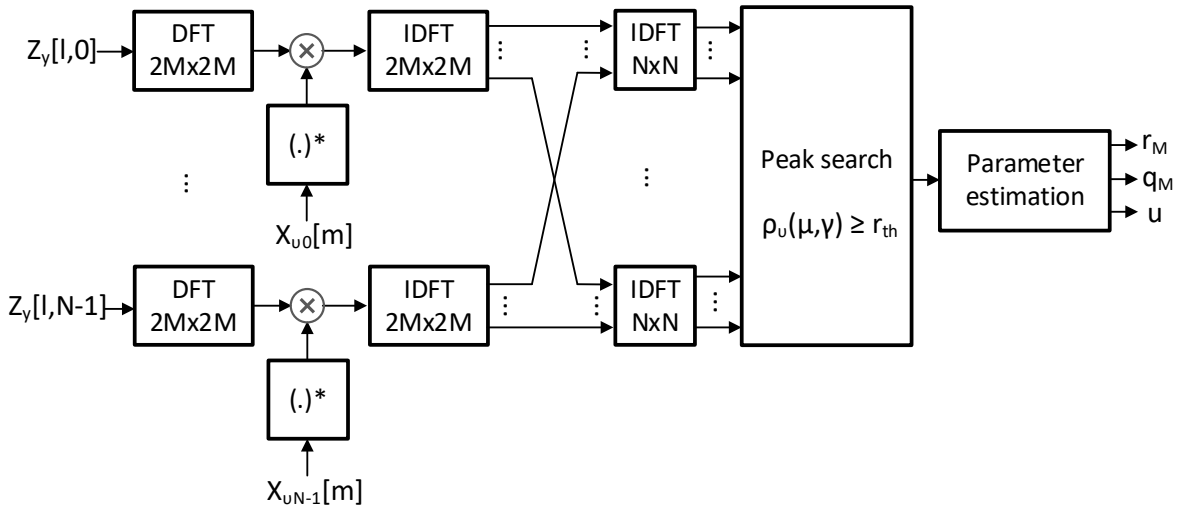

***Figure 115**: Detection scheme*

The whole processing is divided into four steps. The overall computational complexity can be analyzed by examining each step. First of all, the columns of $Z_y[l,k]$ are transformed by means of a DFT of size $2M$. This results in a complexity of $\mathcal{O}(VNM\log M)$, where V is the number of candidate ZC sequences. The next step is to compute the pointwise multiplication with $X^*_{\upsilon k}[m]$, which represents the DFT of $x^*_{\upsilon k}[-l]$. This operation has a linear complexity of $\mathcal{O}(VNM)$. Then, the resulting signal is transformed back to the delay domain by executing an IDFT of 2M points. Bearing in mind the range of μ, we just need to take the first M IDFT outputs, contributing with a complexity of $\mathcal{O}(VNM\log M)$. Finally, the signals processed in different Doppler bins are fed into an N-point IDFT to compute $\rho_\upsilon(\mu,\gamma)$, adding $\mathcal{O}(VMN\log N)$ to the complexity. Hence, the overall computational complexity is given by $\mathcal{O}\big(VNM\log(MN)\big)$.

In the detection scheme, the time resolution is $\frac{1}{M\Delta_f}$, which is controlled by the 2M-point IDFT. Hence, finer time resolution can be achieved by increasing the number of points.

The two-step detection approach has complexity of order $\mathcal{O}\big(VNM\log(M)\big)$ for estimating fractional delays. This fractional value is then used to shift the DFT window and capture integral ZC sequences. Upon applying this alignment, the integer component is obtained by detecting the boundaries of the random access signal. Given that the integer delay estimation involves additional demodulation steps and correlations, the overall complexity remains comparable to that of the proposed detector.

Analysis of the correlation

We start analyzing the special case where the delay is integer and the Doppler frequency shift is zero. In such a case, the most relevant finding is stated in Proposition 2.

Proposition 2. *Assuming that* $\alpha_0 = 0$, $k_0 + \kappa_0 = 0$ *and* $\upsilon = u$, *the correlation defined in Eq.* 6.3.8 *approximates an orthogonal function.*

To ascertain that the approximation is reasonably accurate, we particularize the correlation to $\alpha_0 = 0$, $k_0 + \kappa_0 = 0$ and $\upsilon = u$, yielding

$$C_u(\mu,\gamma) = \sum_{k=0}^{N-1}\sum_{l=0}^{M-1} h_0\, e^{j\frac{2\pi}{N}k(\gamma - q_M)} \times x_{uk}^*[(l-\mu)_{2M}]x_{uk}[(l-r_M)_{2M}].$$

To obtain the closed-form expression, we can exploit a key property of ZC sequences, whereby the cyclic shifted version of a root sequence satisfies $x_u((l+\mu)_M) \propto e^{-j\frac{2\pi}{M}u\mu l}x_u(l)$. Using this result, we get

$$|C_u(\mu,\gamma)| = \begin{cases} MN|h_0| & \mu = r_M, \gamma = q_M \\ \left|\sum_{l=0}^{|r_M-\mu|-1} N\, h_0 e^{j\frac{2\pi}{M}u(r_M-\mu)l}\right| & (\mu,\gamma) \in \mathbb{S}_{\mu,\gamma} \\ 0 & \text{otherwise,} \end{cases}$$

where

$$\mathbb{S}_{\mu,\gamma} = \{\{\mu \neq r_M, \gamma = q_M\} \cup \{\mu > r_M, \gamma = (q_M - 1)_N\} \cup \{\mu < r_M, \gamma = (q_M + 1)_N\}\}.$$

This result reveals that many correlation entries are zero, facilitating detection. From the non-zero entries, it can be inferred that pseudo-peaks may still emerge. In this regard, Figure 116 shows that the power ratio between the main peak and the main pseudo-peak is always higher than 10 dB. The higher the power ratio, the better the correlation characteristics.

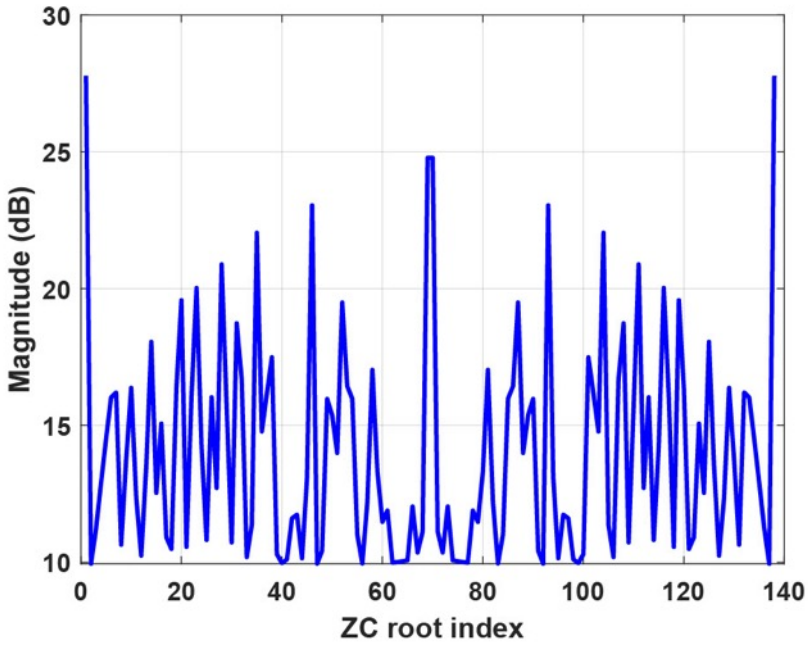

Figure 116: *Power ratio between the main peak and the main pseudo-peak as function of the ZC root index, for M=139*

In light of the above discussion, we can conclude that the approximation stated in Proposition 2 holds true.

Moving beyond ideal conditions, it is worth analyzing the case where the fractional delay is not equal to zero, i.e., $\alpha_0 \neq 0$. In such event, we can infer from Proposition 2 that correlation peaks emerge at $\mu = \{-L + r_M, \cdots, L + r_M\}$ and $\gamma = q_M$. Since the magnitude of $\beta[i]$ will reach the maximum value at $i = 0$, it follows that the highest correlation peak will be observed at $\mu = r_M$. In this specific case, i.e., when $i = 0$, the condition $0 \leq i + r_M \leq M - 1$ is always satisfied. Hence, it is not necessary to address the special cases where $i + r_M < 0$ or $i + r_M > M - 1$. It deserves to be mentioned that in the most detrimental situation where $\alpha = \pm 0.5$, the magnitude of $\beta[0]$ takes the lowest possible value, which depends on the pulse autocorrelation function. Another issue worth considering is the small power imbalance between $\rho_u(r_M, q_M)$ and $\rho_u(r_M \pm 1, q_M)$, for $\alpha = \pm 0.5$. In this situation, the detector may select a peak that is adjacent to the true value. Accordingly, the wrong detection translates into a timing error that is equal to $\pm \frac{1}{M\Delta_f}$. An important conclusion that can be drawn from this analysis is that the performance of the detector will be degraded in the presence of fractional delays.

Concerning the adverse effects induced by the CFO, it becomes evident that as $k_0 + \kappa_0$ increases, the power of the main peak reduces. That is because the energy will spread to all lag indices μ. Under these conditions, the correlation at $\mu = r_M$ and $\gamma = q_M$ becomes

$$C_u(r_M, q_M) = N\beta[0] \frac{\sin\left(\frac{\pi(k_0+\kappa_0)}{N}\right)}{\sin\left(\frac{\pi(k_0+\kappa_0)}{MN}\right)} e^{j\frac{\pi(k_0+\kappa_0)(M-1)}{MN}} + \sum_{k=0}^{N-1} \sum_{i\neq 0} \sum_{l=0}^{M-1} \beta\,[i] x_{uk}^*[(l - r_M)_{2M}] \times x_{uk}[(l - i - r_M)_{2M}] e^{j\frac{2\pi(k_0+\kappa_0)}{MN}l}.$$

The combined effects of the fractional delay and the CFO may cause difficulty in detecting the peak and eventually leading to erroneous detection. To limit the performance degradation that results from the CFO, the waveform parameters shall be set so that $\left|\frac{k_0+\kappa_0}{N}\right| < 1/2$. Otherwise, the main peak could be excessively attenuated, rendering the detector ineffective.

APPENDIX C: GENERALITIES ON THE USE OF ARTIFICIAL INTELLIGENCE IN COMMUNICATION SYSTEMS

Conventionally **Artificial intelligence (AI)** is a broad term that encompasses a wide set of algorithms that have the ability of emulating "cognitive" behaviours that would be associated with sentient being's mind, such as learning, reasoning, problem solving, perception etc. In recent years this is more specifically used to refer to algorithms that learn from data to perform tasks without explicit programming.

The conventional engineering and signal processing design flow consists of using mathematical models which are considered to capture the physics of the problem at hand, and then in developing an optimal or a sub-optimal algorithm with provable performance guarantees (given that the model is accurate). These techniques are known as **model-driven AI**.

On the other hand, **machine learning (ML),** core branch of AI, relies more on observing a system, and collecting data from it by finding patterns in it, rather than acquiring its knowledge from a model. These algorithms learn to perform tasks without explicit instructions, relying instead on patterns and inference. Collected data are used as a **training set** for a learning algorithm, in order to generate a "black-box" machine that is based on a **hypothesis class**. This set is necessarily obtained through some system assumptions that enable the selection of some category of possible models; these assumptions are known as the **inductive bias**. These techniques will be also called **data-driven AI**.

For various practical problems, combining model-driven and data-driven approaches, along with some partial knowledge of the system enables leveraging the performance and complexity trade-off of AI strategies. These techniques with restrictive but well-tailored architectures are referred as **hybrid AI**.

Learning algorithms go through the hypothesis class by evaluating a loss function with a training data set, in order to find the machine that minimizes the loss. Broadly, AI techniques are categorized by learning paradigm: **supervised learning** uses labeled input–output examples to train a model (minimizing prediction error); **unsupervised learning** finds hidden patterns or structure in unlabeled data; and **reinforcement learning** (RL) trains agents to take actions by trial and error to maximize cumulative reward. The latter uses a feedback loop on the machine's actions on the environment, to provide some sort of partial supervision. These paradigms have seen rapid advances in recent decades, from early rule-based systems to modern neural network approaches.

A trained machine is subject to the problem of **underfitting** if the model is not rich enough to capture the variations on the training data. Another extreme situation appears when the machine operates well with the training data, but fails over a distinct validation set, this is called **overfitting**.

Towards 6G standardization and NTN integration

6G is envisioned to be a transformative leap beyond 5G, aiming to provide ubiquitous connectivity, seamless integration of terrestrial and non-terrestrial networks (NTNs), and support for advanced applications such as holographic communications, autonomous systems, and intelligent networks. The standardization process for 6G is still in its early stages, with research and development efforts focused on identifying key technologies and use cases that will define the next generation of wireless communication systems.

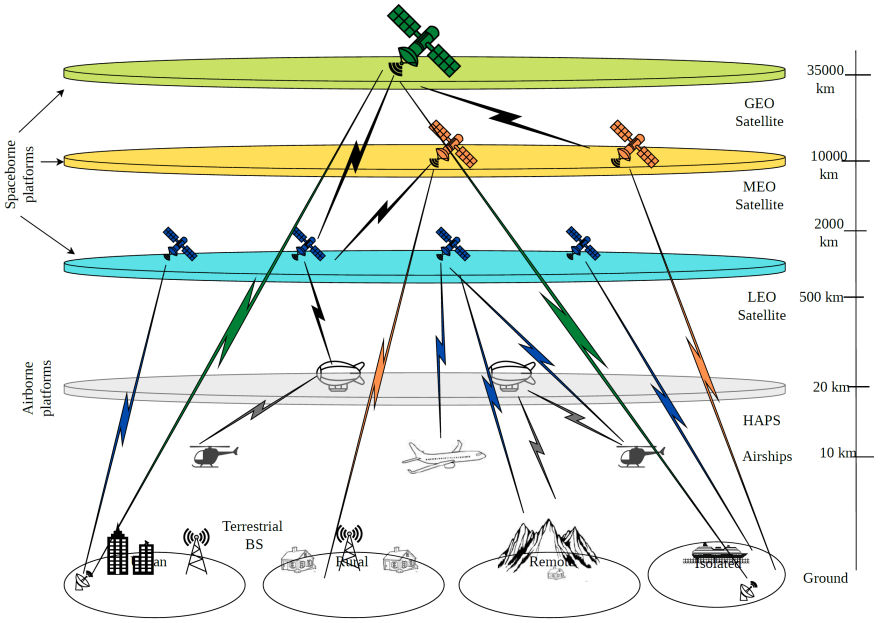

Figure 117: *An illustration of different NTN components possibly involved in 6G*

The integration of NTNs with terrestrial networks presents unique challenges and opportunities for 6G standardization.
Let us elaborate on the NTN use cases that can complement and enhance terrestrial networks:

- NTNs can provide connectivity in remote and rural areas where terrestrial infrastructure is limited or non-existent, this improving **global coverage**. This is particularly important for applications such as IoT, environmental monitoring, and disaster response. Naturally there will be a trade-off between the cost of deployment and the achieved coverage: lower orbit satellites are significantly smaller and easier to deploy, but cover smaller areas and require elaborate signal processing procedures for satellite tracking.
- By integrating satellite and aerial systems, NTNs can offload traffic from terrestrial networks, improving overall **network capacity** and performance. In particular, as the user trends shift from broadcasting services (e.g. television) toward broadband Internet access, conventional satellite operations will shift towards much more flexible and user-specific streaming services. Handling such high capacity transmissions through NTNs would leave more resources on terrestrial networks to address latency-critical services.
- NTNs can provide backup connectivity in case of terrestrial network failures, ensuring continuous service availability and enhancing network **resilience**. With the development of inter-satellite link (ISL) technology and high-altitude platform stations (HAPSs), a novel landscape is available for network deployment, enabling various options for data buffering and **redundancy**.

Naturally, these advantages of NTNs do not come without significant challenges. The integration of NTNs require coping with additional latency due to the long propagation delays in satellite channels which makes synchronization procedures much more critical for real-time applications. The movement of satellites and aerial platforms introduces Doppler shifts, which can affect signal quality and require advanced compensation techniques. This phenomenon is at its peak at the LEO satellites where in addition the problem of handover and beam allocation pose significant challenges. And finally, the coexistence of terrestrial and non-terrestrial networks can lead to interference issues, requiring sophisticated interference management and mitigation strategies.

Hence, the standardization of 6G and the integration of NTNs present both opportunities and challenges. The development of advanced waveforms and the addressing of technical issues will be crucial for realizing the full potential of 6G and providing seamless, ubiquitous connectivity. The physical layer of 6G networks will need to support diverse use cases and operating environments, including NTNs.

The challenges of NTNs on these waveform candidates include **managing latency, compensating for Doppler shifts, and ensuring robust performance in dynamic and heterogeneous environments**. In the remainder we will investigate how AI might provide practical solutions in this regard.

The integration of AI into NTNs is essential for addressing the unique challenges posed by these networks, such as high latency, Doppler shifts, and complex spectrum sharing. Several surveys and studies have explored the application of AI in NTNs, highlighting its potential to revolutionize satellite and aerial communications [47]-[62].